



The  
University  
Of  
Sheffield.

ANALYSIS OF MATERIAL DEFORMATION AND  
FRACTURE MECHANISM IN INCREMENTAL  
SHEET FORMING BY SIMPLIFIED TESTING  
METHODS

Sheng Ai

Supervisor: Prof. Hui Long

Dissertation submitted to the Department of Mechanical Engineering, the  
University of Sheffield in partial fulfilment of the requirements for the  
degree of Doctor of Philosophy

February 2020



## SUMMARY

Incremental sheet forming (ISF) has seen its increasing applications in the sheet metal manufacturing industry in the last decades due to its unique characteristics of process flexibility and enhanced material formability. For single point incremental sheet forming (SPIF), its improved formability is attributed to the localized material deformation caused by a combination of tension, bending, shearing and cyclic loading. For double side incremental sheet forming (DSIF), the deployment of a rear tool introduces an additional compressive loading onto the material, which further strengthens the localized deformation. However, the complicated loading conditions and contact conditions prohibit a systematic and direct analysis of the factors affecting material formability in ISF, especially in DSIF. Furthermore, traditional testing methods have been proved incapable to explain the significant formability enhancement in ISF.

In this research, to investigate the material deformation characteristics in ISF process, SPIF tests using material AA5251-H22 and AA6082-T6 were conducted. To explore damage accumulation in ISF, finite element (FE) damage modelling of ISF process using shear-modified GTN model with AA5251-H22 was developed. By tracing the evolution history of strain and shear-induced damage indicator of target elements in the FE simulation results, bending, shearing and localized deformation were confirmed in both SPIF and DSIF processes. However, comparing the forming depth of the conic parts obtained from the experiment and the FE model, it was found that shear-modified GTN model predicted premature fracture in ISF processes for material AA5251-H22, possibly because of the complicated loading conditions or the material type investigated.

Material formability can be influenced by material properties, loading conditions as well as loading path. In order to investigate the effect of these three factors on material formability enhancement in ISF, two novel testing methods have been proposed in this research. To investigate the effect of individual deformation modes on the material deformation behaviour, a new testing method called Tension under Cyclic Bending and Compression (TCBC) test was developed. In this test, the complicated 3-dimensional geometrical constraints in ISF process was simplified into 2-dimensional. Moreover, the magnitude of the tension, bending, compression and cyclic loading can be explicitly varied by changing corresponding process parameters in the test. Testing rig was developed based on the proposed concept. Two materials, AA5251-H22 and AA6082-T6

were used in the test. By implementing the Taguchi Design of the Experiment, the significance and relative significance of these deformation modes were investigated. According to the statistical analysis of the experimental results, compression was the most significant factor affecting material formability in the test. Material AA5251-H22 showed higher sensitivity to the loading conditions, compared with AA6082-T6. Localized deformation and bending effect were also observed by tracing the strain and damage evolution of the elements during the test in the FE modelling of the test. Suppression of damage and postponement of fracture of the specimens in the TCBC tests were also observed, which can also be attributed to the localized material deformation. It was confirmed that the TCBC test was an appropriate representation of the ISF process.

To further investigate the effect of loading path onto the material deformation behaviour in ISF, another testing method called Biaxial Tension under Bending and Compression (BTBC) test was proposed. Testing rig was developed accordingly. In the BTBC test, instead of uniaxial tension, the cruciform specimen can be stretched in all four directions and the strain ratio of the two perpendicular directions can be varied. The effect of compression, bending and cyclic loading can also be adjusted. Deformation behaviour of the material aluminium alloy AA5251-H22 under two strain conditions, the plane strain and the equi-biaxial tension, were tested. Different combinations of the deformation modes were investigated in each test. The formability of the material in different tests was compared by measuring the distortion of circular grids inscribed onto the surface of the specimen. According to the experimental results and FE simulation results, the introduction of bending and compression contributed to material localized deformation. Material formability could be enhanced by the introduction of bending effect, which could be further improved by additional compression and the cyclic loading effect. The degree of formability improvement under different loading paths was different. Under plane strain condition, material formability can be progressively improved by introducing the deformation modes step by step. While under equi-biaxial tension condition, introducing compression and cyclic loading into bending did not necessarily lead to formability improvement. BTBC test provides more insight into the material deformation characterization of ISF process.

Overall, in this research, the developed two simplified testing methods, the TCBC test and the BTBC test overcome the limitation of current commonly adopted material testing methods and the ISF test. The testing methods provide a fundamental explanation of the

effect of material properties, loading conditions and loading path on the material deformation and fracture behavior in ISF.

## ACKNOWLEDGEMENTS

Thank you to my supervisor, Dr. Hui Long for your invaluable guidance and support on both my academic project and life for the last three years.

Thank you to the Faculty of Engineering, the University of Sheffield for offering me the Faculty Scholarship and the opportunity to study in this prestigious university.

Thank you to Jamie Booth, David Webster and Gareth Barker from the department mechanical workshop, Michael Herbert and Chris Todd from the department electronics workshop. Without your technical advice and work, the whole project will be just on the paper.

Thank you to Dr. Hengan Ou from The University of Nottingham and Dr. Bin Lu for the valuable advice and generous support on the project.

Thank you to all my friends in the UK and from home, your encouragement has always been the source keeping me looking forward. Life would have been more difficult and monotonous than what it should be without you.

Deepest gratitude to my parents and sisters, you are the solid standing ground I am on so that I have always been fearless and always optimistic about the future.

## PUBLICATIONS DURING PH.D. STUDY

1. Ai, S., Dai, R. and Long, H., Investigating formability enhancement in double side incremental forming by developing a new test method of tension under cyclic bending and compression. *Journal of Materials Processing Technology*, 2019. <https://doi.org/10.1016/j.jmatprotec.2019.116349>
2. Ai, S. and Long, H., *A review on material fracture mechanism in incremental sheet forming*. *The International Journal of Advanced Manufacturing Technology*, 2019. <https://doi.org/10.1007/s00170-019-03682-6>
3. Ai, S., et al., 2017. *Evaluation of deformation stability and fracture mechanism in incremental sheet forming*. *International Journal of Mechanical Sciences*, **124**, pp.174-184.
4. Ai, S. and Long, H., 2019. Finite element modelling of material deformation and damage by tension under cyclic bending and compression test. In *AIP Conference Proceedings (Vol. 2113, No. 1, p. 180012)*. AIP Publishing.
5. Ai, S., Lu, B. and Long, H., 2017. An analytical study of new material test method for tension under bending and compression in double side incremental forming. *Procedia engineering*, **207**, pp.1982-1987.
6. Lu, B., Bazeer, M.M., Cao, J.F., Ai, S., et al., 2017. *A study of incremental sheet forming by using water jet*. *The International Journal of Advanced Manufacturing Technology*, **91**(5-8), pp.2291-2301.

# CONTENTS

<b>1 INTRODUCTION.....</b>	<b>1</b>
1.1 RESEARCH BACKGROUND .....	1
1.1.1 Introduction to ISF.....	1
1.1.2 Classification of ISF .....	4
1.1.3 Improved material formability in ISF .....	6
1.1.4 Factors affecting material formability.....	7
1.2 CURRENT RESEARCH GAPS AND CHALLENGES .....	8
1.3 RESEARCH AIMS AND OBJECTIVES .....	9
1.4 RESEARCH NOVELTY .....	10
1.5 THESIS LAYOUT AND STRUCTURE .....	11
<b>2 LITERATURE REVIEW.....</b>	<b>12</b>
2.1 DEFORMATION AND FRACTURE MECHANISM OF ISF .....	12
2.1.1 Single point incremental sheet forming .....	13
2.1.2 Double side incremental sheet forming .....	31
2.2 MATERIAL TESTING METHODS FOR SHEET METAL .....	35
2.2.1 Uniaxial tensile test.....	35
2.2.2 Biaxial tensile tests .....	37
2.2.3 Other test methods for sheet metal.....	47
2.3 PREDICTION OF FAILURE IN SHEET METAL FORMING PROCESSES .....	50
2.3.1 Forming limit diagram.....	50
2.3.2 Damage theories and damage modelling .....	52
2.3.3 Damage modelling of ISF process .....	56
2.4 SHEAR-MODIFIED GTN MODEL AND ITS APPLICATION .....	58
2.4.1 Introduction to the GTN model .....	59
2.4.2 Shear-modified GTN model .....	60
2.4.3 Application of GTN model in FE modelling .....	61
2.5 SUMMARY .....	67
<b>3 EXPERIMENTAL INVESTIGATION AND FE MODELLING OF ISF .....</b>	<b>69</b>
3.1 EXPERIMENTAL ANALYSIS OF MATERIAL FORMABILITY IN ISF.....	69
3.1.1 Design of the experiment.....	70
3.1.2 Experimental procedure.....	72
3.2 COEFFICIENT CALIBRATION IN SHEAR-MODIFIED GTN MODEL.....	73

3.2.1	<i>Verification of the developed subroutine</i>	73
3.2.2	<i>Coefficient calibration in the original GTN model</i>	75
3.2.3	<i>Calibration of shear-related coefficient</i>	85
3.3	FE MODELLING OF ISF PROCESSES	91
3.4	EXPERIMENTAL AND FE MODELLING RESULTS	93
3.4.1	<i>Experimental results</i>	93
3.4.2	<i>FE modelling results</i>	94
3.5	DISCUSSION	101
3.5.1	<i>Deformation characteristics of ISF</i>	101
3.5.2	<i>FE damage modelling of ISF</i>	103
3.5.3	<i>Coefficient calibration for the shear-modified GTN model</i>	105
3.6	SUMMARY	107
<b>4</b>	<b>TENSION UNDER CYCLIC BENDING AND COMPRESSION TEST</b>	<b>108</b>
4.1	TCBC TEST	108
4.1.1	<i>Concept of the TCBC test</i>	110
4.1.2	<i>Design of the TCBC Testing Rig</i>	112
4.2	THEORETICAL ANALYSIS OF THE TCBC TEST	113
4.3	DESIGN OF THE EXPERIMENT AND TESTING PROCEDURES	118
4.3.1	<i>Design of the experiment</i>	118
4.3.2	<i>Experimental procedures</i>	123
4.4	EXPERIMENTAL RESULTS	123
4.4.1	<i>Comparison of tested specimens under different loading conditions</i>	123
4.4.2	<i>Effects of individual process parameters in TCBC test</i>	126
4.4.3	<i>Investigation into the compression and bending effect</i>	128
4.5	FE DAMAGE MODELLING OF TCBC TEST	131
4.5.1	<i>FE modelling of TCBC process</i>	132
4.5.2	<i>FE modelling results</i>	133
4.6	DISCUSSION	141
4.6.1	<i>Effect of investigated deformation modes in the TCBC test</i>	141
4.6.2	<i>Limitations of current TCBC test</i>	144
4.7	SUMMARY	146
<b>5</b>	<b>BIAXIAL TENSION UNDER BENDING AND COMPRESSION TEST</b>	<b>148</b>
5.1	CONCEPT OF BTBC TEST AND RIG DEVELOPMENT	148
5.1.1	<i>Concept of BTBC test</i>	149
5.1.2	<i>Development of BTBC test rig</i>	150

5.2 OPTIMIZATION OF CRUCIFORM SPECIMEN .....	155
5.2.1 <i>Design of the cruciform specimen</i> .....	155
5.2.2 <i>FE optimization of the geometry</i> .....	156
5.2.3 <i>Optimization results</i> .....	158
5.3 DESIGN OF THE EXPERIMENT AND EXPERIMENTAL PROCEDURES .....	162
5.3.1 <i>Design of the experiment</i> .....	162
5.3.2 <i>Experimental procedures</i> .....	164
5.4 EXPERIMENTAL RESULTS .....	164
5.4.1 <i>Plane strain condition</i> .....	164
5.4.2 <i>Equi-biaxial tension condition</i> .....	168
5.5 FE MODELLING OF BTBC TEST .....	172
5.5.1 <i>FE model development</i> .....	173
5.5.2 <i>FE modelling results</i> .....	174
5.6 DISCUSSION.....	181
5.6.1 <i>The effect of BTBC loading conditions on material formability</i> .....	181
5.6.2 <i>Limitations of current test</i> .....	182
5.7 SUMMARY .....	183
<b>6 CONCLUSION AND PERSPECTIVES FOR FUTURE WORK.....</b>	<b>184</b>
6.1 CONCLUSION .....	184
6.1.1 <i>Summary</i> .....	185
6.1.2 <i>Contribution to the Knowledge</i> .....	187
6.2 PERSPECTIVES FOR FUTURE WORK .....	188
<b>7 REFERENCES.....</b>	<b>190</b>
<b>8 APPENDICES .....</b>	<b>205</b>

# LIST OF TABLES

TABLE 3.1 MATERIAL PROPERTIES AND VALUES OF THE COEFFICIENTS USED IN THE VERIFICATION MODEL .....	73
TABLE 3.2 HARDENING LAWS AND CORRESPONDING FITTED VALUES OF THE COEFFICIENTS FOR AA5251-H22.....	76
TABLE 3.3 VALUES OF GTN COEFFICIENTS IN LITERATURE .....	78
TABLE 3.4 RANGES OF THE GTN COEFFICIENTS INVESTIGATED .....	79
TABLE 3.5 TEST RUNS BASED ON CCD.....	79
TABLE 4.1 VARIATION RANGES OF TEST PARAMETERS IN THE SECOND STAGE TCBC EXPERIMENT.....	120
TABLE 4.2 MIXED-LEVEL TAGUCHI DESIGN OF THE EXPERIMENTS FOR AA5251-H22 ..	121
TABLE 4.3 MIXED-LEVEL TAGUCHI DESIGN OF THE EXPERIMENTS FOR AA6082-T6.....	122
TABLE 5.1 RANGES OF THE VALUES OF THE PARAMETERS TO BE OPTIMIZED FOR THE CRUCIFORM SPECIMEN.....	157
TABLE 5.2 DESIGN OF THE EXPERIMENT IN THE BTBC TEST .....	162
TABLE 5.3 VALUES OF THE PROCESS PARAMETERS IN THE BTBC TEST .....	163

# LIST OF FIGURES

FIGURE 1.1 SCHEMATICS OF SOME CONVENTIONAL SHEET METAL FORMING PROCESSES...	2
FIGURE 1.2 SCHEMATIC OF A RECONFIGURABLE DIE SYSTEM [4]: (A) A SIMPLIFIED CROSS-SECTION VIEW OF THE SYSTEM; (B) STRUCTURE OF SINGLE SMALL-SIZED DIE .....	2
FIGURE 1.3 EXAMPLES OF ISF PROCESS CONFIGURATION AND ITS APPLICATIONS: (A) ISF USING A CNC MILLING MACHINE [10]; (B) AEROSPACE CRAWLING; (C) HONDA S800 HOOD MADE BY AMINO [11]; (D) COMPLICATED GEOMETRIES [12]; (E) TITANIUM CRANIAL PLATE [13] .....	3
FIGURE 1.4 CLASSIFICATION OF ISF PROCESSES.....	4
FIGURE 1.5 STRONG SPRINGBACK OF TITANIUM SHEET OF DENTURE PART AFTER TRIMMING [27].....	5
FIGURE 1.6 COMPARISON BETWEEN FLCs FOR CONVENTIONAL FORMING PROCESS AND SPIF FOR MATERIAL AA1050 [37] .....	6
FIGURE 2.1 SCHEMATIC COMPARISON OF PROCESS CONFIGURATIONS BETWEEN SPIF, TPIF AND SHEAR SPINNING [55]: (A) SPIF; (B) TPIF; (C) SHEAR SPINNING.....	13
FIGURE 2.2 CROSS-SECTIONS OF THE DEFORMED PARTS WITH INSCRIBED GRIDS IN DIFFERENT SHEET METAL FORMING PROCESSES [55]: (A) SPIF; (B) TPIF; (C) PRESSING .....	14
FIGURE 2.3 STRAIN COMPONENTS OF ELEMENTS ALONG THE THICKNESS DIRECTION IN FE RESULTS OF SPIF PROCESS [61] .....	16
FIGURE 2.4 SCHEMATIC OF DEFORMATION MECHANISM FOR SPIF .....	17
FIGURE 2.5 THE CBT TEST [48]: (A) SCHEMATIC OF THE CBT TEST; (B)PART OF THE DESIGNED CBT TEST RIG; (C) A COMPARISON BETWEEN UNTESTED SPECIMEN, TESTED SPECIMEN FROM UNIAXIAL TENSILE TEST AND TESTED SPECIMEN FROM CBT TEST USING MATERIAL DC04; (D) MICRO-CRACKS OBSERVED ON THE SURFACE OF THE FRACTURED DC04 SPECIMEN TESTED IN THE CBT TEST .....	18
FIGURE 2.6 FRACTURE MORPHOLOGY OF THE CRACK IN A FRACTURED CONIC PART MADE BY SPIF USING MATERIAL AA1100 [60]: (A) OVERVIEW OF THE MICRO STRUCTURE OF THE CRACK SURFACE; (B) CLOSE OBSERVATION OF THE DISTRIBUTION OF DIMPLES IN THE CRACK SURFACE.....	19

FIGURE 2.7 ZIGZAG SHAPED CRACK IN A FRACTURED CONIC PART IN SPIF: (A)-(D) CRACK INITIATION AND PROPAGATION IN THE PART IN FOUR CONSECUTIVE STEPS WITH MATERIAL AA1100 OBSERVED WITH HIGH SPEED CAMERA [60]; (E) SCHEMATIC OF THE CRACK PROPAGATION PROCESS ON THE BASIS OF THE STRESS STATE [77] .....	20
FIGURE 2.8 DEVELOPMENT OF THE ZIGZAG PATTERN CRACK [78]: (A) ORIENTATION OF THE MAXIMUM PLASTIC STRAIN; (B) PROPAGATION OF THE ZIGZAG CRACK.....	21
FIGURE 2.9 THICKNESS VARIATION ALONG THE DEPTH OF FRACTURED PART MADE BY ALUMINIUM ALLOY [6] .....	21
FIGURE 2.10 FLCs, FFLs OBTAINED FROM MATERIAL PROPERTY TESTS AND THE ISF TESTS USING MATERIAL AA1050-H111 BY: (A) SILVA ET AL. [75] ; (B) ISIK ET AL. [80]....	22
FIGURE 2.11 COMPARISON BETWEEN THE FFLs OBTAINED FROM CONVENTIONAL MATERIAL TESTS AND SPIF TESTS FOR: (A) AA1100; (B) AA5052-O [82] .....	23
FIGURE 2.12 FRACTURE AND PRECEDENT NECKING IN THE INCREMENTAL GROOVE TEST USING DC04 [86] .....	24
FIGURE 2.13 SCHEMATIC OF THE NECK LOSING CONTACT WITH THE TOOL [87].....	24
FIGURE 2.14 MICRO CRACKS ABOVE THE FINAL CRACK IN THE PART MADE BY AN ALUMINIUM ALLOY USING SPIF PROCESS [52] .....	25
FIGURE 2.15 SCHEMATIC OF THE NOODLE THEORY PROPOSED BY MALHOTRA ET AL. [64]: (A) ORIGINAL SPECIMEN; (B) DEVELOPMENT OF NECKING IN CONVENTIONAL FORMING PROCESS; (C) FINAL FRACTURE IN CONVENTIONAL FORMING PROCESS; (D) INITIATION OF THE FIRST NECKING IN SPIF PROCESS; (E)-(F) DEVELOPMENT OF MULTIPLE NECKING DURING SPIF PROCESS .....	25
FIGURE 2.16 TWO DIFFERENT TYPES OF FAILURE IN SPIF WITH DIFFERENT INCREMENTAL TOOL RATIOS AND TOOL RADII: (A) FRACTURE WITH SUPPRESSION OF NECKING AND (B) FRACTURE WITH NECKING [84] .....	26
FIGURE 2.17 CROSS-SECTIONAL VIEW OF THE FRACTURE REGION FOR THE MATERIAL AA1100: (A) CONIC PART IN ISF TEST; (B) PYRAMID PART IN ISF TEST; (C) BULGE TEST PART UNDER PLANE-STRAIN CONDITION; (D) BULGE TEST PART UNDER EQUI-BIAXIAL TENSION CONDITION [82] .....	27
FIGURE 2.18 CROSS-SECTIONAL VIEW OF THE FRACTURE REGION FOR THE MATERIAL AA5052: (A) CONIC PART IN ISF TEST; (B) PYRAMID PART IN THE ISF TEST; (C) BULGE	

TEST PART UNDER PLANE-STRAIN CONDITION; (D) BULGE TEST PART UNDER EQUI-BIAXIAL TENSION CONDITION [82] .....	28
FIGURE 2.19 NAKAZIMA TESTS EQUIPMENT AND SPECIMENS [88]: (A) THE EQUIPMENT; (B) SCHEMATIC OF THE TEST CONFIGURATION; (C) SPECIMENS BEFORE AND AFTER TESTS .....	29
FIGURE 2.20 M-N DIAGRAM WITH RELATION TO THE FAILURE MODE IN TENSION UNDER BENDING [89].....	30
FIGURE 2.21 M-N DIAGRAM WITH RELATION TO THE FAILURE MODE IN TENSION UNDER BENDING [90].....	30
FIGURE 2.22 SCHEMATIC OF DIFFERENT DEFORMATION MODES IN DSIF.....	31
FIGURE 2.23 COMPARISON OF STRESS TRIAXIALITY ALONG THE STRAIN EVOLUTION BETWEEN DSIF AND SPIF[30]: (A) DSIF; (B)SPIF .....	32
FIGURE 2.24 INFLUENCE OF SUPPORTING FORCE IN DSIF USING MATERIAL AA7075-T6 [30]: (A) FRACTURE DEPTHS OF THE CONES WITH VARIED SUPPORTING FORCE; (B) SURFACE MARKS ON THE PART .....	32
FIGURE 2.25 INFLUENCE OF CONTACT FORCE AND RELATIVE POSITIONS BETWEEN THE TOOLS ON THE MATERIAL FORMABILITY DSIF [93]: (A) SCHEMATIC OF THE TOOL POSITIONS; (B) ACHIEVED DEPTHS OF HYPERBOLIC PARTS WITH VARIED CONTACT FORCE AND SHIFTING ANGLES USING MATERIAL ALMn 99.81HH.....	33
FIGURE 2.26 FORMING LIMITS OF MATERIAL AA7075 IN DSIF WITH DIFFERENT RELATIVE LOCATIONS AND DIFFERENT SUPPORTING FORCES [30].....	33
FIGURE 2.27 DEFORMATION ZONES IN DSIF AND ITS EFFECT ON THE FRACTURE INITIATION [94]: (A) DISTRIBUTION OF THE DEFORMATION ZONES IN THE CONTACT AREA; (B) SCHEMATIC OF THE SHEAR STRESS COMPONENTS IN ZONE III AND THE LOCATION OF CRACK INITIATION.....	34
FIGURE 2.28 PART FRACTURE WITH DIFFERENT RELATIVE LOCATIONS BETWEEN THE MASTER TOOL AND THE REAR TOOL [30]: (A) WITH TOOL SHIFT; (B) WITHOUT TOOL SHIFT.....	35
FIGURE 2.29 GEOMETRY OF THE SPECIMEN IN UNIAXIAL TENSILE TEST IN ASTM-E8 STANDARD [95].....	36

FIGURE 2.30 A SCHEMATIC OF BIAXIAL TENSILE TESTS: (A) HYDRAULIC BULGE TEST [101]; (B) DOME TEST [102] .....	38
FIGURE 2.31 NAKAZIMA TEST: (A) SPECIMEN GEOMETRY; (B) SCHEMATIC OF THE FLC OBTAINED FROM THE TEST WITH DIFFERENT STRAIN CONDITIONS OBTAINED BY USING DIFFERENT GEOMETRIES .....	38
FIGURE 2.32 COMPARISON OF FLOW CURVES UNDER FRICTIONLESS DOME, BULGE AND TENSILE TESTS USING DIFFERENT MATERIALS [101]: (A) AL5182-O; (B) JAC 270E; (C) TRIP 980; (D) TRIP 1180 .....	39
FIGURE 2.33 A SCHEMATIC OF THE MARCINIAK TEST [44] .....	39
FIGURE 2.34 STANDARD SHAPE PROPOSED IN ISO 16842 STANDARD [105] .....	41
FIGURE 2.35 CRUCIFORM SPECIMEN DESIGN OPTIMIZED BY ZIDANE ET AL.[113].....	42
FIGURE 2.36 PARAMETERS OF THE SPECIMEN OPTIMIZED IN [114] .....	42
FIGURE 2.37 THIN CRUCIFORM SPECIMENS WITH THICKNESS REDUCTION IN THE CENTRE PROPOSED : (A) GREEN ET AL. [115]; (B) SHAO [116].....	43
FIGURE 2.38 GEOMETRY OF THE THIN CRUCIFORM SPECIMEN OPTIMIZED BY SONG [112] .....	44
FIGURE 2.39 BIAXIAL TENSILE PLATFORMS WITH FIXED STRAIN RATIOS DEVELOPED BY: (A) FERRON ET AL. [117]; (B) MERKLEIN ET AL. [119].....	45
FIGURE 2.40 IN-PLANE BIAXIAL TENSILE TEST PLATFORM DESIGNED BY MAKINDE ET AL. [121].....	46
FIGURE 2.41 BIAXIAL TENSILE TEST PLATFORM DEVELOPED BY THE COMPANY ZWICK/ROELL [122].....	47
FIGURE 2.42 THE SHEAR TEST SETUP AND SPECIMEN GEOMETRY FOR: (A) MIYAUCHI TEST; (B) MODIFIED ASTM-B831 TEST; (C) TWIN-BRIDGE TEST [123].....	48
FIGURE 2.43 CYCLIC TESTS: (A) CYCLIC TENSION-COMPRESSION TEST CONDUCTED BY YOSHIDA ET AL. [128]; (B) CYCLIC TEST USING A CRUCIFORM SPECIMEN BY CLÁUDIO AND FREITAS [129] .....	49
FIGURE 2.44 A COMPARISON BETWEEN DIFFERENT TYPES OF FLDs: (A) THE STRAIN-BASED FLD; (B) STRESS BASED FLD [144] .....	52
FIGURE 2.45 NET AREA REDUCTION IN THE CDM CONCEPT [149].....	53

FIGURE 2.46 AN ILLUSTRATION OF THE EVOLUTION OF THE VOIDS IN THE MATERIAL DURING MATERIAL DEFORMATION [78] .....	54
FIGURE 2.47 COMPARISON OF THE CRACK LOCATIONS IN THE FE DAMAGE MODELLING RESULT AND THE EXPERIMENT BY GATEA ET AL. [67] .....	58
FIGURE 2.48 FLOW CHART FOR THE DEVELOPMENT OF GTN VUMAT SUBROUTINE .....	66
FIGURE 3.1 GEOMETRY OF THE TEST SPECIMEN AND TOOLPATH: (A) CAD MODEL OF THE TEST SPECIMEN; (B) SCHEMATIC OF THE GENERATED TOOLPATH USE IN THE SPIF TEST .....	70
FIGURE 3.2 EXPERIMENTAL SET-UP OF SPIF PROCESS ON A CNC MACHINE.....	71
FIGURE 3.3 GEOMETRY OF THE SPECIMEN FOR UNIAXIAL TENSILE TEST AND THE OBTAINED FORCE-DISPLACEMENT CURVES FOR MATERIAL AA5251-H22 AND AA6082-T6.....	72
FIGURE 3.4 LOADING CONDITION FOR THE ELEMENT IN THE VERIFICATION MODEL FOR THE GTN MODEL .....	74
FIGURE 3.5 COMPARISON OF EVOLUTION OF VVF FROM THEORETICAL CALCULATION AND THE PREDICTION BY THE DEVELOPED GTN MODEL .....	74
FIGURE 3.6 FLOW STRESS CURVE FITTING FOR AA5251-H22: (A) COMPARISON BETWEEN DIFFERENT HARDENING LAWS AND THE EXPERIMENTAL DATA; (B) EXTENDED FLOW STRESS CURVE PREDICTED BY THE VOCE LAW .....	77
FIGURE 3.7 MESH CONVERGENCE TEST FOR THE UNIAXIAL TENSILE TEST FE MODEL: (A) COMPARISON BETWEEN THE DISPLACEMENT-LOAD CURVES OBTAINED FROM DIFFERENT SIZES OF MESH; (B) FINAL MESH OF THE SPECIMEN .....	82
FIGURE 3.8 FE MODELLING OF THE UNIAXIAL TENSILE TEST WITH THE GTN MODEL USING THE OPTIMIZED COEFFICIENTS: (A) COMPARISON BETWEEN DISPLACEMENT-LOAD CURVES OBTAINED FROM THE EXPERIMENT AND FE MODELLING; (B) EVOLUTION OF VVF (SDV2) IN THE FE MODEL.....	84
FIGURE 3.9 ASTM-B831-14 STANDARD PURE SHEAR SPECIMEN FOR THIN ALUMINIUM SHEET [126] .....	86
FIGURE 3.10 MODIFIED ASTM STANDARD SPECIMEN PROPOSED BY KANG ET AL. [216]	86
FIGURE 3.11 IN-PLANE PURE SHEAR SPECIMENS: (A) GEOMETRY PROPOSED BY GAO ET AL. [217]; (B) MODIFIED GEOMETRY PROPOSED BY SUN ET AL. [218].....	87

FIGURE 3.12 THE PURE SHEAR TEST: (A) THE PURE SHEAR TEST; (B) FRACTURED SPECIMEN .....	88
FIGURE 3.13 PLANAR STRAIN DISTRIBUTION IN THE PURE SHEAR SPECIMEN ACCORDING TO DIC MEASUREMENT IN DIFFERENT DIRECTIONS: (A) XY DIRECTION; (B) Y DIRECTION .....	89
FIGURE 3.14 STRAIN PATHS OF THE THREE ELEMENTS IN FE MODELLING OF THE PURE SHEAR TEST .....	89
FIGURE 3.15 COMPARISON BETWEEN DISPLACEMENT-LOAD CURVES OBTAINED FROM THE EXPERIMENT AND FE SIMULATIONS WITH VARIED VALUES OF $kw$ .....	90
FIGURE 3.16 FE MODELLING OF THE ISF PROCESS: (A) SPIF; (B) DSIF; (C) TOP VIEW OF THE MODELS .....	92
FIGURE 3.17 FRACTURED CONIC PARTS MADE BY SPIF: (A) AA5251-H22; (B) AA6082-T6 .....	94
FIGURE 3.18 HISTORY OF RATIO OF BLANK DEFORMATION KINETIC ENERGY TO INTERNAL ENERGY IN THE ISF FE MODELS .....	95
FIGURE 3.19 EVOLUTION OF VVF (SDV2) IN THE CONIC PARTS MADE BY SPIF USING AA5251-H22.....	96
FIGURE 3.20 STRAIN AND VVF EVOLUTION IN SPIF MODELLING OF ELEMENT 45201 ....	97
FIGURE 3.21 VON MISES STRESS DISTRIBUTION IN SPIF ON: (A) INNER SURFACE; (B) OUTER SURFACE .....	97
FIGURE 3.22 EVOLUTION OF VVF IN SPIF MODELLING OF ELEMENTS ALONG THE THICKNESS DIRECTION .....	98
FIGURE 3.23 FE DAMAGE MODELLING RESULTS FOR DSIF: (A) FRACTURE LOCATION; (B) EVOLUTION OF EQUIVALENT PLASTIC STRAIN, VVF AND VVF COMPONENTS IN ELEMENT 29847; (C) EVOLUTION OF VVF IN THE FOUR ELEMENTS ALONG THE THICKNESS DIRECTION .....	99
FIGURE 3.24 VON MISES STRESS DISTRIBUTION IN DSIF ON: (A) INNER SURFACE; (B) OUTER SURFACE .....	100
FIGURE 3.25 STRAIN PATH EVOLUTION OF THE ELEMENT .....	101

FIGURE 3.26 RESPONSE VALUES ON THE EXPERIMENTAL TRUE STRESS-STRAIN CURVE [169] .....	106
FIGURE 4.1 SCHEMATIC OF THE TCBC TEST: (A) SIMPLIFIED CONFIGURATION OF THE TCBC TEST; (B) THE BENDING AND COMPRESSION COMPONENT MOVES TO ONE SIDE OF THE DESIGNED TRAVELLING PATH; (C) THE BENDING AND COMPRESSION COMPONENT MOVES TO THE OTHER SIDE OF THE DESIGNED TRAVELLING PATH.....	111
FIGURE 4.2 KEY COMPONENTS OF THE TCBC TEST RIG .....	112
FIGURE 4.3 CAD SCHEMATIC OF THE LOADING DEVICE .....	113
FIGURE 4.4 SCHEMATIC OF THE SIMPLIFIED THEORETICAL ANALYSIS MODEL: (A) THE SELECTED ELEMENT IN CONTACT REGION FOR ANALYSIS; (B) SCHEMATIC OF THE CONTACT CONDITIONS IN TCBC TEST; (C) STRESS COMPONENTS APPLIED ONTO THE SELECTED ELEMENT .....	115
FIGURE 4.5 THEORETICAL ANALYSIS RESULTS OF THE INFLUENCE OF THE KEY PARAMETERS ON THE TENSILE STRESS: (A) 3D PLOT; (B) TOP VIEW OF THE 3D PLOT .....	116
FIGURE 4.6 SCHEMATICS OF DIFFERENT COMBINATIONS OF LOADING CONDITIONS.....	119
FIGURE 4.7 ELONGATION OF TESTED SPECIMENS UNDER DIFFERENT LOADING CONDITIONS .....	124
FIGURE 4.8 DISPLACEMENT-FORCE CURVES RECORDED FROM TESTS UNDER DIFFERENT LOADING CONDITIONS .....	125
FIGURE 4.9 MAIN EFFECT PLOT FOR THE FACTORS FOR THE MEAN IN TCBC TEST.....	127
FIGURE 4.10 THE INFLUENCE OF COMPRESSION ON THE MAXIMUM ELONGATION IN TCBC .....	129
FIGURE 4.11 MAXIMUM ELONGATION UNDER DIFFERENT COMPRESSION FORCES WITH VARYING: (A) BENDING DEPTH; (B) SPECIMEN THICKNESS .....	131
FIGURE 4.12 FE MODELLING OF TCBC TEST.....	132
FIGURE 4.13 COMPARISON OF MAXIMUM ELONGATIONS OF THE SPECIMENS IN THE TCB AND TCBC TESTS IN THE FE DAMAGE MODELLING AND EXPERIMENT .....	133
FIGURE 4.14 FORCE-DISPLACEMENT CURVES RECORDED FROM TESTS UNDER DIFFERENT LOADING CONDITIONS .....	134

FIGURE 4.15 EVOLUTION OF VVF (SDV2) OF ELEMENTS IN THE THICKNESS DIRECTION IN TCB DAMAGE MODELLING IN THE LAST THREE STEPS UPON FRACTURE .....	135
FIGURE 4.16 EVOLUTION OF EQUIVALENT PLASTIC STRAIN AND VVF OF THREE ELEMENTS AT THE CRACK LOCATION ALONG THE THICKNESS DIRECTION IN DAMAGE MODELLING OF: (A) TCB TEST; (B) TCBC TEST.....	136
FIGURE 4.17 EVOLUTION OF EQUIVALENT PLASTIC STRAINS OF ELEMENTS IN THE THICKNESS DIRECTION IN TCBC AND TCB MODELLING .....	138
FIGURE 4.18 STRESS DISTRIBUTION (MPA) IN THE SPECIMENS IN THE LONGITUDINAL DIRECTION DURING THE UNIFORM MATERIAL DEFORMATION: (A) TCBC TEST CONCAVE SIDE; (B) TCBC TEST CONVEX SIDE; (C) TCB TEST CONCAVE SIDE; (D) TCB TEST CONVEX SIDE .....	139
FIGURE 4.19 STRAIN PATHS OF ELEMENTS IN FE MODELLING OF TCBC AND TCB TESTS .....	140
FIGURE 4.20 DISTRIBUTION OF THE STRESS IN THE THICKNESS DIRECTION IN THE FE RESULT .....	142
FIGURE 4.21 SCHEMATIC OF THE RELATIVE TOOL POSITIONS IN DSIF: (A) TWO ROLLERS SUPPORTING EACH OTHER WITHOUT SHIFT; (B) TWO ROLLERS OPPOSING EACH OTHER WITH A SHIFTING ANGLE OF $\alpha$ .....	145
FIGURE 5.1 SCHEMATIC OF BIAXIAL TENSION UNDER BENDING AND COMPRESSION TEST .....	150
FIGURE 5.2 DEVELOPED BTBC TEST PLATFORM: (A) FULL ASSEMBLY; (B) CAD DESIGN OF THE MECHANICAL STRUCTURE .....	151
FIGURE 5.3 THE BIAXIAL TENSION LOADING COMPONENTS: (A) CAD REPRESENTATION OF THE BIAXIAL LOADING COMPONENTS; (B) CAD DRAWING OF THE BIDIRECTIONAL LINEAR SCREW SLIDER; .....	152
FIGURE 5.4 EXPLOSIVE VIEW OF THE BENDING AND COMPRESSION APPLICATION STRUCTURE IN THE BTBC TEST RIG .....	155
FIGURE 5.5 GEOMETRY OF THE CRUCIFORM SPECIMEN TO BE OPTIMIZED.....	156
FIGURE 5.6 FE MODEL OF THE CRUCIFORM SPECIMEN GEOMETRY OPTIMIZATION .....	156
FIGURE 5.7 EQUIVALENT PLASTIC STRAIN DISTRIBUTION IN THE SPECIMEN WITH DIFFERENT ARM WIDTHS: (A) 30 MM; (B) 32MM; (C) 34MM .....	158

FIGURE 5.8 EQUIVALENT PLASTIC STRAIN DISTRIBUTION IN THE SPECIMEN WITH DIFFERENT RADII OF THE CENTRAL AREA: (A) 10 MM; (B) 9 MM .....	159
FIGURE 5.9 STRAIN DISTRIBUTION IN THE SPECIMEN WITH DIFFERENT NUMBERS OF SLOTS IN THE ARMS: (A) 3 SLOTS; (B) 4 SLOTS; (C) 5 SLOTS; (D) 6 SLOTS .....	160
FIGURE 5.10 OPTIMIZED GEOMETRY OF THE CRUCIFORM SPECIMEN.....	161
FIGURE 5.11 GRID INSCRIBED ONTO THE SURFACE OF THE CRUCIFORM SPECIMEN .....	161
FIGURE 5.12 MEASUREMENT OF THE RADII OF THE UNDEFORMED CIRCLES WITH THE PORTABLE MICROSCOPE .....	164
FIGURE 5.13 SPECIMENS AFTER DEFORMATION UNDER PLANE STRAIN CONDITION: (A) PURE TENSION; (B) TENSION AND BENDING; (C) TENSION, BENDING AND CYCLIC LOADING; (D) TENSION, BENDING AND COMPRESSION; (E) TENSION, BENDING, COMPRESSION AND CYCLIC LOADING.....	166
FIGURE 5.14 DEFORMED CIRCLES ON THE SPECIMEN SURFACE UNDER PLANE STRAIN DEFORMATION: (A) PURE TENSION; (B) TENSION AND BENDING; (C) TENSION, BENDING AND CYCLIC LOADING; (D) TENSION, BENDING AND COMPRESSION; (E) TENSION, BENDING, COMPRESSION AND CYCLIC LOADING .....	167
FIGURE 5.15 FORMABILITY IMPROVEMENT UNDER BTBC LOADING CONDITIONS AND PLANE STRAIN CONDITION.....	168
FIGURE 5.16 SPECIMENS AFTER DEFORMATION UNDER EQUI-BIAXIAL TENSION CONDITION: (A) PURE TENSION; (B) TENSION AND BENDING; (C) TENSION, BENDING AND CYCLIC LOADING; (D) TENSION, BENDING AND COMPRESSION; (E) TENSION, BENDING, COMPRESSION AND CYCLIC LOADING .....	169
FIGURE 5.17 DEFORMED CIRCLES ON THE SPECIMEN SURFACE IN BTBC TEST UNDER EQUI-BIAXIAL TENSION CONDITION: (A) PURE TENSION; (B) TENSION AND BENDING; (C) TENSION, BENDING AND CYCLIC LOADING; (D) TENSION, BENDING AND COMPRESSION; (E) TENSION, BENDING, COMPRESSION AND CYCLIC LOADING .....	170
FIGURE 5.18 FORMABILITY IMPROVEMENT UNDER BTBC LOADING CONDITIONS AND EQUI-BIAXIAL CONDITION .....	171
FIGURE 5.19 SCHEMATIC OF THE LOADING ON TO THE SLIDERS DURING THE TEST .....	172
FIGURE 5.20 FE MODELLING OF BTBC TEST.....	173



## LIST OF ABBREVIATIONS AND ACRONYMS

ISF	Incremental sheet forming
SPIF	Single point incremental sheet forming
TPIF	Two point incremental sheet forming
DSIF	Double side incremental sheet forming
ADSIF	Accumulative-double side incremental sheet forming
FE	Finite element
GTN	Gurson-Tvergaard-Needleman model
TCBC	Tension under cyclic bending and compression
BTBC	Biaxial tension under bending and compression
CBT	Continuous bending under tension
TCB	Tension under cyclic bending
TCC	Tension under compression
TTS	Through-thickness-shear
M-K	Marciniak-Kuczyński
FLC/FLD	Forming limit curve/diagram
FFLC/FFLD	Fracture forming limit curve/diagram
S-FLC	Stress-based forming limit curve
SEM	Scanning electron microscope
DIC	Digital image correlation
CDM	Continuum damage mechanics
MDM	Micromechanical damage mechanics
VVF	Void volume fraction
UMAT	User-defined material mechanical behaviour
VUMAT	Vectorised user-defined material mechanical behaviour
RSM	Response surface method
CCD	Central composite design

GA

Genetic algorithm

EDM

Electrical discharge machining

## LIST OF NOMENCLATURES

$\sigma_{\varphi}^A$	Tensile stress in the longitudinal direction (MPa)
$\sigma_t$	Contact stress between the bending roller and the specimen (MPa)
$\sigma_c$	Compressive contact stress between compression roller and specimen (MPa)
$\sigma_s$	Flow stress of the material (MPa)
$r_t$	Radius of the bending roller and the compression roller (mm)
$w$	Width of the specimen (mm)
$\varphi$	Contact angle between bending roller and the specimen (rad)
$t$	Thickness of the specimen under deformation (mm)
$\mu$	Friction factor between the tools and the specimen
$\varepsilon_l$	Strain of the specimen in the longitudinal direction
$v_t$	Tensile speed (mm/s)
$v_s$	Stroke speed (mm/s)
$\sigma_{eq}$	von Mises equivalent stress (MPa)
$\sigma_0$	Microscopic equivalent yield stress in GTN model (MPa)
$\sigma_m$	Mean stress (MPa)
$\sigma_h$	Hydrostatic stress (MPa)
$f$	Void volume fraction in GTN model
$f^*$	Modified void volume fraction
$f_0$	Original void volume fraction before the material plastically deformed
$f_c$	Critical void volume fraction indicating the start of void coalescence
$f_f$	Void volume fraction at fracture
$\dot{f}$	Void volume fraction growth rate ( $s^{-1}$ )
$\dot{f}_g$	Growth rate of the existing voids ( $s^{-1}$ )
$\dot{f}_n$	Growth rate of new voids due to void nucleation ( $s^{-1}$ )
$\dot{f}_s$	Shear-related void shape distortion rate under plastic deformation ( $s^{-1}$ )

$\varepsilon^p$	Equivalent microscopic plastic strain
$\varepsilon_N$	Mean nucleation strain
$S_N$	Standard deviation
$k_w$	Shear related coefficient in the Nahshon-Hutchinson extension
$\dot{\varepsilon}_{kk}^p$	Plastic strain rate component
$J_3$	The third invariant of the stress
$q_{i(i=1,2,3)}$	Parameters to account for the interaction between voids in GTN model
$s_{i(i=1,2,3)}$	Deviatoric stress tensor in the principal plane (MPa)
$s_{ij(i,j=1,2,3)}$	Deviatoric stress tensor (MPa)
$C^e$	Elastic modulus
$\varepsilon^e$	Elastic strain tensor
$G$	Shear modulus
$K$	Volume modulus
$\lambda$	Lame constant

# LIST OF APPENDICES

APPENDIX 1 SUBROUTINE FOR SHEAR-MODIFIED GTN MODEL..... 206

Equation Chapter (Next) Section 1

# 1 INTRODUCTION

Incremental sheet forming (ISF) process provides an alternative manufacturing route to conventional sheet metal forming processes. Its advantages of high process flexibility and the ability to manufacture complex geometries have attracted research interests from both academia and industry. Material formability is significantly improved in ISF compared with conventional sheet metal forming processes. In this chapter, the ISF process will first be introduced in Section 1.1. With an outline review of the current research on material formability, the research gaps of ISF and corresponding challenges will be discussed in Section 1.2, based on which research aims and objectives will be proposed in Section 1.3 and research novelty will be summarized in Section 1.4. Thesis layout will be outlined in Section 1.5.

## 1.1 Research Background

### 1.1.1 Introduction to ISF

Sheet metal forming technology has been evolving for thousands of years. According to DIN 8582 standard [1], conventional sheet metal forming processes can be classified into different categories, including deep drawing, blanking and bending, based on the main deformation stress applied on the sheet. Simplified schematics of some conventional sheet metal forming processes are shown in Figure 1.1. For all these processes, customised dies and tools are required to manufacture specific geometries. As a result, the cost of the manufacturing and lead time can be considerably high even before entering the production stage. According to a study of die manufacturing in the automotive industry conducted by Altan et al. [2] in 2001, for just the interior components, up to 0.5 million

US dollars and 6 to 9 months were needed to manufacture dies and to ensure the robustness of the dies. For mass production, these costs can be split over large quantities of products so that the high investment cost can be justified. However, for the prototype or customization applications, normally limited quantity of products with unique features are required and a short cycle time is desired, traditional manufacturing processes can be both time and resource consuming.

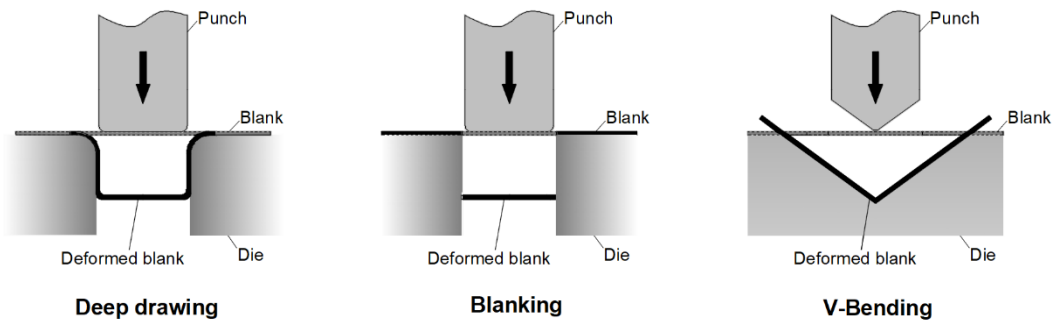


Figure 1.1 Schematics of some conventional sheet metal forming processes

The need to reduce manufacturing cost and to speed up manufacturing process gives birth to the flexible forming processes, in which traditional dies are no longer required. In one flexible forming process, the traditional dies are discretised into multiple reconfigurable dies of small size [3, 4]. As shown in Figure 1.2, the positions of discrete dies can be rearranged to fit the shapes of different geometries before the manufacturing process. In this way, the reconfigurable die system can be reused for products with different geometries, the manufacturing cost and lead time can be reduced.

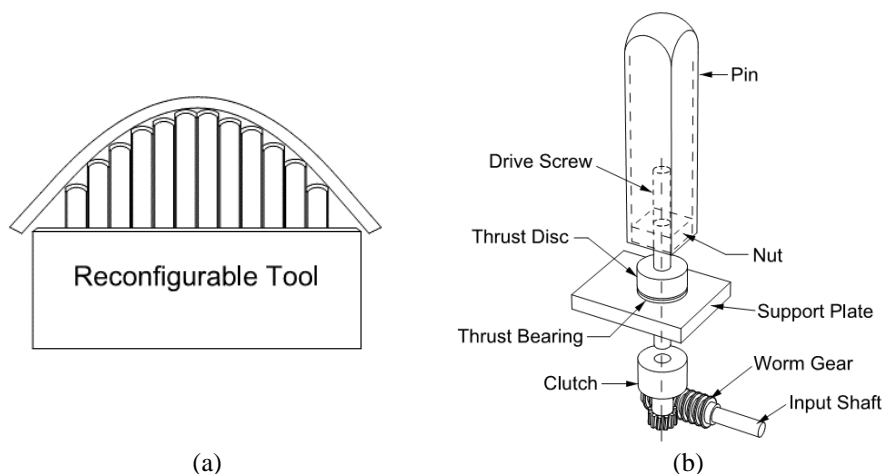


Figure 1.2 Schematic of a reconfigurable die system [4]: (a) a simplified cross-section view of the system; (b) structure of single small-sized die

However, rearranging the positions of the multiple tools in the reconfigurable die system prior to the manufacturing process requires trial and error or a highly delicate automated

system. Nevertheless, the forming accuracy of the manufactured part can still inevitably be compromised due to the unevenness of the surface formed by the discrete dies [5].

One step further, incremental sheet metal forming (ISF) process breaks away completely from using dies. In single point incremental sheet forming (SPIF), only one tool with a simple geometry is required. The tool moves along predefined toolpaths and gradually deforms the clamped sheet metal into a desired shape. As shown in Figure 1.3 (a), a typical SPIF configuration only requires four essential equipment, including a CNC machine, a set of clamping tools, a backing plate and a forming tool. The forming tool is controlled by the CNC machine. Different shapes of parts can be directly manufactured out of their CAD drawings with corresponding toolpaths in the same set-up, making the ISF process highly flexible.

Preparation for an ISF process is minimal. The typical forming tool for ISF is a steel cylinder with a hemispherical head. For simple geometries, for example conic parts, the coordinates in the toolpath can be calculated mathematically. While for more complicated shapes, the toolpath can be generated directly from the CAD designs of the parts with the help of traditional CAM software [6, 7] or specifically developed toolpath generation algorithms [8, 9].

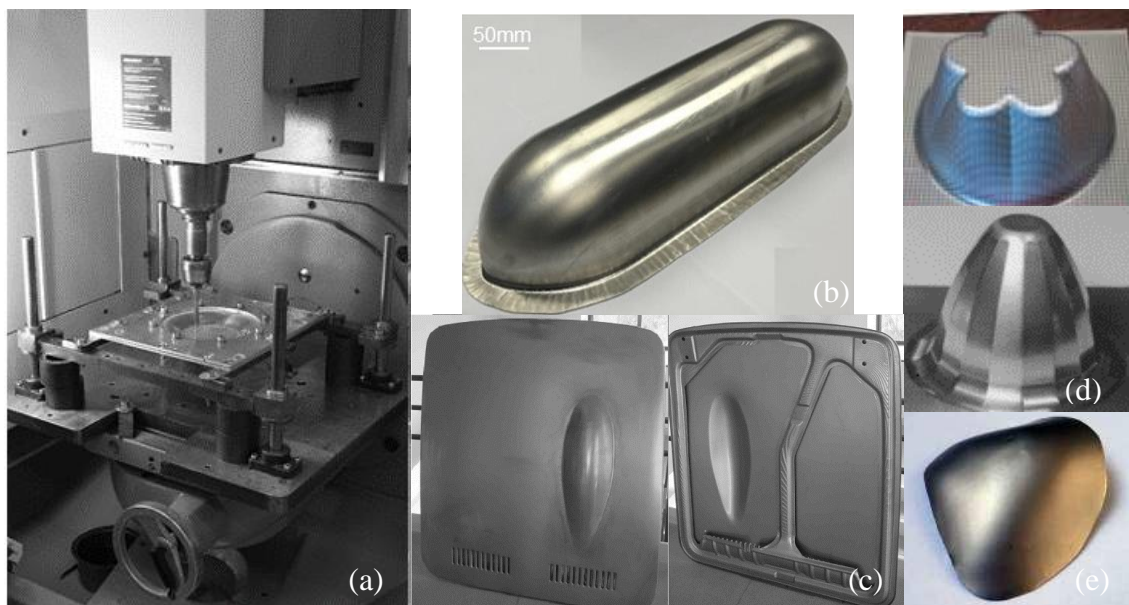


Figure 1.3 Examples of ISF process configuration and its applications: (a) ISF using a CNC milling machine [10]; (b) aerospace crawling; (c) Honda S800 hood made by Amino [11]; (d) complicated geometries [12]; (e) titanium cranial plate [13]

The ISF technology was first patented by Leszak [14] in 1967 and its further development was reviewed by Emmens et al. [15] in 2010 and recently by Li et al. [16] and Behera et

al. [17] in 2017. It has been successfully applied in automotive [11, 12, 18], aerospace [19] and medical [13, 20] applications, a few examples of the ISF applications for various industries are shown in Figure 1.3.

### 1.1.2 Classification of ISF

According to the number of the tools deployed in the process, ISF can be classified into single point incremental forming (SPIF), two point incremental forming (TPIF) and double side incremental forming (DSIF), as shown in Figure 1.4.

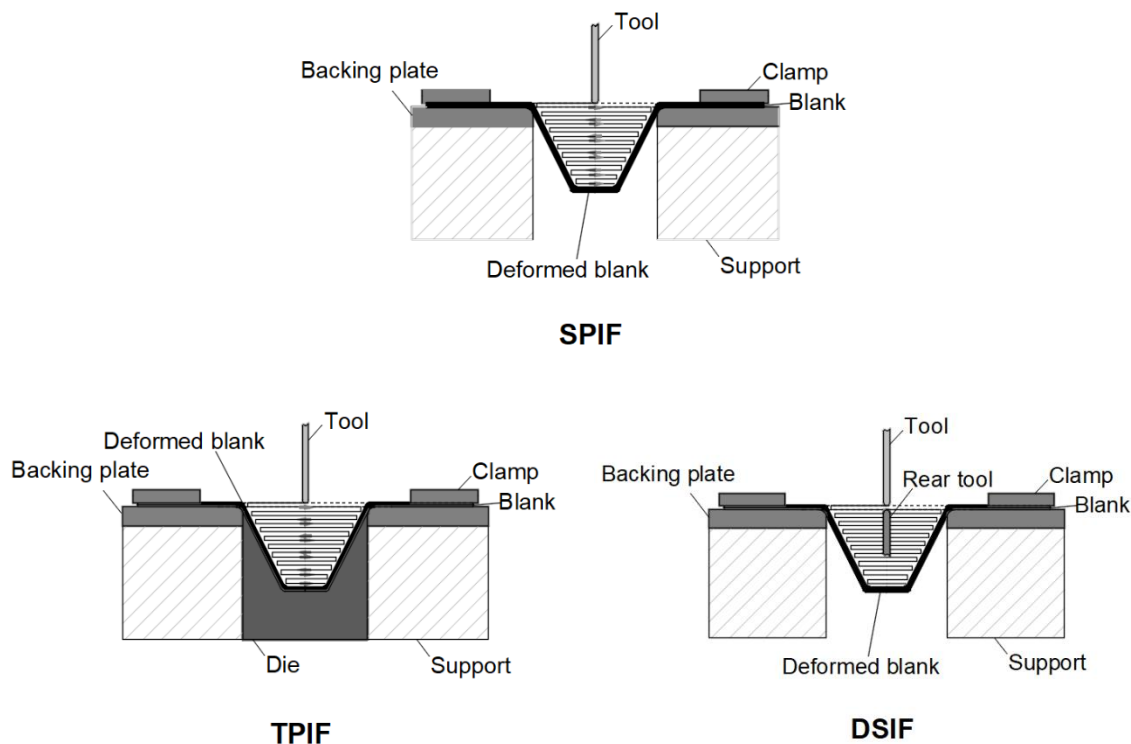


Figure 1.4 Classification of ISF processes

In SPIF, only one forming tool is used to deform the sheet. It requires the least manufacturing equipment while maintaining satisfactory forming accuracy for the prototyping purposes. However, the simple configuration of SPIF process compromises its wider industrial application due to its relatively low forming accuracy and its limitations in manufacturing some complicated geometries [21-23].

Springback is one of the most challenging issues of ISF that affect forming accuracy in SPIF [24]. As shown in Figure 1.5, undesirable strong springback of the part manufactured by SPIF could be observed after trimming. There are two basic methods to control springback, reducing stress gradient through thickness or introducing additional deformation to compensate for springback [25]. Based on these methods, two variations of ISF have been developed. The first one is TPIF [26]. In TPIF, only partial die is needed,

the male die or the female die, as shown in Figure 1.4. The die is not necessarily made of steel, it can be made with wood or other materials that are easy to be manufactured thus the cost of materials and lead time can still be reduced. The partial die provides a supporting force to the sheet, thus less tensile force is needed to achieve the plastic deformation required to deform the sheet. Stress gradient across the thickness is reduced thus springback can be reduced.



Figure 1.5 Strong springback of titanium sheet of denture part after trimming [27]

However, designing and manufacturing the partial die compromise the flexibility of the ISF process. Instead of using a traditional die, DSIF introduces a rear tool as a partial die on the other side of the sheet metal, as shown in Figure 1.4. The two tools can be independently controlled and their relative position can be adjusted. When the rear tool is pressed against the top forming tool, additional compressive force is applied. The pressure can be applied by pre-set interference fit between the rear tool and the sheet [28, 29], flexible spring or air compressor [30]. The DSIF process was first proposed by Meier et al. [8]. By developing a purposely designed DSIF equipment [28, 30, 31], no backing plates are required for specific geometries in DSIF, thus the manufacturing time is further reduced. In addition to maintaining all the advantages of SPIF, DSIF improves forming accuracy as well as process flexibility when manufacturing highly complicated geometries [32], as demonstrated by the parts produced by Wang et al. [28] and Smith et al. [31].

According to the tool movement strategy, DSIF can be divided into traditional DSIF and Accumulative DSIF (ADSIF) [33]. In ADSIF, the tools move outwards rather than inwards. Geometries with more complicated shapes can be manufactured by ADSIF due to the reduction of the tensile force and less geometric constraint from the formed part of the product. As a result, the flexibility of the process is further enhanced.

### 1.1.3 Improved material formability in ISF

In the field of the sheet metal forming, in order to quantify material formability, formability of a material is defined by the maximum level the material can be deformed before the occurrence of fracture [34-36]. According to this definition, material formability can be reflected by the maximum elongation, maximum bending depth or maximum drawing angle of a forming part, depending on the interpretation of the specific process.

Forming limit curve (FLC) is widely used to evaluate material formability in conventional sheet metal forming processes. It is a curve in the major strain-minor strain space, and it is determined by the maximum principal strain components in the planar directions in the uniform deformation process. The FLC defines the boundary of stable deformation and unstable deformation of the material in a forming process. If the strain point is lower than the FLC, the deformation process is stable, otherwise it is not. As shown in Figure 1.6, the FLC for material AA1050 in the conventional sheet metal forming process was a V-shaped curve. By comparison, for SPIF, a FLC with a negative slope in the first quadrant was obtained. In addition, the FLC for SPIF was above the FLC of the conventional sheet metal forming process, especially under plane strain condition, indicating higher material formability for AA1050 in SPIF than that in the conventional forming processes [37].

In addition, according to the experimental investigations conducted by various researchers [38-40], material formability for various materials, including aluminium alloys, steels and copper alloys could be significantly improved in SPIF, compared with conventional sheet metal forming processes. For DSIF, the material formability was reported to be further enhanced [30, 33].

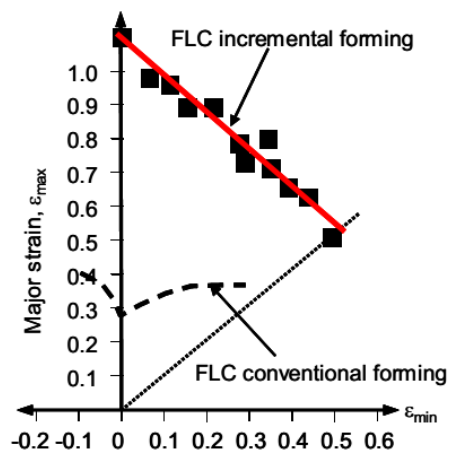


Figure 1.6 Comparison between FLCs for conventional forming process and SPIF for material AA1050

[37]

#### 1.1.4 Factors affecting material formability

Formability of a material is subject to its intrinsic mechanical properties, loading conditions and the loading path.

Material mechanical properties can be reflected by various parameters, including yielding stress, work-hardening, maximum tensile stress and hardness. Among these parameters, the most commonly evaluated parameter is material work-hardening. In the uniaxial tensile test, Considère criterion [41] is widely used to predict the effect of work-hardening coefficient on the occurrence of the material deformation instability. For SPIF, the individual and interactive effects of these parameters on the formability of various materials were investigated by Fratini et al. [39] and it was concluded that work-hardening coefficient  $n$  and the combined effect of  $n$  and strength coefficient  $K$  were the most influential factors.

In the microscale, material mechanical properties can be affected by its microstructure [41], including grain compositions and grain sizes [42]. The material microstructure can be affected by the temperature. Increasing temperature would facilitate the annealing process which reduces the propagation of dislocations and promotes recrystallization, thus affecting the material formability [43].

Different loadings, such as tension, compression and shearing may be applied to the material in different manufacturing processes or in different phases of the same manufacturing process. Loading conditions affect the distribution of stress and strain in the part being deformed. Based on the Marciniak-Kuczyński (M-K) theory [44], the influence of through-thickness-shear (TTS) and normal stress on the material formability was investigated by Eyckens et al. [45] and Allwood and Shouler [46] respectively. In the theory proposed by Emmens [36], fracture would eventually occur at the weak spot of the material under tensile loading. As a result, any operation that could suppress the damage propagation at the weak spot should improve material formability. In the stamping process, by adjusting the clamping force, the tensile condition may be alleviated and the formability of the material can also be improved without sacrificing the geometric accuracy of the parts [47]. In the continuous bending under tension (CBT) test performed by Emmens and von den Boogaard [48], by applying cyclic bending loading onto the material, the weakest spot in the test specimen kept changing, leading to a significantly increased maximum elongation of 430% for material DC04.

In monotonic loading, as reflected in the traditional FLC in Figure 1.6, the material shows clearly different deformation behaviour under different strain paths, such as uniaxial tension, plane strain and biaxial tension [35]. Generally, a material undergoes higher degree of deformation under biaxial tensile condition than it is under plane strain condition in the conventional sheet metal forming processes. Using M-K model, the path-dependence of the FLC of the material was reported by Yoshida et al. [49] by adopting two broken linear loading paths. Under cyclic loading, the Bauschinger effect will create cyclic softening of the material and improve material formability for some materials [50]. Serrated loading paths were reported by Eyckens et al. [51] in SPIF process by performing FE simulation. By applying the obtained loading paths into the M-K model, higher material formability was obtained. Using pre-strained specimens in the two-step tension-tension test, He et al. [52] also concluded that strain path would affect material deformation behaviour.

## 1.2 Current Research Gaps and Challenges

The unique advantages of ISF are accompanied by its distinct material deformation behaviour from the conventional sheet metal forming processes. It has already been widely acknowledged that the material deformation in SPIF is a localized deformation caused by the combination of tension, bending, shearing and cyclic effect. For DSIF, additional compression from the rear tool brings more complexity to the material deformation behaviour.

Current research on material deformation and fracture mechanism in ISF mostly focuses on ISF process itself, as reviewed by Li et al. [16] and Gatea et al. [53]. However, owing to the complexity of the process, including the contact conditions and geometric constraints, the deformation modes in ISF are closely interconnected so that their influence on the material deformation and fracture behaviour in ISF cannot be investigated in a separate and controllable way by conducting ISF tests themselves. The influence of the deformation modes on the deformation and fracture mechanism cannot be fundamentally explained, especially for DSIF.

As discussed in Section 1.1, apart from material properties and loading conditions, material formability is also affected by the loading path. The strain state of deformed material in ISF is between plane strain and equi-biaxial tension condition [40, 54] and the deformation accumulates incrementally. Based on the strain distribution characteristics, conic shapes and pyramid shapes are widely used in the ISF tests as benchmark

geometries. For a conic shape, the material is deformed under plane strain state. For a pyramid shape, the corners of the geometry undergo the equi-biaxial tensile deformation while the rest of the geometry is still under plane strain condition. However, most of the research only focuses on the plane strain condition, while biaxial tension conditions have been largely overlooked, making the understanding of ISF process incomplete.

In conventional sheet metal forming processes, deformation behaviour of a material is commonly explained by the material testing and its related formability test results, such as the FLC. However, as shown in Figure 1.6, the material formability in ISF is significantly improved, the traditional material formability testing methods are incapable to explain the observation of material formability improvement in ISF process. In addition, in ISF, the material is under a combination of multiple deformation modes and the its deformation generally follows a serrated strain path [10]. While in traditional material testing methods, materials are generally tested under monotonic and simple loading conditions, making it insufficient to describe material deformation behaviour in ISF.

Based on the above considerations, developing material testing methods considering the unique deformation characteristics of ISF will be essential to achieve a fundamental understanding of material deformation and fracture mechanism in ISF. However, unlike standard material testing methods, in which normally only simple loading conditions are applied, multiple deformation modes exist in ISF. How to extract the key deformation modes from ISF and to integrate them into a simple testing method are challenging. Furthermore, for the standard material testing methods, commercial purposely-built testing platforms are widely available to perform the test. For the new testing methods, considering the complexity of the loading conditions, no testing platforms exist to carry out the proposed research containing multiple loading conditions. Testing platforms suiting the research purpose should be developed.

### 1.3 Research Aims and Objectives

An in-depth understanding of material deformation and failure mechanism in ISF process will facilitate the analysis and designing procedures for the process, maximizing the potential of the ISF process. This PhD project aims to investigate the influence of material properties, deformation modes and loading path on the material deformation and fracture behaviour in ISF. The research objectives are:

- To obtain deformation characteristics of the investigated materials in ISF by experimental testing and finite element modelling;
- To develop simplified testing methods which represent the loading conditions and loading path in ISF and to develop testing platform on which the proposed simplified tests can be performed;
- To design and to perform experiment to investigate the individual and interactive effects of the deformation modes on the material deformation and fracture behaviour in the simplified test methods using the developed testing platform;
- To design and perform experiment to investigate the effect of loading path on the material deformation and fracture behaviour using the simplified test methods on the developed testing platform;
- To explain the deformation and fracture behaviour in ISF based on experimental and FE modelling results from the simplified test methods.

## 1.4 Research Novelty

The novelty of this PhD. project lies in using simplified material testing method instead of the ISF test itself to get an in-depth understanding of material deformation in the ISF process. In terms of the details, the following novel contribution to the knowledge has been achieved in this research:

- Implemented the shear-modified GTN model in the damage modelling of ISF process to identify the complex loading conditions and the deformation behaviour during the ISF process;
- Proposed two simplified material testing methods to investigate the effect of key factors, including material mechanical properties, loading conditions and loading paths on the material deformation behaviour and fracture behaviour in ISF;
- Developed two material testing platforms to conduct the proposed simplified material test methods, based on which the influence of the investigated factors on material deformation behaviour was examined.

## 1.5 Thesis Layout and Structure

This thesis is structured into 6 chapters.

In Chapter 1, the research background is introduced and research gaps are identified, based on which the research aims and objectives of this PhD project are proposed.

In Chapter 2, a literature review of the material deformation and fracture mechanism in ISF, the material formability testing methods and the damage theories are presented.

In Chapter 3, the experimental and FE modelling of the ISF process, including SPIF and DSIF are conducted to evaluate the deformation characteristics of ISF for material AA5251-H22 and AA6082-T6.

In Chapter 4, the Tension under Cyclic Bending and Compression (TCBC) test is presented as a simplified test method for ISF process. The experimental investigation and FE damage modelling of the test are conducted and analysed.

In Chapter 5, to investigate the effect of biaxial tensile loading condition on the deformation behaviour in ISF, the Biaxial Bending under Tension and Compression (BTBC) test is developed and corresponding experimental and FE modelling are conducted.

In Chapter 6, a conclusion summarizing the research of the project is made, based on which the contribution of current research to the knowledge is stated and future works to improve the current work are proposed.

Equation Chapter (Next) Section 1

## 2 LITERATURE REVIEW

In this chapter, a literature review of the deformation and fracture mechanism of ISF, including SPIF and DSIF are presented in Section 2.1. To investigate material deformation behaviour and material formability under different loading conditions, various testing methods have been developed, as reviewed in Section 2.2. To reveal the damage evolution in the tests and manufacturing processes in an explicit way, FE damage modelling has been developed in various studies. Commonly used damage theories and damage models in the field of metal forming are reviewed in Section 2.3. Specifically, the shear-modified GTN model and its application in the FE modelling are introduced in Section 2.4. A summary of the literature review is presented in Section 2.5.

### 2.1 Deformation and Fracture Mechanism of ISF

Traditional sheet metal forming processes generally present very straightforward and predictable material deformation behaviour and failure mechanism. For example, in deep drawing process, the entire sheet under deformation can be divided into three parts based on the stress/strain distributions. The flange area is subject to compressive stress in the circumferential direction and tensile stress in the radial direction, and the rim opening area undergoes bending and tension, the straight wall area is under simple tension in the depth direction while the bottom area around the head of the tool is under bending and tension. With a clear understanding of the material deformation mechanics, the material deformation behaviour and failure mechanism in deep drawing process can be clearly explained. It leads to the conclusion that wrinkling will happen in the flange area while fracture takes place in the other two areas affected by bending.

For SPIF, it is now widely accepted that the deformation mode is a combination of tension, bending, shearing and cyclic loading. For DSIF, the superimposed compression further improves the material formability. However, for ISF, it can be quite difficult to identify the dominant deformation mode affecting the deformation behaviour. Constantly changing contact conditions and localized plastic deformation make it hard to identify the stress/strain distributions in the sheet material under deformation thus hindering further analysis of the effect of the material deformation modes on material deformation behaviour. The failure behaviour in ISF, especially the suppression of necking before fracture, is still in need of an in-depth investigation.

### 2.1.1 Single point incremental sheet forming

#### 2.1.1.1 Deformation mechanism of SPIF

Due to the complexity of its deformation mechanism, at the early stage of ISF research, the ISF process was deemed analogous to shear spinning because of their similarities in process configuration and gradual material deformation during the forming process, especially when forming the simple conic parts, as illustrated in Figure 2.1.

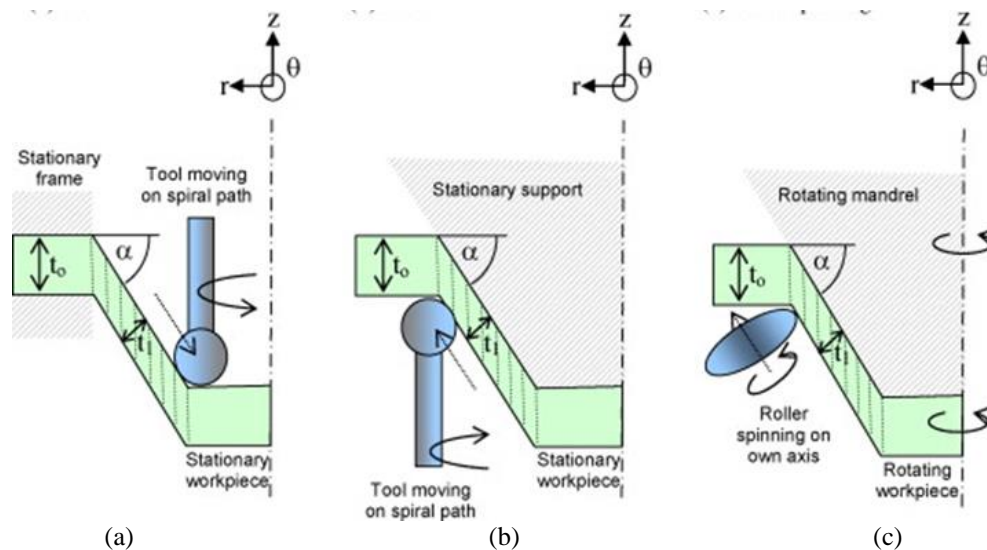


Figure 2.1 Schematic comparison of process configurations between SPIF, TPIF and shear spinning [55]:

(a) SPIF; (b) TPIF; (c) shear spinning

In fact, the thickness distribution in the formed parts manufactured by SPIF could be predicted by the same rule derived from the shear spinning process, the *Sine Law* [56]. It further strengthened the theory that shearing was the dominant deformation mode in SPIF. To detect the existence of shearing effect in SPIF process, Lu et al. [57] drilled holes in the sheet blank used in the test. Shearing effect was confirmed by different degree of distortion of the hole through the thickness direction after deformation. The difference

of shear strain components was reflected by different degree of the hole distortion in different directions.

However, it was recognised that a similar thickness distribution could also be achieved under other deformation modes, such as a combined deformation of bending and tension [58]. In addition, by setting pins in the direction perpendicular to the tool movement direction, Allwood et al. [59] discovered that the pins were still perpendicular to the surfaces of the sheet after deformation, which was unexpected if shear deformation was dominant. The deformation modes in ISF might be more than just shearing.

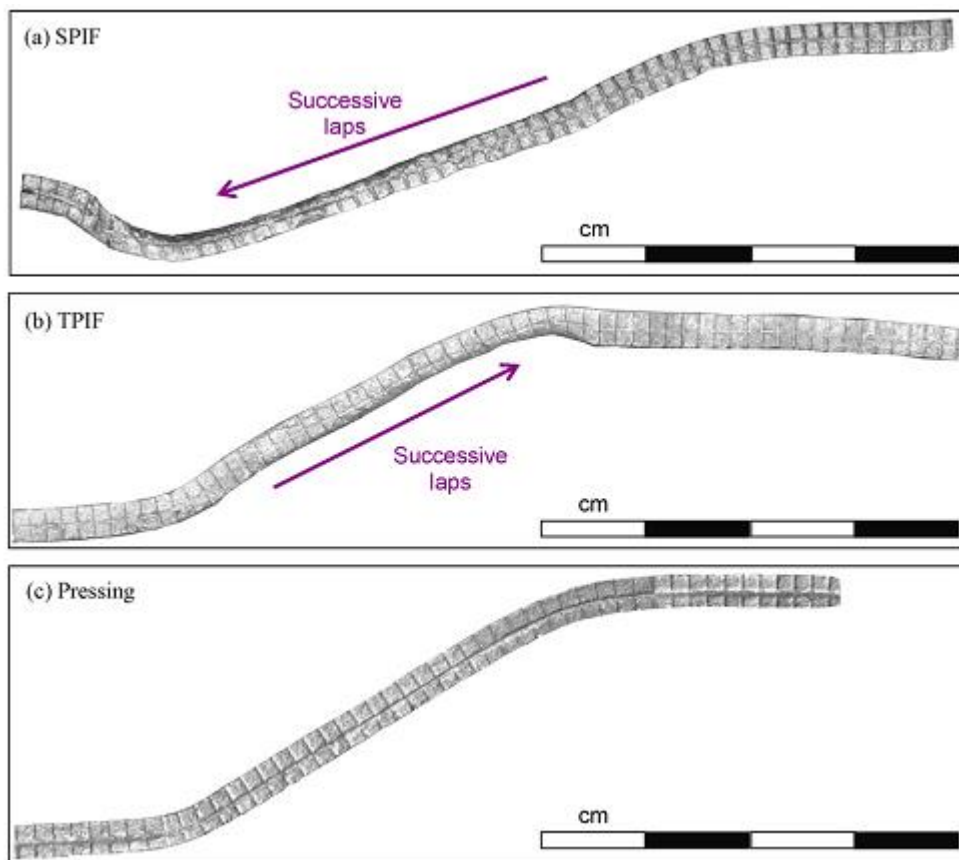


Figure 2.2 Cross-sections of the deformed parts with inscribed grids in different sheet metal forming processes [55]: (a) SPIF; (b) TPIF; (c) pressing

To obtain a better understanding of the existing deformation modes in ISF, various experimental tests have been carried out by the researchers. Jackson and Allwood [55] used welded copper sheet C101 with two layers of marked grids in the cross-section in SPIF, two point incremental forming (TPIF) and pressing processes. The strain components after the deformation could be obtained by measuring the distortion of the grids, as shown in Figure 2.2. It was observed that in SPIF and TPIF, the deformation mode was a combination of tension, bending and shearing, while in pressing it was only bending and tension. In terms of shearing effect in ISF, shear strains were detected both

in the direction parallel to the tool movement direction and in the radial direction however shearing in the tool movement direction was more obvious. Both shear components were also obtained by Allwood et al. [59] by measuring the deviation of the scribed lines on the top and bottom surfaces of the deformed sheet. According to their results, the shear strain component parallel to the tool movement direction was much more obvious than that in the radial direction.

Filice et al. [37] evaluated the strain evolution in the SPIF process by tracing marked circular grids on the surface of the sheet with the help of digital image correlation (DIC) measurement. It was found that the circular shape was stretched into an elliptical shape with its long axis positioned along the wall of the part in the depth direction, which indicated that tension was a main deformation mode.

Fang et al. [60] studied the effect of bending in a theoretical analysis by considering strain gradient in the thickness direction in the simplified SPIF model. To validate the model, the morphology of the cracks was examined by using scanning electron microscope (SEM), which showed that the cracks evidently initiated from the outer surface of the sheet and developed towards the inner surface. It clearly indicated the effect of bending on the occurrence of the fracture.

In addition to the experimental work, FE modelling of the SPIF process was also performed in various studies to reach a more comprehensive understanding of the deformation modes in SPIF. By performing a FE simulation with material AA7075-O, Li et al. [61] obtained the strain components of the elements through the thickness of the sheet at a certain depth. As shown in Figure 2.3, for a single element, the strain along the wall direction was the largest, which indicated the existence of strong tensile effect. The shear effect was demonstrated by the in-plane and tangential shear strain components. While the bending effect was confirmed by the variation of the strain components of the elements along the thickness direction.

Combining the analytical calculations and FE simulation, Maqbool and Bambach [62] obtained the quantitative energy contribution to the plastic deformation from membrane tension, bending and shearing effects in manufacturing a pyramid shape with SPIF. Comparing them with the total internal energy, it was confirmed that these three deformation modes dominated in the SPIF process.

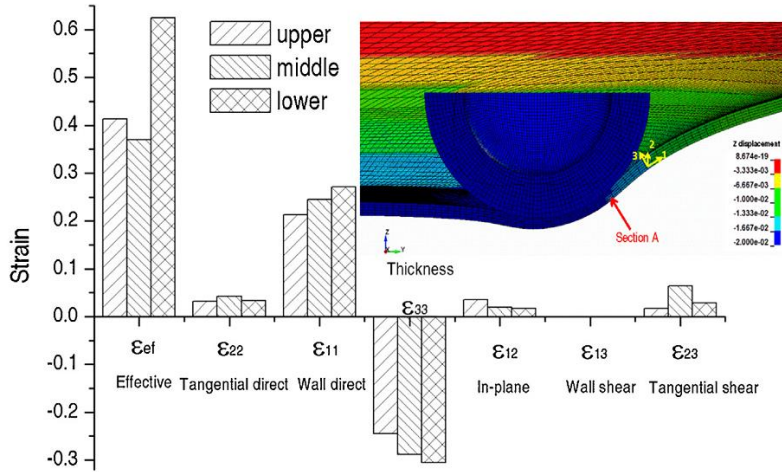


Figure 2.3 Strain components of elements along the thickness direction in FE results of SPIF process [61]

By simulating SPIF process of manufacturing the conic shape and the funnel shape using FE software LS-DYNA with an incorporated damage model developed by Xue [63], Malhotra et al. [64] observed higher plastic deformation and higher value of the damage indicator on the outer surface of the sheet than the inner surface, which suggested the existence of local bending. Through-thickness-shear was also detected in the FE model by examining the shear strains of the elements.

A similar distribution of the damage accumulation was observed in the simulation performed by Mirnia and Shamsari [65], in which the Modified Mohr-Coulomb ductile fracture criterion was used. Wu et al. [66] implemented the modified GTN (Gurson-Tvergaard-Needleman) model in the SPIF process modelling, in which the shearing effect was taken into consideration by introducing a shear-affected factor, demonstrating the existence of strong shear strain through thickness direction. Gatea et al. [67] adopted the GTN model with the Nahshon-Hutchinson shear extension to predict the fracture when deforming pure titanium. In their simulations, compared with the original GTN model, the GTN model with shear mechanism predicted different maximum forming depths for both the conic shape and the pyramid shape, which suggested a clear influence of shear deformation in the SPIF process.

Based on the experimental, analytical and FE findings, it has now been widely acknowledged that material deformation in SPIF is localized plastic deformation owing to the combined effect of tension, bending, shearing and cyclic loading [68], as shown in Figure 2.4. However, from a static point of view, it is still debatable which one is the most dominant deformation mode among tension, bending and shearing effects, affecting material formability in SPIF. According to the digital image correlation (DIC)

observation by Eyckens et al. [69], different deformation modes dominated in SPIF when different process parameters were used. Bending effect was more dominant when manufacturing parts with a greater wall angle while TTS was more dominant for the parts with a smaller wall angle. The same conclusion was reported by Maqbool and Bambach [62]. By varying process parameters including tool size, sheet thickness and wall angle in the FE simulation, the composition of the internal energy and the ratio between different energy components in the FE model also varied, suggesting a shift of relative importance of the deformation modes.

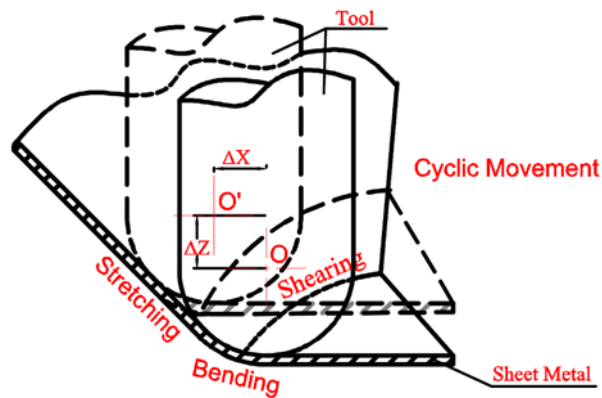


Figure 2.4 Schematic of deformation mechanism for SPIF

The individual and combined effect of the deformation modes on material formability has already been reported in sheet metal forming processes. The combined effect of bending and tension was investigated by the stretch-bending test performed by Demeri [70] using AK steel, HSLA-F50, DP-80 and AA2036-T4. El-Domiaty et al. [71] developed a mathematical model, in which the effect of material properties as well as the loading conditions on the material formability could be investigated. It was shown in their developed model that the introduction of bending into pure tension could lead to material formability improvement due to the reduced tensile effect caused by the compression effect on the concave side of the sheet along the thickness direction. However, it would not produce such a dramatic change of material formability as observed in SPIF, compared with that predicted by the traditional forming limit curve (FLC).

The contact stress between the tool and sheet metal will also lower the tensile stress needed for yielding thus strengthening localized deformation resulted from bending effect. In the monotonic loading case, the existence of localized deformation will eventually propagate to fracture since it creates a weak spot in the material. However, in SPIF, the cyclic contact between the forming tool and the sheet metal will create a shift of the weakest spot, thus suppressing the development of damage in one spot and resulting

a significantly improved material formability. This theory has been proved by the Taraldsen test, in which OFHC copper obtained a maximum uniform elongation of 600% [72] and the mild steel reached 590% [73].

Eyckens et al. [45] investigated the effect of TTS on the material formability under various strain modes including plane strain and equi-biaxial strain conditions by using the extended M-K model. It was found that the existence of TTS could create a slight decrease or obvious increase of the forming limit depending on the strain mode. The largest increase of the material forming limit occurred when the TTS was in the plane perpendicular to the direction of the major in-plane strain. Using an extended M-K analysis and a newly developed paddle test [59], Allwood and Shouler [46] proved that repetitive normal loading onto the material and the generated TTS would lead to a significant improvement to material formability.

The research on the individual deformation modes on the material formability undoubtedly enhanced the understanding of SPIF. From this perspective, considering the difficulties in a direct approach to study the ISF process itself, replicating the deformation modes of ISF by developing a simplified material formability test will provide in-depth insights into ISF.

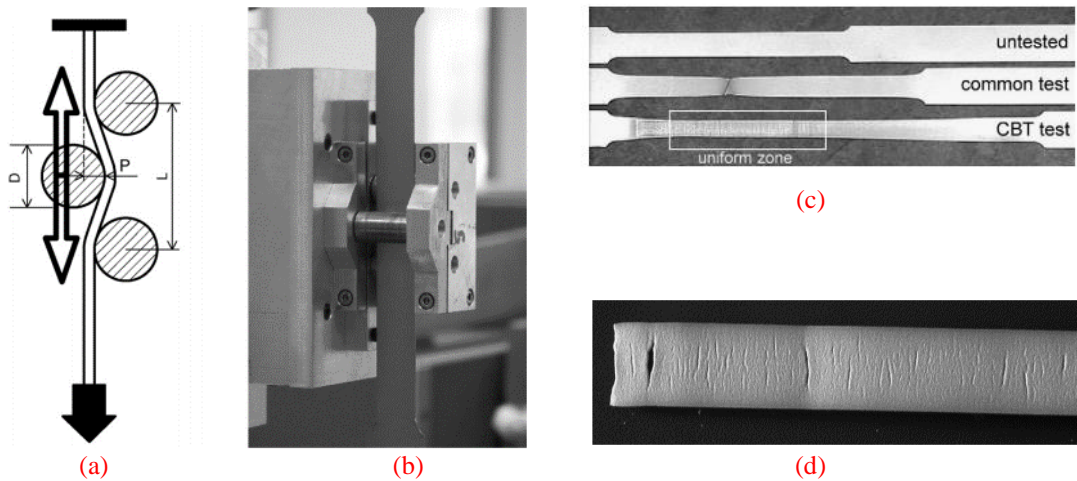


Figure 2.5 The CBT test [48]: (a) schematic of the CBT test; (b) part of the designed CBT test rig; (c) a comparison between untested specimen, tested specimen from uniaxial tensile test and tested specimen from CBT test using material DC04; (d) micro-cracks observed on the surface of the fractured DC04 specimen tested in the CBT test

The latest representative test of SPIF proposed is the continuous bending under tension (CBT) test. The CBT test was firstly proposed by Benedyk et al. [74] to investigate the enhanced formability of materials and then explored by Emmens and Boogaard [48] for

SPIF. In the CBT test, as shown in Figure 2.5, the complicated contact conditions in ISF were simplified into a two-dimensional model. The tension, bending and cyclic effects were superimposed onto each other. They could be independently investigated by simply changing the controlling parameters of each deformation. For example, the bending depth of the roller could change the degree of bending, while the travelling speed of the rollers could vary the frequency of the localized deformation.

Using CBT tests, localized deformation and reduced levels of tensile force to achieve the required plastic deformation were observed. In addition, multiple locations of necking were observed on the failed specimens, which supported the Noodle Theory proposed by Malhotra et al. [67]. It was also observed that when the tensile speed was high enough, the CBT condition was degenerated to be simple tension and the bending effect was less noticeable. Hadoush et al. [85] performed complementary finite element simulation of the CBT test and tracked the tensile stress distribution across the thickness of the specimen. It was found that the fracture of the CBT specimen occurred when the bending effect was overcome by the tensile effect and the whole thickness section was under tension. A similar test was performed by Barret et al. [86] using material AA6022-T4.

#### 2.1.1.2 Fracture mechanism of SPIF

The existence of complex deformation modes also leads to unique fracture behaviour in SPIF. Investigation into the material fracture behaviour in the sheet metal forming process includes the damage initiation and evolution to fracture in the deformed part during the forming process.

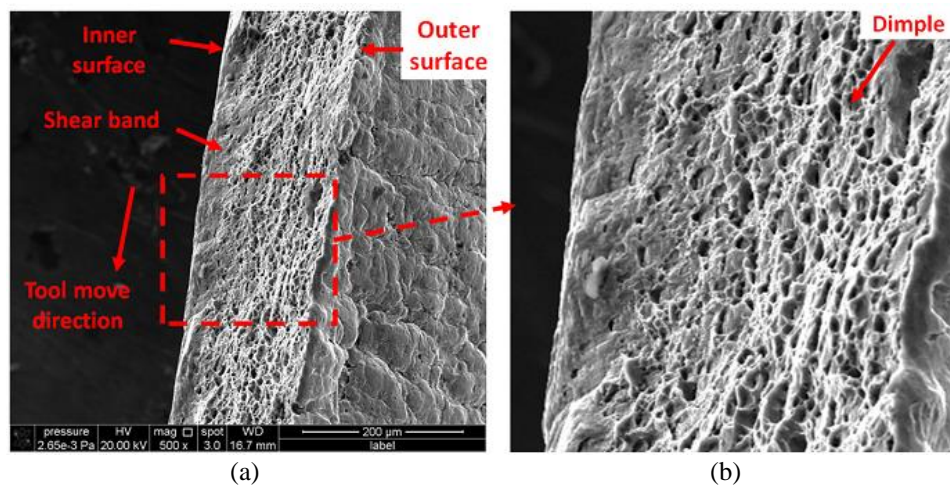


Figure 2.6 Fracture morphology of the crack in a fractured conic part made by SPIF using material AA1100 [60]: (a) overview of the micro structure of the crack surface; (b) close observation of the distribution of dimples in the crack surface

According to the fractography analysis of the cracks in the conic parts manufactured by SPIF with material AA1100, Fang et al. [60] reported that the fracture of the parts was Mode I fracture, namely opening fracture, as shown in Figure 2.7. The same conclusion was made by Silva et al. [75] when manufacturing both conic and pyramid shapes using the material AA1050-H111. In addition, Fang et al. [60] recorded the development of the crack while manufacturing a conic part and observed a zigzag-shaped fracture, as can be seen in Figure 2.7 (a)-(d). A similar shape of the cracks was also obtained by Hussain et al. [76] and Silva et al. [77]. Silva et al. [77] reported that the fracture was triggered by the meridional tensile stress in the plastic deformation zone in the contact area, which then propagated to the elastic zone, as illustrated in Figure 2.7 (e).

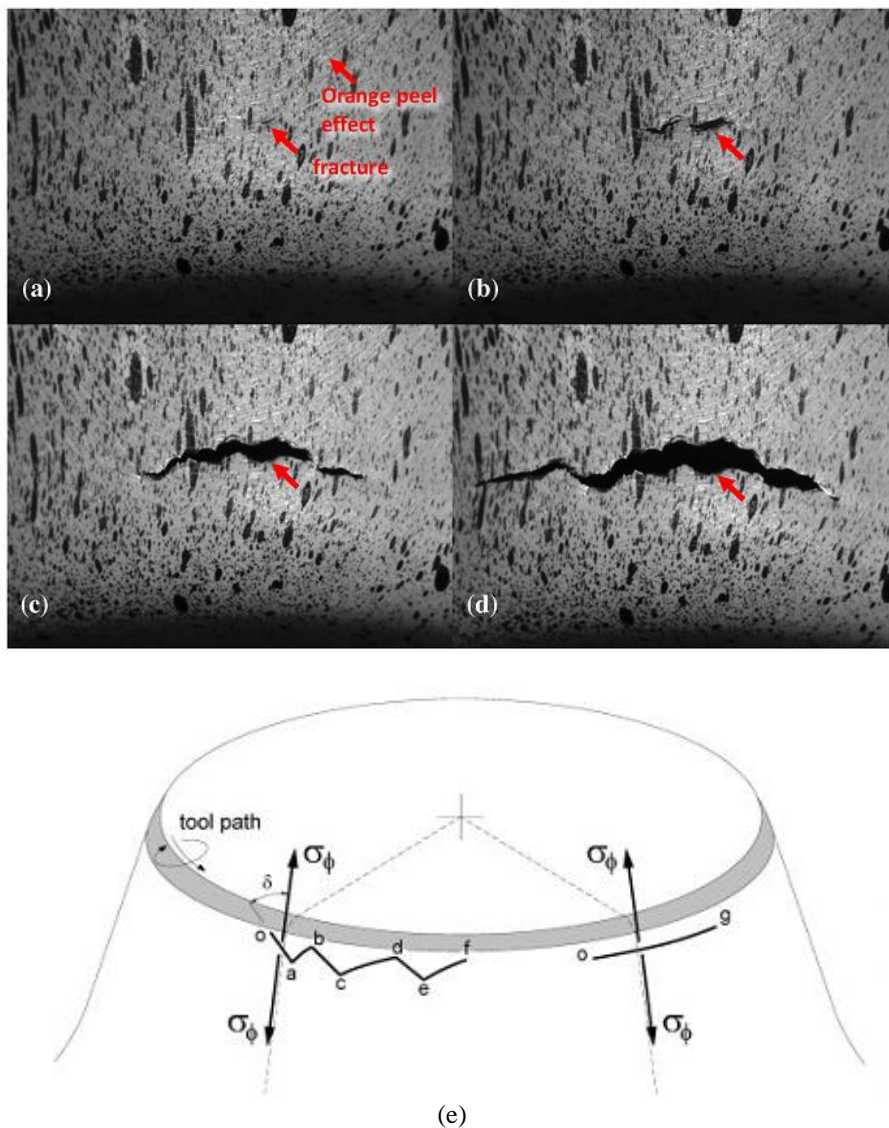


Figure 2.7 Zigzag shaped crack in a fractured conic part in SPIF: (a)-(d) crack initiation and propagation in the part in four consecutive steps with material AA1100 observed with high speed camera [60]; (e) schematic of the crack propagation process on the basis of the stress state [77]

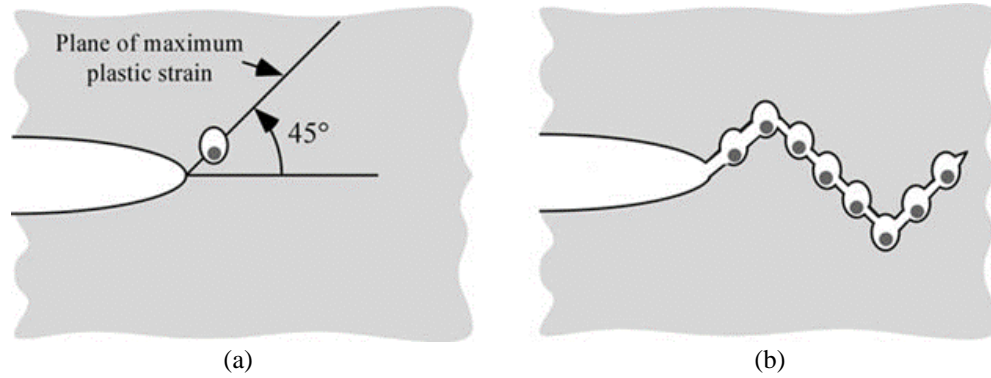


Figure 2.8 Development of the zigzag pattern crack [78]: (a) orientation of the maximum plastic strain; (b) propagation of the zigzag crack

The zigzag-shaped crack is a typical appearance of the tension-induced fracture under the Mode I loading condition and plane strain condition. For the conic shape, the ratio of the radius of the forming tool to the curvature of the part is quite small, the material would be generally under plane strain condition in SPIF. Under the plane strain loading condition, the maximum plastic strain occurs at a 45-degree angle from the crack plane because of the existence of the tensile force, however the global constraints from the neighbouring material create a zigzag pattern according to ductile crack growth theory, as explained by Anderson [78] in Figure 2.8.

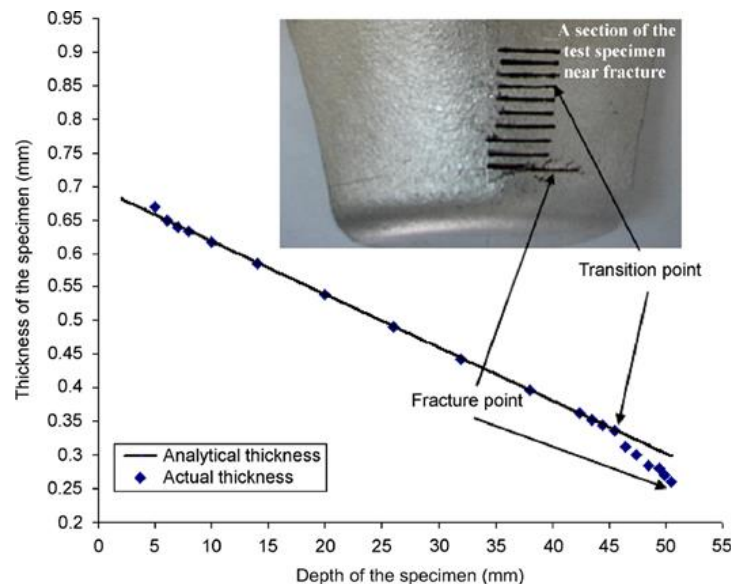
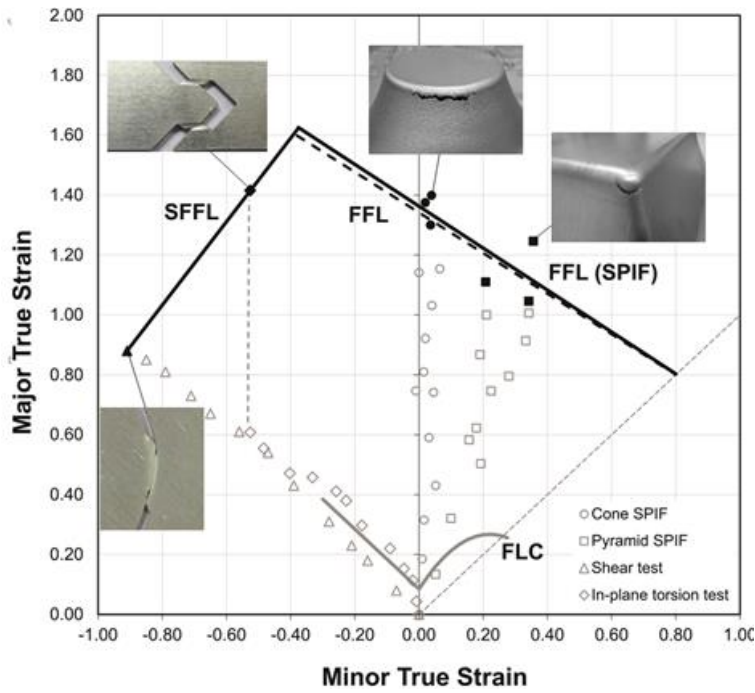


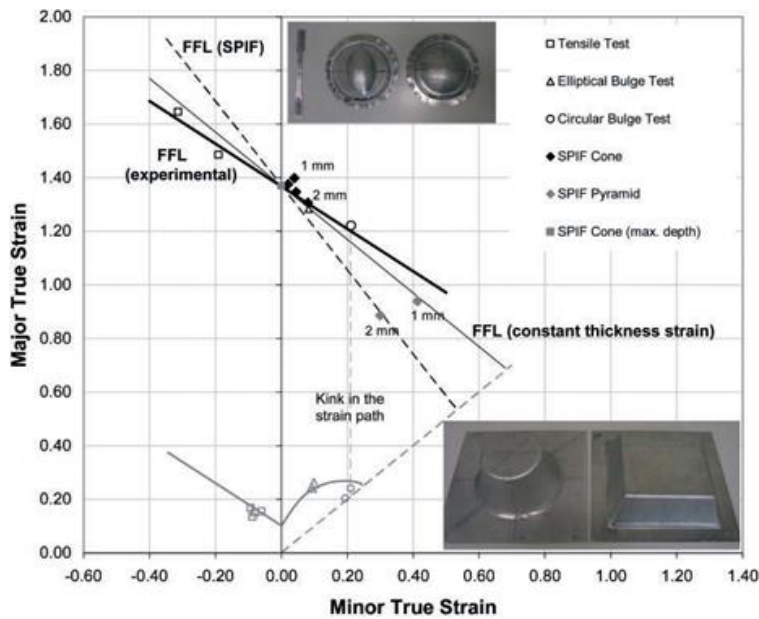
Figure 2.9 Thickness variation along the depth of fractured part made by aluminium alloy [6]

Regarding the material deformation mechanism behind fracture occurrence in SPIF, different theories have been proposed by the researchers. As shown in Figure 2.9, in the experiments using aluminium alloy by Hussain and Gao [6] and commercially pure titanium by Hussain et al. [79], a “transition point” was found where the thickness of the sheet started to be obviously reduced than the predicted thickness distribution. It indicated

that the fracture of the material in SPIF might be an intrinsic property of the material and it followed the fracture forming limit (FFL) or forming limit of the material. Once the limit had been met, fracture occurred.



(a)



(b)

Figure 2.10 FLCs, FFLs obtained from material property tests and the ISF tests using material AA1050-H111 by: (a) Silva et al. [75] ; (b) Isik et al. [80]

Based on the FE analysis and experiments using material AA1050-H111, Silva et al. [75] concluded that the failure of the SPIF parts should be predicted by the FFL curves rather than the conventional FLCs. As can be seen in Figure 2.10 (a), the FFLs for SPIF are quite close to the FFLs derived from conventional fracture tests, especially near the plane

strain condition. A similarity of the FFLs between conventional tests and SPIF was also reported by Isik et al. [80] by testing the same material AA1050-H111, as shown in Figure 2.10 (b). According to their findings, the fracture in SPIF purely depended on an inherent property of the material, thus a FFL should be used to predict the forming limit of the material in SPIF. The same opinion was also supported by Martins et al. [54].

Incorporating the FFL curve-related fracture criterion into the FE simulation software LS-DYNA, Suresh and Regalla [81] predicted the maximum forming depth of the conic and pyramid parts using EDD (extra deep drawing) steel. Compared with the experimental results, the maximum error of FE simulation result was below 4%, which was acceptable. This study supported the conclusion that although the fracture in ISF could be delayed, it still could not go beyond the intrinsic material fracture point for the material used. Therefore, the fracture forming limit of the material could be a useful solution method for the fracture prediction in SPIF.

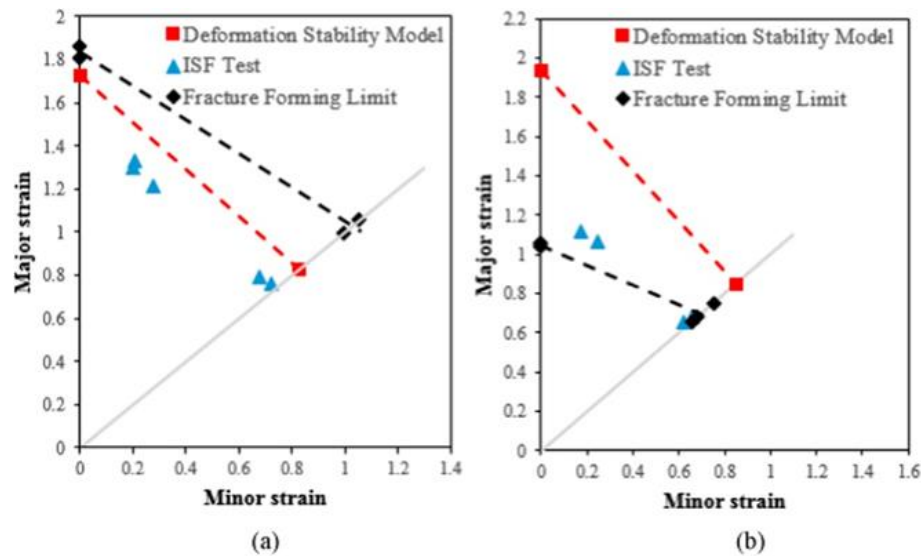


Figure 2.11 Comparison between the FFLs obtained from conventional material tests and SPIF tests for: (a) AA1100; (b) AA5052-O [82]

However, the limited types of materials tested by the researchers are not sufficient to reach the conclusion that the FFL can be a universal prediction of the forming limit in SPIF for materials with varied mechanical properties. Ai et al. [82] compared the thickness of the sheet near the cracks obtained from different tests using materials AA1100 and AA5052-O, including the dome test and SPIF test under commonly used process parameters. It was found that for one material, a competition between the deformation instability limit and material FFL existed, whoever was reached first, the fracture occurred, as shown in Figure 2.11. For material AA1100, the onset of the fracture was predicted by the conventional FLC, while for AA5052-O, rupture happened and it

was predicted by FFL instead. Generally, materials with different properties would follow different fracture criteria in SPIF process.

One step further, more detailed research was carried out to investigate the development of the fracture in the parts made by SPIF and suppression of necking phenomenon before fracture was observed. In the experiment conducted by Silva et al. [75] with the material AA1050-H111, no prior necking was observed before the final fracture. It indicated that once the thickness strain had reached a threshold value, abrupt fracture from uniform thickness occurred without any sign of necking.

In the ductile fracture, it was common that localized necking appeared before the occurrence of final fracture for the processes in which tension was the dominant deformation mode, as reported by El-Sebaie and Mellor [83]. Silva et al. [84] and Madeira et al. [85] observed a necking phenomenon in the parts produced in SPIF by using conventional deep drawing steel and AA1050-H111, respectively. Bambach et al. [86] detected visually noticeable necking when using the material DC04 with a sheet thickness of 1.0 mm in an incremental groove test, as shown in Figure 2.12. The necking of the sheet appeared in the contact area near the lowest point of the tool.

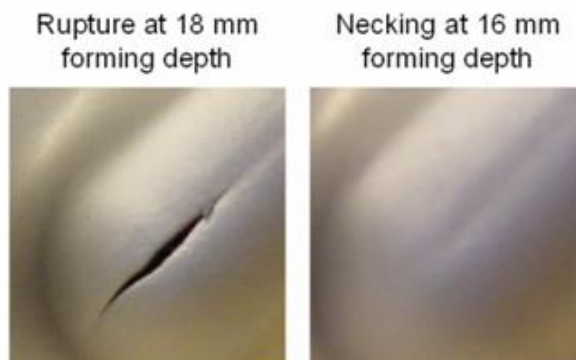


Figure 2.12 Fracture and precedent necking in the incremental groove test using DC04 [86]

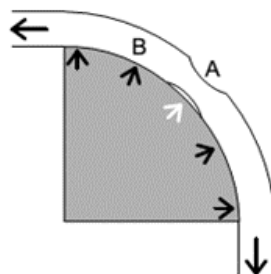


Figure 2.13 Schematic of the neck losing contact with the tool [87]

From a static perspective, an interesting theory was proposed by Emmens and van den Boogaard [87] to account for the suppression of development of necking in the tool

bending process. In their theory, it was assumed that the necking zone in the contact area might lose contact with the tool, as shown in Figure 2.13, thus minimizing the effect of stress concentration on the development of the necking based on the yield criterion. Furthermore, based on this explanation, the forming limit of the material can be enhanced.

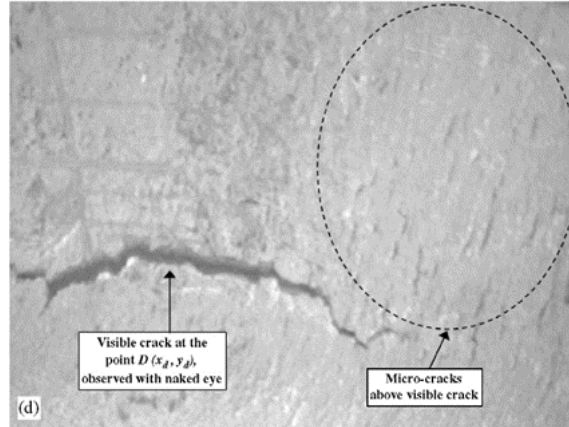


Figure 2.14 Micro cracks above the final crack in the part made by an aluminium alloy using SPIF process [52]

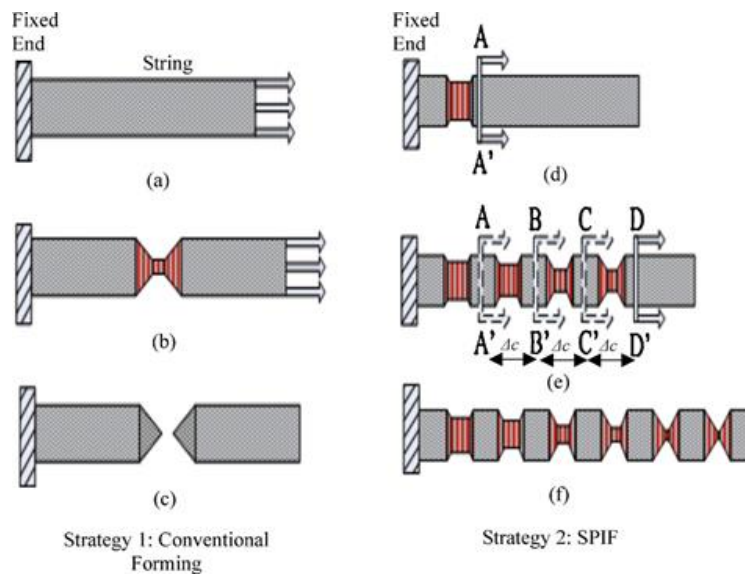


Figure 2.15 Schematic of the Noodle Theory proposed by Malhotra et al. [64]: (a) original specimen; (b) development of necking in conventional forming process; (c) final fracture in conventional forming process; (d) initiation of the first necking in SPIF process; (e)-(f) development of multiple necking during SPIF process

Hussain et al. [52] observed numerous micro cracks above the visible crack when manufacturing a cone with an aluminium alloy by SPIF, as shown in Figure 2.14. They attributed it to the necking-like phenomenon in tensile tests. Multiple visible neckings were also observed by Malhotra et al. [64] in the part manufactured by SPIF. In order to explain the suppression of the necking phenomenon, a *Noodle Theory* was proposed by Malhotra et al. [64]. According to this theory, although the bending effect contributed to

the damage accumulation in the material, the weaknesses created in the previous passes shared the total necking so that the final necking was still postponed. An illustration of the proposed theory is shown in Figure 2.15. Therefore, instead of obeying the traditional necking or fracture limit theory, developing a new damage model may be required as a more appropriate method for predicting the fracture in the ISF process.

Both necking-preceded failure and rupture phenomena were observed by Silva et al. [84] in the SPIF experiment by changing the tool size. As shown in Figure 2.16, when the incremental tool ratio (the ratio of the part radius to the tool radius) was increased, the failure behaviour for material AA1050-H111 changed from abrupt rupture to necking. The transition of the failure modes was explained by the stabilizing effect from the dynamic tension under bending. When the tool radius was large, the stabilizing effect was not strong enough to suppress the necking phenomenon compared to the tools with smaller sizes. However, there was only one material being investigated in this study. Different materials might present different fracture behaviours even under the same experimental conditions. The influence of the material mechanical properties should also be taken into consideration.

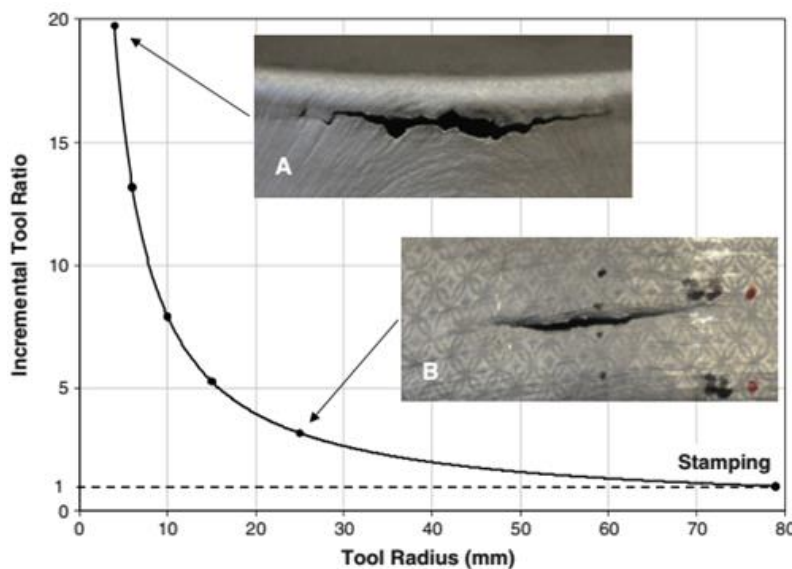


Figure 2.16 Two different types of failure in SPIF with different incremental tool ratios and tool radii: (A) fracture with suppression of necking and (B) fracture with necking [84]

In the experiment conducted by Ai et al. [82], two types of materials, aluminium alloys AA1100 and AA5052-O, were tested using the same sets of process parameters. In addition to bending, the influence of material properties on the deformation and fracture behaviours was investigated. The conic shape and the pyramid shape with an increasing

wall angle were adopted, representing plain strain and equi-biaxial tension conditions. Fracture occurred when the depth of the part reached a certain value.

The thickness distribution along the meridional direction near the cracks in ISF parts were compared with that under the bulge test. As shown in Figure 2.17 and Figure 2.18, obvious necking was found in the AA1100 sheet under deformation conditions in both ISF and bulge tests. However, for the material AA5052, necking appeared before the fracture in the bulge test while only abrupt fracture could be observed during the ISF process under both plain strain and equi-biaxial tension conditions, indicating that necking was suppressed in the AA5052 sheet in SPIF.

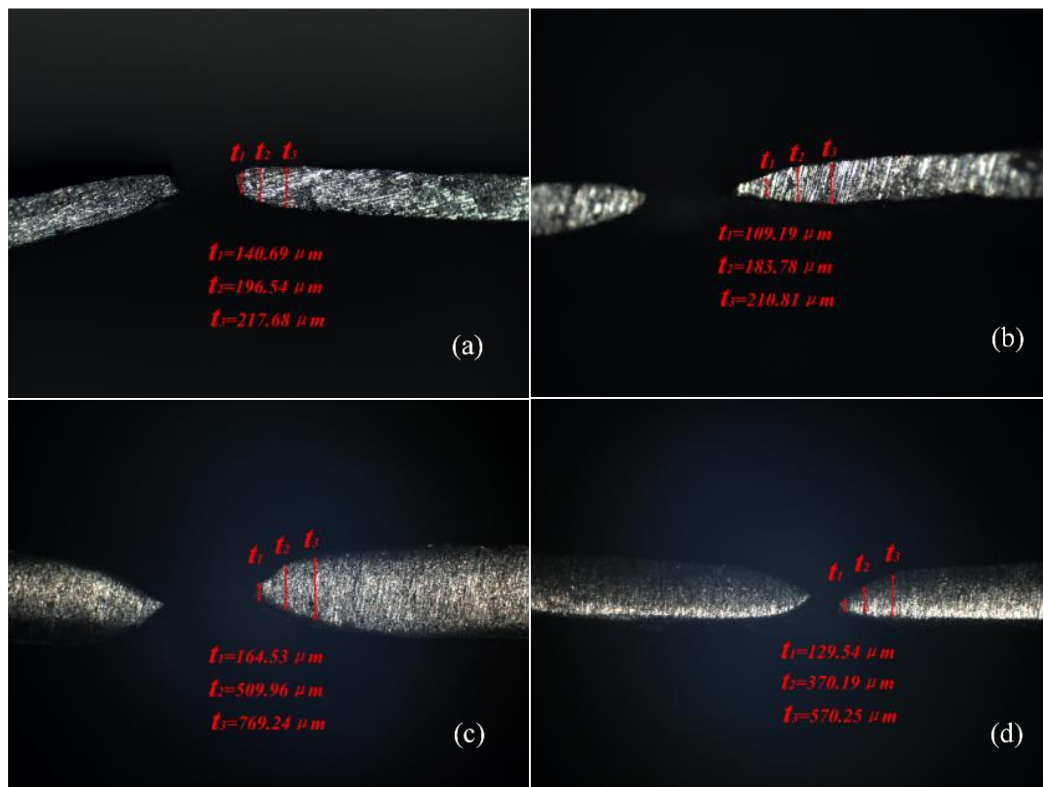


Figure 2.17 Cross-sectional view of the fracture region for the material AA1100: (a) conic part in ISF test; (b) pyramid part in ISF test; (c) bulge test part under plane-strain condition; (d) bulge test part under equi-biaxial tension condition [82]

In addition, in the incremental groove test [86], it was found that the FFL for SPIF varied with different testing geometries, process parameters and strain paths, which contradicted the conclusion reported by Silva et al. [84] that the material forming limit in SPIF was determined by its intrinsic properties. In the experiment conducted by Ai et al. [82], the appearance of necking or rupture in the process was found to be dependent on the type of the material tested. However, only parameters commonly used in the SPIF were tested during the reported study, even though different fracture behaviours for different

materials were captured, the transition from necking to rupture using only one type of the material was insufficient. The fracture behaviour in SPIF should not be an inherent property of the material only, it should also be process-related. The fracture mechanism in ISF is far more complicated than that in the conventional sheet metal forming processes due to the existence of the multiple deformation modes and complicated toolpaths.

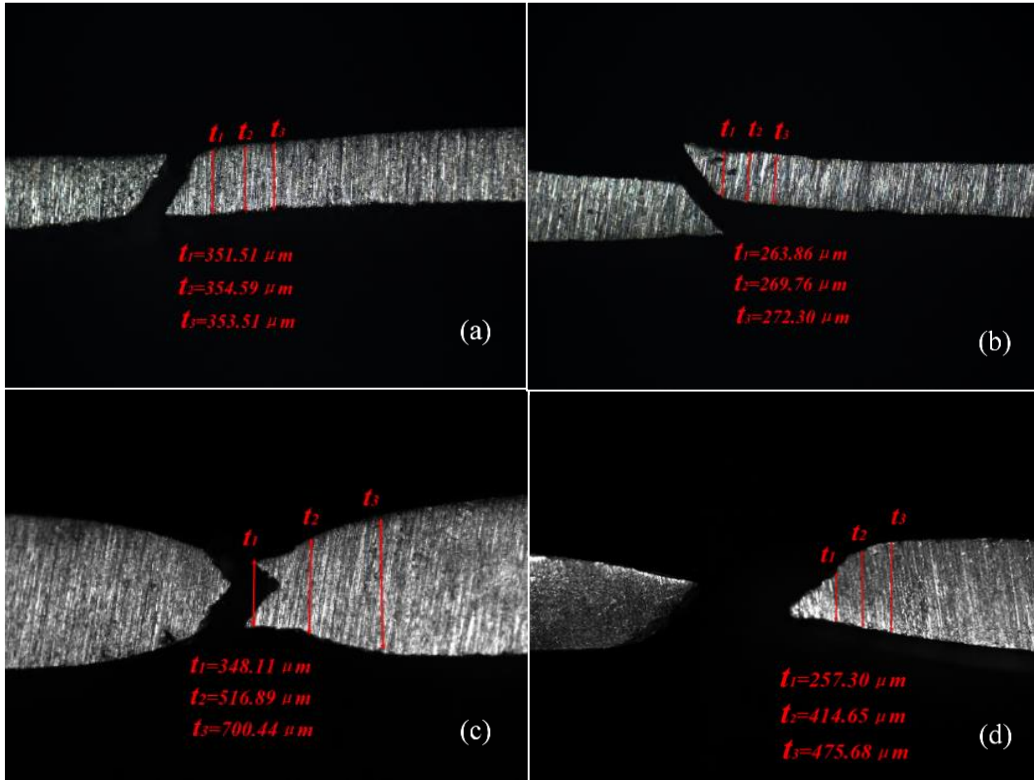


Figure 2.18 Cross-sectional view of the fracture region for the material AA5052: (a) conic part in ISF test; (b) pyramid part in the ISF test; (c) bulge test part under plane-strain condition; (d) bulge test part under equi-biaxial tension condition [82]

Because tension and bending are two of the main deformation modes in SPIF, for the purpose of comparison, Nakazima tests were conducted by Centeno et al. [88] to obtain the FLC of the material AISI 304 steel sheet with a thickness of 0.8 mm, as shown in Figure 2.19. In the tests, a cylindrical punch was used to push the specimens to certain depth until fracture took place therefore the fracture behaviours of the specimen under tension and bending condition could be investigated.

No prior necking was observed before fracture by the eyes or even DIC devices during the tests. However, by observing the thickness distribution of the specimen near the cracks, necking was confirmed to appear in a considerably short time before the fracture happened. As a result, the authors proposed that the failure mode in ISF was postponed necking followed by ductile fracture, however the clear evidence of the necking

phenomenon depended on the degree of bending deformation, which was controlled by the ratio of sheet thickness to the tool radius. When the bending effect was moderate, the through-thickness strain/stress gradient would be limited. As a result, the final fracture of the sheet depended on the total deformation instability of the sheet across its thickness. More specifically, the fracture of the part would be determined by the plastic instability of the inner side of the sheet due to its relatively lower tensile stress resulted from the compression effect produced by bending, and necking would happen eventually. While when the bending effect was severe, the through-thickness strain/stress gradient would be increased, a crack would happen even before the whole sheet across the thickness entered the zone of deformation instability, the fracture of the part would be determined by the plastic instability of the outer side of the sheet. Once a crack initiated on the outer surface, it would propagate instantly and fracture happened without the development of necking. Furthermore, it was concluded that the bending effect was not the only factor that improved the formability of the material, evidenced by the difference between the forming limits of the material under ISF and stretch-bending tests. This study provided a valuable insight into the fracture behaviours in ISF.

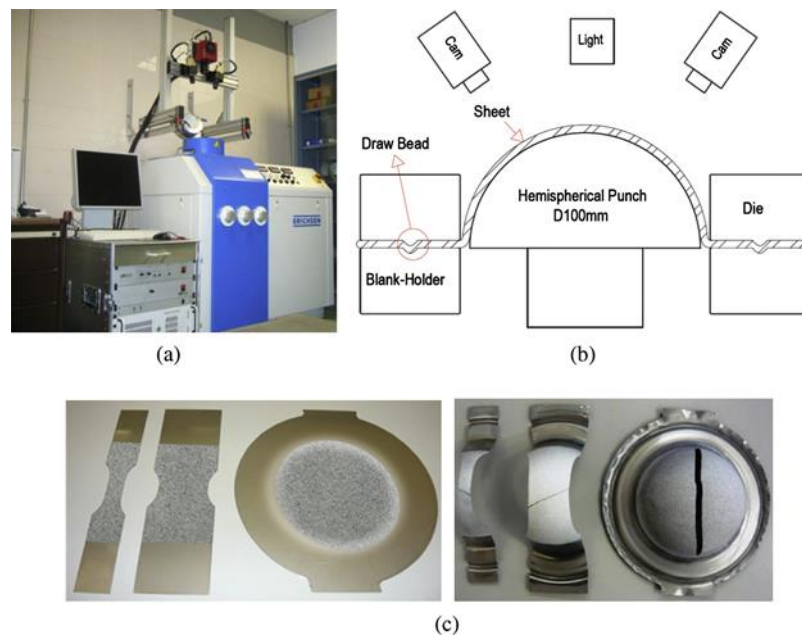


Figure 2.19 Nakazima tests equipment and specimens [88]: (a) the equipment; (b) schematic of the test configuration; (c) specimens before and after tests

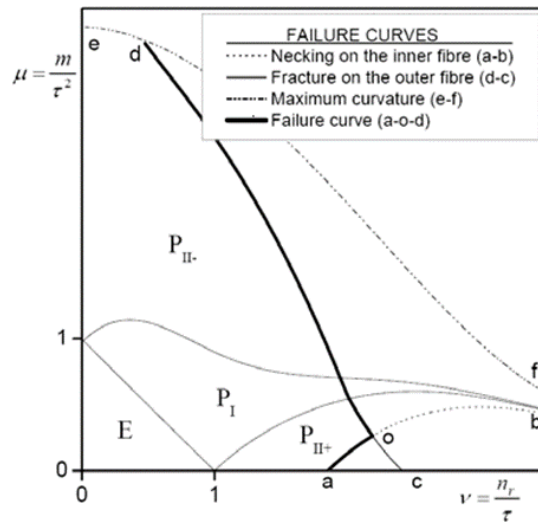


Figure 2.20 M-N diagram with relation to the failure mode in tension under bending [89]

Morales et al. [89] suggested a similar opinion and proposed a mathematical model to further explain this phenomenon. In the proposed model, fracture took place when the maximum values of tensile force,  $\nu$  and bending moment,  $\mu$ , were reached. Depending on the ratio of the force to the moment, limit lines indicating the onset of different types of failures were plotted, as shown in Figure 2.20. Necking-controlled fracture happened when the tensile stress on the concave side of the sheet reached a certain value (curve a-b). When the tensile stress on the concave side of the sheet reached a certain value (curve d-c), fracture-initiated failure took place. With the increasing of the ratio, the fracture mode transitioned from fracture-initiated failure to necking-initiated failure (curve d-o-a), which was consistent with the experiment conducted by Silva et al. [84].

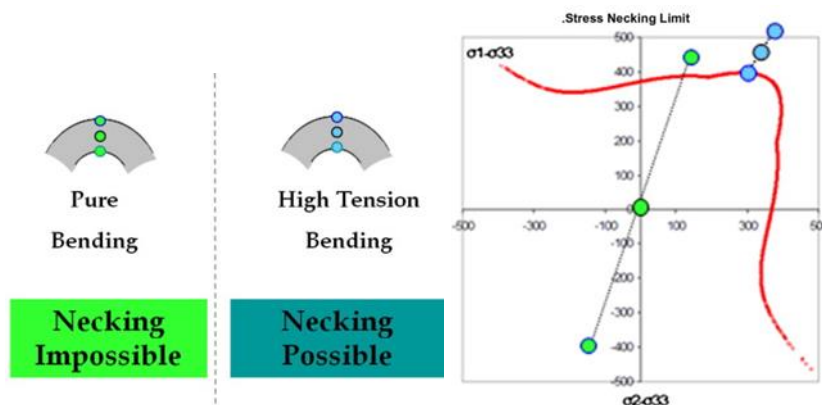


Figure 2.21 M-N diagram with relation to the failure mode in tension under bending [90]

An explanation to the transition from fracture to necking phenomena was given by Stoughton and Yoon [90]. In their theory, as shown in Figure 2.21, only when the compressive stress resulting from the bending of the tool on the concave side of the sheet was overcome by the superimposed high tension, and the whole section of the sheet was

under tension, necking became possible. A similar theory was proposed by Seong et al. [91], concluding that the occurrence of necking of the material under bending preceding the fracture depended on the magnitude of the superimposed tensile stress. If the tensile stress was large enough, necking happened first.

### 2.1.2 Double side incremental sheet forming

Apart from tension, bending and cyclic deformation, an additional loading, compression (squeezing effect) is introduced in the DSIF by the rear tool, as shown in Figure 2.22. The superimposed compression leads to a reduction of the gradient of the compressive stress in the radial direction as well as the tensile stress in the inclined wall direction in DSIF. Reduced tensile stress led to less springback of the deformed part and eventually increased forming accuracy.

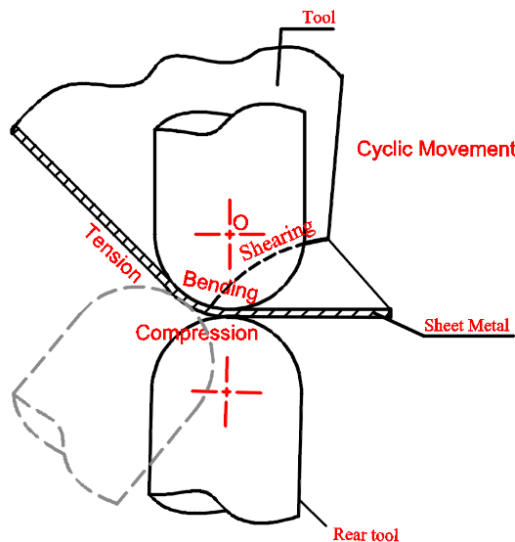


Figure 2.22 Schematic of different deformation modes in DSIF

However, compared with SPIF, published studies on the experiments or FE simulations of DSIF are very limited probably due to greater difficulties in performing DSIF than SPIF. Malhotra et al. [29] compared the forming depth of conic shapes manufactured by SPIF and DSIF and reported that the forming limit of the material was further enhanced in DSIF.

In general, the existence of the imposed contact force would increase the formability of the materials, as reported by Smith et al. [92]. Smith et al. [31] compared the deformation mechanics of SPIF and DSIF by performing FE modelling and found that the existence of the compression caused higher hydrostatic pressure and shear strains in the material, which might delay the initiation and development of fracture, thus improving formability.

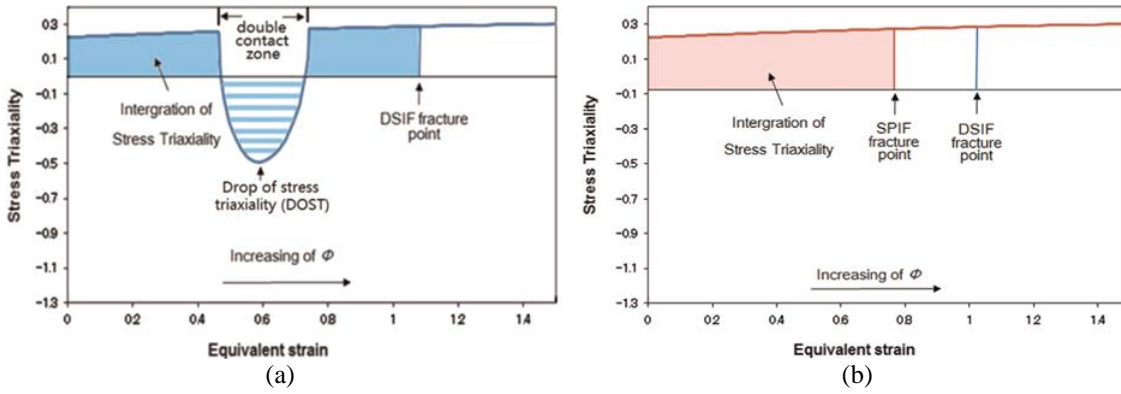


Figure 2.23 Comparison of stress triaxiality along the strain evolution between DSIF and SPIF[30]: (a) DSIF; (b)SPIF

By establishing an analytical model, Lu et al. [30] obtained the stress distribution in the contact areas of the tool-material interface, including the single-contact area and the dual-contact area, and observed a phenomenon defined as Drop of Stress Triaxiality (DOST). In DOST, stress triaxiality suddenly dropped to a negative value in the dual-contact area. A smaller stress triaxiality means less chance of damage development in the material thus achieving better material formability, as shown in Figure 2.23.

In the experiment conducted later by Lu et al. [30], a wide range of the supporting force from the rear tool was investigated, ranging from 160 to 640N. As shown in Figure 2.24 (a), the maximum forming depth of the cone was increased considerably by about 50% at first when the supporting force was increased to 480 N; however, it started to decrease when a higher compressive force of 560 N was applied. The decrease of the forming depth under higher compressive force was explained by the observation that the extremely high squeezing effect between the sheet and the contacting tools caused surface damage and severe sheet stretching in the master tool movement direction, which could be reflected by the mark left on the surface of the part, as shown in Figure 2.24 (b).

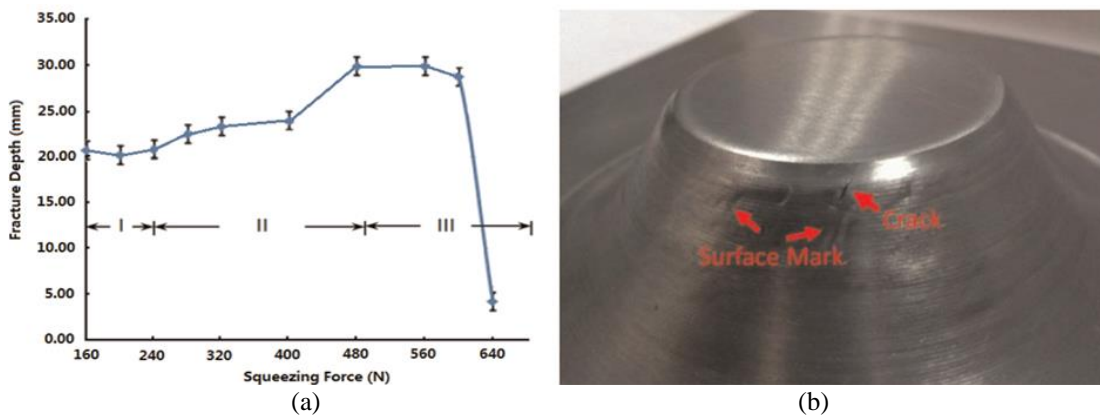


Figure 2.24 Influence of supporting force in DSIF using material AA7075-T6 [30]: (a) fracture depths of the cones with varied supporting force; (b) surface marks on the part

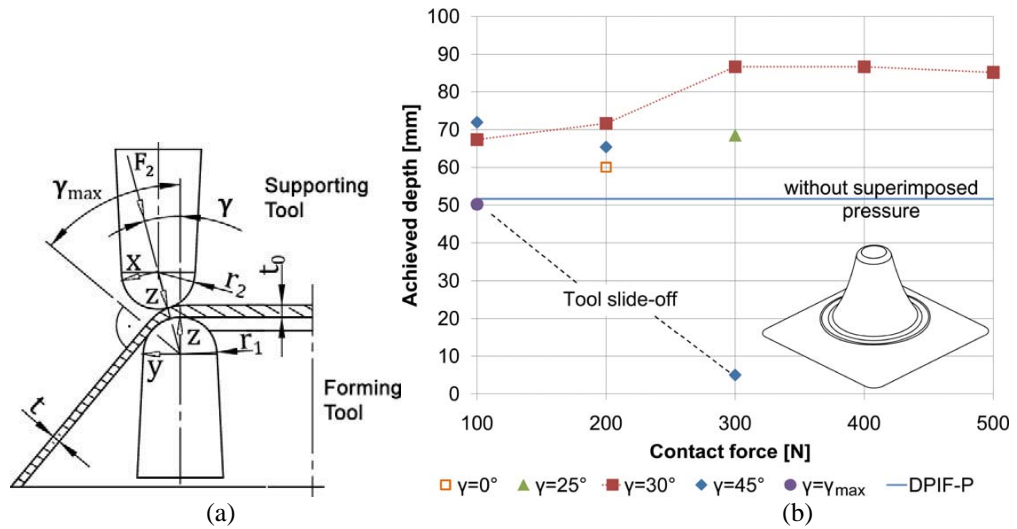


Figure 2.25 Influence of contact force and relative positions between the tools on the material formability DSIF [93]: (a) schematic of the tool positions; (b) achieved depths of hyperbolic parts with varied contact force and shifting angles using material AlMn 99.81hh

The effect of the compression includes not only the magnitude but also the relative position of the two tools, as illustrated in Figure 2.22. Meier et al. [93] changed the supporting force and the relative position of the tools and achieved a maximum increase of the drawing angle by 12.5% with an optimized parameters of 300 N and 30 degree using alloy AlMn 99.81hh, as shown in Figure 2.25.

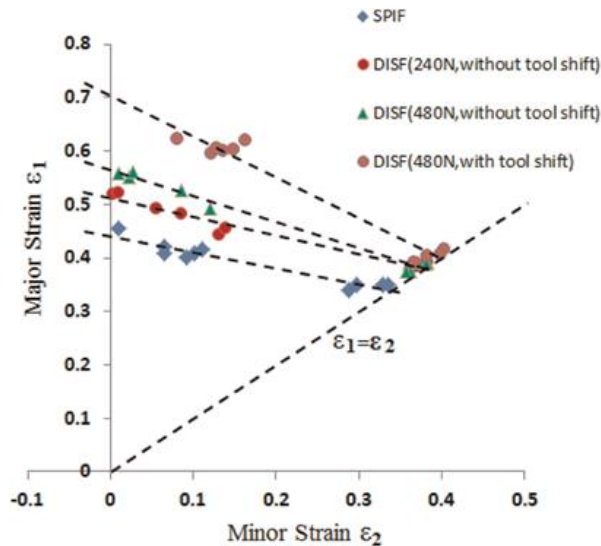


Figure 2.26 Forming limits of material AA7075 in DSIF with different relative locations and different supporting forces [30]

Adjusting the relative position of the two tools in DSIF will simultaneously change the division of the deformation zones, thus affecting the strain and stress distributions in the deforming sheet. Consequently, the forming limit can be influenced. As shown in Figure

2.26, Lu et al. [30] found that under the supporting force of 480N, the FLC for DSIF with tool shift was higher than that without tool shift.

In terms of fracture in DSIF, Valoppi et al. [94] manufactured a double curved part with electricity-assisted DSIF and conducted fractography analysis of the fracture surface of the samples by using scanning electron microscope (SEM). According to their analysis, Mode I opening fracture was prone to occur in zone III due to its higher stress triaxiality and tapered thickness compared to that in zone II and I. At the same time, the local bending and through-thickness-shear effect intensified, leading to the initiation of the crack on the outer surface in zone III, as shown in Figure 2.27. The analysis was supported by the appearance and direction of dimples observed on the crack surface.

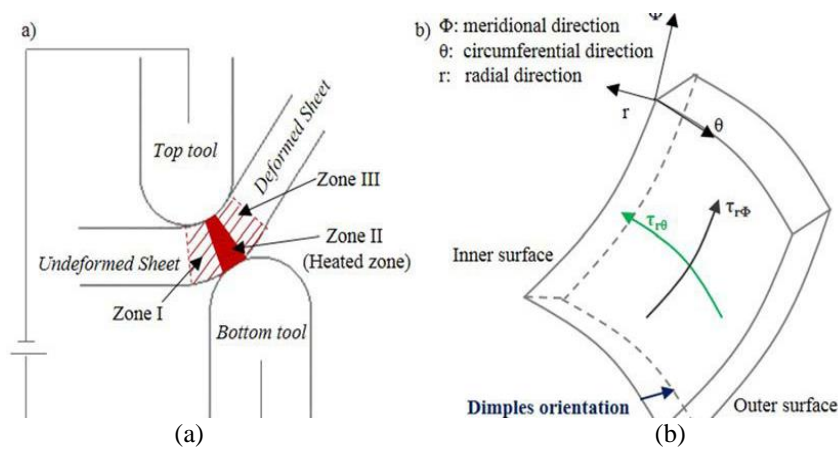


Figure 2.27 Deformation zones in DSIF and its effect on the fracture initiation [94]: (a) distribution of the deformation zones in the contact area; (b) schematic of the shear stress components in zone III and the location of crack initiation

Lu et al. [30] observed the location and morphology of the fracture and claimed that they could be influenced by both the supporting force and the relative position of the tools. As shown in Figure 2.28, tearing cracks were observed when the position of the tools was adjusted. Both cracks were initiated in the single-contact zones, however, they propagated in different directions. In Figure 2.28 (a), the crack propagated into the dual-contact zone while in Figure 2.28 (b), the crack stayed in the single-contact zone, parallel to the tool movement direction. The authors concluded that the crack propagation in Figure 2.28 (b) was caused by the post-stretching from the forming tool. The relative position of the tools and magnitude of the supporting force applied changed the stress and strain distributions in the affected zones, leading to a different fracture behaviour in DSIF.

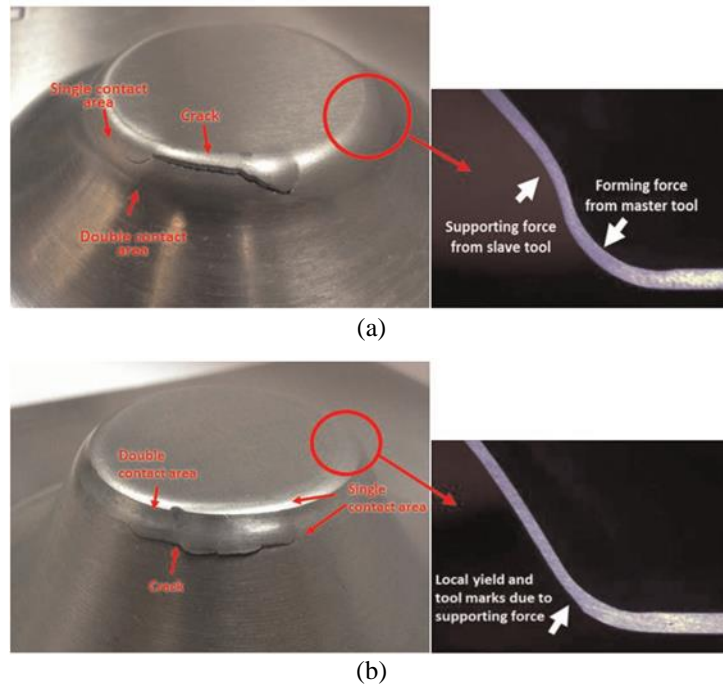


Figure 2.28 Part fracture with different relative locations between the master tool and the rear tool [30]:  
 (a) with tool shift; (b) without tool shift

## 2.2 Material Testing Methods for Sheet Metal

An accurate interpretation of the material deformation in a forming process requires a detailed description of the material properties during deformation process. To obtain the material mechanical properties, material testing needs to be carried out. According to the number of directions the load is applied in the test, commonly used material tensile testing methods can be divided into the uniaxial tensile test and biaxial tensile test. In addition, to describe material deformation behaviour under complex loading conditions, for example shearing and cyclic loading, other testing methods have also been developed.

### 2.2.1 Uniaxial tensile test

Uniaxial tensile test is undoubtedly the most popularly used material testing method due to its simplicity and effectiveness to describe the material behaviour for most sheet metal forming processes. Testing platform for uniaxial tensile test has already been industrialized and geometries for testing specimen and testing procedures have been detailed in ASTM-E8 standard [95].

In the uniaxial tensile test, for sheet material, a dog-bone shaped specimen is used, as shown in Figure 2.29. Reduction of the width in the central part of the specimen guarantees that the plastic deformation will be limited to the targeted gauge zone. During the test, the specimen is clamped first on both ends and then pulled steadily by the testing

equipment until fracture occurs. The elongation of the specimen and the reactive tensile force exerted on the specimen will be recorded from which the flow stress curve can be obtained. Based on the flow stress curve, the material deformation behaviour in other manufacturing processes with more complicated deformation modes can be evaluated. In FE simulation models, the stress-strain data obtained from the uniaxial tensile test is usually used to describe the deformation and work-hardening behaviour of the material.

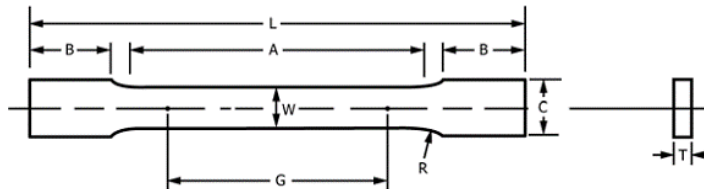


Figure 2.29 Geometry of the specimen in uniaxial tensile test in ASTM-E8 standard [95]

However, the simple uniaxial tensile test has its limitations. Firstly, the maximum strain obtained from the uniaxial tensile test is usually too small compared with actual sheet metal forming processes. For example, for pure aluminium sheet, the maximum elongation rate can be even below 10%. While in DSIF, its formability can be largely enhanced, exceeding the maximum deformation predicted by the uniaxial tensile test. As a result, material deformation behaviour after the necking point of the specimen cannot be described by the result obtained from uniaxial tensile test.

To overcome the limitation of using uniaxial tensile test data in the FE modelling of sheet metal forming processes, the extrapolation methods have been applied to cover the stress and strain regions where the uniaxial tensile test cannot reach. Different extrapolation strategies are adopted. For example, in the software Abaqus, linear extrapolation is automatically implemented when the strain calculated during the deformation is greater than the data provided in the definition of the flow stress curve [96]. To get better predictions, various material work-hardening laws have also been developed so the flow stress curves of the material can be described directly by using mathematical equations. Hollomon's law and Voce's law are proved to fit the flow stress curve data quite well for the materials when the strain is not too large [97]. However, diversions appear after the strain reaches a certain value, which means that the extrapolation strategies are not reliable without experimental validation of the flow stress curve.

In addition, in uniaxial tensile test, the material is tested in only one direction. However, in sheet metal forming, material anisotropy is a significant factor that cannot be ignored. Material anisotropy will cause distinctive deformation behaviours in different directions. One of the most common effects resulting from anisotropy is the earing effect in the deep

drawing process [98]. Consequently, in order to describe and simulate the anisotropic behaviours of the material, material properties in different directions should be obtained first.

Material anisotropy can be tested by performing uniaxial tensile tests of the specimens cut from certain angles to the rolling direction. Normally, specimens cut in parallel, 45 degrees and perpendicular to the rolling directions are used. However, it still cannot reflect the influence of loading path on the material formability. For example, materials generally show higher equivalent strain at fracture under biaxial tensile state than that in uniaxial tensile state. As a result, material testing method considering more complex loadings should be used to obtain a more comprehensive and accurate description of the material mechanical properties.

### 2.2.2 Biaxial tensile tests

In order to obtain the material deformation behaviour under biaxial tensile condition, biaxial test of materials needs to be performed. Unlike uniaxial tensile tests, for which international standards have already been established, majority of biaxial tensile tests was conducted on the self-developed testing platforms and samples. Generally, the biaxial testing methods can be divided into two categories according to the conformity of the loading axes to the plane that the load is applied: out-of-plane biaxial tensile test and in-plane biaxial tensile test.

#### 2.2.2.1 Out-of-plane biaxial tensile test

Out-of-plane biaxial tests include the hydraulic bulge test and the dome test. According to ISO 16808 standard [99], in the hydraulic bulge test, as shown in Figure 2.30 (a), the clamped circular sheet blank is gradually deformed by the pressurized fluid. The opening shape of the upper die can be hemispherical or elliptical to achieve different strain paths [100]. The strain path achieved from the hydraulic bulge test can be varied between plane strain and equi-biaxial. The strain distribution at the apex area of the blank can be captured by the DIC equipment during the deformation process. Using the inverse method, corresponding stress distributions can be obtained.

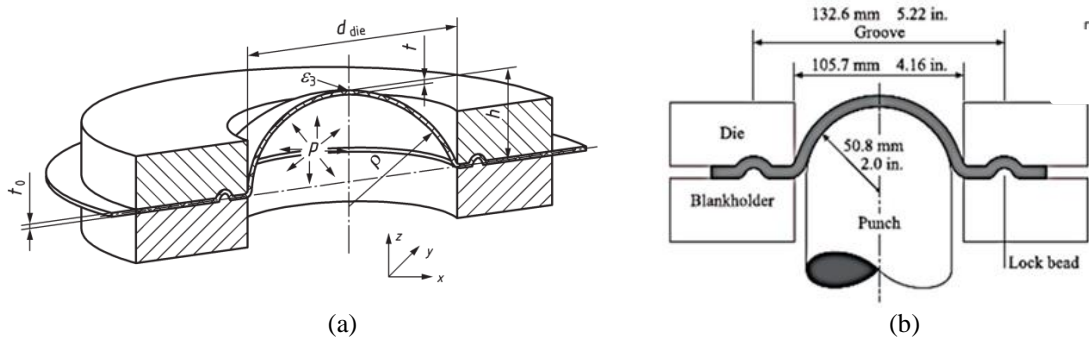


Figure 2.30 A schematic of biaxial tensile tests: (a) hydraulic bulge test [101]; (b) dome test [102]

In the dome test or Nakazima test [103, 104], instead of using pressurized fluid, a solid hemispherical punch is used to apply the load onto the blank, as shown in in Figure 2.30 (b). To reduce the friction between the punch and the blank, lubricant must be applied. To obtain the material deformation behavior under various strain conditions, instead of using circular blank, different types of dog-bone shaped specimens are used in the Nakazima test, as show in Figure 2.31 (a). To accommodate different loading paths, three parameters of the geometry need to be optimized with the help of FE modelling. By performing the dome test, the FLC can be obtained, as shown in Figure 2.31 (b).

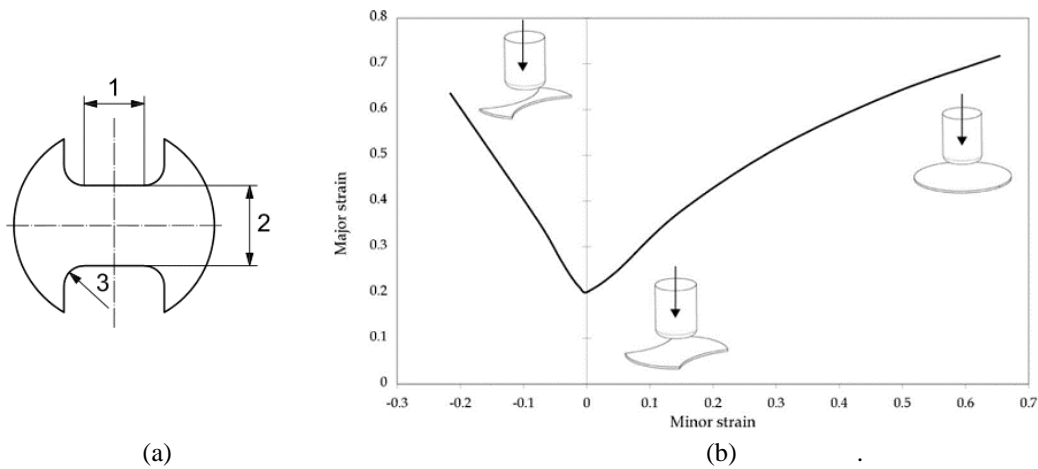


Figure 2.31 Nakazima test: (a) specimen geometry; (b) schematic of the FLC obtained from the test with different strain conditions obtained by using different geometries

The adoption of the liquid in the bulge test requires that the testing environment to be totally sealed to avoid liquid leakage during the test. In comparison, the simplicity of the testing equipment for the dome test promotes its application in the industry. However, the bulge test still has its disadvantage due to the fact that pure tension is difficult to achieve in the dome test even with proper lubrication used in the dome test [102]. The difference between the flow curves for different materials using different testing methods was reported by Groseclose et al. [101], as shown in Figure 2.32.

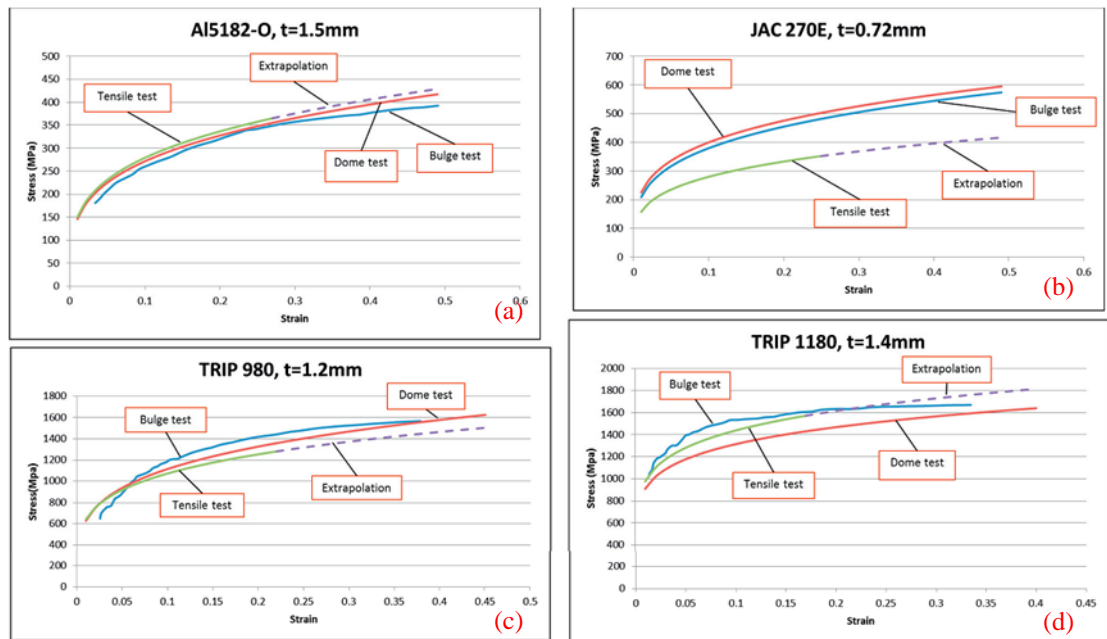


Figure 2.32 Comparison of flow curves under frictionless dome, bulge and tensile tests using different materials [101]: (a) Al5182-O; (b) JAC 270E; (c) TRIP 980; (d) TRIP 1180

### 2.2.2.2 In-plane biaxial tensile test

The shape of hemispherical punch in the out-of-plane testing methods inevitably introduces bending and contact effects into the test thus ideal pure tension cannot be obtained. This defect can be solved by the in-plane biaxial testing methods. One of the most popularly used in-plane testing methods is the Marciniak test [44]. As shown in Figure 2.33, in the Marciniak test, a punch is used to apply the load. Depending on the strain path to be achieved, the cross-section of the punch can be cylindrical, elliptical or rectangular. To avoid friction between the punch and the sheet and to avoid earlier fracture in the corner of the punch, a ring-shaped metallic blank is positioned between the punch and the test specimen. The Maciniak test shares specimen with similar geometry shown in Figure 2.31 (a).

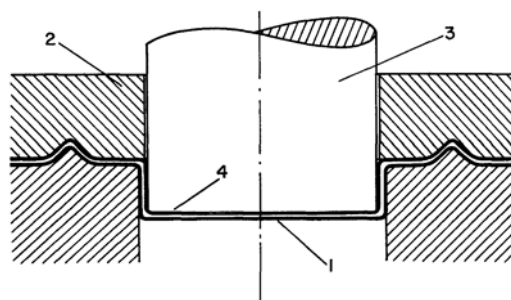


Figure 2.33 A schematic of the Marciniak test [44]

In order to realize different strain paths, all the biaxial tensile tests introduced, in-plane and out-of-plane tests, require an optimization of the geometry of the tool or the specimen or both beforehand for each strain path. The strain condition of the target area in the specimen is dependent on the geometric constraint created by the punch/fluid and the specimen.

To simplify the designing process of the specimen, another in-plane biaxial tensile test, the planar biaxial tensile test was developed. This testing method is very straightforward, a cruciform specimen is directly stretched in two directions perpendicular to each other so that the bending effect and contact effect to the tested area can be eliminated from the test. The standard for this kind of biaxial tensile test, ISO 16842 standard [105] is currently under development.

For the uniaxial tensile test, international standards have already been well developed, in which specimen dimensions and testing procedures are strictly defined for different purposes, even for the specified types of materials [106]. As a result, the same rules are followed by all the researchers, which makes the published literature credible and easy to compare. However, for the in-plane biaxial tensile tests, the cruciform specimen dimensions have not been defined in the uncompleted international standard. The cruciform specimen has to be designed for the specific materials or to suit specific purposes.

The specimen proposed in the ISO 16842 standard is based on the geometry developed by Kuwabara et al. [107] and Hanabusa et al. [108], as shown in Figure 2.34. The four arms transfer the stretching to the central target area while the slots in the arms reduce the influence of transverse forces from the arms. It has already been confirmed by FE simulation results that the existence of the slots leads to a more evenly distributed strain field in the target central region. The number, dimensions and the position of the slots could be crucial to the stress/strain distribution in the specimen [109]. However, the effective strains obtained from test using this shape of specimen were comparatively small. Fracture first occurs in the arms rather than in the centre as expected due to the width reduction caused by the slots.

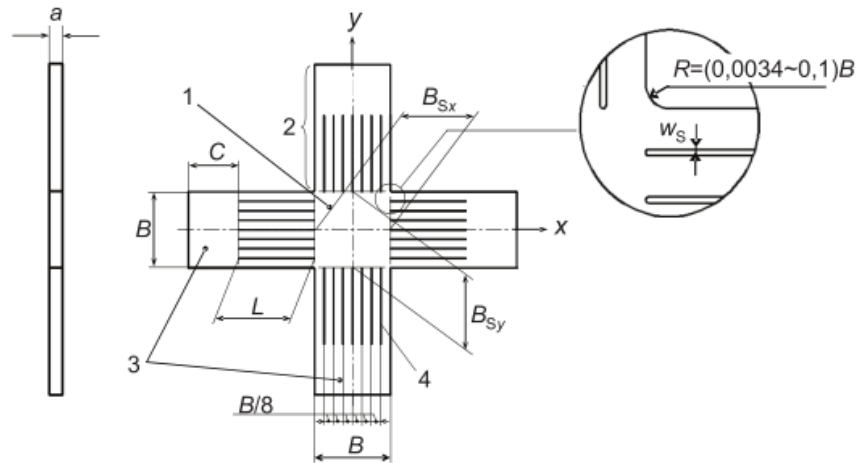


Figure 2.34 Standard shape proposed in ISO 16842 standard [105]

Geometries that can generate greater uniform deformation in the in-plane biaxial tensile test should be developed. According to Hannon and Tiernan [110], in order to design an ideal cruciform specimen for the biaxial tensile test, three criteria should be met:

- The plastic deformation of the specimen should happen in the gauge area, which should be in the centre of the specimen;
- The plastic deformation should be as homogeneous as possible in the gauge area;
- The centre of the specimen should stay in the same place for the convenience of measurement and more importantly, for the determination of the principal strain and stress axes.

FE method has been proved effective in optimizing the geometry of the specimens in order to satisfy the deformation requirements in the biaxial tensile test [111, 112]. In order to guarantee homogeneous deformation in the centre of the specimen, imperfections have been created in the central area of the specimen. There are two methods to create imperfection in the central area. In the first method, the thickness of the target area can be reduced. The sheet can be thinned on one side or on both sides. The shape of the area with tapered thickness can be circular or rectangular. While in the second method, on the contrary, the thickness of the arms can be reinforced, making them thicker than the central area so that imperfection can still remain in the centre.

Based on the work done in the previous studies, Zidane et al. [113] concluded that four geometrical parameters were the most important when deciding the shape of cruciform specimen, including the length between the end of the slot and the edge of the central square  $L$ , the fillet between the arms  $R_c$ , the thickness of the central test region  $T$  and the

diameter of the central test region  $D_i$ , as shown in Figure 2.35. By performing parametric study with the help of the FE analysis, the best set of parameters was obtained for material AA2017,  $L=4.5\text{mm}$ ,  $R_c=8\text{mm}$ ,  $T=0.75\text{mm}$ ,  $D_i=10\text{mm}$ . Using the specimens designed by these parameters, equi-biaxial tensile experiments with rolled AA2017 sheet metal were conducted and it was proved that the central area of the circle was under equi-biaxial tension.

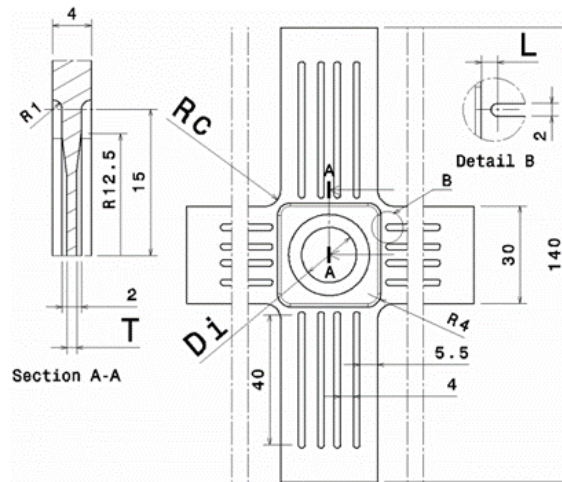


Figure 2.35 Cruciform specimen design optimized by Zidane et al.[113]

Standard deviation of the stress in the gauge area was proposed by Demmerle and Boehler [114] as the criterion to quantify the effect of the specimen parameters on the distribution of the stress and strain. Seven shapes of specimens were compared first and the specimen with uniformly thinned central region of square shape was proved to be the one most close to the criterion, as shown in Figure 2.36.

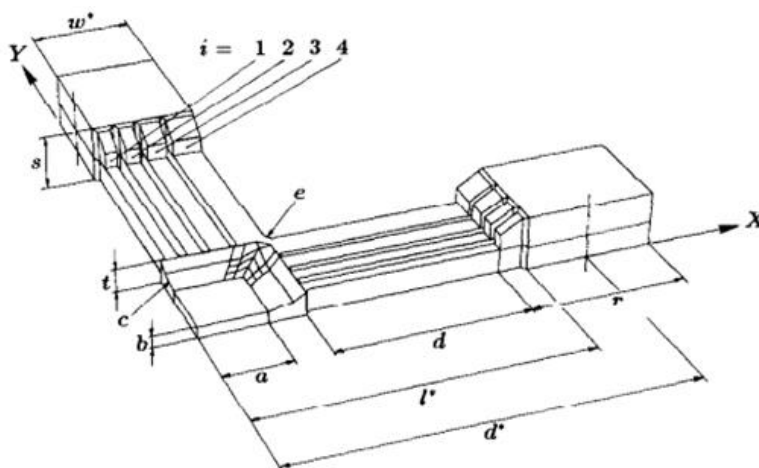


Figure 2.36 Parameters of the specimen optimized in [114]

Furthermore, 10 parameters of the specimen geometry were selected in the optimization process, including the half-length of the thinned central section  $a$ , half-thickness of the

thinned central section  $b$ , transition radius of the fillets between the initial thickness and the thinned central section  $c$ , length of the arms  $d$ , radius of the corner fillet between two adjacent arms  $e$ , area of the slots, width of the slots, width of the limbs, length of the grip head  $r$  and half-thickness of the grip head  $s$ . Using the criterion proposed, the best two sets of parameters were obtained. In addition, it was proved that the thickness of the thinned section was the most important parameter, while the influence of the slot width was negligible [114].

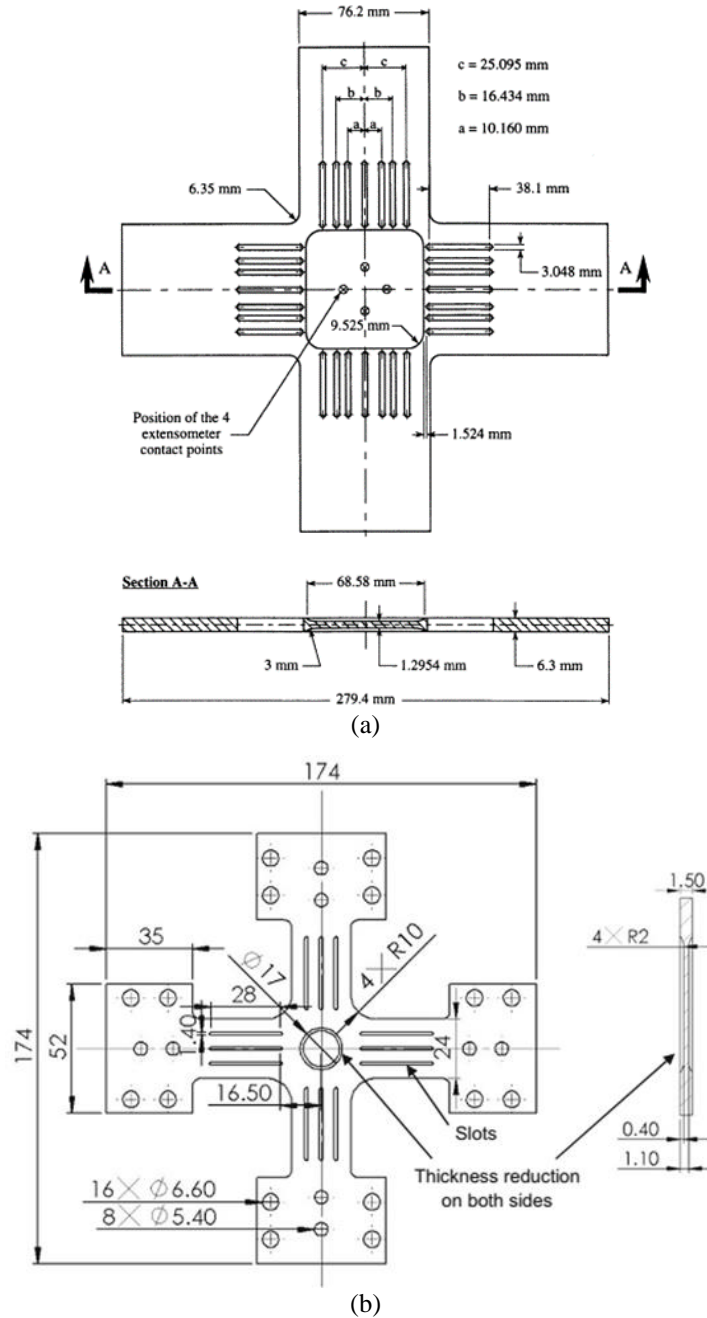


Figure 2.37 Thin cruciform specimens with thickness reduction in the centre proposed : (a) Green et al. [115]; (b) Shao [116]

However, for the thin sheet material, excessive thickness reduction of the central region or keeping a grip area with larger thickness is not realistic considering the manufacturing difficulty and cost. Green et al. [115] proposed a cruciform specimen with tapered thickness on both sides of the centre of the specimen, as shown in Figure 2.37 (a). The flow stress curves obtained from the experiment and predictions from the FE simulations using the yield criteria of planer anisotropy were compared. The experimental results showed great uniformity with the yielding locus predicted by the yield criteria, which meant that the homogeneous biaxial tension area in the centre of the specimen was large enough and the shear effect from the arms nearby was eliminated by the introduction of the slots in the arms. A similar specimen design with a circular thickness reduction area in the centre was designed by Shao et al. [116], as shown in Figure 2.37 (b).

The disadvantage of the specimen with thickness reduction on both sides is that the high manufacturing cost compared with the one with thickness reduction on just one side. In order to constrain the fracture location to the very centre of the specimen, Song [112] concluded that two criteria should be met,

- The length of the slots in the arms should not be equal and the tips of the slots in the arms should form an angle;
- The thickness of the central area should gradually decrease and the central point should be the thinnest.

Based on the criteria, FE optimization of the specimen geometry for the material AA5086 was performed and the optimized geometry is shown in Figure 2.38.

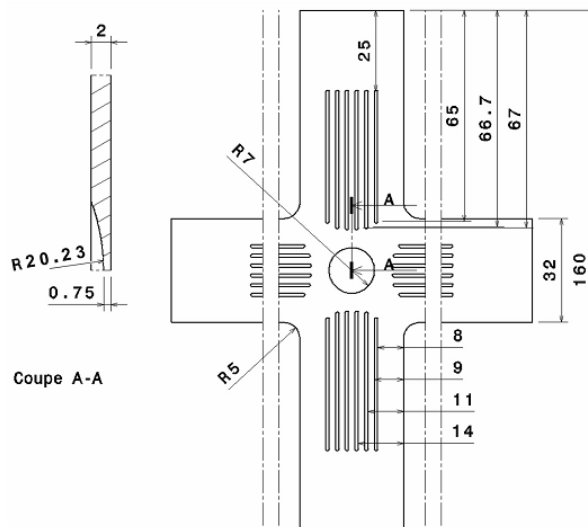


Figure 2.38 Geometry of the thin cruciform specimen optimized by Song [112]

In order to apply the biaxial tension, a testing machine needs to be designed specifically. Various testing equipment has been developed by the researchers, as reviewed by Hannon and Tiernan [110]. According to the structure adopted to apply biaxial loading, the developed biaxial tensile testing platforms can be classified into two types. In the first type, a mechanical structure, as shown in Figure 2.41 (a), normally consisting of four arms with different length in the opposite directions, converts the downward movement of the CNC machine into stretching in the planar directions [117-119]. By adjusting the

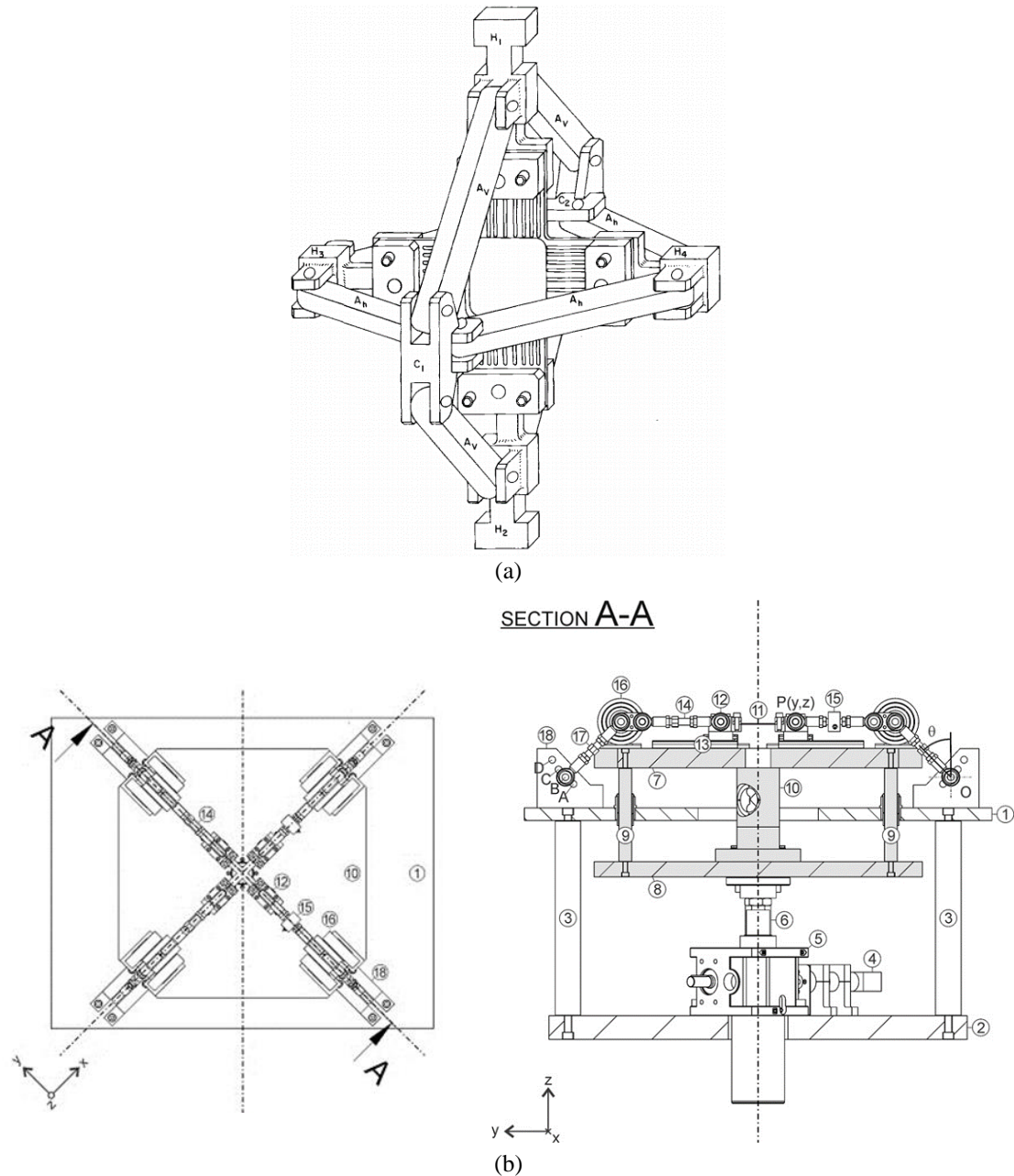


Figure 2.39 Biaxial tensile platforms with fixed strain ratios developed by: (a) Ferron et al. [117]; (b) Merklein et al. [119]

length of the arms, the tensile speed in the planar directions can be varied, so that the strain ratio of the two stretching directions can be changed. As a result, the strain ratio is fixed if the length of the arms is kept the same.

In the other type of test platforms, the tension onto each arm is directly applied by the linear motion generated by hydraulic cylinders [120] or motors [121]. As shown in Figure 2.40, in the biaxial tensile test platform designed by Makinde et al. [121], the cruciform specimen could be stretched in four directions simultaneously by the actuators, one on each side. By changing the speed ratio of the actuators, various strain ratios can be achieved without changing the structure of the test platform. In order to control the motor movement, a control system is required for this type of test platform.

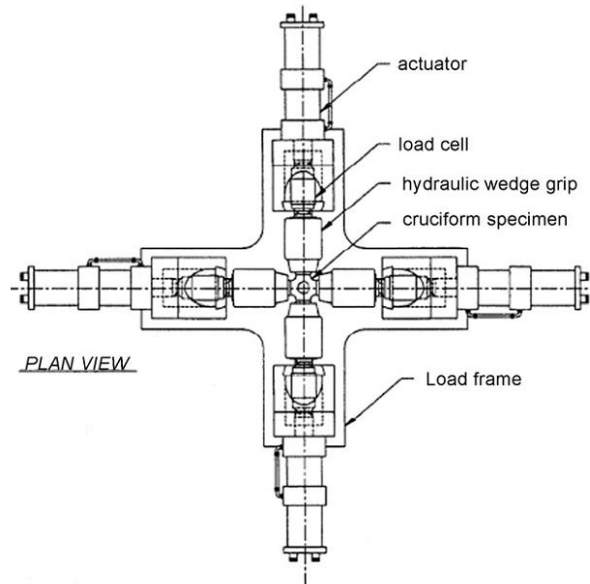


Figure 2.40 In-plane biaxial tensile test platform designed by Makinde et al. [121]

In the commercial testing platform developed by the company Zwick/Roell [122], as shown in Figure 2.41, the tensile forces are supplied by four electro-mechanical linear motors which can provide up to a maximum test force of 150 kN. The motors' travel resolution can be as high as 0.1  $\mu\text{m}$ . However, the motors are costly and the alignment and the synchronization of the movement of the motors are complex.

Compared with the second type of biaxial tensile machine, the whole link mechanism structure used in the first type is much simpler since no controlling system needs to be integrated into the system. While the movement of the punch is normally driven by a commercial CNC machine, the positioning accuracy of the punch can be guaranteed. However, it also requires that high manufacturing accuracy and assembly accuracy of the structure. For example, the length of the arms needs to be precise in order to guarantee

the speed ratio in the two directions. By comparison, the highly integrated system in the second type maintains high structure rigidity and robustness. No more structure needs to be replaced to change the loading path. The positioning accuracy mainly depends on the structure rigidity, precision and degree of synchronization of the motors. In addition, in the second type of structure, more space can be allowed for a further development of the machine. For example, a DIC measurement system can be mounted on the frame to measure the deformation evolution history during the test on the platform developed by Zwick/Roell [122].



Figure 2.41 Biaxial tensile test platform developed by the company Zwick/Roell [122]

### 2.2.3 Other test methods for sheet metal

In the uniaxial and biaxial tensile tests, only monotonic tension is applied onto the specimen. However, in sheet metal forming processes, material can be deformed under various loading conditions. A better description of material properties in the sheet metal forming processes requires that the material can be tested under more realistic conditions. Commonly existing complex loading conditions include non-tension dominated loading, such as shearing, and cyclic loading.

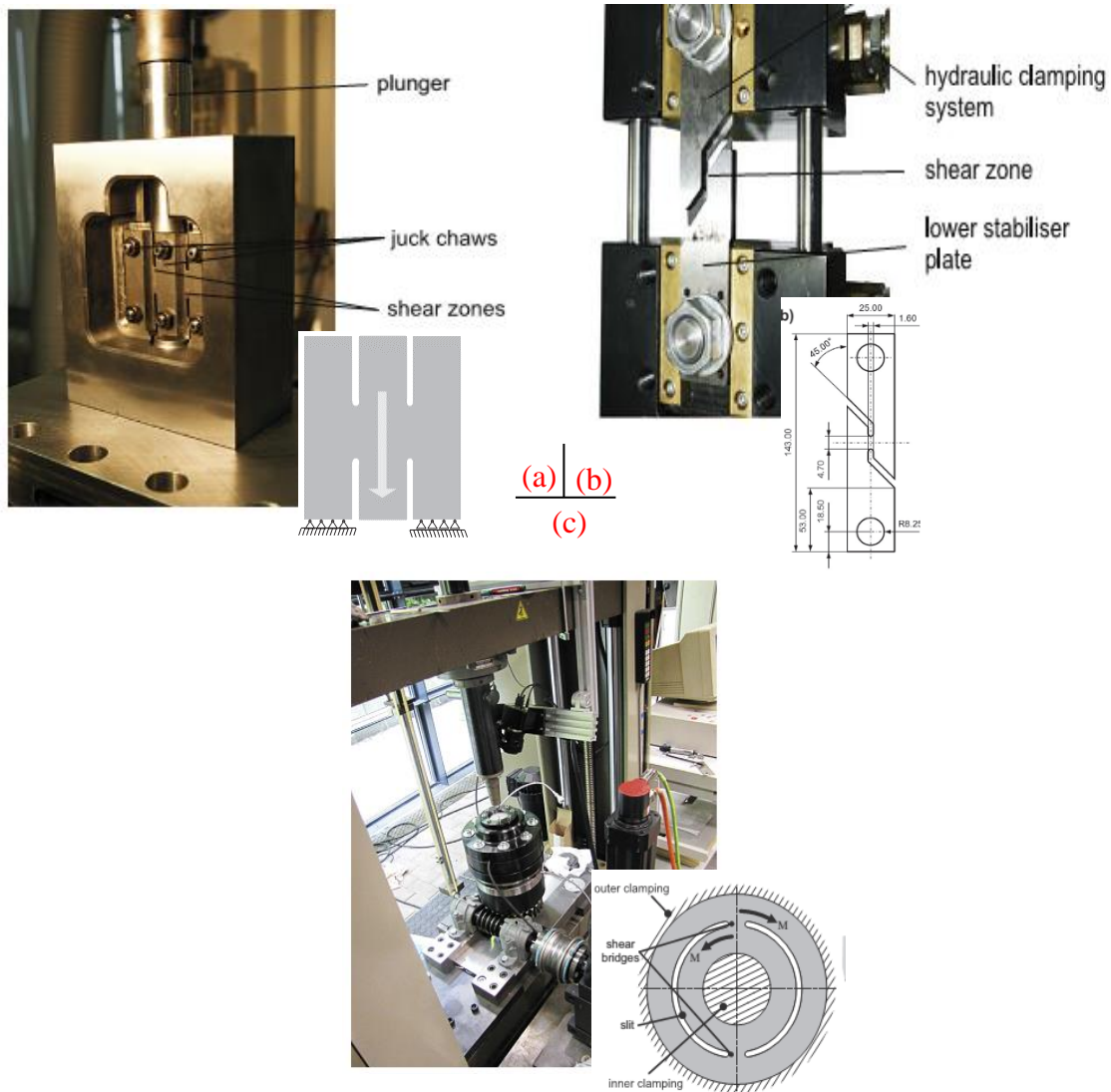
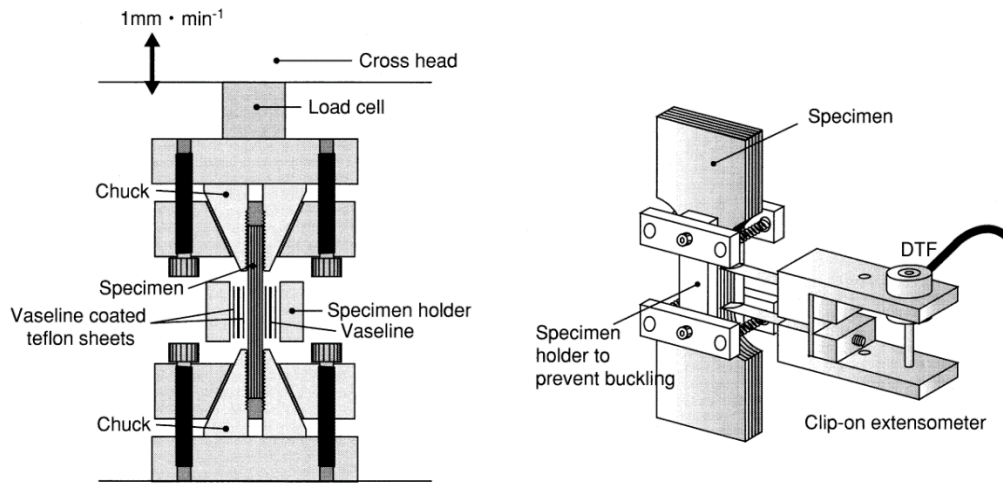


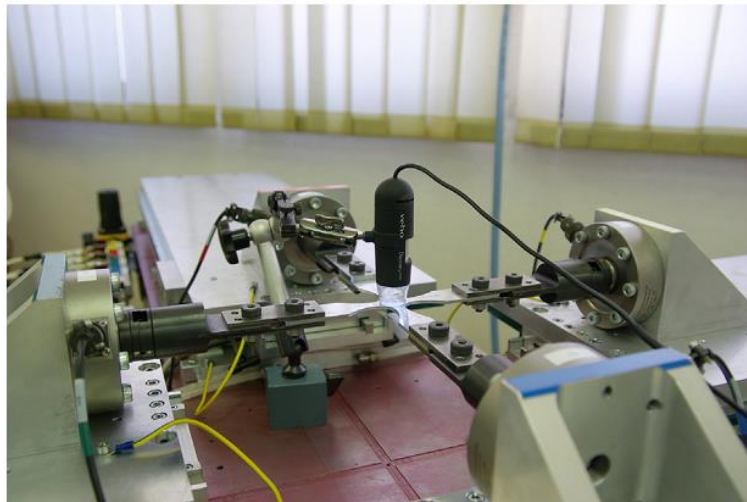
Figure 2.42 The shear test setup and specimen geometry for: (a) Miyauchi test; (b) modified ASTM-B831 test; (c) twin-bridge test [123]

For material under shear-dominated loading condition, the material deformation behavior cannot be predicted by the data obtained from these tensile tests [124]. As a result, pure shear test methods were proposed by the researchers. In the test proposed by Miyauchi [125], the pure shear specimen was divided into three parts, the ends of both the left and right part were fixed so that pulling the central part would generate two shear deformation zones, as shown in Figure 2.42 (a). While in the pure shear test with the modified ASTM-B831 [126] specimen, only one shear zone exists, as shown in Figure 2.42 (b). A third variety is the in-plane twin-bridge torsion test [127], as shown in Figure 2.42 (c), in which the disk is fixed on the outer edge while the central axis is fixed to tool. The shear could be generated by the rotational movement of the tool in the connecting region between the central area and outer ring area. All the three types of tests showed good agreement

between the shear strain-stress curves obtained from the experiment, as proved by Yin et al. [123].



(a)



(b)

Figure 2.43 Cyclic tests: (a) cyclic tension-compression test conducted by Yoshida et al. [128]; (b) cyclic test using a cruciform specimen by Cláudio and Freitas [129]

Furthermore, material can present different deformation behaviour when the loading applied is not monotonic. Change of yielding strength of the material when subjected to cyclic reversed loading condition, or the Bauschinger effect was first revealed by Bauschinger [130]. Material can be softened or hardened under cyclic loading [131]. To describe material deformation behaviour under cyclic loading, material cyclic tests have been developed. The ASTM E606/E606M-12 standard defines the basic requirement for the strain-based cyclic test [132]. To avoid buckling of the specimen in the cyclic tension-compression test, laminated sheet specimens were used by Yoshida et al. [128], as shown in Figure 2.43 (a). A step further, the material response under biaxial loading conditions

were investigated by adopting cruciform specimens [129, 133], as shown in Figure 2.43 (b).

In addition to these traditional material testing methods, various testing methods have been developed to accommodate the unique deformation characteristics of sheet metal forming process, such as the continuous bending under tension test [48].

In conclusion, the purpose of material testing is to accurately describe or predict material deformation behaviour in a sheet metal forming process. Materials are prone to behave in different ways when subject to different loading conditions. Consequently, appropriate testing method should be selected for different processes. The selection of a suitable testing method requires an understanding of not only the material deformation during the forming process, but also the purpose of performing test.

## 2.3 Prediction of Failure in Sheet Metal Forming Processes

To predict material formability under simple loading conditions, theoretical models were first developed to predict the material formability based on the localized necking theory by Hill [134] and Swift [135]. To improve its applicability and accuracy, more complicated models, including the M-K model [44] were proposed. Although the mathematical models are straightforward, they can be complicated and require a sound understanding of the continuum mechanics theories. In addition, simplifications of the loading conditions and material properties are commonly adopted in these models to facilitate the analysis process, resulting in deviations of predicted results from the experimental observations. As a result, for material under linear and proportional loading, for example the deep drawing process, the material formability can be assessed by the forming limit diagram/curve (FLD/FLC). For complicated loading conditions, other methods, for example the stress based forming limit diagram [136] or damage models [137, 138], have been developed to predict material deformation failures in metal forming processes.

### 2.3.1 Forming limit diagram

The FLD is the most commonly adopted method to predict material failure in sheet metal forming processes. It was first proposed by Keeler and Backofen [139] and Goodwin [140]. Generally, in FLD, a forming limit curve (FLC) is used to delineate the boundary between the safe zone and the potential failure zone in the major strain-minor strain space. To draw the FLD for specific material, the material forming limits under various loading

paths should be obtained, various tests ranging from the pure shear test to the uniaxial tensile test and the equi-biaxial tensile test need to be conducted using the testing methods reviewed in Section 2.2. Normally, the FLC follows a trend of V shape, as shown in Figure 2.31 (b).

However, Emmens et al. [141] claimed that FLDs could only be an effective method to predict the formability of the materials under the precondition that plane stress was the main loading condition and a linear strain path was applied. While in the conventional forming processes, the critical areas are usually under simple plane stress conditions but more complicated loading conditions may be present in other areas of deforming part. Taking deep drawing as an example, the bottom edge of the deforming part is under bending and tension so that the fracture generally occurs there. While in ISF, however, apart from simple tension, bending and shearing effects also contribute largely to the material deformation. In addition, progressive toolpaths in ISF create non-linear loading strain paths. Consequently, as explained by Benedyk et al. [74], the FLDs for ISF could be easily influenced by the process parameters, such as vertical feed and toolpath generation algorithm. It makes the FLD unreliable and unrealistic to predict the onset of the fracture accurately for a specific case in ISF. As a result, the FLDs cannot be considered as a reliable tool to analyse and predict the processing failure of the materials in ISF. Furthermore, the FLD method is purely empirical, it is not accurate enough to account for the occurrence of fracture in ISF. More fundamental studies taking into account of unique deformation characteristics of ISF and their effects on the prediction of the material processing failure should be pursued.

To overcome the issue of the FLD's dependence on the strain path and loading history, the stress-based FLC was first proposed by Kleemola and Pelkkikangas [142] and Arrieux [136], and it was further developed by Stoughton [143] and Stoughton and Yoon [144]. Direct measurement of the stress components during the forming process is impractical, the establishment of the stress-based FLD is still based on the strain measurement. Using the reversed calculation method, the corresponding stress distribution can be obtained. A comparison between the stress-based and strain-based FLDs is shown in Figure 2.44. Contrary to the obvious deviations between the FLDs obtained for material 2008 T4 Al with and without prestrain, the difference between the stress-based FLD was minor, the impact of the strain history on the FLD was compromised [144].

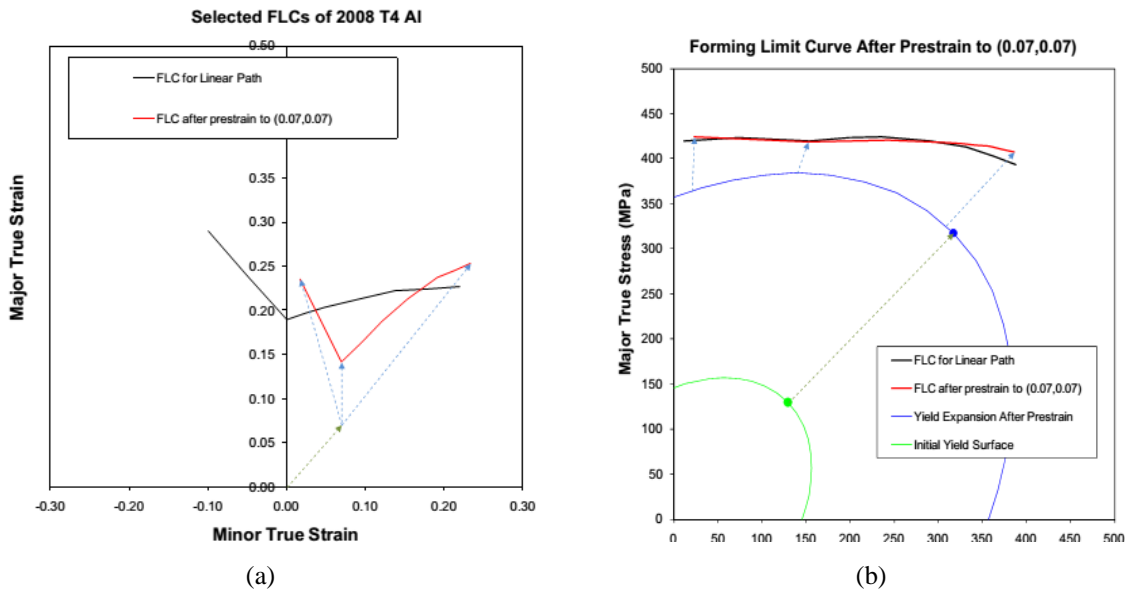


Figure 2.44 A comparison between different types of FLDs: (a) the strain-based FLD; (b) stress based FLD [144]

Haque and Yoon [145] introduced the stress-based FLD to predict the formability of the materials in SPIF process. According to their calculations, in the stress-based FLD, the influence of the loading history could be ignored and a uniform curve was obtained for the process even though different parameters were applied.

The second limitation of FLD is that it cannot differentiate material rupture from fracture with previous strain localization. For some materials, necking would not appear before the fracture, FLD could over or under-estimate their forming limits, which promoted the development of failure forming limit diagram/curve (FFLD/FFLC) [146]. The only difference between the FLD and FFLD is that the strain components for FFLD are measured only when the final fracture through the thickness happens while in FLD they are measured upon the occurrence of non-uniform deformation of the material.

### 2.3.2 Damage theories and damage modelling

Unlike strain or stress components, material damage or material deterioration during plastic deformation is a parameter that can hardly be directly measured. In order to characterize the severity of structural discontinuity in the material, Kachanov [147] and Rabotnov [148] first introduced a macroscopic damage indicator when studying material creep deformation. Their research promoted the birth of continuum damage mechanics (CDM) [138].

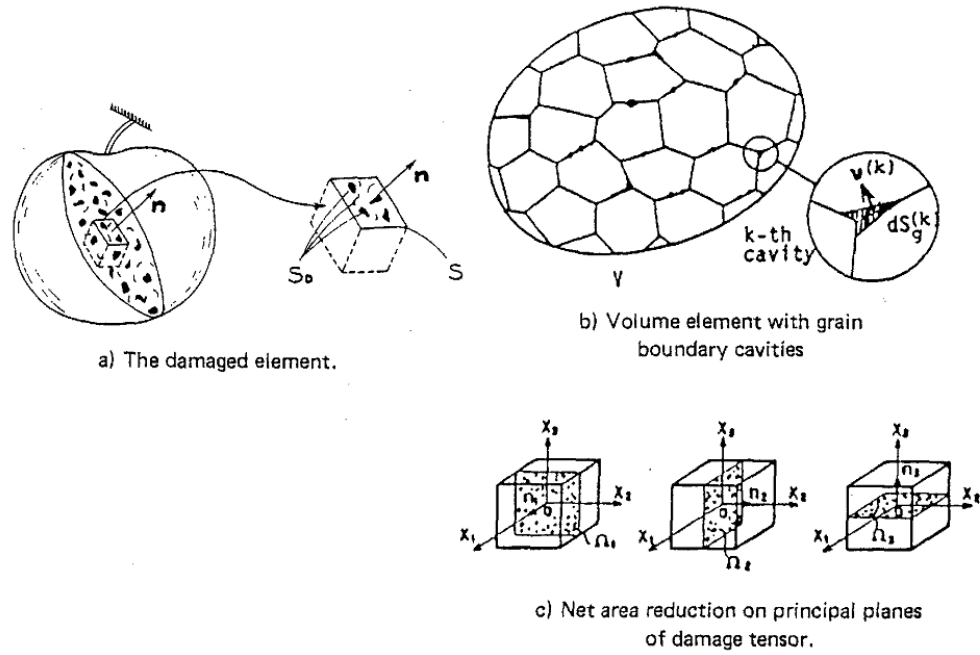


Figure 2.45 Net area reduction in the CDM concept [149]

The CDM is built on a macroscale level, so it is also called phenomenological damage mechanics. In CDM model, the severity of the damage in the material is represented by the reduction of area of the active resisting plane of the material [149], as illustrated in Figure 2.45,

$$D = \frac{S_D}{S} = \frac{S - S^*}{S}$$

where  $D$  is the damage variable,  $S_D$  is the area of active resisting plane and  $S$  is the total area of the resisting plane,  $S^*$  is the area of the cavity. When the damage indicator  $D$  reached a critical value, the material loses its ability to defend further plastic deformation and fracture happens. The change of the area of active resisting plane can be reflected by material physical properties such as the density [150] and fatigue limit [151] of the material.

By coupling material degradation into the constitutive models, material deformation behaviour at the material point during the deformation process can be described. The most popularly used CDM model is the Lemaitre model [152], in which the reduction of the area of the element surface could be a reflection of the change of the elastic modulus of the material,

$$D = 1 - \frac{E^*}{E}$$

where  $E^*$  and  $E$  are the elastic modulus of the damaged and undamaged materials respectively. In the constitutive model, the stress is replaced by the effective stress due to the resisting surface area reduction. Moreover, the damage indicator evolution during the plastic deformation is governed by the stress and strain state. The Lemaitre model has been successfully applied in predicting damage evolution in various sheet metal forming processes, including the punchless piercing [153], blanking [154] and hot rolling process [155].

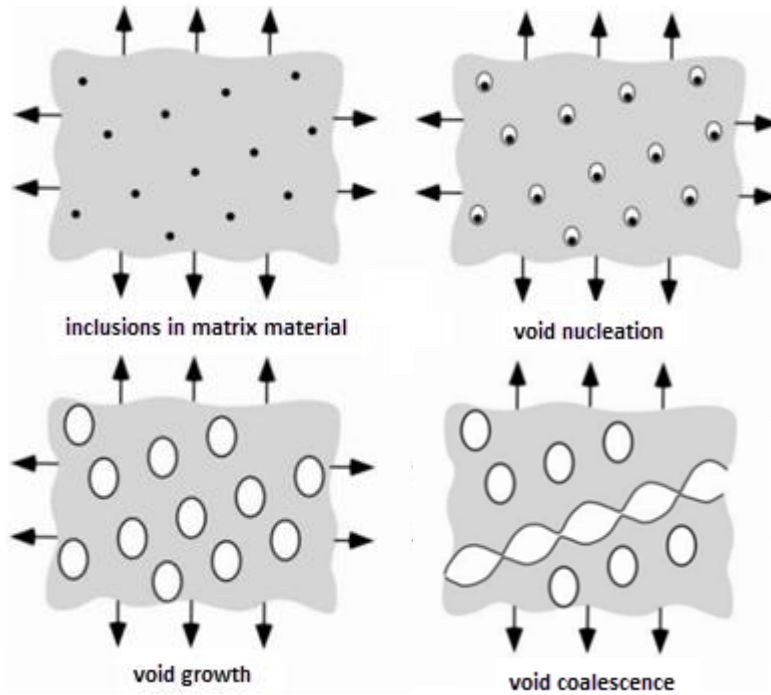


Figure 2.46 An illustration of the evolution of the voids in the material during material deformation [78]

Straightforward as CDM is, it oversimplifies or ignores the effect of material microstructure on the damage initiation and development. According to the experimental evidence concluded by Garrison Jr. and Moody [156] and Anderson [78], ductile fracture is fundamentally a result of the nucleation, growth and coalescence of voids in the material, as shown in Figure 2.46. The voids exist in the material even before the plastic deformation. With the deformation progressing, the voids grow to larger sizes, new voids appear due to nucleation around second phase particles such as inclusions, and larger voids coalesce thus micro cracks can be formed. Micro cracks ultimately develop into macro cracks, leading to fracture of the material. In order to model the behaviour of the voids during deformation and their effect on the material mechanical behaviour, the micromechanical damage mechanics (MDM) was developed.

The MDM is based on the micro-mechanics/porosity plasticity theory, in which material deterioration is caused by the voids in the material. It was pioneered by the work done by McClintock [157, 158], in which the growth of a cylindrical or elliptical void in an infinite base material was modelled under axial stretching. While Rice and Tracey [159] modelled the growth of spherical void under high stress triaxiality. In both models, only void growth was considered. The void growth was defined by the normalized void radius. When the radius reached a critical value, fracture happened.

Gurson [160] further improved the theory by taking account of the interactions between the voids and softening effect of the material due to the growth of the voids, leading to the development of the Gurson model. In the Gurson model, the void volume fraction (VVF) was treated as the damage indicator.

However, it was found that the Gurson model was limited because of its incapability to describe the coalescence between the voids and its inaccuracy in predicting void growth. To overcome its disadvantages, Tvergaard and Needleman [161] modified the Gurson model by introducing new parameters into the original Gurson model. The new model is known as the Gurson-Tvergaard-Needleman (GTN) model.

Nevertheless, the GTN model was still reported to be inaccurate in predicting damage in processes where the material was under shear-dominated deformation or under low or negative stress triaxiality [162]. To promote the application of the GTN model in these areas, further developments to the GTN model were reported by various researchers [163, 164]. However, Nielson and Tvergaard [165] discovered that the effect of shear extension introduced was exaggerated when the material was under plane strain condition and high stress triaxiality. To address this, an additional stress dependent coefficient was introduced into the modified GTN model [162, 166]. The GTN model and its variants have been proven to be in good agreement with the experimental results when applied in the modelling of tearing process [167], deep drawing process [168] and small punch test [169].

In spite of their differences, both the CDM and MDM models provide physical meanings of the damage inside the material in the form of cavity or void. Both models are developed based on the systematic damage mechanics theories. The incorporation of these models into the constitutive models not only enables the description of the evolution of the damage, but also modelling material deformation behaviour. They are called coupled damage models. Another widely applied damage models are the uncoupled damage

models. Different from the coupled damage models, the uncoupled damage models are largely phenomenological and the damage criteria are independent of the constitutive equations. For example, in the Oyane damage criterion [170], fracture occurs when the influence of hydrostatic stress reaches a critical value along the plastic deformation strain path,

$$\int_0^{\bar{\varepsilon}_f} \left( 1 + \frac{\sigma_m}{C_1 \cdot \sigma_{eq}} \right) d\bar{\varepsilon} = C_2$$

Where  $C_1$  and  $C_2$  are material dependent constants. While in the Cockcroft-Latham criterion [171], fracture takes place when the integral of principal stress along the strain path reaches a critical value. Compared with coupled damage models, the uncoupled ones are generally presented in a simpler form and the coefficients are easier to calibrate. Other widely applied uncoupled damage models include Johnson-Cook model [172], Xue-Wierzbicki model [173] and Bai-Wierzbicki model [174].

Malcher et al. [175] made an assessment of four popularly adopted isotropic damage models, including Gurson-Tvergaard-Needleman (GTN) model, GTN model with shear mechanism enhancement [163], Lemaitre model [152] and Bai-Wierzbicki model [174]. by comparing the simulation results with the damage models with the experiment. In the experiment, different geometries were designed to achieve a larger coverage of stress triaxiality. According to their research, the GTN model with Xue's shear modification and the Lemaitre model presented better accuracy in predicting the damage location and deformation in low stress triaxiality zone than the Bai-Wierzbicki model; while all of them achieved acceptable agreement with the experimental results under high and moderate triaxiality zone.

The inability of the damage models in predicting ductile damage evolution at low stress triaxialities promotes the development of more advanced damage models taking stress triaxiality and Lode angle parameter into consideration [176, 177]. The selection of damage model for a specific forming process should take the characteristics of the forming process, including loading conditions, material properties into consideration.

### 2.3.3 Damage modelling of ISF process

The equipment configuration and unique feature of progressive localized material deformation in ISF make it hard to observe damage accumulation in the critical locations during the manufacturing process. Unfortunately, general FE modelling tools offered by

the commercial FE modelling software, such as Abaqus, can only provide material deformation indicators such as stress/strain distribution. However, these indicators cannot predict material damage during the forming process in an explicit way. FE damage modelling provides a solution to this problem. A few damage models has already been incorporated in the FE modelling software, for examples in Abaqus/Explicit solver, the Johnson-Cook model [172] and the FLD model can be used for material property definition directly. However, as mentioned in Section 2.3.1, for some materials or some processes, a specific damage model may be more appropriate than others. Under this circumstance, if this damage model have not been included in the commercial FE software, it needs to be incorporated into the FE solver by the second development tool provided by the solver.

As a popular CDM model, the Lemaitre model was used in the FE damage modelling of ISF processes. Kumar [178] used Lemaitre model coupled with Johnson-Cook constitutive equation to model SPIF process with material AA6061-T6, it was reported that the FE model provided a good prediction of the crack location and the fracture depth. An enhanced Lemaitre model was adopted by Wang et al. [179] in the modelling of TPIF process with material AA7075, it was concluded that the FE damage modelling overestimated the fracture depth of the hemispherical geometry by 3.93% compared with the experiment.

Compared with the Lemaitre model, the GTN-related damage models were more widely explored in the FE damage modelling of ISF process. Ilyas et al. [180] conducted the FE damage modelling of the incremental groove test with the original GTN model for material AA2024-O on LS-DYNA. Premature fracture was predicted by the FE model, nevertheless, the error between the FLCs obtained from FE prediction and the experiment was negligible. It suggested that the GTN model could be used for the modelling of SPIF process.

The GTN models with two different shear extensions were successfully applied by Gatea et al. [67, 181] in manufacturing pure titanium sheet with SPIF on the Abaqus/Explicit solver, as shown in Figure 2.47. The predicted maximum forming depths of the cones matched well with the experimental tests. Using GTN model with Nahshon-Hutchinson extension, Smith et al. [182] performed the FE damage modelling of the SPIF process with material AA7075 on the LS-DYNA solver. It was found that varying the value of the shear coefficient affected the forming depth of the formed part in the model, which acknowledged the existence of shearing effect in the SPIF process. Incorporating GTN

model into the Hill' 48 constitutive equation [134], Li et al. [183] investigated the influence of GTN model coefficients on the fracture behaviour of the conic part with DC06 steel in SPIF process. It was found that the fracture depth was significantly affected by the nucleation related coefficients. Wu et al. [66] compared the original GTN model, GTN model with Xue's extension and Lemaitre model in the modelling of pyramid shape in SPIF process. It was shown that during the SPIF process, a wide range of stress triaxiality occurred. Compared with the GTN models, the Lemaitre model overestimated the fracture depth of the part formed.

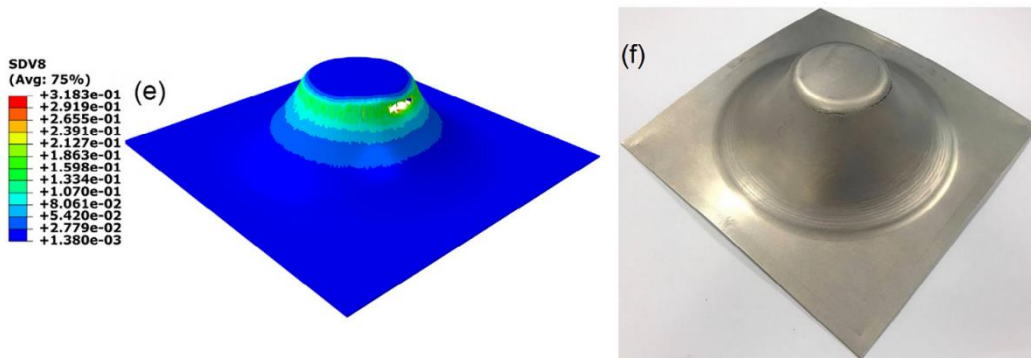


Figure 2.47 Comparison of the crack locations in the FE damage modelling result and the experiment by Gatea et al. [67]

As for DSIF, the research on its FE simulations is limited, no damage modelling of the process has been reported in the published literature.

In conclusion, the GTN models with shear extensions were proved to be more suitable to model processes in which low stress triaxiality would occur than other damage models considering their currently reported applications. While in ISF, the contact between the tool and the sheet and localized material deformation inevitably creates a variety of stress triaxiality. Moreover, based on the current investigations on the applicability of various damage models in the ISF process, the GTN models with shear extensions have demonstrated considerable accuracy in predicting the fracture depth and location of ISF-made parts. The shear-modified GTN model can be used as a tool to investigate the material deformation and fracture behaviours in ISF.

## 2.4 Shear-modified GTN Model and Its Application

In this section, the mathematical expression of the GTN model and its shear-modified extension are first introduced, based on which the discretization of the mathematical model and its incorporation into the FE solver Abaqus/Explicit is presented.

### 2.4.1 Introduction to the GTN model

Based on the work of McClintock [157] and Rice and Tracey [159], Gurson [160] proposed the micromechanical damage model to describe micro void evolution in plastic deformation. The mathematical expression of Gurson model is,

$$\Phi = \left( \frac{\sigma_{eq}}{\sigma_0} \right)^2 + 2f \cosh \frac{3\sigma_m}{2\sigma_0} - (1 + f^2) = 0 \quad (2-1)$$

In the Gurson model, VVF  $f$  is treated as an indicator of the severity of the damage in the material. Assuming that the initial VVF in the material is  $f_0$ , when the material deformation is elastic,  $f$  stays constant and  $f = f_0$ . If the deformation continues and the material is plastically deformed, VVF increases. Eventually, when  $f$  reaches  $f_f$ , fracture occurs.

The increase of VVF consists of two parts, growth of the existing voids and nucleation of new voids. The increase rate of VVF can be calculated by

$$\dot{f} = \dot{f}_g + \dot{f}_n \quad (2-2)$$

where  $\dot{f}_g$  is the growth rate of the existing voids and  $\dot{f}_n$  is the nucleation rate of the new voids. Their values depend on the severity of the plastic deformation,

$$\dot{f}_g = (1 - f) \dot{\varepsilon}_{kk}^p \quad (2-3)$$

$$\dot{f}_n = A \dot{\varepsilon}^p + B \dot{\sigma}_m \quad (2-4)$$

where  $\varepsilon^p$  is equivalent microscopic plastic strain. According to Chu and Needleman [184],  $A > 0$  and  $B = 0$  for strain-controlled material deformation, and  $A$  can be calculated by,

$$A = \frac{f_n}{S_N \sqrt{2\pi}} \exp \left[ -\frac{1}{2} \left( \frac{\varepsilon^p - \varepsilon_N}{S_N} \right)^2 \right] \quad (2-5)$$

where  $\varepsilon_N$  is the mean critical values for void nucleation and  $S_N$  is the appropriate standard deviation.

However, it was found by Tvergaard [161, 185, 186] that the accuracy of Gurson model was limited by its incapability to describe void coalescence phenomenon in the material when the plastic deformation reached a threshold value. To overcome this disadvantage,

Tvergaard and Needleman [161] introduced new coefficients into the original Gurson model,

$$\Phi = \left( \frac{\sigma_m}{\sigma_0} \right)^2 + 2q_1 f^* \cosh \left( -\frac{3q_2 \sigma_m}{2\sigma_0} \right) - (1 + q_3 f^{*2}) = 0 \quad (2-6)$$

where the coefficients  $q_1$ ,  $q_2$  and  $q_3$  were introduced by Tvergaard [185] to account for the interactions between the voids. In the GTN model,  $q_3 = q_1^2$ . If  $q_1 = q_2 = q_3 = 1$ , the GTN model degrades to the Gurson model. The damage coefficient  $f^*$  was introduced by Tvergaard and Needleman [161] to describe the rapid closure of the voids when rupture happens. The void coalescence takes place once VVF reaches a critical value  $f_c$ .  $f^*$  is defined as a function of  $f$ ,

$$f^* = \begin{cases} f & f < f_c \\ f_c + k_f \cdot (f - f_c) & f \geq f_c \end{cases} \quad (2-7)$$

where  $k_f$  is a constant determined by  $f_f$  and  $f_c$ ,

$$k_f = \frac{f_u^* - f_c}{f_f - f_c} \quad (2-8)$$

And  $f_u^*$  is a constant related to the coefficients  $q_1$ ,  $q_2$  and  $q_3$ ,

$$f_u^* = \frac{q_1 + \sqrt{q_1^2 - q_3}}{q_3} \quad (2-9)$$

#### 2.4.2 Shear-modified GTN model

The original GTN model was proved to be inaccurate in predicting damage evolution for processes in which the material was under relatively low stress triaxiality or under shear deformation when the hydraulic tension was low [162, 187]. To improve the GTN model, additional shear contribution to the void volume fraction has been introduced into the GTN model using shear extensions, among which the extensions proposed by Xue [163] and Nahshon and Hutchinson [164] are the most widely adopted by the researchers. In both extended GTN models, shear damage mechanism is incorporated into the damage model by introducing the void shape distortion factor  $\dot{f}_s$ . As a result, the accumulation of VVF is contributed by void growth, void nucleation and shear-induced void distortion,

$$\dot{f} = \dot{f}_g + \dot{f}_n + \dot{f}_s \quad (2-10)$$

The comparison between Nahshon-Hutchinson extension and Xue extension was reported by Reis et al. [188]. Compared with Nahshon-Hutchinson extension, Xue extension was shown to be inaccurate in predicting fracture location under tensile/shear loading condition. Tvergaard and Nielsen [166] compared the original GTN model with the modified GTN model with Nahson-Hutchinson extension in a plane strain uni-cell test, it was found that the modified GTN model showed reasonable accuracy in both high and low stress triaxiality. In this study, Nahshon-Hutchinson extension was used in the FE damage modelling of ISF process. The shear-related VVF increase rate in Nahshon-Hutchinson extension can be calculated by

$$\dot{f}_s = k_w \cdot f \cdot w(\sigma) \cdot \frac{s_{ij} : \dot{\epsilon}_{ij}^p}{\sigma_m} \quad (2-11)$$

where  $k_w$  is a shear related coefficient and  $w(\sigma)$  is defined by

$$w(\sigma) = 1 - \left( \frac{27J_3}{2\sigma_{eq}^3} \right)^2 \quad (2-12)$$

where  $J_3$  is the third invariant of the stress, and  $\sigma_{eq}$  is the equivalent stress,

$$\begin{aligned} J_3 &= \det(s) = (\sigma_1 - \sigma_m) \cdot (\sigma_2 - \sigma_m) \cdot (\sigma_3 - \sigma_m) \\ \sigma_{eq} &= \sqrt{J_2} = \sqrt{3s_{ij}s_{ij}/2} \end{aligned} \quad (2-13)$$

### 2.4.3 Application of GTN model in FE modelling

Two solvers are provided by Abaqus to simulate material deformation, Abaqus/Standard and Abaqus/Explicit. The difference of the two solvers lies in integration algorithms applied in the solvers. For Abaqus/Standard, implicit integration procedures are followed and in each step iterations are performed to guarantee equilibrium and convergence in the model. While in Abaqus/Explicit, the central difference integration method is used and no iterations are needed for the convergence check. For quasi-static problems where smooth nonlinearity exists, the solver Abaqus/Standard is more efficient and accurate. While for extreme discontinuous problems, in which large quantities of nonlinear equations need to be solved, Abaqus/Explicit is computationally less expensive with good accuracy [96]. In the ISF processes, high nonlinearity exists due to large displacement, large plastic deformation and complex contact conditions. As a result, the FE models in this study were all established by using the Abaqus/Explicit solver.

The damage model can be incorporated into the commercial FE software Abaqus by the user subroutine to define material mechanical behaviour [96]. For the Abaqus/Standard solver, UMAT (user-defined mechanical material behavior) subroutine is used. While for Abaqus/Explicit, VUMAT (vectorized user-defined mechanical material behavior) subroutine needs to be applied. VUMAT subroutine was used in this study consequently.

In the VUMAT subroutine, the damage model needs to be discretized so that the stress components and other state variables can be updated at the end of each analysis step. The backward-Euler numerical algorithm was proposed by Simo and Hughes [189] for the discretization of constitutive equations and first applied to the GTN model by Aravas [190]. Generally, in this algorithm, the updating process of the stress components and state variables are split into two steps. In the first step, elastic predictors of the stress components are calculated based on the prescribed strain increment determined by the solver. Using the predicted stress components, the yielding criterion will be checked. If the yielding criterion has been satisfied, the plastic correction will be made in the second step. If not, the elastic predictor will be used as the updated stress components and proceed to the next time step. Therefore, this algorithm is also called return mapping algorithm. The mathematical description of the return mapping algorithm for general plasticity model and one step further for the GTN model will be detailed in this section.

#### 2.4.3.1 Return mapping algorithm for general elasto-plastic model

In the elastic stage, the stress components can be obtained according to Hooke's Law,

$$\sigma = C^e : \varepsilon^e \quad (2-14)$$

where the elastic modulus  $C^e$  can be updated by,

$$C_{ijkl}^e = 2G\varepsilon_{ik}\varepsilon_{jl} - \lambda\varepsilon_{ik}\varepsilon_{jl} \quad (2-15)$$

where  $G, \lambda$  are material property-related constants and they are defined by Young's modulus  $E$  and Poisson's ratio  $\nu$ ,

$$G = \frac{E}{2(1+\nu)}$$

$$\lambda = K - \frac{2}{3}G$$

$$K = \frac{E}{3(1-2\nu)}$$

The yielding criterion is a function of stress state and state-related variables. The stress state can be determined by the hydrostatic stress  $\sigma_h$  and the equivalent stress  $\sigma_{eq}$ . As a result, the yielding criterion can be expressed as a function of hydrostatic stress, equivalent stress and state-related variables,

$$\Phi(\sigma_h, \sigma_{eq}, H^\alpha) = 0 \quad (2-16)$$

where  $H^\alpha$ ,  $\alpha = 1, 2, \dots, n$ , is a series of state-related variables. And,

$$\sigma_h = -\frac{1}{3}\sigma_{ii} \quad (2-17)$$

$$\sigma_{eq} = \sqrt{\frac{3}{2}\sigma:\sigma} \quad (2-18)$$

where  $\sigma$  is the stress tensor.

After entering the plastic deformation zone, according to the normality rule, the flow direction of the material is normal to the yielding surface,

$$\Delta\varepsilon^p = d\Lambda \frac{\partial\Phi}{\partial\sigma} \quad (2-19)$$

where  $\Lambda$  is a coefficient. The stress tensor  $\sigma$  is a function of  $\sigma_h$  and  $\sigma_{eq}$ , according to the chain rule, Equation (2-19) can be expressed as,

$$\Delta\varepsilon^p = d\Lambda \left( -\frac{1}{3} \frac{\partial\Phi}{\partial\sigma_h} I + \frac{\partial\Phi}{\partial\sigma_{eq}} n \right) \quad (2-20)$$

where  $n$  is the material flow direction in the yielding space, in the von Mises-related yielding laws,  $n$  can be defined by,

$$n = \frac{3}{2} \frac{\sigma}{\sigma_{eq}} \quad (2-21)$$

Assume,

$$\begin{aligned} \Delta\varepsilon_{\sigma_h} &= -d\Lambda \frac{\partial\Phi}{\partial\sigma_h} \\ \Delta\varepsilon_{\sigma_{eq}} &= d\Lambda \frac{\partial\Phi}{\partial\sigma_{eq}} \end{aligned} \quad (2-22)$$

Equation. (2-20) can be rewritten as,

$$\Delta \varepsilon^p = \frac{1}{3} \Delta \varepsilon_{\sigma_h} I + \Delta \varepsilon_{\sigma_{eq}} n \quad (2-23)$$

On the other hand, the stress tensor can be decomposed into,

$$\sigma = -\sigma_h I + \frac{2}{3} \sigma_{eq} n \quad (2-24)$$

Combining Equations (2-14), (2-15), (2-23) and (2-24), the stress components in the next time step can be updated on the basis of the elastic predictor from the last time step,

$$\begin{aligned} \sigma_h &= \sigma_h^e + K \Delta \varepsilon_{\sigma_h} \\ \sigma_{eq} &= \sigma_{eq}^e - 3G \Delta \varepsilon_{\sigma_{eq}} \end{aligned} \quad (2-25)$$

As a result, by solving the values of  $\Delta \varepsilon_{\sigma_h}$  and  $\Delta \varepsilon_{\sigma_{eq}}$ , the stress components can be updated. Eliminating  $d\lambda$  from Equation (2-22), it can be obtained that,

$$\Delta \varepsilon_{\sigma_h} \frac{\partial \Phi}{\partial \sigma_{eq}} + \Delta \varepsilon_{\sigma_{eq}} \frac{\partial \Phi}{\partial \sigma_h} = 0 \quad (2-26)$$

At the same time, the state related variables will be updated,

$$\Delta H^\alpha = \Delta H^\alpha(\varepsilon^p, \sigma, H^\beta) \quad (2-27)$$

The yielding law needs to be satisfied at all time, combining Equations (2-16), (2-25) and (2-26), the value of  $\Delta \varepsilon_{\sigma_h}$  and  $\Delta \varepsilon_{\sigma_{eq}}$  can be solved. The stress components and state related variables can be updated subsequently.

#### 2.4.3.2 Return mapping algorithm for GTN model

The initial condition at the beginning of time step  $t + \Delta t$  is given as,

$$\sigma_t, \varepsilon_t, H_t^i, \Delta \varepsilon_{t+\Delta t} \quad (2-28)$$

In the GTN model, there are two core state related variables defined, the void volume fraction  $f$  and the equivalent microscopic plastic strain  $\bar{\varepsilon}^p$ . Based on the elastic assumption, the trial stress for the next time step can be calculated,

$$\begin{aligned} \sigma_{t+\Delta t}^{trial} &= \sigma_t + C : \Delta \varepsilon_{t+\Delta t} \\ \sigma_{ht+\Delta t}^{trial} &= -\frac{1}{3} \sigma_{kk}^{trial} + C : \Delta \varepsilon_{t+\Delta t} \\ \sigma_{eqt+\Delta t}^{trial} &= \sqrt{\frac{3}{2} S_{ij}^{trial} : S_{ij}^{trial}} \end{aligned} \quad (2-29)$$

The state variables are related to the plastic deformation, so the trial state related variables will remain the same with the last time step,

$$\begin{aligned} f_{t+\Delta t}^{trial} &= f_t \\ \bar{\varepsilon}_{t+\Delta t}^{p\,trial} &= \bar{\varepsilon}_t^p \end{aligned} \quad (2-30)$$

Putting the trial values into the yield function, it can be obtained,

$$\Phi_{t+\Delta t}^{trial} = \Phi(\sigma_{t+\Delta t}^{trial}, H_t^i) = \Phi(\sigma_{ht+\Delta t}^{trial}, \sigma_{eqt+\Delta t}^{trial}, H_t^i) \quad (2-31)$$

If  $\Phi_{t+\Delta t}^{trial} \leq 0$ , the material is still under elastic deformation, so that the trial stress  $\sigma_{t+\Delta t}^{trial}$  and trial state related variables are the final values to be updated. Otherwise, if  $\Phi_{t+\Delta t}^{trial} > 0$ , the yielding criterion has been met, the trial stress needs to be corrected to meet the yielding criterion. As discussed in Section 2.4.3.1, plastic corrector can be obtained by solving the set of equations

$$\begin{cases} \Delta\varepsilon_{\sigma_h} \frac{\partial\Phi}{\partial\sigma_{eq}} + \Delta\varepsilon_{\sigma_{eq}} \frac{\partial\Phi}{\partial\sigma_h} = 0 \\ \Phi(\sigma_h, \sigma_{eq}, H^\alpha) = 0 \end{cases} \quad (2-32)$$

The high non-linearity of these equations makes it impossible to solve the equations explicitly. Instead, Newton-Raphson method is used to solve the equations numerically by assuming

$$\begin{cases} f_1 = \Delta\varepsilon_{\sigma_h} \frac{\partial\Phi}{\partial\sigma_{eq}} + \Delta\varepsilon_{\sigma_{eq}} \frac{\partial\Phi}{\partial\sigma_h} \\ f_2 = \Phi(\sigma_h, \sigma_{eq}, H^\alpha) \end{cases} \quad (2-33)$$

Taylor linearization method is further used to simplify the equations, in the  $k+1$  iteration,

$$\begin{cases} f_1^{k+1} = f_1^k + \frac{\partial f_1^k}{\partial\Delta\varepsilon_{\sigma_h}} d\Delta\varepsilon_{\sigma_h}^{k+1} + \frac{\partial f_1^k}{\partial\Delta\varepsilon_{\sigma_{eq}}} d\Delta\varepsilon_{\sigma_{eq}}^{k+1} \\ f_2^{k+1} = f_2^k + \frac{\partial f_2^k}{\partial\Delta\varepsilon_{\sigma_h}} d\Delta\varepsilon_{\sigma_h}^{k+1} + \frac{\partial f_2^k}{\partial\Delta\varepsilon_{\sigma_{eq}}} d\Delta\varepsilon_{\sigma_{eq}}^{k+1} \end{cases} \quad (2-34)$$

So the values of  $d\Delta\varepsilon_{\sigma_h}^{k+1}$  and  $d\Delta\varepsilon_{\sigma_{eq}}^{k+1}$  can be obtained as,

$$\begin{bmatrix} d\Delta\varepsilon_{\sigma_h}^{k+1} \\ d\Delta\varepsilon_{\sigma_{eq}}^{k+1} \end{bmatrix} = \begin{bmatrix} \frac{\partial f_1^k}{\partial\Delta\varepsilon_{\sigma_h}} & \frac{\partial f_1^k}{\partial\Delta\varepsilon_{\sigma_{eq}}} \\ \frac{\partial f_2^k}{\partial\Delta\varepsilon_{\sigma_h}} & \frac{\partial f_2^k}{\partial\Delta\varepsilon_{\sigma_{eq}}} \end{bmatrix} \cdot \begin{bmatrix} -f_1^k \\ -f_2^k \end{bmatrix} \quad (2-35)$$

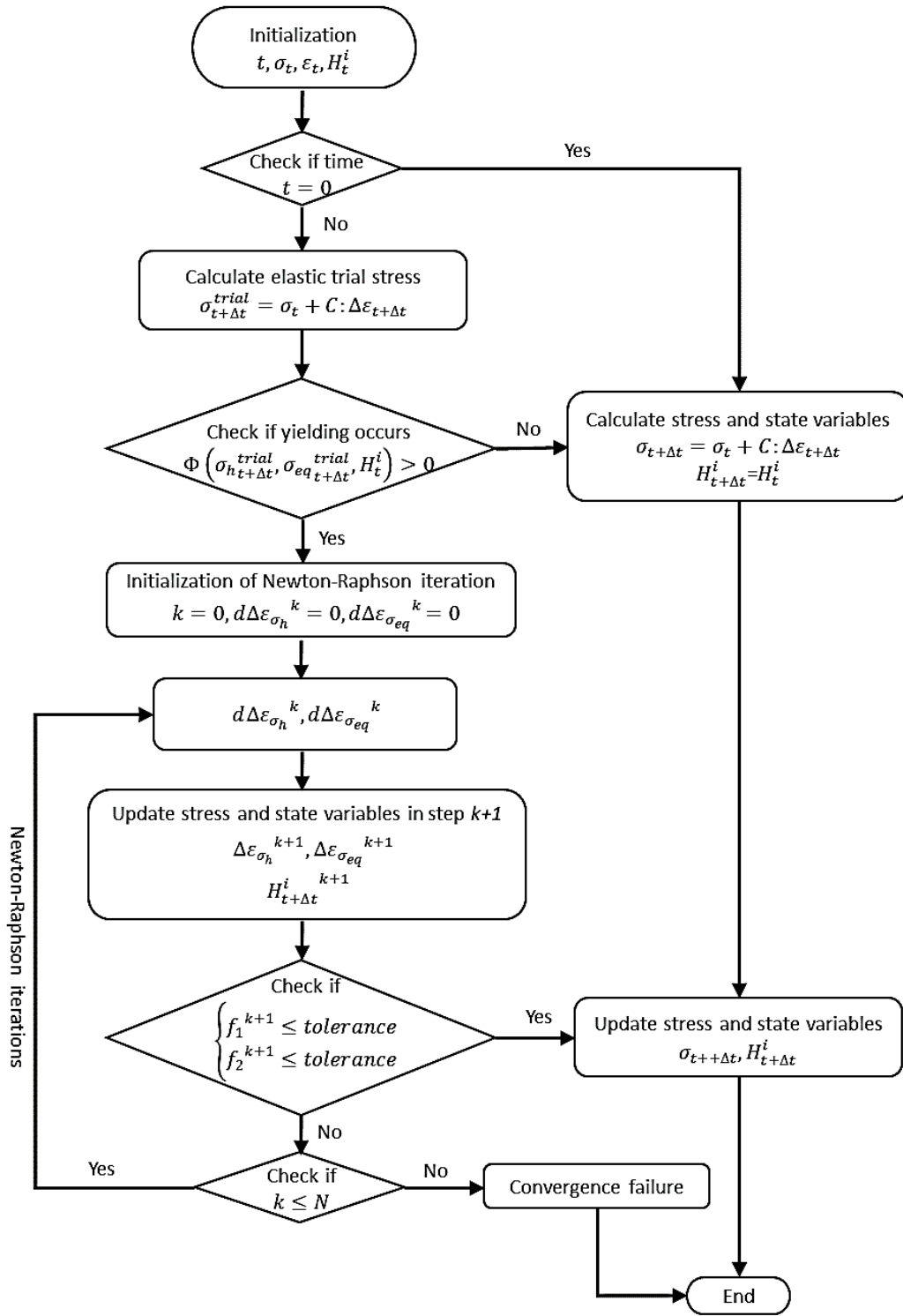


Figure 2.48 Flow chart for the development of GTN VUMAT subroutine

Then values of the plastic correctors can be updated as,

$$\begin{cases} \Delta \epsilon_{\sigma_h}^{k+1} = \Delta \epsilon_{\sigma_h}^k + d\Delta \epsilon_{\sigma_h}^{k+1} \\ \Delta \epsilon_{\sigma_{eq}}^{k+1} = \Delta \epsilon_{\sigma_{eq}}^k + d\Delta \epsilon_{\sigma_{eq}}^{k+1} \end{cases} \quad (2-36)$$

Accordingly intermediate variables can be updated during the iteration,

$$\begin{aligned}
\sigma_y^{k+1} &= \sigma_y^k + h \cdot (\Delta \bar{\varepsilon}^p)^{k+1} \\
\sigma_h^{k+1} &= \sigma_{ht+\Delta t}^{trial} + K \Delta \varepsilon_{\sigma_h}^{k+1} \\
\sigma_{eq}^{k+1} &= \sigma_{eqt+\Delta t}^{trial} - 3G \Delta \varepsilon_{\sigma_{eq}}^{k+1}
\end{aligned} \tag{2-37}$$

According to the energy conservation during plastic deformation,

$$(1-f) \sigma_y d\bar{\varepsilon}^p = \sigma : d\varepsilon^p \tag{2-38}$$

Equivalent plastic strain increment can be obtained by,

$$d\bar{\varepsilon}^p = \frac{\sigma : d\varepsilon^p}{(1-f) \sigma_y} = \frac{-p \Delta \varepsilon_{\sigma_h} + q \Delta \varepsilon_{\sigma_{eq}}}{(1-f) \sigma_y} \tag{2-39}$$

As a result, the state-related variables can be updated by,

$$\begin{aligned}
\Delta \bar{\varepsilon}^{pk+1} &= \frac{-\sigma_h^{k+1} \Delta \varepsilon_{\sigma_h}^{k+1} + \sigma_{eq}^{k+1} \Delta \varepsilon_{\sigma_{eq}}^{k+1}}{(1-f^k) \sigma_y^k} \\
\Delta f^{k+1} &= (1-f^k) \Delta \varepsilon_{\sigma_h}^{k+1} + A \cdot \Delta \varepsilon_{\sigma_h}^{k+1} + Kw \cdot f^k \cdot w \cdot \Delta \bar{\varepsilon}^{pk+1} \\
f^{k+1} &= f^k + \Delta f^{k+1}
\end{aligned} \tag{2-40}$$

The iteration will continue until the values of  $f_1^{k+1}$  and  $f_2^{k+1}$  are smaller than the tolerance values defined, which means both constraint equations are satisfied at acceptable accuracy. A flow chart for the stress update algorithm of the GTN model in the VUMAT subroutine is shown in Figure 2.48.

## 2.5 Summary

In this chapter, the material deformation and fracture mechanisms of SPIF and DSIF are reviewed. For SPIF, the material is locally deformed by the forming tool, resulted from the combination of tension, bending, shearing and cyclic loading effect. For DSIF, the introduction of compression further improves material formability, owing to the decreased tensile effect and increased shearing effect. Furthermore, the deformation modes and material mechanical properties bring variations to the initiation and propagation of fracture in the metal sheet in the ISF process, such as the suppression of necking in SPIF and drop of formability with higher supporting force applied in DSIF.

However, current research on the material deformation and fracture mechanisms in ISF is more descriptive than explanative. Extensive observations on the deformation and fracture behaviours of materials in ISF have been reported without further consolidating

explanations. An in-depth understanding on the deformation and fracture mechanisms of ISF has yet to be developed.

Material testing methods have been widely used in both academia and industry to describe material deformation behaviour and evaluate material formability under different loading conditions. The testing methods not only provide a straightforward and fundamental understanding towards the material deformation behaviours in the metal forming processes, but also a standard to compare different processes. The commonly used material testing methods are reviewed in this chapter.

However, for SPIF and DSIF processes, the material is under much more complicated loading conditions than traditional sheet metal forming processes. The traditional testing-based material formability methods cannot provide accurate description or prediction of the material deformation behaviours and formability in ISF process. Nevertheless, a proper material testing will provide a viable way to investigate ISF process in a simplified and structured manner. For example, the effect of different loading conditions, such as bending or compression can be investigated by applying the loading conditions onto the material respectively and the effect of strain ratio can be effectively analyzed by using biaxial tensile test. A suitable testing method will help to advance the investigations into the deformation and fracture behavior in ISF.

The theories for the prediction of material forming limit in sheet metal are also reviewed in this chapter. The complicated contact conditions and localized material deformation characteristics in ISF prohibit a direct observation of material deformation behaviour and damage development, making the fracture prediction in ISF challenging. Damage models provide a promising tool to present the damage evolution in ISF in an explicit way and to give an explanation to the unique deformation and fracture mechanism in ISF. The shear-modified GTN model has demonstrated its applicability in predicting material deformation and fracture behaviours in ISF. As a result, it has been selected to model ISF processes in the current research. The shear-modified GTN model can be incorporated into Abaqus/Explicit solver by the VUMAT subroutine using the return mapping algorithm.

Equation Chapter (Next) Section 1

# 3 EXPERIMENTAL INVESTIGATION AND FE MODELLING OF ISF

To obtain the material deformation characteristics in SPIF, SPIF experiment with aluminium alloys AA5251-H22 and AA6082-T6 was conducted, which will be described in Section 3.1. To obtain the material deformation history in both SPIF and DSIF processes, FE damage modelling with the shear-modified GTN model of both processes were carried out. The calibration of the coefficients in the shear-modified GTN model will be reported in Section 3.2. The development of the FE models for ISF processes will be reported in Section 3.3. The experimental and FE modelling results will be presented and compared in Section 3.4, followed by discussions of the results in Section 3.5 and a summary of the work in this chapter in Section 3.6.

## 3.1 Experimental Analysis of Material Formability in ISF

As presented in Chapter 1, according to the research by Hussain and Gao [6], the maximum forming angle can be an indicator to the formability of the material in SPIF. As a result, the conic shapes with varied forming angle along the depth direction have been widely selected by the researchers to test material formability in SPIF process [60, 67, 79].

### 3.1.1 Design of the experiment

In the SPIF test, the dimensions of the tested conic shape are shown in Figure 3.1 (a). The profile of the geometry follows a circular curve, which forms a starting forming angle of 10 degrees and an ending angle of 90 degrees. The forming angle increases with the forming depth. According to the *Sine law* [56], when the forming angle reaches 90 degrees, the thickness of the deformed sheet will be zero. As a result, the sheet will lose its ability totally to defend further deformation, which will definitely lead to a final fracture of the sheet under deformation. Therefore, the maximum forming depth of the conic part can be an indicator to the material formability in SPIF process.

Tool with a hemispherical head was used in the test, and the radius of the tool head was 5 mm. Based on the CAD design of the geometry, a spiral toolpath was generated by the toolpath generation algorithm developed by Lu et al. [9], as shown in Figure 3.1 (b). The vertical step per revolution about the central axis of the conic part was set to be 0.3 mm to ensure that the surface quality of the part would not be damaged while at the same time a reasonable manufacturing time could be achieved [53].

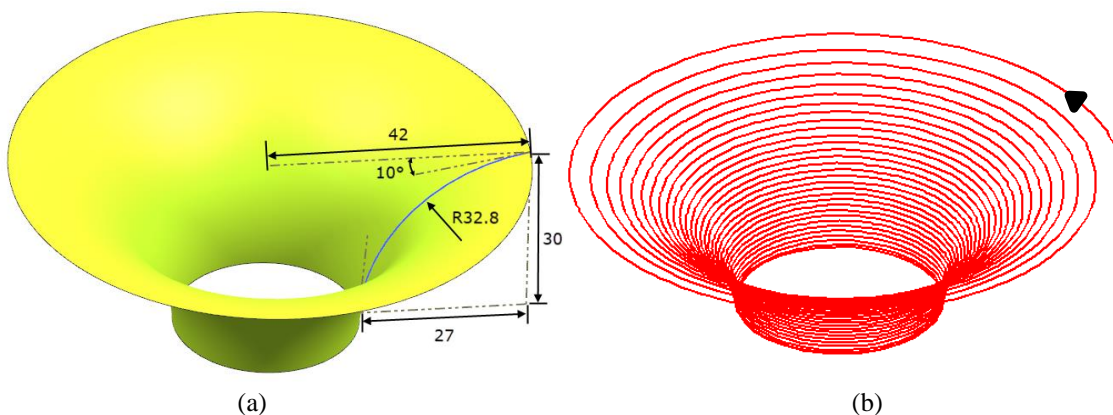


Figure 3.1 Geometry of the test specimen and toolpath: (a) CAD model of the test specimen; (b) schematic of the generated toolpath use in the SPIF test

The SPIF tests were performed on a CNC machine, the experimental set-up is shown in Figure 3.2. Square sheets with a dimension of 170×170×1 mm were used in the tests. A backing plate with an opening radius of 50 mm was positioned under the sheet to increase the stiffness as well as the geometric accuracy of the part to be manufactured. The tool was controlled by the CNC machine, and it moved along the pre-designed toolpath at a constant linear speed of 1800 mm/min to avoid oscillation of the CNC machine at higher speeds. In order to reduce friction between the tool and the sheet, a liquid lubricant was applied onto the surface of the sheet. The process was terminated when obvious crack(s)

was observed in the part. The coordinates of the tool upon fracture of the part was recorded to calculate the maximum forming depth of the fractured part.

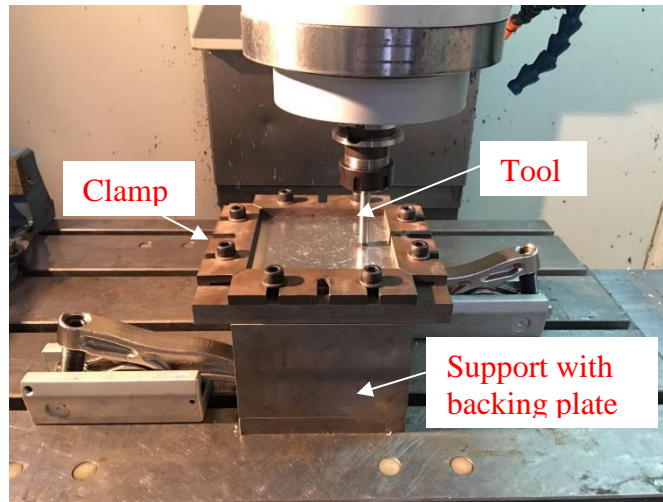


Figure 3.2 Experimental set-up of SPIF process on a CNC machine

In order to investigate the influence of the material properties on the material formability in SPIF, different materials should be used in the research. According to the experimental and theoretical analysis performed by Ai et al. [82] and experimental investigation by Fratini et al. [39], material ductility could be a deciding factor affecting material deformation behaviour in ISF. As a result, materials with different degrees of ductility should be chosen in this research. Considering the material properties and their applications in the academia and industry, two types of materials were tested, the aluminium alloys AA5251-H22 and AA6082-T6. In order to test the mechanical properties of the materials, uniaxial tensile tests were performed. The specimen used in the test was designed based on the ASTM-E8 standard [191], the geometry of the specimen is shown in Figure 3.3.

The test was performed on the Zwick Proline Z020 material mechanical testing frame. The test speed was set to be 0.9 mm/min and the displacement-force curves were recorded during the test, as shown in Figure 3.3. Compared with AA5251-H22, material AA6082-T6 underwent much higher deformation before final fracture of the specimen, while at the same time, AA6082-T6 also required much higher loading force for the plastic deformation of the specimen to continue. The necking phenomenon of the specimen was much more obvious for material AA5251-H22 than AA6082-T6, which could be reflected by the necking part of the force-displacement curves. Judging from the distinct deformation behaviours of the two materials in the uniaxial tensile test, it is reasonable to

use these two materials in the future tests to investigate the influence of material properties on material deformation behaviour.

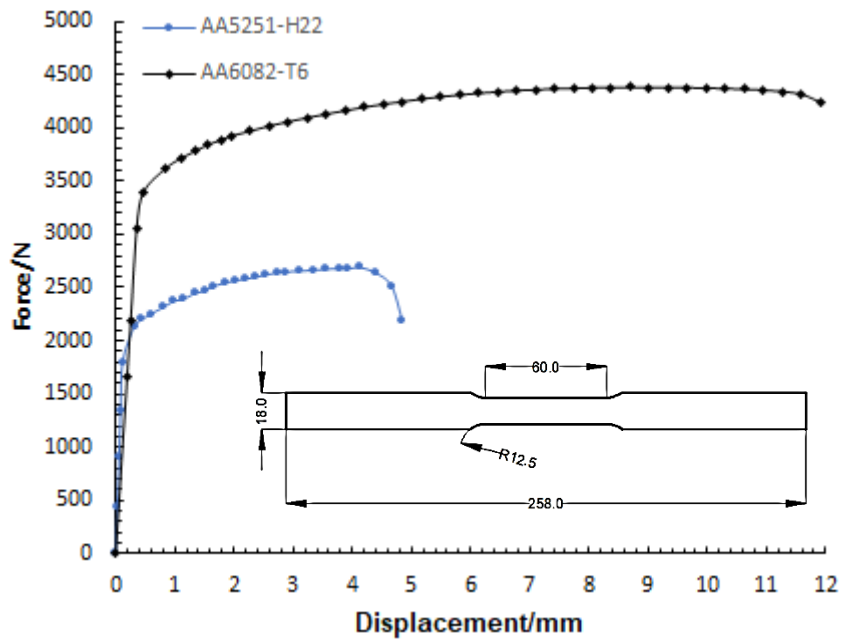


Figure 3.3 Geometry of the specimen for uniaxial tensile test and the obtained force-displacement curves for material AA5251-H22 and AA6082-T6

### 3.1.2 Experimental procedure

In the SPIF test, the square sheet was first placed on the backing plate and the edges of sheet were firmly clamped. The generated toolpath was imported into the CNC machine. After that, the tool was positioned to the centre of the specimen for the calibration of the starting point. Then the tool was moved away from the sheet surface and the lubricant was applied onto the surface of the sheet with a brush. The moving speed of the tool was first set to zero to avoid potential damage resulting from possible wrong operations before. After the test preparations were completed, the CNC machine was started. The moving speed of the tool was slowly increased to the designed speed if the tool was confirmed to follow the designed toolpath and no contact between the tool and the clamps happened. The test would be terminated when obvious crack(s) appeared in the part. The coordinates shown on the screen of the CNC machine would be recorded to calculate the maximum forming depth for every test. Each material would be at least tested twice to ensure the repeatability of the test.

### 3.2 Coefficient Calibration in Shear-modified GTN Model

According to Equations (2-5), (2-6) and (2-11), there are 10 coefficients in total needed to be calibrated in the shear-modified GTN model, consisting of nine damage coefficients ( $q_1, q_2, q_3, \varepsilon_N, S_N, f_0, f_n, f_c, f_f$ ) in the original GTN model and one shear-related coefficient ( $k_w$ ) in the shear extension.

For metallic materials, the values proposed by Tvergaard [185],  $q_1 = 1.5, q_2 = 1$  and  $q_3 = 2.25$  have been widely used in a number of studies. The standard deviation coefficients  $S_N$  and  $\varepsilon_N$  were found to have little influence on the simulation results, and  $S_N = 0.1$  and  $\varepsilon_N = 0.3$  were proposed by Chu and Needleman [184]. As a result, for the original GTN model, only four coefficients, namely  $f_0, f_c, f_n$  and  $f_f$  need to be identified in this study. For the shear-modified GTN model, five coefficients are required to be calibrated in total. According to Nahshon and Hutchinson [164], the value of  $f_0$  and  $f_c$  should be decided before the calibration of  $k_w$ .

#### 3.2.1 Verification of the developed subroutine

The VUMAT subroutine for the GTN model was developed using the programming language Fortran. The developed program can be seen in Appendix 1. In order to test the accuracy of the developed GTN model, a verification procedure was proposed by Aravas [190]. In the verification model, only the enlargement of the existing voids and nucleation of the new voids were considered while the modification of the VVF was neglected. By comparing the evolution history of VVF in the model with that obtained from theoretical calculations, whether the developed subroutine was correct or not could be verified. The material property definition and values of the coefficients used in the verification model are shown in Table 3.1.

Table 3.1 Material properties and values of the coefficients used in the verification model

Parameter	$\sigma_y/E$	$\nu$	$n$	$q_1$	$q_2$	$f_0$	$f_n$	$\varepsilon_N$	$S_N$
Value	$1/300$	0.3	0.1	1	1.5	0.04	0.4	0.3	0.1

The material hardening behaviour in the verification model was also defined in the verification model,

$$\frac{\sigma_s}{\sigma_y} = \left( \frac{\sigma_s}{\sigma_y} + \frac{3G}{\sigma_y} \bar{\varepsilon}^p \right)^n \quad (3-1)$$

where  $\sigma_s$  is the yielding stress of the material during the deformation and  $\sigma_y$  is the initial yielding stress of the material.

In the verification model, a hydrostatic stretch test of a single element was performed. The element was a cube with an edge length of 1 mm in all three directions. Displacement loading boundary condition was applied onto the element. Detailed boundary conditions on each node of the element is shown in Figure 3.4. Element type C3D8R was assigned to the element in the meshing process.

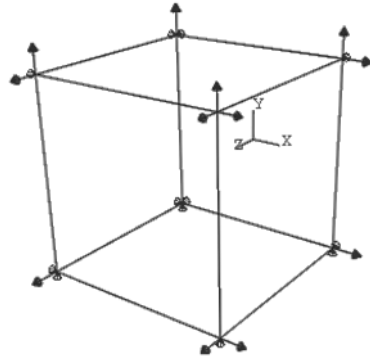


Figure 3.4 Loading condition for the element in the verification model for the GTN model

The displacement and VVF of the element at the integration point along deformation history were extracted from FE simulation results, based on which the relationship between volumetric strain and VVF was obtained. A comparison between the theoretical calculation reported by Avaras [190] and FE prediction with the developed GTN model is shown in Figure 3.5. A good match between them can be observed, which confirmed the credibility and accuracy of the developed numerical model in this study.

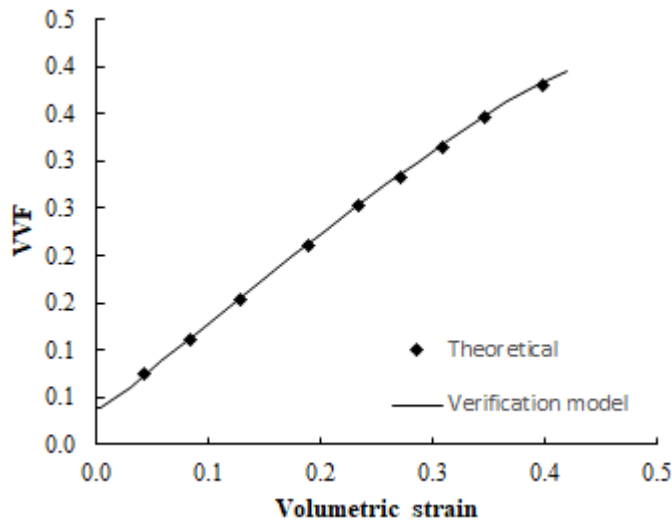


Figure 3.5 Comparison of evolution of VVF from theoretical calculation and the prediction by the developed GTN model

### 3.2.2 Coefficient calibration in the original GTN model

Generally, three different methods have been adopted to calibrate the coefficients in the GTN model:

- **Direct calibration.** This includes metallographic method [67] and tomographic method [192]. Both methods are quite straightforward. In the metallographic method, with the help of the scanning electron microscope (SEM) and image processing software, the area of the voids in the processed section of the specimen can be calibrated. The ratio of the area to the total area of the section is treated as the VVF at the current deformation stage. The specimens for calibration can be obtained from tensile tests at different stages. As a result, the VVF at different stage can be calibrated. While in the tomographic method, powerful X-ray equipment is used to obtain the 3D image of the tested specimen and the cavity inside can be directly observed. The ratio of the volume of the cavities to the total volume of the material in the target zone is used to determine the VVF at that deformation stage.
- **Inverse method** [168, 169, 193]. In its simplest form, multiple simulation models with different sets of the coefficient values are run by the FE software, and the model producing the most matching results with the uniaxial tensile test will be chosen as the optimized values [194].
- **Single representative volume element (RVE) method** [195]. In this method, the initial VVF will be calibrated first and the evolution of VVF will be simulated in a single element thus the value of nucleation related VVF and fracture related VVF can be obtained.

Guiglionda and Poole [196] concluded that lower porosity-related coefficients might be obtained from the porosity measurement with the help with SEM, due to the difficulties in the metallographic preparations of the specimens. While Zhang et al. [197] and Chhibber et al. [198] reported that miscounting the inclusions in the sections as voids in the porosity measurement process would lead to an overestimation of the porosity coefficients. In addition, for the tomographic method, the equipment required can be very costly. For both methods, a large quantity of specimens are needed, which is both time-consuming and cost-ineffective. The RVE method is not robust enough generally. As a result, in this study, the inverse method was adopted.

## 3.2.2.1 Flow rule selection for material AA5251-H22

Material AA5251-H22 was used in the FE simulations. True plastic strain-stress curve of the material from the uniaxial tensile test is shown in Figure 3.6 (a). As reviewed in Chapter 2, it has been widely proved that material formability can be significantly enhanced in ISF compared with conventional sheet metal forming processes. As a result, the data obtained from the uniaxial tensile test is not sufficient to describe material deformation behaviour when the strain is larger than the necking limit predicted by the uniaxial tensile test.

In order to obtain the material strain-stress relationship in the extended range of the deformation, hardening laws should be introduced. According to the experiment reported by Bhattacharya et al. [199], the feed rate of the forming tool did not necessarily contribute to the material formability in SPIF for material AA5052. No rational speed was introduced in the ISF test to increase the frictional effect and lubricant was applied to reduce the friction, the heat generate by the friction between the tool and the sheet was not enough to present significant influence on the material formability [200]. As a result, the effects of strain rate and temperature were ignored when selecting the hardening laws to describe the flow behaviour of the materials. Three different work-hardening laws, including Ludwik law [201], the Swift law [135] and Voce law [202] were fitted against the experimental stress-strain data, as shown in Figure 3.6 (a). The optimized parameters for the hardening laws are presented in Table 3.2. Corresponding root sum square (RSS) of the errors between the predictions and experimental data were calculated.

By comparison, it was shown that the prediction made by the Voce law not only was the closest to the experimental data but also followed the trend of the data so that it was used in the FE models to describe the plastic stress-strain curve in this study. The prediction of the Voce law in the extended range is shown in Figure 3.6 (b).

Table 3.2 Hardening laws and corresponding fitted values of the coefficients for AA5251-H22

Hardening Laws	AA5251-H22	RSS
Ludwik	$\sigma = 149.09 + 248.48 * \varepsilon_p^{0.41}$	33.16
Swift	$\sigma = 318.76 * (0.002725 + \varepsilon_p)^{0.12}$	24.86
Voce	$\sigma = 162.1181 + 70.97 * (1 - e^{-37.72\varepsilon_p})$	16.61

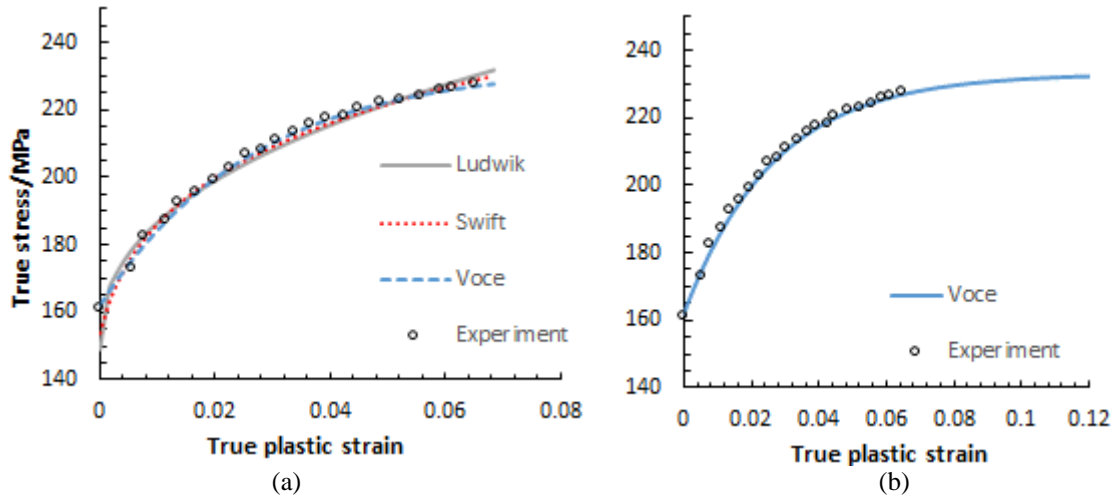


Figure 3.6 Flow stress curve fitting for AA5251-H22: (a) comparison between different hardening laws and the experimental data; (b) extended flow stress curve predicted by the Voce law

### 3.2.2.2 Design of the experiment

As discussed at the beginning of this section, inverse method was adopted in this research to calibrate the values of the coefficients in the GTN model for a specific material. The objective of the calibration process is to minimize the difference between the results obtained from the FE simulation and the experiment. The uniaxial tensile test was used in this research to provide the experimental results and it has already been conducted for the material mechanical property description, as shown in Figure 3.6. FE simulations were conducted based on the response surface method (RSM) and the optimization process was performed using the genetic algorithm (GA). In detail, the inverse method was developed in three steps in this research:

- (a) Running FE simulations of the uniaxial tensile test with varied values of the coefficients according to the central composite design (CCD) simulation runs and extract the load-displacement curve from each simulation;
- (b) Comparing the curves obtained from the FE simulations and the experiment and establishing a relationship between the response and the coefficients based on RSM;
- (c) Running GA optimization algorithm to obtain the optimal set of coefficients, with which the difference between the load-displacement curve obtained from simulation and that from the uniaxial tensile test can be minimized.

More detailed description of the implementation of the inverse method is reported as follows.

#### (a) Design of the FE simulations

The combinations of the coefficient values within the ranges can be unlimited and it is impossible to apply every combination to the simulation to find out the optimal set of these combinations. In order to cover the whole investigated ranges with efficiency, the response surface method (RSM) was adopted in this study. In RSM, each set of input values will yield an output (response). Then a mathematical relationship between the responses and the inputs in the investigated ranges can be obtained. By optimizing the mathematical equation, the optimal combination of the input coefficients within the ranges can be obtained.

First of all, the ranges of the investigated coefficients should be narrowed down. In order to determine reasonable ranges of the coefficients for material AA5251-H22, the coefficient values calibrated for similar materials in previous studies published in literature were firstly reviewed, as shown in Table 3.3. Combined with the work by Kami et al. [168], the ranges of the GTN coefficient values for material AA5251-H22 were selected for optimization, as shown in Table 3.4.

Table 3.3 Values of GTN coefficients in literature

<b>Authors</b>	<b>Material</b>	$f_0$	$f_n$	$f_c$	$f_f$
He et al. [203]	AA5052-01	0.002978	0.0249	0.030103	0.04854
Brunet et al. [204]	AA5182	0	0.035		
	AA5754	0	0.034		
Chen et al. [205]	AA5052	0	0.04	0.02	0.045
Liu et al. [206]	AA5052-0	0.003	0.025	0.027	0.043
Amaral et al. [207]	AA5182-0	0.001	0.01	0.021	0.04
Teng et al. [208]	AA5A06	0.0012	0.032	0.034	0.042
Feng et al. [209]	AA5052-0	0.00112	0.0132	0.0206	0.0299

Table 3.4 Ranges of the GTN coefficients investigated

<b>Coefficient</b>	<b>Minimum limit</b>	<b>Maximum limit</b>
$f_0$	0.0001	0.005
$f_n$	0.005	0.05
$f_c$	0.01	0.05
$f_f$	0.02	0.06

Although the ranges of the investigated coefficients have been narrowed down to certain limits, the combination of the coefficients can still be unlimited. To obtain the relationship between the coefficients and the response in the GTN model by RSM effectively with a limited combinations of the coefficients, a four-factors-three-level central composite design (CCD) method of the coefficients was adopted, based on the research by Ying et al. [169] and Abbasi et al. [210].

The CCD method is used for the RSM to obtain quadratic response, the combinations of the simulation runs by the CCD can be generated using the software Minitab 17 [211] with the boundaries of the coefficients defined in Table 3.4. The generated design is shown in Table 3.5, in which 30 sets of simulations needed to be run. In each set, different values of the coefficients in the GTN model were used and corresponding FE simulation results were outputted, based on which the response value could be calculated and analysed.

Table 3.5 Test runs based on CCD

<b>Run</b>	$f_0$	$f_n$	$f_c$	$f_f$	<b>Response</b>
1	0.005	0.05	0.01	0.06	217512.8
2	0.0001	0.05	0.05	0.06	29707.2
3	0.005	0.005	0.01	0.06	28646.0
4	0.00255	0.0275	0.03	0.04	268408.4
5	0.00255	0.0275	0.03	0.04	268408.4
6	0.005	0.005	0.01	0.02	81608.6
7	0.0001	0.005	0.05	0.02	260498.3
8	0.0001	0.005	0.01	0.02	165271.2

Experimental Investigation and FE Modelling of ISF

9	0.00255	0.0275	0.03	0.04	268408.4
10	0.005	0.05	0.05	0.05	75965.2
11	0.005	0.05	0.01	0.02	246451.5
12	0.005	0.05	0.05	0.02	178374.6
13	0.0001	0.05	0.01	0.06	139611.3
14	0.0001	0.05	0.05	0.02	114441.4
15	0.0001	0.005	0.03	0.04	258601.8
16	0.00255	0.0275	0.03	0.055	268408.4
17	0.0001	0.005	0.01	0.06	258601.8
18	0.005	0.005	0.05	0.06	258044.7
19	0.005	0.005	0.05	0.02	154372.4
20	0.0001	0.005	0.05	0.06	260498.3
21	0.005	0.0275	0.03	0.04	61833.9
22	0.00255	0.005	0.03	0.04	255332.6
23	0.00255	0.0275	0.03	0.02	219862.1
24	0.00255	0.0275	0.03	0.06	268408.4
25	0.00255	0.0275	0.05	0.04	45908.5
26	0.00255	0.0275	0.03	0.04	268408.4
27	0.00255	0.0275	0.01	0.04	149209.0
28	0.00255	0.05	0.03	0.04	124206.3
29	0.00255	0.0275	0.03	0.04	268408.4
30	0.0001	0.0275	0.03	0.04	29665.2

(b) Response calculation and response surface generization

The response can be defined based on the specific process investigated. In this study, the response variable was defined as the aggregation of the difference between the loading

forces obtained from the experiment and from the FE simulation at selected deformation stages,

$$R = \sum_{i=1}^n |F_{exp}^i - F_{num}^i| \quad (3-2)$$

where  $R$  is the response,  $i$  is the number of the point selected in the tensile displacement-load curve,  $F_{exp}^i$  is the force in the experimental tensile test while  $F_{num}^i$  is the force obtained from the FE simulation at the same displacement.

To describe the relationship between the input and the response, a quadratic or cubic model can be used. According to the Engineering statistics handbook [212], in the industrial applications, a second-order quadratic model should be sufficient to describe the relationship. From the CCD simulation run results, a quadratic polynomial regression analysis between the response and the four variables can be obtained in the form of,

$$R = b_0 + \sum_{i=1}^4 b_i X_i + \sum_{i=1}^4 b_{ii} X_i^2 + \sum_{i=1}^3 \sum_{j=i+1}^4 b_{ij} X_i X_j \quad (3-3)$$

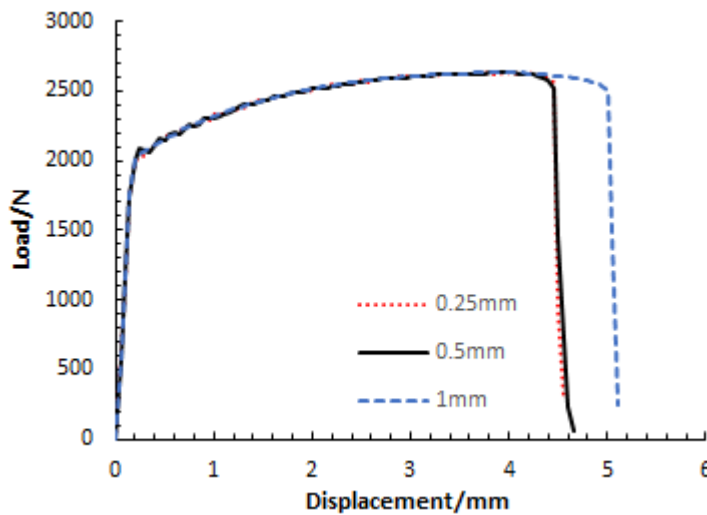
where  $X_i$  ( $i=1,2,3,4$ ) are the variables. Based on Equation (3-3), all possible combinations in the investigated ranges outlined in Table 3.4 can be analysed. The optimized values of coefficients can be obtained when the displacement-force curve obtained from the uniaxial tension simulation is as close to that obtained from the uniaxial tensile test as possible. That is, from mathematical point of view, when the response variable  $R$  reaches its minimum value possible in the defined ranges.

#### (c) Optimization of coefficients by GA

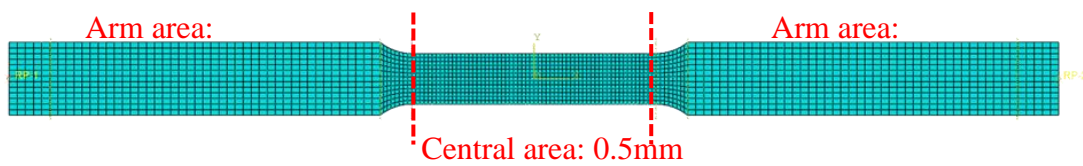
With the relationship between the response and the coefficients obtained using the RSM method, the optimization of the values of the four coefficients can be performed using the genetic algorithm (GA) provided by GA solver in the Matlab software [213]. Genetic algorithm is an optimization method for solving both constrained and unconstrained optimization problems. Based on natural selection, random individuals are selected from the population pool and evolve to next generation, which are used for the next step of optimization. Through the successive evolution, the best set of parameters can be selected from the population pool generated. The difference between the genetic algorithm and the traditional optimization algorithms lies on the number of the points selected during the optimization process. By comparison, only one point is used in the traditional optimization algorithms, therefore, higher efficiency can be obtained from the GA.

### 3.2.2.3 FE simulations and optimization of the coefficients

The dimensions of the specimen used in the FE modelling of the uniaxial tensile test is shown in Figure 3.3. Displacement boundary condition was used in the simulation, maintaining a constant tensile speed of 0.9 mm/min as that in the experimental uniaxial tensile test. In order to reduce the computational cost while maintaining accuracy, the first-order, reduced-integration continuum element C3D8R was used in this model.



(a)



(b)

Figure 3.7 Mesh convergence test for the uniaxial tensile test FE model: (a) comparison between the displacement-load curves obtained from different sizes of mesh; (b) final mesh of the specimen

Mesh dependence of the FE analysis with continuum damage mechanics have been reported by various researchers [138, 214] and by Gatea et al. [67] for the GTN model. To ensure the simulation accuracy without compromising the computational efficiency, a mesh convergence check was first performed. In the convergence check, the first set of coefficients in the CCD were used, and the values were set to be 0.005, 0.05, 0.01 and 0.06 respectively. The mesh size of the arm area was set to be 2mm while the central gauge area was set to be varied between 0.25 mm and 1 mm. The load-displacement curve was extracted from each test and compared. As shown in Figure 3.7 (a), it is clear that the simulation did not converge until the mesh size was close to 0.5mm or below. As a result, the mesh size in the arm zone was determined to be 2mm, while in the central testing zone it was set as 0.5 mm in the FE model, as shown in Figure 3.7 (b). The shear-related

coefficient  $k_w$  was set to be zero. The simulations were terminated when fracture appeared in the specimen.

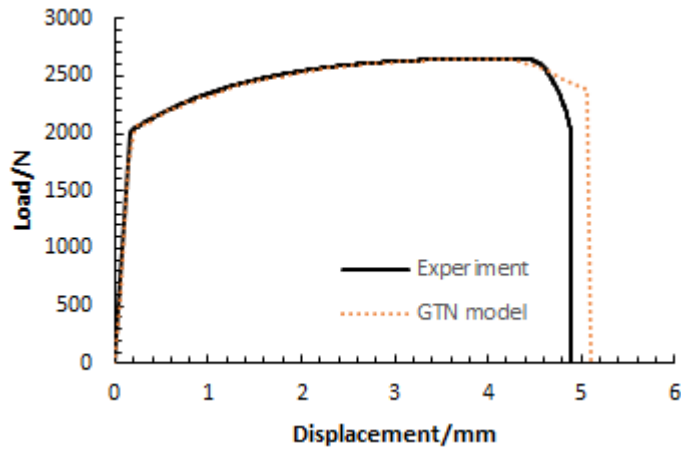
The load-displacement curves were extracted from the FE simulations. According to the FE results, the maximum elongations before fracture using different combinations of coefficient values varied from 4.40 mm to more than 6.0 mm, while in the experimental uniaxial tensile test, as shown in Figure 3.8 (a), the maximum elongation of the specimen upon fracture was 4.89 mm. As a result, as suggested by Kami et al. [168], in order to obtain a reasonable relationship between the combination of the coefficients and the response, only data obtained before the elongations of 5.38 mm was used for the regression analysis, the extreme data obtained after the elongations of 5.38 mm was ignored. The regression analysis can be done by using the software Minitab 17 by providing the calculated response values, as shown in Table 3.5. The mathematical regression model between the response and the coefficients can be solved as,

$$\begin{aligned}
 R = & 297984 + 66706520f_0 - 1074383f_N + 12290925f_c - 13956299f_f \\
 & - 20999029377f_0^2 + 35502585f_N^2 - 185593794f_c^2 + 180847555f_f^2 \\
 & + 889797571f_0f_N + 318212732f_0f_c + 37953551f_0f_f \\
 & - 93932501f_Nf_c - 40618292f_Nf_f + 3764030f_cf_f
 \end{aligned} \tag{3-4}$$

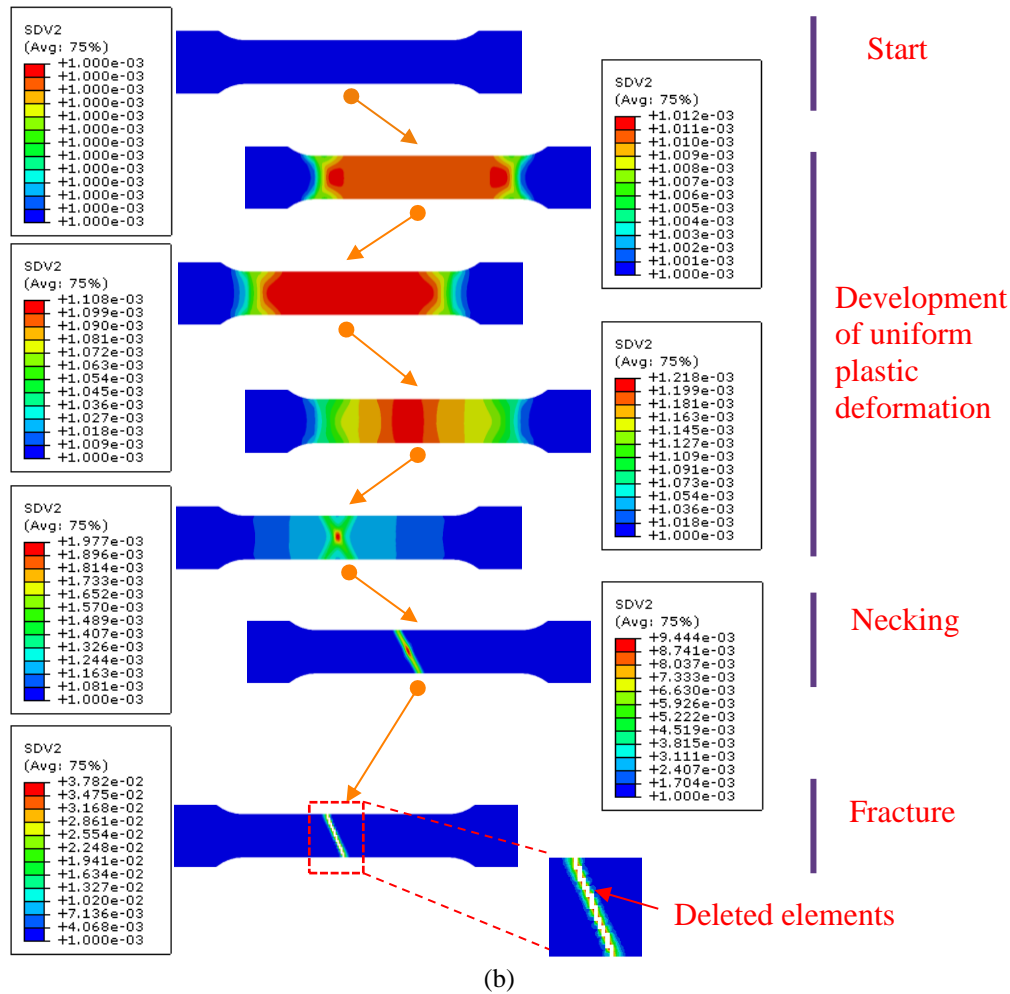
However, as reported by Gen and Cheng [215], GA was effective in searching for the optimal values in the global scale while it was ineffective in determining the local optima. As a result, in this study, 100 runs of GA algorithm were performed. Excluding the abnormal combinations from the results, the average values of the remaining values were treated as the ultimate optimal set of coefficients,

$$f_0 = 0.001, \quad f_n = 0.011, \quad f_c = 0.023, \quad f_f = 0.042 \tag{3-5}$$

The comparison between the load-displacement curve obtained from the experiment and the simulation with the GTN model using optimized coefficient values is shown in Figure 3.8 (a). Compared with the experiment, the FE model overestimated the maximum elongation of the specimen before fracture. The predicted maximum elongation was 5.10 mm, which was larger than that obtained from experiment by 4.3%. Overall, at beginning, the predicted load-displacement curve matched the experimental one well before the displacement reached around 4.2 mm. After that, the difference between the curves became obvious. The difference between the curves was probably caused by the inaccurate prediction of the response surface method adopted in this research. The whole



(a)



(b)

Figure 3.8 FE modelling of the uniaxial tensile test with the GTN model using the optimized coefficients: (a) comparison between displacement-load curves obtained from the experiment and FE modelling; (b) evolution of VVF (SDV2) in the FE model

optimization process by the genetic algorithm was only based on one regression equation, making the optimized values possibly close to the global optimum and the deviation between the simulation and experiment occurred. Nevertheless, the difference between the FE simulation and the experiment was below 5%, and the predicted values were in

the ranges defined in Table 3.4. Consequently the optimized coefficients would be used in this study for the FE modelling of ISF processes.

The evolution of the damage indicator VVF (SDV2) during the FE uniaxial tensile test is shown in Figure 3.8 (b). Firstly, the damage was uniformly distributed along the central gauge area when the plastic deformation was uniform. It then concentrated on one area with the test progressing and when VVF in certain elements reached  $f_f$ , these elements were deleted and fracture occurred.

### 3.2.3 Calibration of shear-related coefficient

A similar inverse method to identify the original GTN model coefficients was used to calibrate the shear-related coefficient in the Nahshon-Hutchinson extension model. In order to achieve low stress triaxiality, a pure shear test was conducted. FE simulations of the pure shear test using the shear-modified GTN model with varied values of  $k_w$  were also performed. Then load-displacement curves obtained from the FE simulations were compared with that obtained from the experiment and the one providing the closest result to the experiment was selected as the optimal value of the shear-related coefficient.

#### 3.2.3.1 Pure shear test

Material AA5251-H22 was used in the test. For pure shear test of thin aluminium alloy, a standard specimen has already been proposed by ASTM standard [126], as shown in Figure 3.9. By loading the specimen onto a uniaxial tensile test machine, a single shear zone can be created at the centre of the specimen.

However, specimen rotation was observed during the test using this design of specimen, which compromised the accuracy of the test, as reported by Yin et al. [123]. A modified specimen based on the ASTM standard was proposed by Kang et al. [216], as shown in Figure 3.10, which provided satisfactory low stress triaxiality. Nevertheless, the precision requirement on the manufacturing of the thickness reduction in the centre of the specimen in a thin sheet can be demanding, which compromised its application.





observe the strain distribution in the target area of the specimen during the test, a LA VISION DIC measuring system was deployed. The digital image correlation (DIC) technology is an optical measurement system, in which the movement of the points in the area of interest can be tracked by the camera and recorded. One step further, the strain distribution in the target area can be computed processing the images obtained [219]. In this test, the central region of the shear specimen was supposed to be the area where major material deformation should happen and it was treated as the area of interest. The bottom clamp was fixed while the upper clamp was set to move at a constant speed of 1 mm/min. The test was terminated as soon as fracture occurred. The load-displacement curve was recorded by the testing platform while the testing process was recorded by DIC system for analysis.

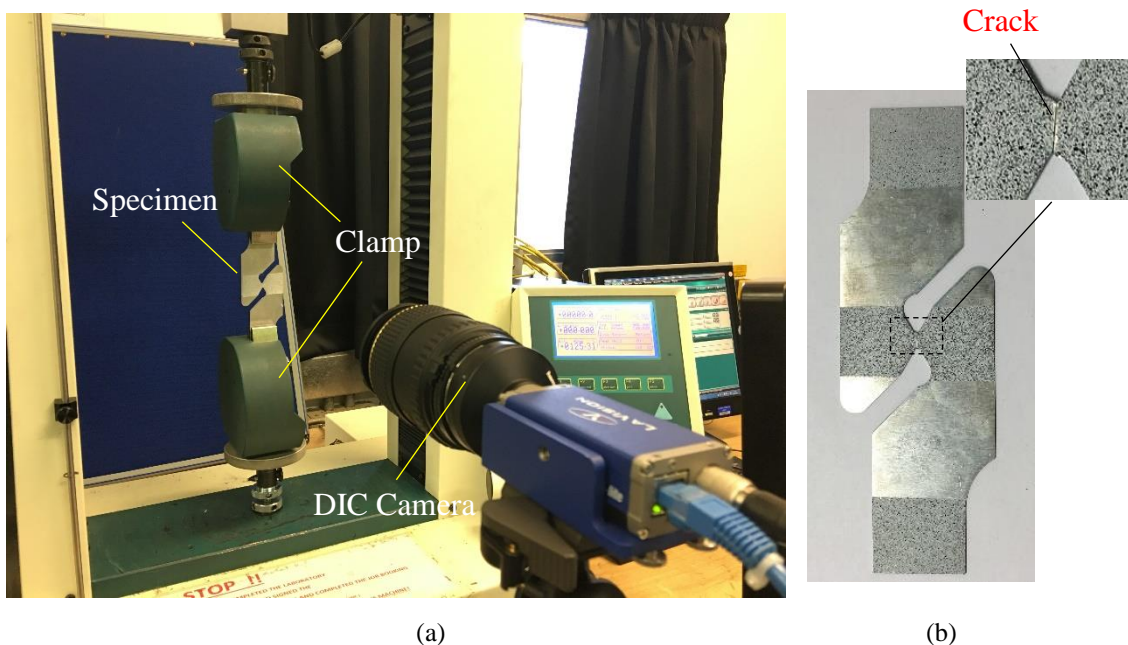


Figure 3.12 The pure shear test: (a) the pure shear test; (b) fractured specimen

The fractured specimen is shown in Figure 3.12 (b). It was obvious that the fracture happened without obvious sign of necking. Using the DIC software, the strain distribution before the final fracture in the central zone near the location of the crack was obtained and a qualitative analysis of the material deformation in the central was performed. As shown in Figure 3.13, the planar shear strain in the central area was higher than 0.32 while the strain component in the lateral direction was around 0.05 by comparison. The deformation of the material in the central zone was clearly shear-dominated.

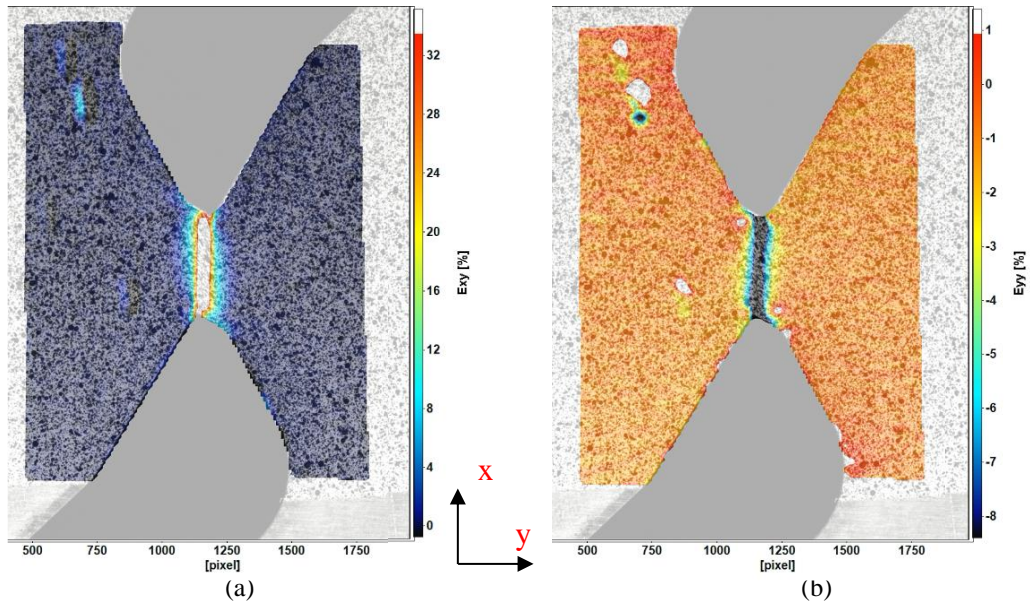


Figure 3.13 Planar strain distribution in the pure shear specimen according to DIC measurement in different directions: (a) xy direction; (b) y direction

In order to obtain the strain state of the material in the central zone during the deformation process, an FE simulation of the pure shear test was conducted using the solver Abaqus/Standard. Element type C3D8R was used, the central zone was meshed with an element size of 0.25 mm while in the arms the element size was 2mm to save the computational time. The mesh of the specimen is shown in Figure 3.14.

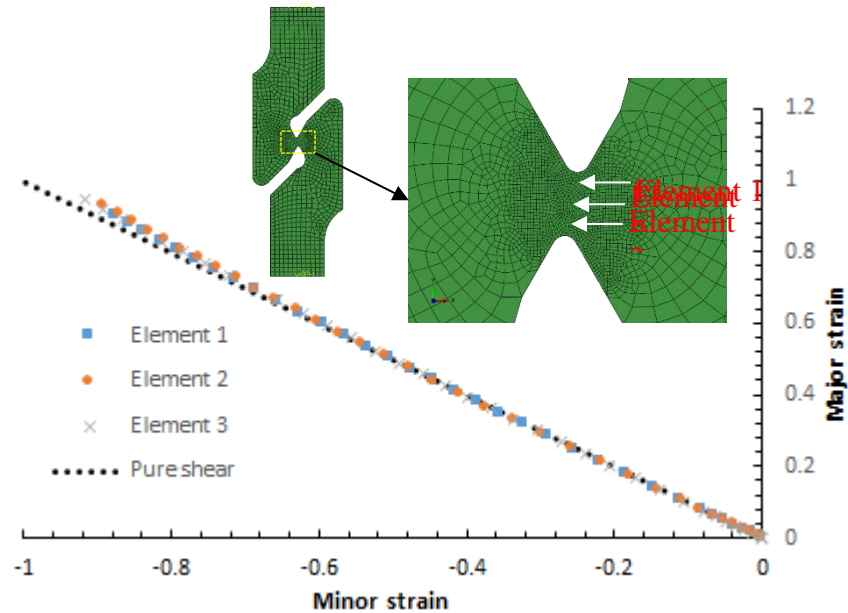


Figure 3.14 Strain paths of the three elements in FE modelling of the pure shear test

In the simulation, the clamp on the one end moved at a constant speed of 1mm/min for two minutes. The maximum and minimum principal stress components of three elements

in the central area along longitudinal direction of the specimen were extracted from the FE results and plotted in the minor strain-major strain space. As shown in Figure 3.14, all strain paths of the three elements complied well with the ideal strain path in the pure shear deformation state. As a result, this specimen can be treated as a pure shear specimen and can be used in this study to determine the shear-related coefficient  $k_w$ . The load-displacement curve obtained from the pure shear test with this specimen can be used for the later study of coefficient calibration.

### 3.2.3.2 Calibration of $k_w$

Nahshon and Hutchinson [164] reported that the value of  $k_w$  should be in the range between 0 and 3. Instead of running a complicated design of experiment as performed in the last section to determine the coefficient values in the original GTN model, the value of  $k_w$  was varied between 0 and 3 in this part of study. The simulation was run on the Abaqus/Explicit solver using the developed shear-modified GTN model with values of the four coefficients identified in the last section. The mesh of the specimen was the same as that in the FE modelling of the pure shear test on Abaqus/Standard. The load-displacement curves were extracted from the FE simulation results to be compared with that measured in the experiment. As shown in Figure 3.15, it was confirmed that the curve obtained in the FE model using  $k_w = 1$  provided the most satisfactory match to the experimental result. As a result, the value of  $k_w$  was determined to be 1.

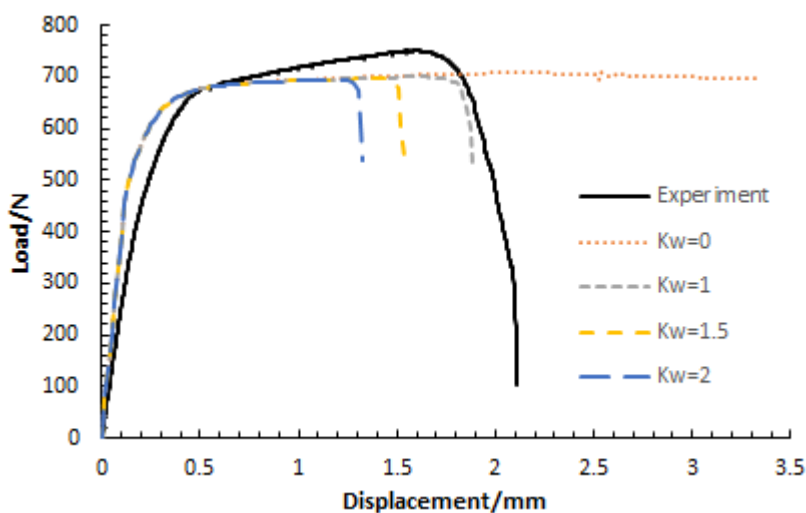


Figure 3.15 Comparison between displacement-load curves obtained from the experiment and FE simulations with varied values of  $k_w$

Nevertheless, there was a difference between the experimental curve and that from the simulations. Generally, at the elastic stage of the test, the specimen in the simulation was shown to be more resistant than that in the experiment. On the contrary, after yielding,

the loads in the simulations kept stable while in the experiment it was increasing until fracture occurred. The difference might result from the clamping of the specimen in the experiment. In the experiment, the specimen was not ideally clamped, a slight sliding between the specimen and the clamp might lead to a postponed yielding. Another factor might affect the loading-displacement curve in the shear test was the rotation of the specimen during the test. The geometry of the shear specimen would inevitably cause twisting of the specimen during the test, which would possibly lead to an increase of the loading force. By comparison, in the FE modelling, the boundary conditions were ideal and neither of the drawbacks mentioned would occur during the simulation. As a result, the difference between the results obtained from the experiment and the FE simulations occurred.

### 3.3 FE Modelling of ISF Processes

To obtain material deformation characteristics of material AA5251-H22 in the ISF process, the material deformation history during the process should be obtained, which is not feasible in the experiment due to the complexity of the experiment configuration. In this section, FE damage modellings of the SPIF and DSIF processes with the shear-modified GTN model were developed.

In the FE models, as shown in Figure 3.16 (a) and (b), a blank with a dimension of  $170 \times 170 \times 1$  mm was positioned on a backing plate, the tool with a head radius of 5 mm was first positioned above the blank. The backing plate and the tool(s) were defined as rigid shell while the blank was plastically deformable. Surface-to-surface contact was defined between the tool and the blank and Columbus friction law was adopted to describe the frictional behaviour between the tool and the sheet. As lubricant was applied in the SPIF experiment to reduce frictional effect, the frictional coefficient was set to be 0.1, as recommended by Nguyen et al [220] and Benedetti et al. [221] in their FE models of SPIF processes with aluminium alloys and the experimental calibration by Durante et al. [222] and Lu et al. [57] for material AA7075 and AA1100 respectively.

The backing plate was fixed during the whole process, as well as the edges of the blank. The tool movement was controlled by the displacement boundary conditions. The tool(s) moved at a constant linear speed of 1800 mm/min to avoid oscillation of the CNC machine. To save the computational time, mass scaling was applied. Mass scaling reduces the time increment by artificially increasing the density of the material. In this study,

adaptive mass scaling was adopted and it would be applied onto the model automatically if the stable step time was less than  $5 \times 10^{-5}$ s.

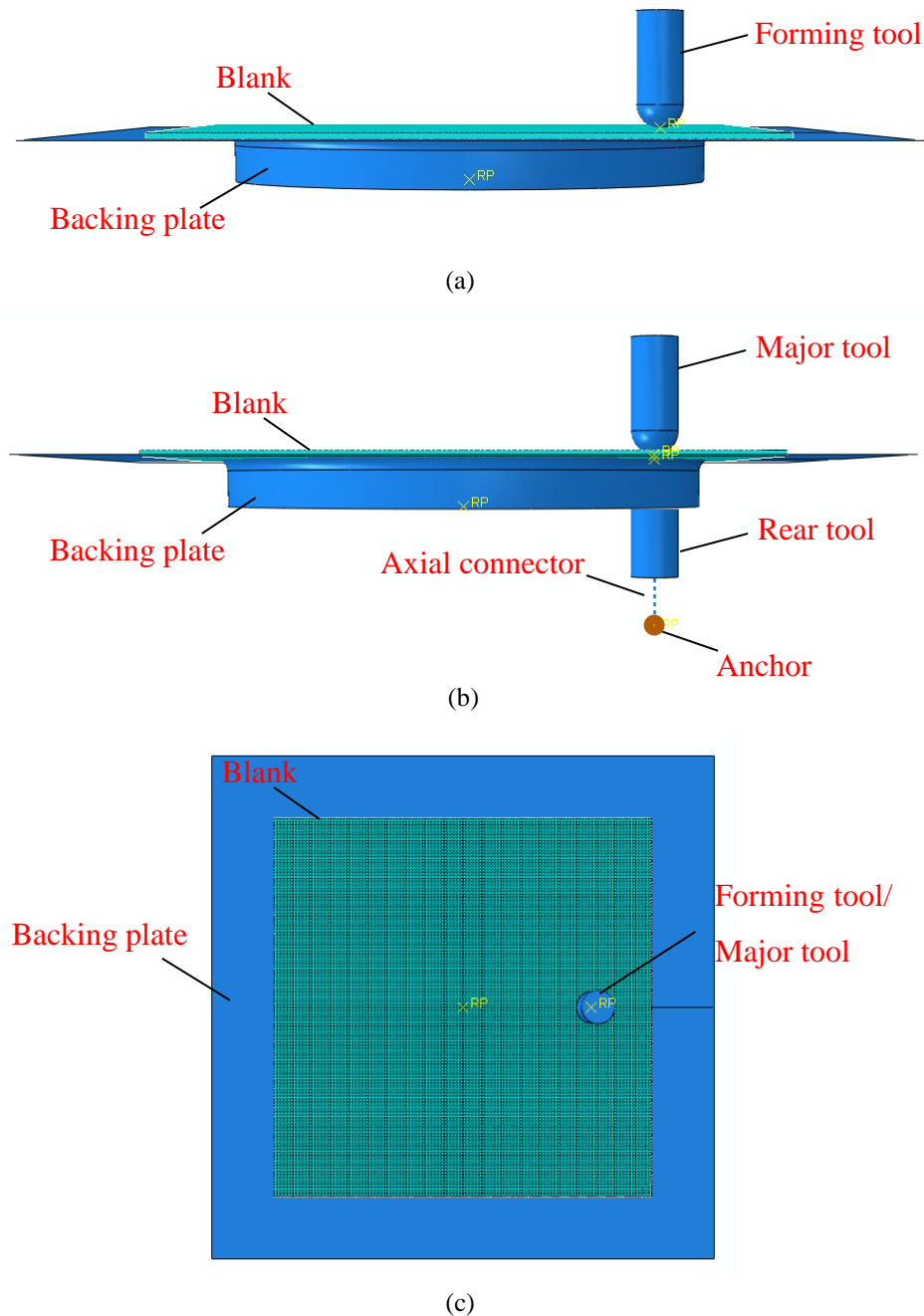


Figure 3.16 FE modelling of the ISF process: (a) SPIF; (b) DSIF; (c) top view of the models

Three-dimensional 8-node linear hexahedral solid element with reduced integration C3D8R was used for the meshing of the blank in the FE models for its accuracy and efficiency in the modelling of SPIF process [223-226]. In the FE simulation conducted by Esmailpour et al. [225], the element size was set to be 0.7 mm in the planar directions while in the FE model of TPIF process established by Wang et al. [179], the element size was 0.5 mm and a good match between the FE modelling results and the experiment was

achieved. According to the mesh convergence check in Section 3.3, the FE result of the uniaxial tensile test converged when the element size was 0.5 mm or less when the GTN model was incorporated into the Abaqus Explicit solver. Considering the computing cost and the convergence of the FE model, the element size in the planar directions was set to be 0.5 mm. In the thickness direction, four layers of elements were used in order to observe the effect of bending and compression on the material deformation behaviour and to avoid hourglass effect caused by the reduced integration elements. As a result, there were 360000 elements in the model. Meshing of the specimen is shown in Figure 3.16 (c).

The main difference between SPIF and DSIF FE models was the superimposed compression been added in the DSIF FE model. As shown in Figure 3.16 (b), in the DSIF model, a rear tool was positioned against the forming tool on the opposite side of the blank. In the purposely built DSIF platform developed by Lu et al. [30], an air compressor was used to guarantee that the rear tool was kept in contact with the blank while at the same time keeping the supporting force constant and controllable. To provide a preload on to the sheet through the rear tool in the FE modelling of DSIF while keeping the load constant during the whole process, an axial connector modelling mechanism was used. As shown in Figure 3.16 (b), the connector was defined by a wire connecting the reference point of the rear tool and a fixture point. The axial connector functioned as a spring, generating 200 N supporting force to the blank.

Using the amplitude modelling tool provided by Abaqus, the coordinates of the tool(s) movement along the deformation time could be defined based on the toolpath generated for the ISF experiment. In order to provide a constant supporting force, the fixture point in the DSIF model also followed the predefined toolpath for the tools.

The simulations were run on the University of Sheffield high performance computers (HPC) system SHARC with 16 cores used. They would be terminated automatically when the fracture occurred in the sheet metal.

## 3.4 Experimental and FE Modelling Results

### 3.4.1 Experimental results

The fractured parts in the SPIF tests are shown in Figure 3.17. The maximum forming depth for material AA5251-H22 was 21.8mm, which corresponded to a maximum forming angle of 71.4 degrees according to the CAD drawing of the part. For material

AA6082-T6, the maximum forming depth of the conic part was 15.95 mm so that the maximum forming angle was 60.1 degrees. Material AA5251-H22 presented better formability in the SPIF test.

The cracks in both parts appeared without a clear sign of necking and propagated along the tool movement direction. Similarly, neither of the cracks located at the bottoms of the tool-sheet contact areas but above that. However, it was hard to tell whether they located in the contact areas or not.

In addition, compared with the part made by AA5251-H22, the part made by AA6082-T6 presented much higher degree of springback after unclamping because of its higher yield stress during the plastic deformation. The strong springback resulted in an obvious distortion of the sheet, as shown in Figure 3.17.

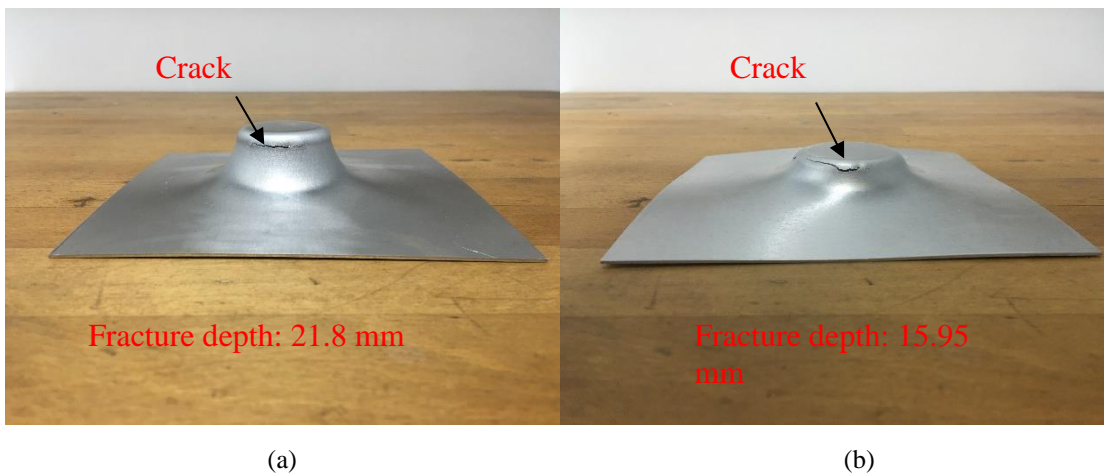


Figure 3.17 Fractured conic parts made by SPIF: (a) AA5251-H22; (b) AA6082-T6

### 3.4.2 FE modelling results

#### 3.4.2.1 The effect of mass scaling

In order to make sure that the inertia effect caused by mass scaling did not affect the simulation results significantly, the ratio of the kinetic energy to the internal energy of the blank deformation should stay below 0.05-0.1 for the majority of forming time [194, 227, 228]. The history of the blank deformation kinetic energy and the internal energy was extracted from the FE simulation results, based on which the evolutions of the ratio of the kinetic energy to the internal energy were plotted for both SPIF and DSIF processes.

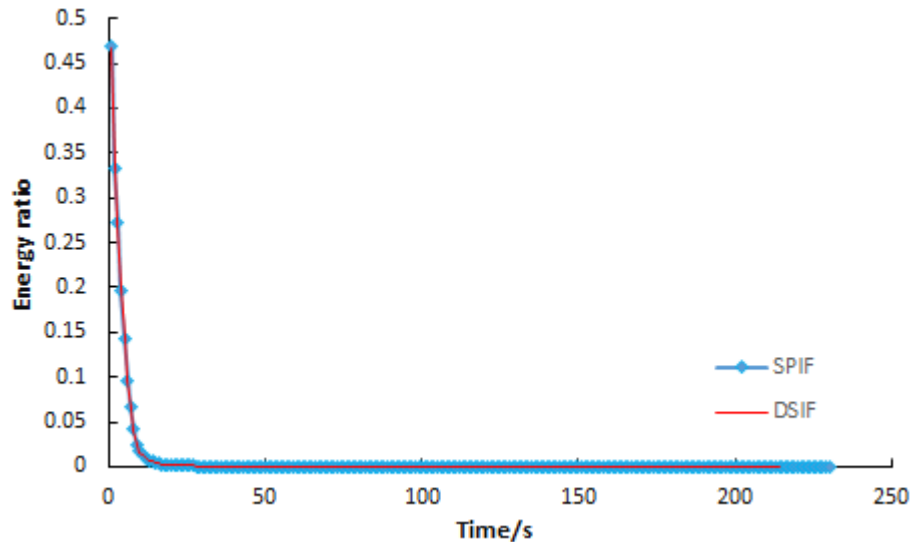


Figure 3.18 History of ratio of blank deformation kinetic energy to internal energy in the ISF FE models

As shown in Figure 3.18, the energy ratio was higher than 0.1 at the beginning but it quickly dropped below 0.1 after 5 seconds. With the processing continuing, the energy ratio kept decreasing and stayed close to 0 after 10 seconds. As a result, the energy ratio was below 0.1 for the majority of the forming process and it can be confirmed that the FE simulation results were not significantly influenced by the mass scaling applied.

#### 3.4.2.2 FE damage modelling results for SPIF

In the damage modelling of SPIF process, for material AA5251-H22, the cone fractured after a total forming time of 230.1 seconds, which corresponded to the fractured depth of 11.33 mm according to the toolpath and a maximum forming angle of 50.3 degrees, as shown in Figure 3.19 (e).

The deformation history of the conic shape and evolution of the distribution of VVF in SPIF process with time is shown in Figure 3.19. As shown in Figure 3.19 (d), element deletion first started when the step time reached 185s. However, different from the FE damage modelling of the uniaxial tensile test, in which the concentration of the damage and element deletion immediately led to fracture, as shown in Figure 3.8, material deformation in SPIF continued and final fractured occurred 45.1s later. More elements were deleted before the occurrence of final fracture, as shown in Figure 3.19 (e).

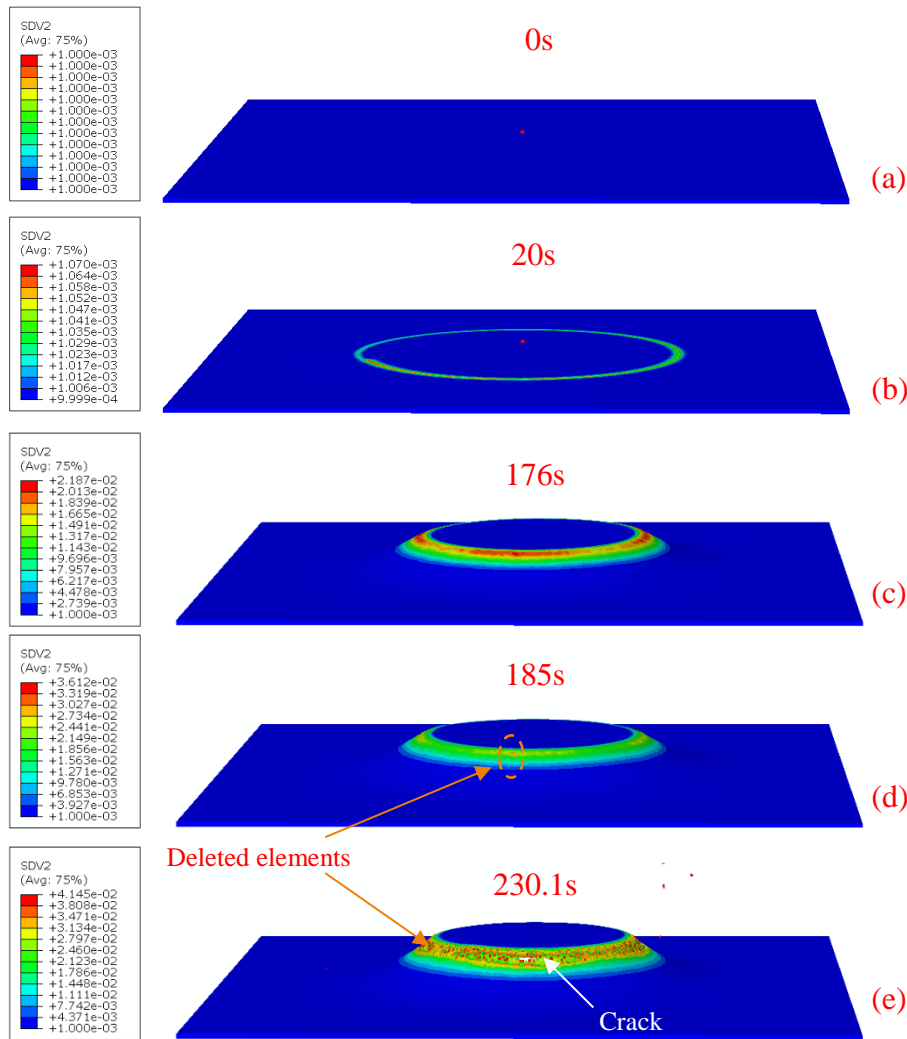


Figure 3.19 Evolution of VVF (SDV2) in the conic parts made by SPIF using AA5251-H22

The history of equivalent plastic strain, VVF, void growth component and shear component in VVF for the deleted element 45201 in the crack area were extracted from FE results. As shown in Figure 3.20, a stair-like evolution of all these parameters can be observed, indicating strong localized material deformation in SPIF. Plastic deformation only accumulated when the forming tool moved past or close to the element. In addition, VVF and void growth component increased significantly in the last two steps before fracture, suggesting the existence of high tensile effect during that period.

By comparing the value of the shearing-induced damage component with the total VVF and the void growth component, it is clear that although the damage contribution resulting from the shearing effect was not as much as the void growth component, it was a non-negligible factor in SPIF. In the second last contact between the element and the tool, the value of the shear component was 0.0031, while at the same time the total value of the damage indicator was 0.0256 and the void growth component was 0.012.

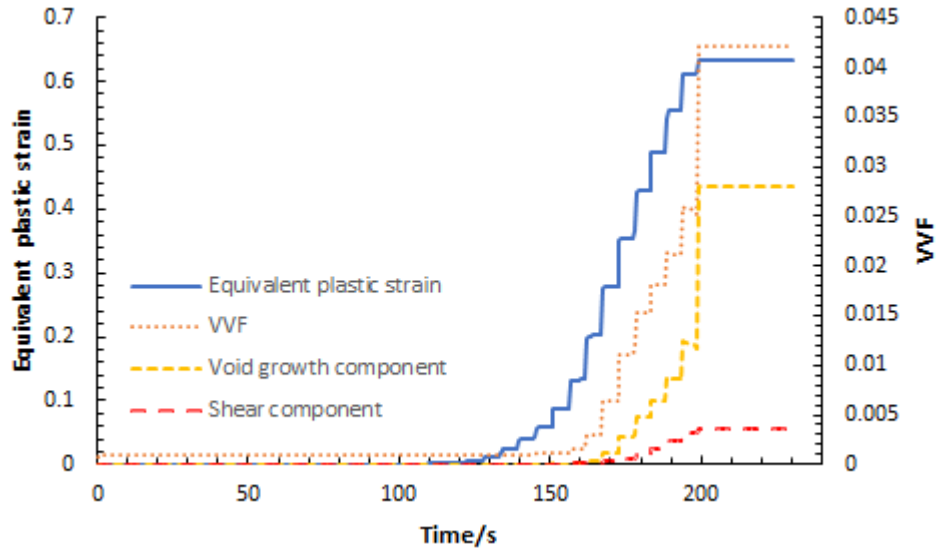


Figure 3.20 Strain and VVF evolution in SPIF modelling of element 45201

The von Mises stress distributions on the inner and outer surfaces of the sheet before the deletion of the elements were also extracted from FE results of SPIF. As shown in Figure 3.21 (a), on the inner surface, the highest degree of von Mises stress appeared at the opening area of the conic part where bending effect was significant and the contact area between the tool and the sheet. The high von Mises stress in the contact area was in agree with the material plastic deformation localization reflected by the evolution of the equivalent plastic strain and VVF in Figure 3.20.

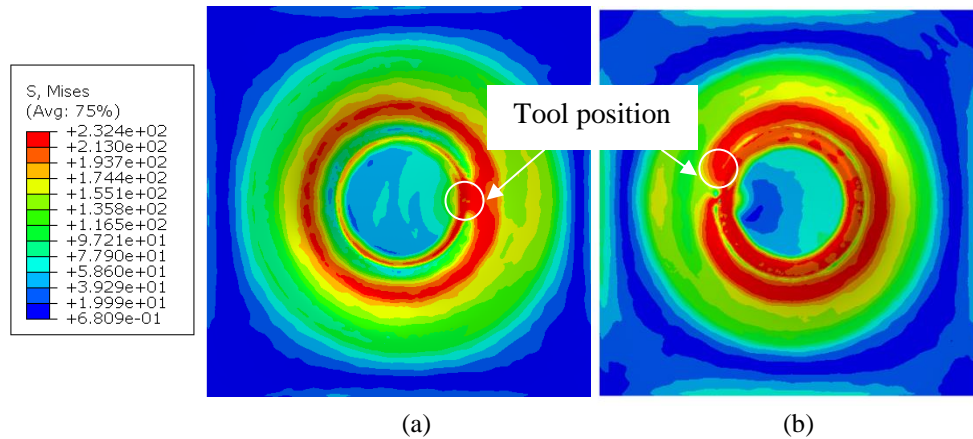


Figure 3.21 von Mises stress distribution in SPIF on: (a) inner surface; (b) outer surface

In addition, on the outer surface of the sheet, as shown in Figure 3.21 (b), the highest degree of von Mises stress still existed at the opening area of the conic part where bending effect was significant and the edge of the bottom. However, comparing with the stress distribution on the inner surface, the material on the outer surface generally underwent higher von Mises stress. The difference of the distribution of von Mises stress could be

explained by the bending effect, which caused higher degree of tensile stress on the outer surface of the sheet.

To further demonstrate the effect of bending, the history of VVF for the four elements in the crack location across the thickness were extracted from the FE results. As shown in Figure 3.22, the element 45201 lied on the outer surface of the sheet, element 315201 lied on the inner surface while the other two were in the middle layers. It is clear that at the same time, the element on the outer surface underwent the highest level of damage and it was first deleted, while elements on the inner surface was the least damaged and it was deleted until about 45 seconds after the first element was deleted. The inhomogeneous distribution of VVF along the sheet thickness and postponed deletion of the elements on the inner layers of the sheet indicted the bending effect in SPIF process.

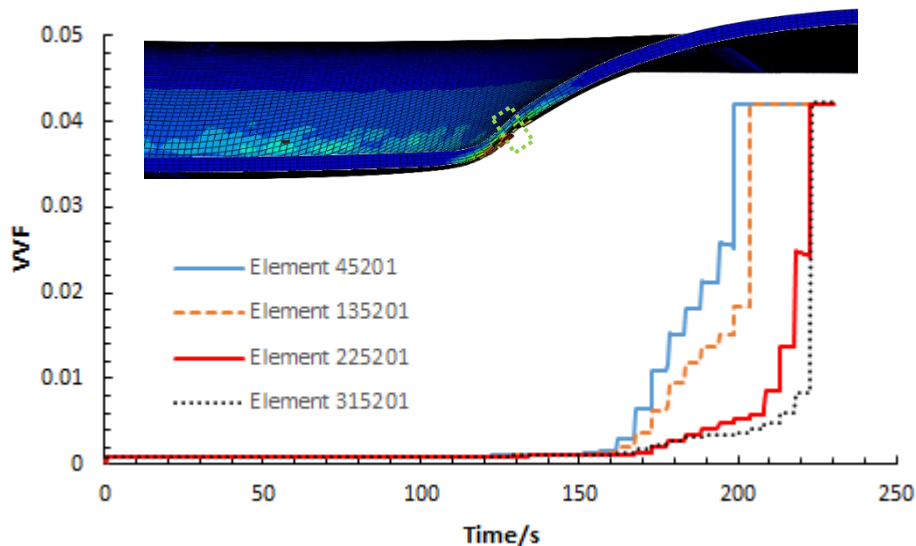
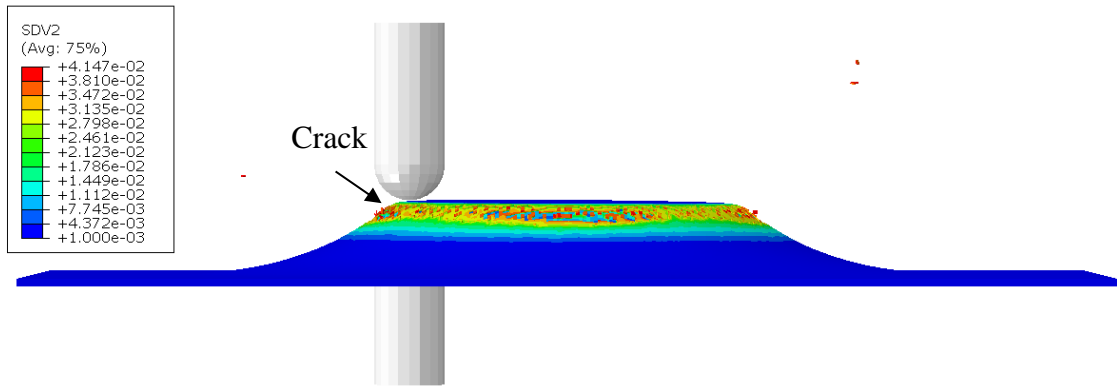


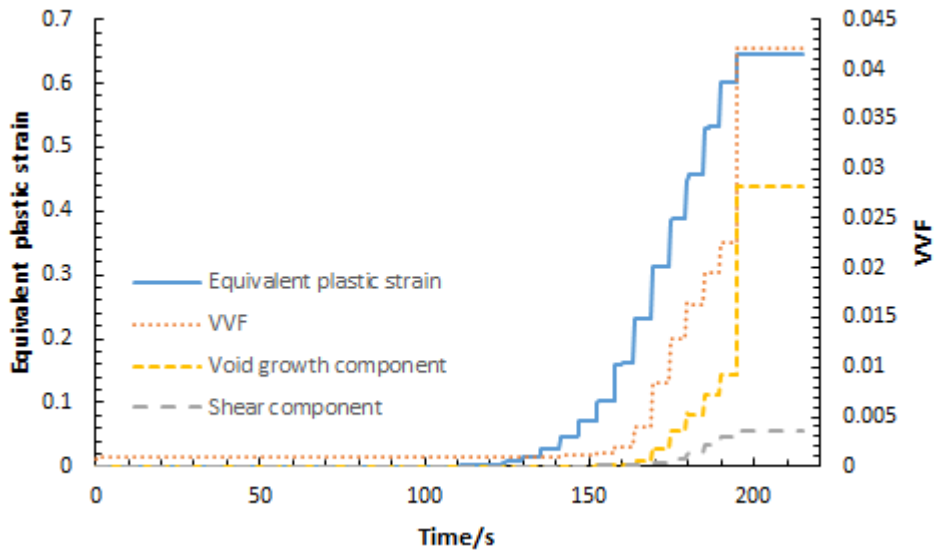
Figure 3.22 Evolution of VVF in SPIF modelling of elements along the thickness direction

### 3.4.2.3 FE damage modelling results for DSIF

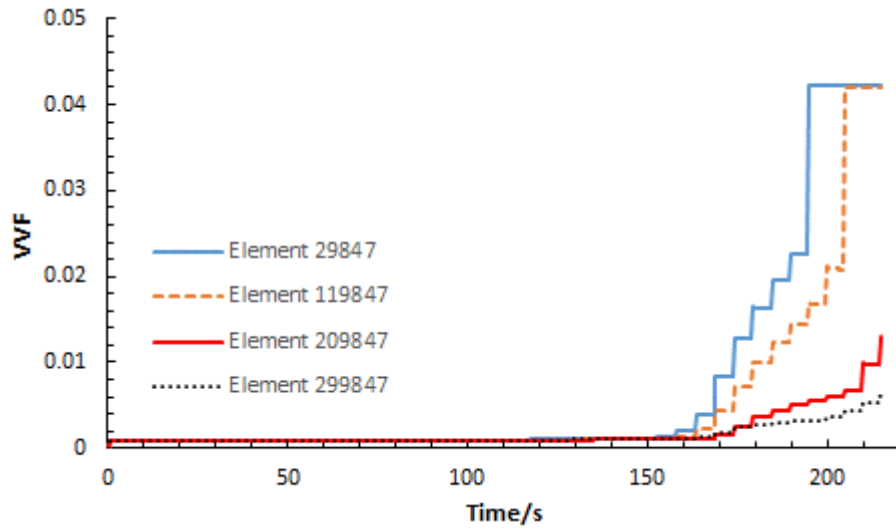
For DSIF, the total time of the FE simulation before the fracture of the part was 214.8 seconds, corresponding to a forming depth of 10.36 mm. As shown in Figure 3.23 (a), similar to SPIF, the final fracture in DSIF FE damage modelling occurred long after the start of element deletion.



(a)



(b)



(c)

Figure 3.23 FE damage modelling results for DSIF: (a) fracture location; (b) evolution of equivalent plastic strain, VVF and VVF components in element 29847; (c) evolution of VVF in the four elements along the thickness direction

The evolution of equivalent plastic strain, VVF, void growth component and shear component in the deleted element 298477 on the surface of the sheet in the crack area

(shown in Figure 3.23 (a)) were extracted from FE results. As shown in Figure 3.23 (b), similar to the SPIF process, strong localized material deformation also existed in DSIF process. Shearing played an important role in the material deformation in DSIF. The difference of VVF in the elements in the crack area along the thickness direction indicated the existence of bending effect, as shown in Figure 3.23 (c).

The von Mises stress distributions on the inner and outer surfaces of the sheet before the deletion of the elements were extracted from the FE results of DSIF process. As shown in Figure 3.24, similar with the results obtained from SPIF, the highest von Mises stress appeared at the opening area of the part and the contact area between the tool and the sheet, indicating the bending effect and the material deformation localization.

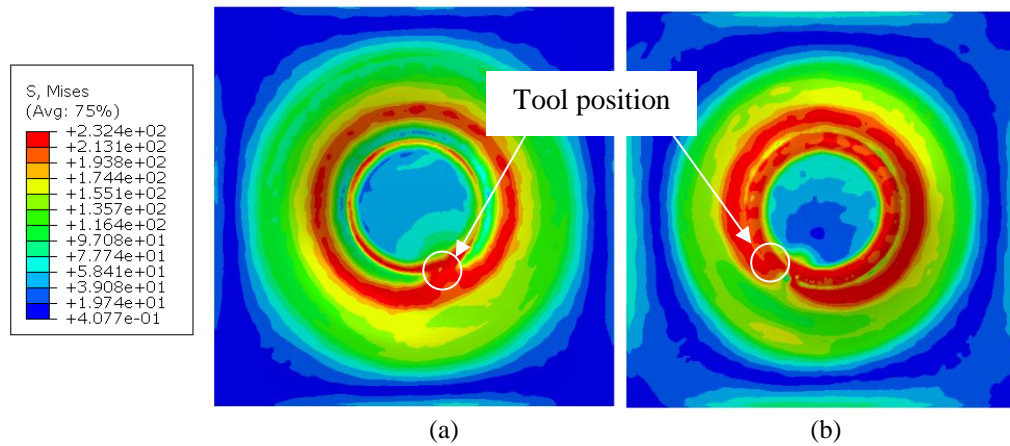


Figure 3.24 von Mises stress distribution in DSIF on: (a) inner surface; (b) outer surface

#### 3.4.2.4 Strain path evolution in ISF processes

In the FE damage modelling of ISF processes, the fracture of the part was premature compared with the experiment, leading to earlier deletion of the elements and weakened part structure. As a result, the results predicted by the FE damage models can not be accurate for the ISF process especially in the later stage of the process. In order to present a better prediction of the material deformation in ISF processes, FE modelling of the processes without the damage model was developed. All the parameters were kept the same in the FE models as the previous FE damage models, as described in Section 3.4.

According to the toolpath, for material AA5251-H22, the conic part fractured when the processing time reached 360.56 seconds in SPIF. As a result, strain components of the element 45201 and element 29847 were extracted from both SPIF and DSIF FE models respectively, from which the strain paths were plotted, as shown in Figure 3.25. The non-linear strain paths reflected the effect of cyclic loading on the material deformation and complexity of the deformation modes in ISF.

In addition, as shown in Figure 3.25, for both elements, the major strain was much larger than the minor strain, ultimately the major strain was close to 0.38 while the minor strain was around 0.05. The nearly-plane strain distribution matched the findings in the reported literature. According to the calibrations of strain distribution on the surface of the cone shapes manufactured by ISF process by Fang et al. [60], Eyckens et al. [69] and Emmens et al. [10], the material deformation of the cone shape in ISF process was close to plane strain condition.

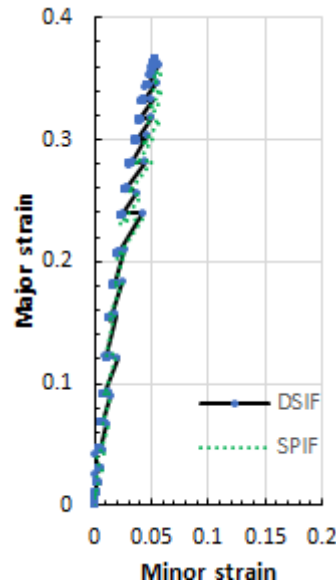


Figure 3.25 Strain path evolution of the element

## 3.5 Discussion

### 3.5.1 Deformation characteristics of ISF

Material deformation behaviour can be influenced by their mechanical properties. As demonstrated by the forming limits in the uniaxial tensile test and the SPIF test in Figure 3.1 and Figure 3.17, materials AA5251-H22 and AA6082-T6 presented different material deformation behaviours in both tests. As discussed in Chapter 1, in the uniaxial tensile test, the difference of the formability between materials could be explained by their work-hardening coefficients. While for ISF, the effect of material mechanical properties on the material deformation behaviour and formability is more complicated. The material mechanical properties not only can affect the material formability but also the fracture behaviour, as reported by the research conducted by Fratini et al. [39] and Ai et al. [82]. As a result, in order to obtain a comprehensive understanding towards ISF, it is essential to take the material properties into account when conducting the investigation into ISF processes.

However, on the other hand, different from the uniaxial tensile test, in which the maximum elongation of the specimen made by AA5251-H22 was smaller than that made by AA6082-T6, in SPIF test, the maximum forming depth of the conic shape made by AA5251-H22 was much higher than that made by AA6082-T6. The different deformation behaviours of the same material under different loading conditions suggested that loading conditions played an important part in deciding the material deformation behaviour in the deformation process. In the uniaxial tensile test, tension was predominant, while in SPIF, the loading condition was more complicated. Multiple deformation modes including tension, bending, shearing and cyclic loading existed in SPIF. The effect of the loading conditions on the material formability and the current research progress has been discussed in Chapter 1 and Chapter 2. Since the uniaxial tensile test has been widely used to describe material deformation behaviour in sheet metal forming processes, how the loading conditions existing in ISF influence the material deformation behaviour is another topic worth looking into in the research on ISF.

The FE damage modelling with the shear-modified GTN model confirmed that material deformation in ISF, including SPIF and DSIF, was localized deformation caused by a combination of tension, bending, shearing and cyclic loading effect. The tension effect was apparent since the tool moved in the part depth direction and pushed the sheet material. It could also be reflected by the sheet thinning and void growth component in the FE damage modelling.

While for the bending effect, in the damage modelling of both SPIF process and DSIF process, material deletion started first on the outer surface of the sheet and propagated to the inner surface when the deformation processes continued, suggesting the existence of bending effect. It agreed with the crack fractography observation made by Fang et al. [60], in which the formation of the shear bands and the orientation of the closed ends of the dimples on the crack location indicated that the fracture of the part initiated from the outer surface and propagated to the inner surface.

The shearing damage indicator suggested the existence of shearing effect in ISF processes. However, compared with other deformation modes, shearing effect was less important. In the FE damage model of SPIF, the shearing damage component accounted for only 8.6% of the whole damage in the targeted element at fracture; while in DSIF, the shearing damage component accounted for only 8.5% of the whole damage in the targeted element, as demonstrated in Figure 3.20 and Figure 3.23 (b). It agreed well with the research by Lu et al. [57] that material formability in SPIF would not significantly be affected by

shearing effect. However, when comparing the ratio of shearing effect damage indicator to the void growth damage indicator in the two FE damage models at fracture, it was found that it increased from 30% to 38.9%, shearing effect was more obvious in the DSIF process. This was also reported by Lu et al. [30] by measuring the distortion of drilled holes in the sheet after SPIF and DSIF processes, in which the more distorted in the DSIF process than that in the SPIF process in the tool movement direction, suggesting shearing effect was more significant in the DSIF process.

Shearing effect can be contributed by the friction between the tool(s) and the sheet. Obviously, higher friction will result in higher surface traction and consequently more shear deformation. In this test, the friction coefficient was set to be 0.1 taking account of the reported research. According to the analysis by Lu et al. [57], the through-thickness-shear caused by friction can be both beneficial and damaging to the material formability in ISF, as a result, the effect of friction is compromised. In addition, in the experiment conducted by Skjødt et al. [7, 229] and Kim and Park [230], the reduction of friction by tool rotation or lubricant application did not necessarily lead to an obvious improvement of material formability in SPIF. The limited effect of friction on the material formability was also reported by Silva et al. [231]. In FE damage modelling of SPIF process, as shown in Figure 3.20, the contribution of shear deformation to the overall damage accumulation was considerably small compared with the tensile effect. Both of the FE simulation results and the experimental should not be affected by the selection of the friction coefficient and the lubricant to an obvious degree.

Localized material deformation can be reflected by the progressive accumulation of the damage indicator and the equivalent plastic strain of the elements, and the delayed fracture of the part in the FE damage models. For SPIF and DSIF, the final fracture of the part occurred 45 seconds and 20 second respectively after the first deletion of elements. The accumulation of damage in the material only took place when the tool(s) was in contact with or close to the targeted areas.

In conclusion, the unique material deformation behaviour in ISF is related to both the material mechanical properties and the loading conditions applied in the processes, a comprehensive investigation into ISF must include both factors.

### 3.5.2 FE damage modelling of ISF

Compared with the experimental result, the FE damage modelling with shear-modified GTN model predicted premature fracture of the conic part made in SPIF process. For

material AA5251-H22, in the experimental test, the maximum forming angle of the cone was 71.4 degrees, while in the FE model, the prediction was 50.3 degrees, resulting in a substantial difference of 30%. A similar result was reported by Guzman et al. [232] and they attributed the underestimation of the maximum forming angle in SPIF to the inability of the coalescence modelling in the GTN model. By changing the coalescence modelling method for the GTN model thus delaying void coalescence, the predicted maximum forming angle of DC01 steel increased from 47 degrees to 51 degrees. Nevertheless, in the experiment the maximum forming angle for DC01 steel could reach 67 degrees, the difference between the experiment and the FE prediction was still significant.

By varying the value of nucleation related coefficients  $\varepsilon_N$  and  $f_N$  in the GTN model for DC06 steel in the FE simulation of SPIF process, Li et al. [183] found that the material deformation behaviour could be significantly affected by the nucleation related coefficients. The coefficient  $\varepsilon_N$  would affect the distribution of plastic deformation and damage indicator while the coefficient  $f_N$  could affect the maximum value of the damage indicator, thus affecting the deletion of the elements and fracture behavior of the sheet in the process. The coalescence model in the GTN model or the nucleation model may not be suitable for the ISF process.

However, in the FE damage modellings of SPIF using pure titanium with different shear extensions by Gatea et al. [67, 181], the predictions of the fracture depth of the conic parts were both in good agreement with the experiments. By comparing the modelling results obtained from the GTN models with shear extensions and those from the original GTN model, it was found that the original GTN model overestimated the fracture depths of the cones. In this case, the shear-modified GTN model was appropriate for the modelling of SPIF process.

Current research on the FE damage modelling of ISF process with GTN-related damage models is still limited. Based on the research by Guzman [233] and Gatea [67], the applicability of the GTN-related models in SPIF process may be affected by multiple factors, including the material mechanical properties, complex loading conditions in SPIF process and the resulting stress and strain distributions. Some materials, for example pure titanium, may be suitable for the FE damage modelling in ISF, while others for example steel DC04 and aluminium alloys may not. The GTN-related models may also have inherent drawbacks in modelling complicated sheet metal forming processes. The contact conditions in ISF process provides a challenge for the damage model. More research on

the GTN model and its application in SPIF process are required for a clear explanation to the difference in the reported literature and in the current research.

For DSIF, the maximum forming depth at fracture for material AA5251-H22 predicted by the damage modelling was 10.36 mm, which was even smaller than that in the SPIF FE damage modelling. Although DSIF experiment has not been done in this study, according to the experiment reported by other researchers for the similar types of materials [31, 234], material formability should have been improved in DSIF compared with SPIF. The even lower formability in DSIF in the FE damage modelling can be explained by the ineffectiveness of the GTN model under low or even negative stress triaxiality in DSIF due to the supporting force from the rear tool, as discussed in Section 2.3. As a result, the applicability of the FE damage modelling with shear-modified GTN model for DSIF process is questionable.

Nevertheless, the FE damage modelling method provided a more direct way to study the material deformation behaviour in ISF processes than the conventional FE modelling method. However, the selection of the damage model for a specific process, especially for the processes with complex loading conditions is challenging. Considering the incapability of the GTN model in simulating DSIF process, other damage models or different materials should be tested in the future in order to select a suitable damage model for the ISF process.

### 3.5.3 Coefficient calibration for the shear-modified GTN model

The inverse method comprised of response surface method and the genetic algorithm provided an efficient way to calibrate GTN model coefficients. However, the accuracy of the response surface method is affected by the investigated ranges of the parameters as well as the complexity of the problem to be investigated. In the original GTN model coefficients calibration process, four coefficients are needed to be identified, leading to a possible inaccurate mathematical description of the relationship between the coefficients and the response. While the optimization process by the genetic algorithm is stochastic by its nature, the predicted values cannot be precise.

In this study, using the optimal set of coefficients generated from inverse method, the maximum elongation of the specimen predicted by the FE model of the uniaxial tensile test was larger than that obtained from the experiment. According to the meaning of the coefficients in the GTN model, changing the values of the coefficients can bring the prediction closer to the experiment. For example, increasing initial void volume fraction

$f_0$  or nucleation coefficient  $f_n$  can lead to a decrease of the material formability. However, five coefficients exist in the shear-modified GTN model, it is possible that multiple coefficients predicted by the inverse method are not accurate, changing the value of one coefficient may make the prediction of fracture in the uniaxial tensile test more accurate, it will not necessarily lead to a better optimization of the values of the coefficients.

Instead of optimizing the four coefficients with one regression model, four regression models were used by Ying et al. [169] and Abbasi et al. [210] to run the optimization process. Compared with the method adopted in this research, in which the accumulation of deviation between the load-displacement curves obtained from the simulation and the experiment of the uniaxial tensile test were treated as the response, in the work conducted by Ying et al. [169] and Abbasi et al. [210], the coordinates of the highest point and the fracture point (R1, R2, R3, R4) in the true strain-stress curve were used as the responses, as shown in Figure 3.26. As a result, there were four regression models in total, one for each coordinate value. The genetic algorithm was adopted for each regression model to make the response as close to the experiment as possible. The average values of the optimized values obtained from the optimization of the four regression models were treated as the ultimate optimized coefficients. The adoption of four responses in the method could avoid the randomness of the genetic algorithm to a degree since more constraints were applied onto the optimizing process. On the other hand, in this method, the two response points representing the initiation of instability and fracture were treated as the optimizing objects, as a result, the obtained values may present a better performance in predicting the material deformation behaviour after the initiation of the deformation instability in the uniaxial tensile test compared with the method used in this research.

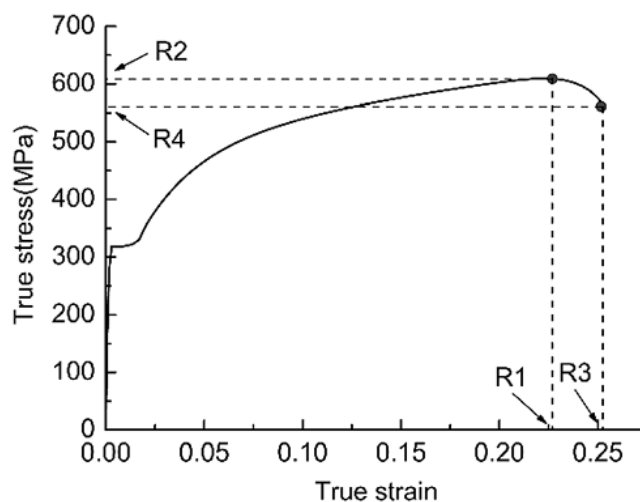


Figure 3.26 Response values on the experimental true stress-strain curve [169]

On the other hand, in the direct calibration method, making samples and performing the tests can be time-consuming. In addition, possible errors may be introduced when processing the specimens or calculating the void volume fraction using the image processing software or mathematical equations.

A combination of the direct calibration method and the inverse method may provide a more accurate calibration of the coefficients in the GTN model with considerable efficiency. The inverse method can provide a rough prediction for the coefficients' values, which can be further improved by the direct calibration. For example, in the direct calibration method, in the uniaxial tensile test, the initial state and final fracture state can be easily obtained without trying multiple specimen, while the identification of critical status and the nucleation requires constant monitoring of the deformation process and preparation of samples at different stages. As a result, the void volume fraction of the untested specimen and the fractured specimen can be calibrated using the direct calibration method. While the void volume fraction related to the critical deformation status and the nucleation can be obtained by using the response surface method. The reduction of the optimizing factors in the regression model may increase the randomness of the optimized value. As a result, a compromise between the efficiency and accuracy can be achieved.

### 3.6 Summary

In this chapter, in order to characterize the material deformation behaviour in ISF processes, SPIF experiment using materials AA5251-H22 and AA6082-T6 were conducted and FE damage modelling of the SPIF and DSIF processes was performed with the shear-modified GTN model. Based on experimental and FE results, it was confirmed that deformation mechanisms in SPIF and DSIF processes were both localized material deformation caused by tension, bending, shearing and cyclic loading. Different material presented different deformation behaviours in ISF. However, the shear-modified GTN model predicted premature fracture in both SPIF and DSIF processes for material AA5251-H22. The reason can be the limitation of the GTN model itself or the effect of the material property on deformation and fracture. For a better prediction of the ISF process, other damage models, materials, or material models should be evaluated.

Equation Chapter (Next) Section 1

# 4 TENSION UNDER CYCLIC BENDING AND COMPRESSION TEST

In this chapter, a new testing method, named as Tension under Cyclic Bending and Compression (TCBC), was developed to investigate the material deformation behaviour in ISF. The concept of the TCBC test and the test rig developed for the TCBC test will be introduced in Section 4.1. An analytical model for the test was first developed, as presented in Section 4.2. The design of the TCBC experiment will be elaborated in Section 4.3 and the results obtained will be reported in Section 4.4. FE damage modelling of TCBC test was developed for a better analysis of the TCBC test, the FE model and results obtained will be reported in Section 4.5. Based on the experimental, analytical and FE simulation results, discussions will be made in Section 4.6. The key conclusions obtained from the study on the TCBC test will be summarized in Section 4.7.

## 4.1 TCBC Test

As reviewed in the Chapter 1 and Chapter 2 and confirmed in Chapter 3, material deformation in ISF is a localized deformation combined with tension, bending, and cyclic effect (SPIF) and compression (DSIF). Obviously, material formability can be influenced by the loading conditions. Under simple loading conditions, for example, material under low or negative stress triaxiality generally will reach higher material formability. And the existence of pure bending will affect the distribution of stress, the concave side of the

material will be under tensile stress while the concave side will be under compressive stress, the final fracture of the material depends on the severity of the damage created by the tensile stress on the convex side. The shearing effect can prevent the necking phenomenon, which is generally induced by the tensile effect. As a result, the material formability can be improved. Cyclic loading alone, on the other hand, has already been proved to be able to influence material deformation behaviour due to the Baushinger effect. The effect of these common loading conditions alone have been thoroughly investigated by the researchers using different material property testing method, as reviewed in Chapter 2. The obtained data, for example, the FLC curves, are widely used to describe material deformation behaviour in different material processing processes. In addition, the simplified and standardized testing methods provide a benchmark, based on which only the effect of the focused factor can be investigated independently while the effects of peripheral factors are minimized. For the ISF process, simplified testing methods representing the loading conditions in ISF process provide more insights into the deformation mechanism in ISF. Specifically, Eyckens et al. [45] investigated the TTS effect by performing the M-K test.

However, in the real material forming processes, loading conditions are generally more complicated and different combinations of different loading conditions lead to the final plastic deformation of the material. For example, the shear effect generally comes with tension and it will lower the tensile stress needed to reach the yielding point, thus creating localized deformation. The combination of the loading conditions and the magnitude of each loading condition will both affect the material deformation behaviour in the process.

The interaction between tension effect and bending effect was investigated by Morales et al. [89] using the Nakazima test. Furthermore, Emmens and von den Boogaard [48] adopted the continuous bending and tension test (CBT), in which the complicated loading conditions in SPIF were simplified into a two-dimensional problem. Each deformation mode, including tension, bending and cyclic effect, could be independently investigated by varying corresponding magnitude.

In ISF, the effect and existence of these deformation modes were mainly investigated by the ISF tests themselves by varying the process parameters [16, 53]. However, the existence of multiple deformation modes and complex contact conditions prohibits a systemic evaluation of the influence of individual deformation factors on the material deformation behaviour in ISF, especially in DSIF. For example, in ISF test, the conic shape has been widely used as the benchmark geometry and the maximum fracture depth

of the conic part is used as an indicator of the material formability. The larger the maximum fracture depth is, the higher the material formability can be. However, at different depths, the ratios of the tool radius to the geometry radius are also different. According to Silva et al. [84], material formability could also be affected by the ratio, which means the effect of the target factor cannot be individually investigated. In addition, changing one parameter may affect multiple loading conditions. For example, cyclic effect can be affected by changing the linear moving speed of the tools, which in turn creates an impact on the tensile effect. Moreover, material formability in ISF has already been reported to be affected by the toolpath [9, 235]. Different toolpath strategies have been adopted by different researchers to investigate material deformation behaviour in ISF process, which makes the test results hard to be compared. In conclusion, the ISF test itself is not sufficient in understanding the individual and combined effect of loading conditions on the ISF process.

The simplified testing methods, including the CBT test, provide an alternative investigation method into the material deformation in ISF. However, in the CBT test, the tool moving speed was set to be constant. The tool moving speed is a reflection of the cyclic effect in the ISF process, ignoring its variation may undermine the significance of its effect on the material deformation. In addition, the compression is ignored, making it impossible to investigate the DSIF process. An improvement of the test method is required for a more comprehensive understanding of the ISF process. Regarding to investigating the damage evolution in the material, the progressive deformation of ISF makes it difficult to directly observe the initiation and evolution of the damage in the material.

#### 4.1.1 Concept of the TCBC test

In the CBT test platform developed by Emmens and van den Boogaard [48], the specimen was stretched in the longitudinal direction while bent at a certain depth against a cylindrical roller, which moved cyclically along the specimen length direction, thus the material deformation under tension and bending with cyclic effect could be investigated. To accommodate the superimposed compression force from the additional tool employed in DSIF, in the newly developed TCBC test, another cylindrical roller is positioned against the bending roller to provide a compressive force from the other side of the specimen. The concept of the TCBC test is illustrated in Figure 4.1.

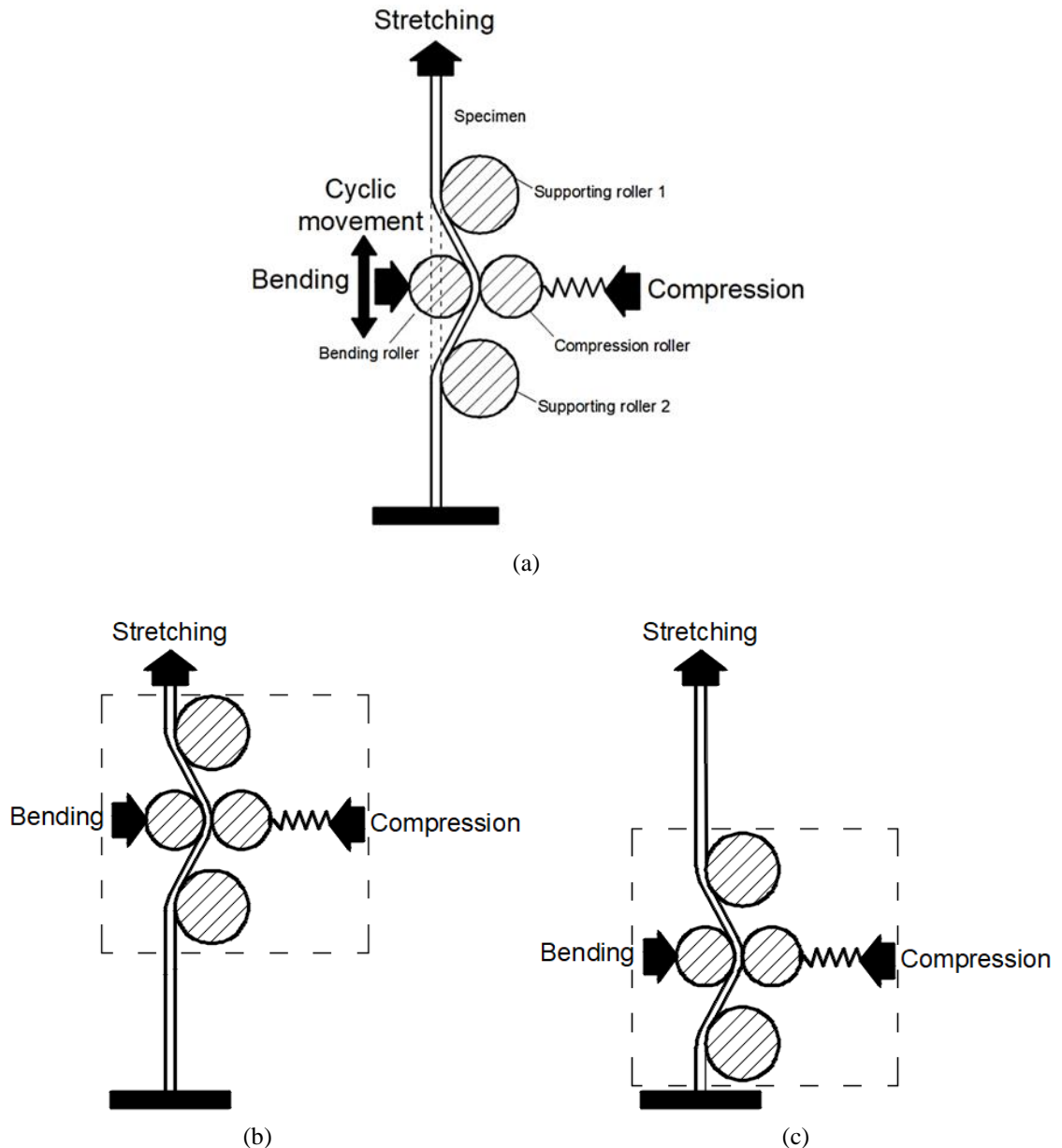


Figure 4.1 Schematic of the TCBC test: (a) simplified configuration of the TCBC test; (b) the bending and compression component moves to one side of the designed travelling path; (c) the bending and compression component moves to the other side of the designed travelling path

The compression roller is supported by cylindrical springs to provide compression force as well as to maintain the contact between the compression roller and the specimen. The length and stiffness of the springs can be adjusted thus the magnitude of the supporting force from the additional tool in DISF can be varied. In order to ensure the bending effect applied to the target zone and to maintain the presence of the bending effect, the specimen is kept in position by two supporting rollers positioned with a constant distance, as shown in Figure 4.1 (a). All four rollers, which forms a bending and compression component, move cyclically along the longitudinal direction of the specimen within the predefined travelling distance, a schematic of the component travelling to different locations during

the test is shown in Figure 4.1 (b) and (c). The cyclic movement will create localized deformation of the target zone on the specimen representing the deformation characteristic of cyclic loading in ISF.

#### 4.1.2 Design of the TCBC Testing Rig

Based on the concept of the TCBC test, a test rig has been designed and manufactured to perform the experiment. The developed rig is shown in Figure 4.2, consisting of two specially designed components, a loading device and a motor controlling system.

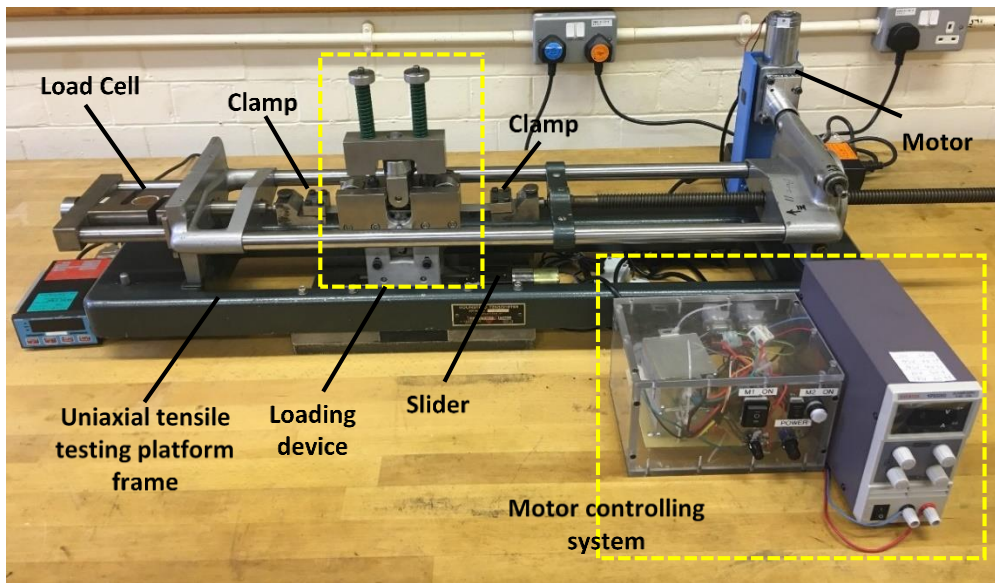


Figure 4.2 Key components of the TCBC test rig

Various loadings conditions can be applied onto the specimen by using the loading device. The loading device is mounted on a uniaxial tensile test platform so that its stiffness and position accuracy can be guaranteed. Both ends of the specimen are clamped and the specimen is stretched from one end by the movement of the linear screw mechanism driven by a DC motor.

Bending and compression loadings onto the specimen are applied by the loading device in which two cylindrical rollers, bending and compression rollers, positioned against each other with a gap. A CAD schematic of the loading device is shown in Figure 4.3. The specimen can be inserted through the gap and bent from below by the bending roller and compressed from above by the compression roller. The compressive force can be varied by adjusting the length of the springs with the compression adjustment cap. The bending depth can be adjusted by another screw set beneath the bending roller. By tightening the screws on both sides of the device, the bar connecting the two screws will be raised, pushing the bending roller against the specimen to certain depth. All the rollers are

designed to be free to rotate around its own axis to reduce friction. The loading device can move along a slider, which is mounted on the base of the uniaxial tensile test platform. The slider is driven by another DC motor. On both ends of the slider, a micro switch is placed, once the loading device hits the switch, the rotating direction of the DC motor will be reversed, creating a cyclic movement of the loading device. The speed and the starting direction of both motors can be controlled by the controller.

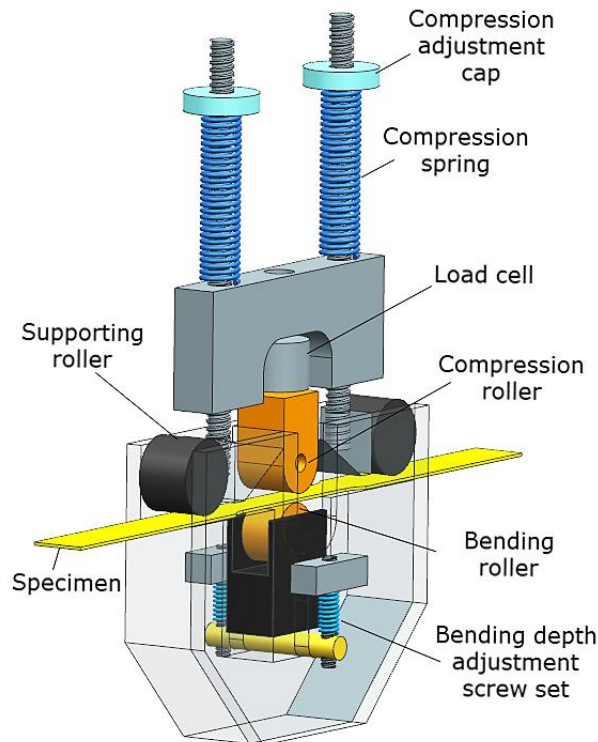


Figure 4.3 CAD schematic of the loading device

In summary, by using the developed TCBC test rig, the stroke speed of the slider, the tensile speed, the bending depth and the compression can be independently controlled and varied in the experiment. These correspond to the effect of each deformation mode in DSIF, including cyclic effect, tension effect, bending effect and compressive effect. A load cell is installed on the left-hand side of the uniaxial tensile test platform so that the tensile force during the test can be measured and recorded.

## 4.2 Theoretical Analysis of the TCBC Test

Material deformation can be determined by the stress and strain states during the manufacturing process. Theoretical analysis of the targeted deformation area can provide a detailed and explicit description of the stress and strain distributions of the material under deformation, which in turn enables the formability analysis. Due to the cylindrical geometry of the rollers, the contact zone between the specimen and the bending roller is

only in partial contact with the compression roller, as shown in Figure 4.4 (a). According to the contact conditions between the rollers and the specimen, the testing region of the specimen in the TCBC test,  $L$ , can be divided into three zones, the single contact zone, the dual contact zone and the uniaxial tensile zone, as shown in Figure 4.4 (b). For the simplicity of the theoretical model, the following assumptions are made:

- The bending depth is small so that the single contact zone is comparatively much smaller than the dual contact zone, therefore the single contact zone can be ignored;
- For a material with good ductility, the thickness reduction of the specimen upon fracture is considerably large and the specimen is thin so that the stress variation across the thickness direction can be ignored [236];
- The contact stresses in the contact zone on both sides of the specimen are uniformly distributed.

To obtain the stress distribution of the deformed area, an infinitely small element is extracted from the dual contact area of the specimen, as shown in Figure 4.4 (a). The dimension of the element in the lateral direction is equal to the width of the specimen at the deformation point while the dimension in the longitudinal direction is assumed to be infinitely small. The dimensions to define the element and the stress components applied onto the element are shown in Figure 4.4 (c). From the force equilibrium of the element in the radial direction of the curved specimen, the following equation can be obtained:

$$\begin{aligned} & \left[ \sigma_{\varphi} \cdot (t + dt) \cdot (w + dw) + (\sigma_{\varphi} + d\sigma_{\varphi}) \cdot t \cdot w \right] \cdot \sin \frac{d\varphi}{2} + \\ & \sigma_c \cdot (r_t + t) \cdot d\varphi \cdot \frac{2w + dw}{2} = \sigma_t \cdot r_t \cdot d\varphi \cdot \frac{2w + dw}{2} \end{aligned} \quad (4-1)$$

By ignoring higher-order terms, Equation (4-1) is reduced to:

$$\sigma_{\varphi} \cdot (2t \cdot w + t \cdot dw + w \cdot dt) + d\sigma_{\varphi} \cdot t \cdot w = \left[ \sigma_t \cdot r_t - \sigma_c (r_t + t) \right] \cdot (2w + dw) \quad (4-2)$$

According to the volume conservation law in plastic deformation,

$$\frac{dw}{w} + \frac{dt}{t} + d\varepsilon_l = 0 \quad (4-3)$$

Substituting Equation (4-3) into Equation (4-2), it can be obtained that,

$$\sigma_{\varphi} \cdot (2 - d\varepsilon_l) + d\sigma_{\varphi} = \left[ \sigma_t \cdot \frac{r_t}{t} - \sigma_c \left( \frac{r_t}{t} + 1 \right) \right] \cdot \left( 2 + \frac{dw}{w} \right) \quad (4-4)$$

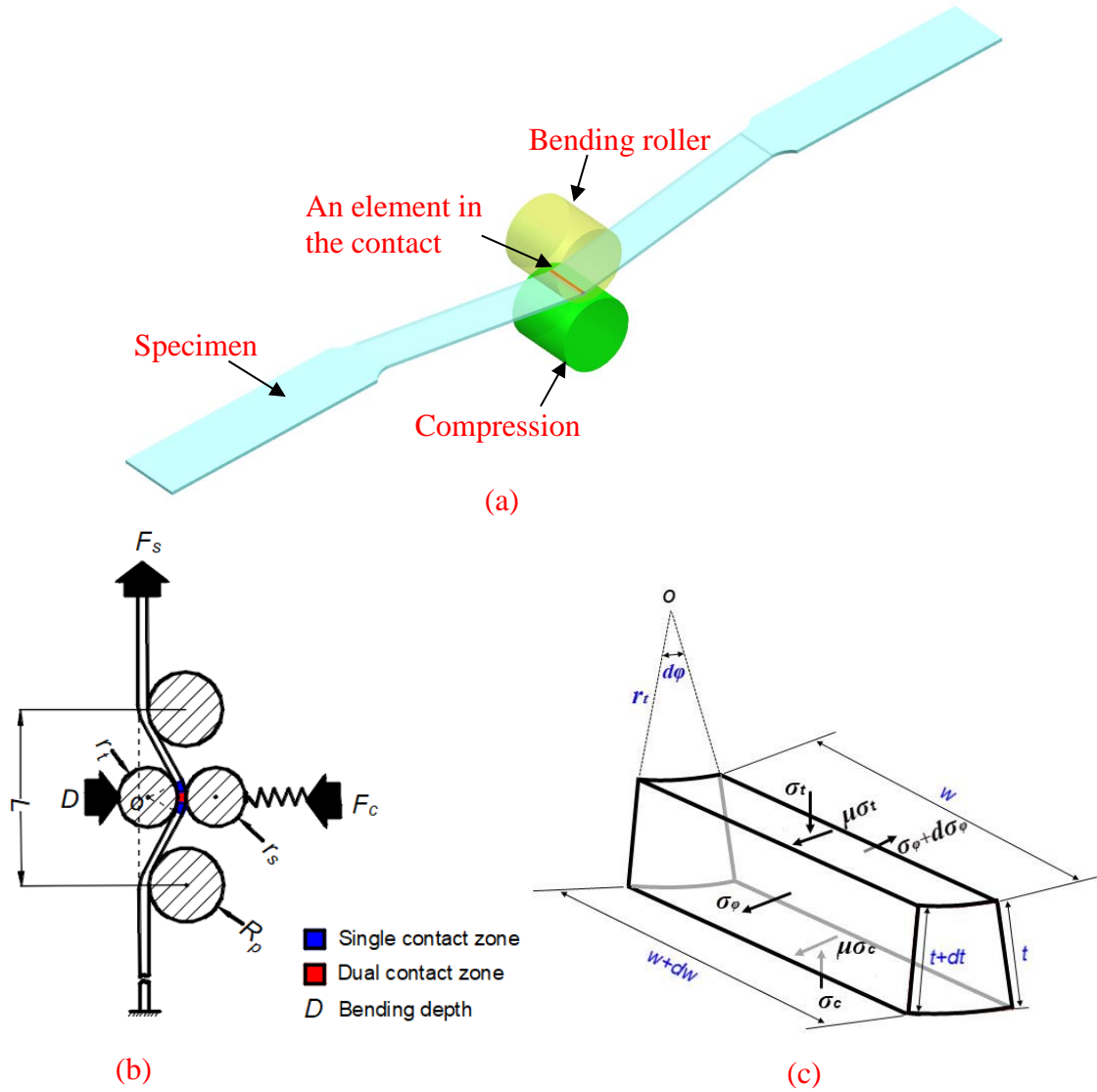


Figure 4.4 Schematic of the simplified theoretical analysis model: (a) the selected element in contact region for analysis; (b) schematic of the contact conditions in TCBC test; (c) stress components applied onto the selected element

The radius of the bending roller and the compression roller of the developed TCBC rig is  $r_t = 10\text{mm}$  while the thickness of the specimen is generally in the range of 1.0~1.5 mm. As a result,  $\frac{r_t}{t}$  is much larger than 1 while at the same time  $\frac{dw}{w}$ ,  $d\epsilon_l$  and  $\sigma_\phi$  are infinitely small, therefore Equation (4-4) can be further simplified as,

$$\sigma_\phi = (\sigma_t - \sigma_c) \cdot \frac{r_t}{t} \quad (4-5)$$

Combining the Tresca yielding criterion,  $\sigma_\phi + \sigma_t = \sigma_s$ , with Equation (4-5), the relationship between the stress components and dimensions of the selected element can be obtained as,

$$\sigma_t = \frac{\sigma_s + \sigma_c \cdot \frac{r_t}{t}}{1 + \frac{r_t}{t}} \quad (4-6)$$

$$\sigma_\varphi = \frac{\frac{r_t}{t}}{1 + \frac{r_t}{t}} (\sigma_s - \sigma_c)$$

Using these equations, the relationship between the normalized compressive stress  $\frac{\sigma_c}{\sigma_s}$ , the ratio of tool radius to the sheet thickness  $\frac{r_t}{t}$  and the normalized tensile stress  $\frac{\sigma_\varphi}{\sigma_s}$  can be obtained, as shown as a 3D plot in Figure 4.5 (a) and a top view of the 3D plot in Figure 4.5 (b).

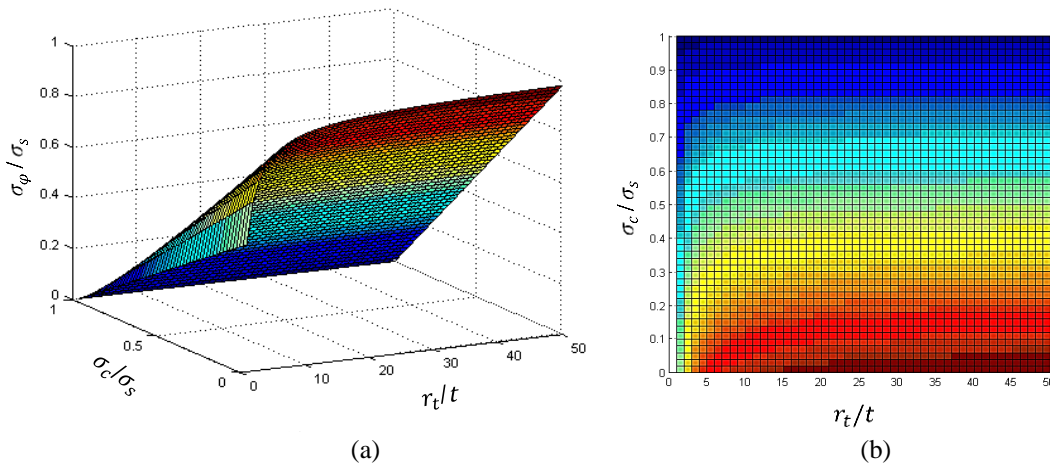


Figure 4.5 Theoretical analysis results of the influence of the key parameters on the tensile stress: (a) 3D plot; (b) top view of the 3D plot

According to the results reported by Fang et al. [60] and Emmens and van den Boogaard [48], the fractures of the deforming sheets in SPIF process and CBT test were all caused by material tension. In addition, according to the Tresca yielding criterion and current design of the TCBC test rig, tension is essential to create localized plastic deformation in the TCBC test. Therefore, the tensile stress in the longitudinal direction of the tested specimen can be considered as a driving factor of the material deformation in the TCBC test. From Figure 4.5 (a) it is evident that the higher the compression stress is, the smaller tensile stress is required to reach the plastic deformation of the material in TCBC test. Viewing the variation of the tool radius/sheet thickness ratio in Figure 4.5 (b), its effect on the required tensile stress for plastic deformation, shown by the variation of colors, is less obvious. However, when the tool radius/sheet thickness ratio is less than 15, it is clear

that this ratio has an effect on the tensile stress required for reaching the plastic deformation.

Bending effect is not explicitly considered in the theoretical analysis model, mainly due to neglecting the thickness effect in the derivations. However, the bending roller radius/sheet thickness ratio can still be used as an indicator of the bending effect due to the existence of the curvature of the analysed element. The effect of the bending varies depending on the magnitude of the ratio. When the radius of the bending roller becomes too large, the bending effect is minimised and the sheet material is mainly under compression and tension. An obvious transition of the significance of the bending effect can be seen in Figure 4.5 (b), showing the normalized tensile stress variations under varying bending radius/sheet thickness ratio and normalized compressive stress. When the bending effect is strong by using a bending roller with a smaller radius, the tensile stress required for plastic deformation is obviously smaller than that using a bending roller with a larger radius. Furthermore, when the bending effect is reduced to a certain level, the bending deformation would no longer contribute to the tensile stress reduction and the tensile stress remains almost constant.

In addition, a competition of the dominance on the material deformation also exists between the compressive effect and the bending effect. As shown in Figure 4.5 (b), when the compressive stress is comparatively small, the bending effect is more dominant, while when the compressive stress is increased, the bending effect becomes less influential.

In the developed test rig, the designed stroke speed  $v_s$  is much higher than the tensile speed  $v_t$ , the time needed for the rollers to travel through the contact zone in one loading cycle can be calculated as,

$$\Delta T = \frac{r_t \cdot \varphi}{v_s} \quad (4-7)$$

Thus the strain increment of the contact zone in this time period can be determined as,

$$\Delta \varepsilon_l = \frac{v_t \cdot \Delta T}{r_t \cdot \varphi} = \frac{v_t \cdot \Delta T}{v_s \cdot \Delta T} = \frac{v_t}{v_s} \quad (4-8)$$

The frictional effect due to the contact between the rollers and the specimen is ignored based on the fact that the rollers are not fixed thus free to rotate, resulted in small rolling contact friction. In the longitudinal direction of the specimen, the force equilibrium of the element without considering frictional force can be established as,

$$\sigma_{\varphi} \cdot (t + dt) \cdot (w + dw) \cdot \cos \frac{d\varphi}{2} = (\sigma_{\varphi} + d\sigma_{\varphi}) \cdot t \cdot w \cdot \cos \frac{d\varphi}{2} \quad (4-9)$$

By simplification and combining Equation (4-3) and Equation (4-9), it can be obtained that,

$$-d\varepsilon_l = \frac{d\sigma_{\varphi}}{\sigma_{\varphi}} \quad (4-10)$$

It can be solved as,

$$\varepsilon_l = \ln(C \cdot \sigma_{\varphi}) \quad (4-11)$$

where  $C$  is an integration constant.

Combining Equations (4-6), (4-8) and (4-11), it can be obtained that,

$$\ln \frac{\sigma_{\varphi_{n+1}}}{\sigma_{\varphi_n}} = \frac{v_t}{v_s} \quad (4-12)$$

where  $n$  is the number of loading cycles that the material has been subjected to during the TCBC test. From Equation (4-12) it can be concluded that, the higher the difference between the tensile speed and the stroke speed is, the greater difference of the tensile stresses exists between the two ends of the dual contact zone. If the speed difference is large enough, when the stroke speed  $v_s$  is considerably small or  $v_t$  is reasonably high, the tension under cyclic bending and compression loading condition will degenerate to a simple tensile loading condition, therefore material formability could not be improved. In general, a higher stroke speed and lower tensile speed will be beneficial to the formability enhancement of the material in the TCBC test.

## 4.3 Design of the Experiment and Testing Procedures

### 4.3.1 Design of the experiment

The experiment was conducted in three stages. In the first stage, in order to understand the effect of the TCBC loading conditions on the material formability enhancement, the maximum elongations of the specimens under different combinations of the loading conditions were compared, including uniaxial simple tension, tension under cyclic compression (TCC), tension under cyclic bending (TCB). The schematics of these loading conditions are shown in Figure 4.6.

As can be seen from Figure 4.1, to reflect the influence of each loading condition, five parameters can be varied during the TCBC test. These are the compressive force from the compression roller, the bending depth from the bending roller, the stroke speed of the slider, the pulling speed of the linear screw, and the specimen thickness. Other parameters of the test rig in these tests were kept the same. The maximum elongations of the specimens and displacement-force curves were measured and recorded.

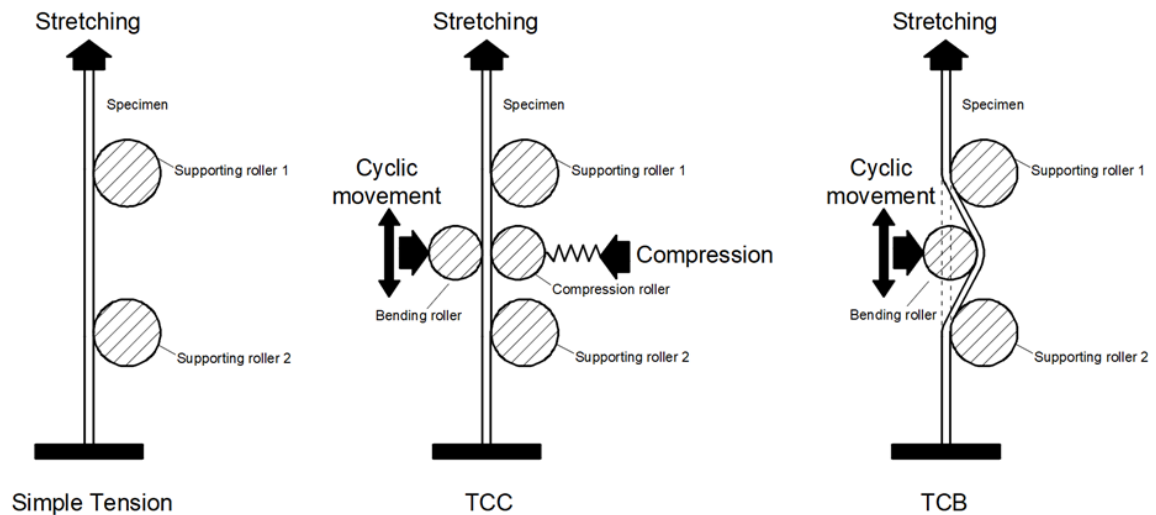


Figure 4.6 Schematics of different combinations of loading conditions

To accommodate the dimensions of the test rig, a specimen based on the ASTM-E8 standard [126] was designed, the dimensions are shown in Figure 3.3. Material AA5251-H22 was used in the first stage of the experiment.

In the second stage of the experiment, the effect and significance of individual parameters on the maximum elongation of the specimen in the TCBC test were investigated. The tested ranges of the parameters are shown in Table 4.1. The parameter variation ranges were decided by taking into consideration of the dimensions of the test rig, the characteristics of the motors and the equivalent process parameter values commonly used in ISF. For the compressive force, according to Lu et al. [30], for material AA7075-T6, which had a high yielding strength of 380MPa, material formability dropped when the supporting force from the rear tool was increased to 480N in DSIF test. According to the uniaxial tensile test reported in Chapter 3, the ultimate tensile strength for material AA5251-H22 was 162MPa. Considering that the introduction of the supporting force in DSIF was to improve material formability and the area of the contact zone between the roller and the specimen, the highest compressive force was limited to be 900N. While the lowest value of the compressive force investigated was set to be 150N in order to cover a reasonable range. As for the bending depth, the highest bending depth was set to be

slightly smaller than the radius of the bending roller, which was 10mm. The lowest bending depth was decided when bending of the specimen was noticeable, which was 3mm. The stroke speed and the tensile speed was decided based on the configuration of the corresponding motor. In order to investigate the influence of the material properties on the formability in this stage of experiment, two types of materials with distinct flow stress properties were tested, the aluminium alloy AA5251-H22 and AA6082-T6. The flow stress curves of the two materials obtained from the uniaxial tensile tests are shown in Figure 3.6.

Table 4.1 Variation ranges of test parameters in the second stage TCBC experiment

Tested parameters	Parameter Variation Range	
	AA5251-H22	AA6082-T6
Compressive force	150-900N	600-1200N
Bending depth	3-9mm	3-9mm
Stroke speed	0.5-2.5mm/s	0.5-2.5mm/s
Tensile speed	1.6-3.2mm/min	1.6-3.2mm/min
Specimen thickness	1.0, 1.2, 1.5mm	1.0, 1.5mm

Considering the number of the parameters investigated, a full factorial experiment design would be resource-and-time-consuming. To minimize the number of the tests of experiment to be conducted and at the same time to ensure that the experimental results provide important insights into the interactive effects of the tested parameters, Taguchi Design of Experiments method has been applied to optimize the design of test runs. Since material properties can be reflected by several factors, for example yielding stress, work-hardening coefficient and ultimate tensile strength, the material type was not chosen to be a factor in the second stage TCBC experiment.

The tests of the materials AA5251-H22 and AA6082-T6 were conducted separately based on the Taguchi Design of Experiments. Details of the tests of AA5251-H22 by the mixed-level Taguchi design of the experiments are shown in Table 4.2. A L18 orthogonal array was generated with the help of the statistical analysis software Minitab 17 [211]. A similar mixed-level Taguchi design of the experiments for AA6082-T6 was also created according to the levels defined in Table 4.1, as shown in Table 4.3.

Table 4.2 Mixed-level Taguchi design of the experiments for AA5251-H22

<b>Test number</b>	<b>Compressive force(N)</b>	<b>Bending depth (mm)</b>	<b>Stroke speed (mm/s)</b>	<b>Tensile speed (mm/min)</b>	<b>Thickness (mm)</b>
1	150	3	0.5	1.6	1.0
2	150	6	1.5	2.4	1.2
3	150	9	2.5	3.2	1.5
4	300	3	0.5	2.4	1.2
5	300	6	1.5	3.2	1.5
6	300	9	2.5	1.6	1.0
7	450	3	1.5	1.6	1.5
8	450	6	2.5	2.4	1.0
9	450	9	0.5	3.2	1.2
10	600	3	2.5	3.2	1.2
11	600	6	0.5	1.6	1.5
12	600	9	1.5	2.4	1.0
13	750	3	1.5	3.2	1.0
14	750	6	2.5	1.6	1.2
15	750	9	0.5	2.4	1.5
16	900	3	2.5	2.4	1.5
17	900	6	0.5	3.2	1.0
18	900	9	1.5	1.6	1.2

Table 4.3 Mixed-level Taguchi design of the experiments for AA6082-T6

Test number	Compressive force(N)	Bending depth (mm)	Stroke speed (mm/s)	Tensile speed (mm/min)	Thickness (mm)
1	600	3	0.5	1.6	1.0
2	600	6	1.5	2.4	1.0
3	600	9	2.5	3.2	1.0
4	900	6	0.5	1.6	1.0
5	900	9	1.5	2.4	1.0
6	900	3	2.5	3.2	1.0
7	1200	3	0.5	2.4	1.0
8	1200	6	1.5	3.2	1.0
9	1200	9	2.5	1.6	1.0
10	600	9	0.5	3.2	1.5
11	600	3	1.5	1.6	1.5
12	600	6	2.5	2.4	1.5
13	900	9	0.5	2.4	1.5
14	900	3	1.5	3.2	1.5
15	900	6	2.5	1.6	1.5
16	1200	6	0.5	3.2	1.5
17	1200	9	1.5	1.6	1.5
18	1200	3	2.5	2.4	1.5

As a useful statistical method, Taguchi Design of Experiments provides considerably robust response for a wide range of investigated parameters from a small number of experiments. However, some of the intermediate values are ignored and a trend of the effect of the parameter based on the Taguchi Design of the Experiments may only be partially correct. In ISF, bending and compression effects are considered to be the most

important and the interaction of these two deformation mechanisms affects the material formability in ISF considerably. To better understand the influence of these two mechanisms, in the final stage of the experiment, additional two sets of experiments were performed. In the first set of the final stage of the experiments, the influence of the compression force was investigated by only varying the value of the compressive force. While in the second set of the final stage of the experiments, the bending depth and specimen thickness were adjusted to investigate the bending effect. Other parameters remained unchanged in both sets of tests in the final stage of the experiments.

### 4.3.2 Experimental procedures

Before each test to commence, the specimen was inserted between the rollers and bent by the bending roller in the middle of the specimens to the tested bending depth shown in Table 4.1, 4.2 and 4.3. Then the compressive force was applied by adjusting the compression springs. Both ends of the specimens were then clamped. The speed of the both motors was adjusted to the tested values and could be switched on simultaneously. The specimen was deformed and stretched until fracture occurred. The load-displacement curve during the test was measured and recorded by the load cell on the fixed end of the specimen. The maximum elongation of the specimen was also measured as an indicator of the material formability in each test. To ensure the repeatability of the test results, each set of the test was performed twice to ensure the robustness of the results and an average value of the maximum elongations obtained was calculated. If the discrepancy between the maximum elongations obtained in the first two trials exceeded 5%, a third test was conducted and the two values of similar maximum elongations was used to calculate the average value of the maximum elongation for the test.

## 4.4 Experimental Results

### 4.4.1 Comparison of tested specimens under different loading conditions

#### 4.4.1.1 Maximum elongations of the tested specimens

In the first stage of the experiment, a comparison of the maximum elongation values between the tests have been made. During the first stage tests, the tensile speed and the stoke speed were fixed to be 2.4 mm/min and 1.5 mm/s respectively. The bending depth was adjusted to be 9 mm and the compression force was set to be 900N in the TCC, TCB and TCBC tests, if the parameters were applicable to each type of the tests. A comparison of the final length of the specimens after test under different loading conditions is shown

in Figure 4.7. In the uniaxial tensile test, the averaged maximum elongation was 10.2 mm, while for the TCBC test, the averaged maximum elongation almost reached 70 mm. Compared to the uniaxial tension condition, TCC and TCB achieved a significant increase of the maximum elongation. The TCBC condition achieved the highest formability enhancement among all tests, in which the tested region of the specimen was elongated almost as twice as its original effective length.

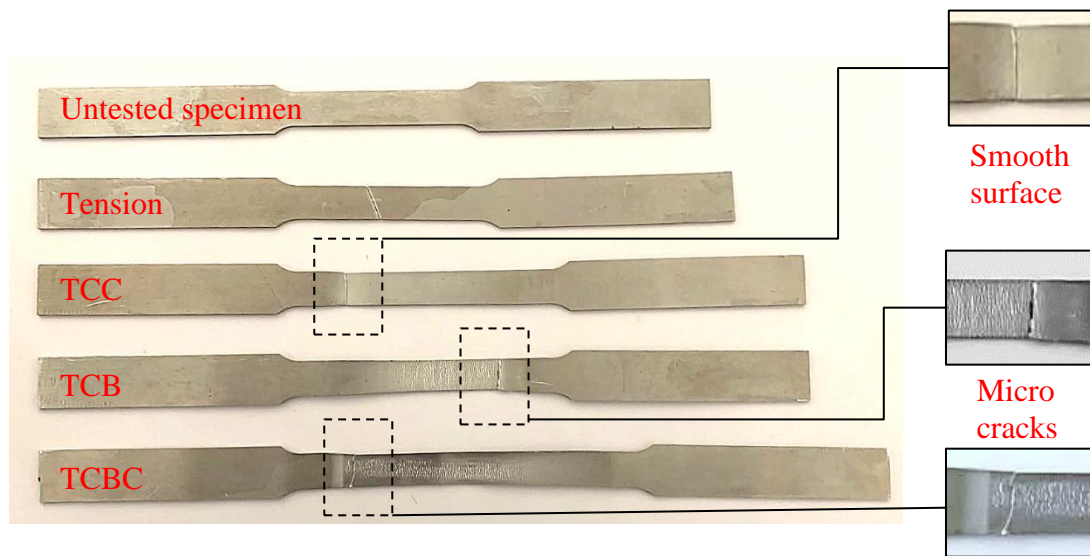


Figure 4.7 Elongation of tested specimens under different loading conditions

#### 4.4.1.2 Fracture behaviours of the tested specimens

The fracture behaviour of the specimens was also different under different test conditions, as shown in Figure 4.7. In the simple uniaxial tension test, the crack occurred at an angle to the lateral direction of the specimen. While in other tests, the cracks were all parallel to the lateral direction. The difference of the crack directions was resulted from the different stress distribution in the deformation zone of the specimen induced by different loading conditions. In the simple uniaxial tension test, the whole central target zone was under uniform tensile stress and the angle of the crack direction matched the orientation of the maximum shearing stress plane. While in the TCC, TCB and TCBC tests, the introduction of compression / bending or both promoted localized plastic deformation and confined the deformation zone to a small area within or near the contact zone. As a result, the shift of the orientation of the crack indicated a change to localized deformation in the specimen under TCC, TCB and TCBC loading conditions.

In addition, as shown in Figure 4.7, multiple micro cracks can be observed on the convex surface of the specimens due to bending effect under TCB and TCBC conditions, however the concave surface shows no crack. Under simple uniaxial tension and TCC loading

conditions, no evident trace of micro cracks is observed on either side of the specimens before the final fracture. This phenomenon indicates that the effect of bending on the deformation behaviour during bending-related processes of TCB and TCBC. The existence of bending leads to higher stress triaxiality and tensile stress in the longitudinal direction of the specimen, which promote the development of micro cracks on the convex surface of the specimen. However, the existence of compression strengthens the localized deformation in the contact area of the specimen thus significantly reduces the tensile stress required for the plastic deformation. As a result, instead of undergoing a rapid evolution of the cracking, as occurred in the uniaxial tensile test, the propagation of the micro cracks is suppressed by compression in the TCBC test. The micro cracks continue existing and increasing while the deformation process progresses until the final fracture occurs.

#### 4.4.1.3 Force-displacement histories of the tests

The tensile force-displacement histories recorded during the tests are shown in Figure 4.8. Contrary to the maximum elongation each test produced, the force needed was the highest for the simple uniaxial tension test but the lowest for the TCBC test. While for the TCC and TCB test, the tensile forces required were almost equal for the same degree of deformation.

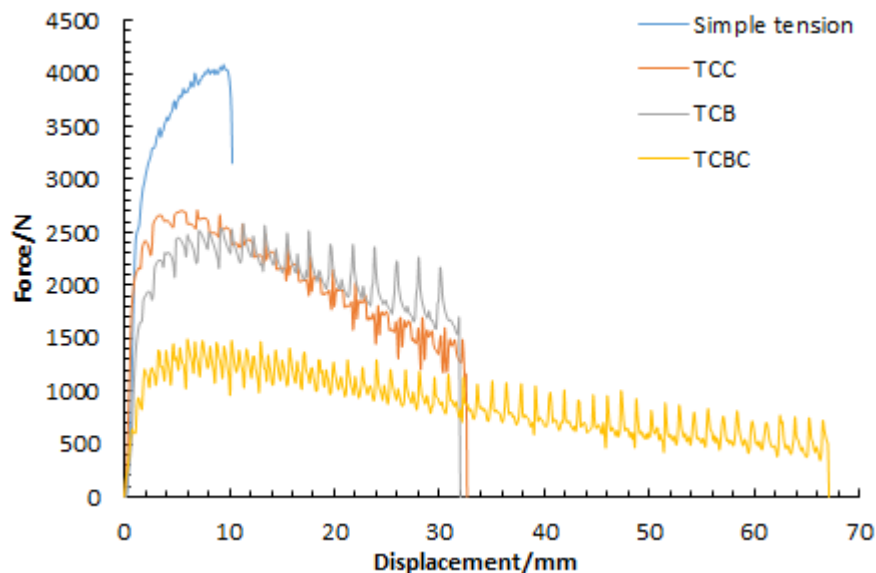


Figure 4.8 Displacement-force curves recorded from tests under different loading conditions

Obvious oscillations of the forces in the TCC, TCB and TCBC tests could be observed in Figure 4.8, which appeared in certain patterns, corresponding to the cyclic movement of the rollers. In addition, in terms of the evolution of the stretching force, the force change

during the test in the TCBC test was more moderate overall when compared with that in the TCC and TCB tests.

#### 4.4.2 Effects of individual process parameters in TCBC test

##### 4.4.2.1 Significance of individual parameters

The recorded maximum elongation in each test of the experiment was regarded as the response in the Taguchi Design of Experiments method. With the help of the software Minitab 17 [211], the influence of each factor on the maximum elongation in the TCBC test, representing the formability of the material, was analysed. Since only one response has been defined in the Taguchi Design of the Experiments, only signal-to-noise (S/N) ratio and means of the response could be used for the analysis of the significance of the factors. In the mean value analysis, the p-value is used as an indicator to determine the statistical significance of the investigated factors. For a significance level of 0.1 (confidence level of 90%) in testing AA5251-H22, the compression (p-value=0.045), bending depth (p-value=0.062) and the stroke speed (p-value=0.072) were the most significant factors affecting the maximum elongation, while the tensile speed (p-value=0.105) and the specimen thickness (p-value=0.286) were not important. The statistical analysis result based on the experiments in this study was quite different to the observation in the CBT test reported by Emmens and van den Boogaard [48], in which the bending depth and tensile speed, representing the actual bending effect in SPIF, were the most important factors. While in testing AA6082-T6 in this study, the p-values were all greater than 0.1, which meant none of the investigated factors was found to have a significant effect on material formability in the TCBC test at a significance level of 0.1.

##### 4.4.2.2 Relative significance of individual parameters

The relative significance of the investigated factors can be reflected by ranks based on the Delta statistics in Taguchi method [211]. In another word, for the investigated factors, their significance against each other can be obtained by comparing the variation (the Delta) of the chosen target for analysis. The target is affected by the factors and it is chosen based on the purpose of the analysis. In this study, the focus is to maximize the elongation of the specimen. Therefore, the mean value of the maximum elongation was chosen to be the target for the analysis of relative significance of the tested factors.

As shown in Figure 4.9, in the investigated variation ranges of the factors, all factors for both types of materials had a main effect on the means. However, it was obvious that

material AA5251-H22 was far more sensitive to the variation of the five factors investigated than that of AA6082-T6. The maximum and minimum values of the averaged maximum elongation achieved in the experiment were marked in Figure 4.9. The minimum difference of the mean of means for material AA5251-H22 was 14.9% and the maximum difference was 86.3%; while the maximum difference for material AA6082-T6 was only 18.9%. By comparing formability enhancement achieved by SPIF between material AA5052 and AA1100, Ai et al. [82] concluded that a material with lower work-hardening but higher ductility was more easily influenced by the SPIF process parameters. This observation supported the findings obtained in the TCBC test in this study. A possible explanation could be that among all the deformation mechanisms, a single mechanism may dominate not just because varied process parameters, as pointed out by Eyckens et al. [69] and by Maqbool and Bambach [62], but also due to the difference in material properties. For a material with greater work-hardening, tension effect dominated over bending and shearing. As a result, for material AA6082-T6, the deformation behaviour was not significantly influenced by the factors applied in the TCBC test.

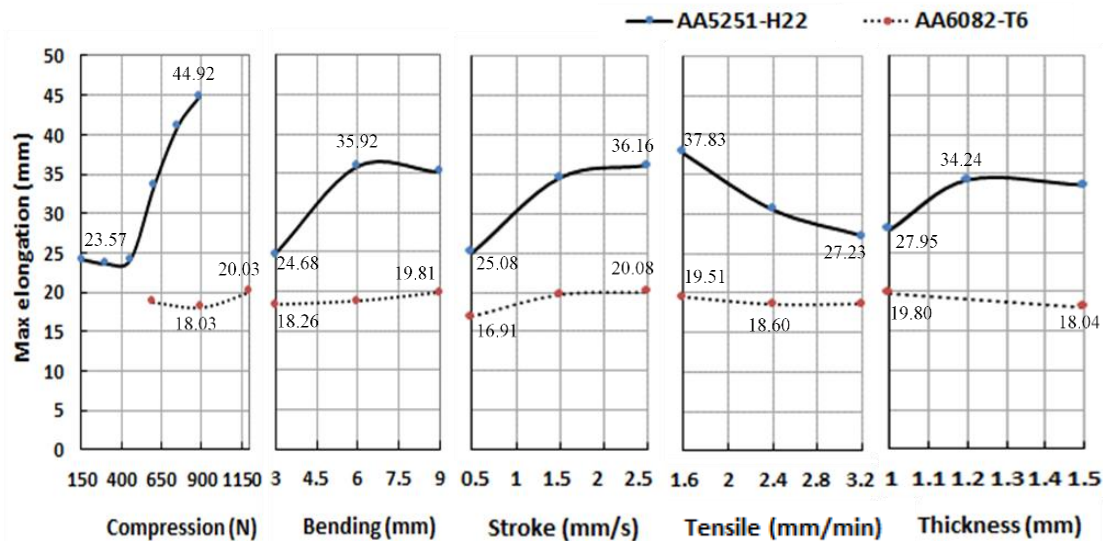


Figure 4.9 Main effect plot for the factors for the mean in TCBC test

The relative significance between individual factors also varied for the same type of material. For material AA5251-H22, as shown in Figure 4.9, the compression showed the largest variation between all the levels, meaning the greatest effect on the maximum elongation, while bending depth was the second and stroke speed was the third most important factor. Tensile speed and specimen thickness were still the least significant factors, a similar observation with the analysis made by using the p-value analysis. For

material AA6082-T6, stroke speed was the most influential factor, and compression force was the second most important factor, while specimen thickness, bending depth and tensile speed were the least important factors.

#### 4.4.2.3 Significance of individual parameters at different levels

The slope of the lines in Figure 4.9 can be used to compare the relative magnitude of the effect of each factor at different levels. For material AA5251-H22, for compression, no significant effect was shown between 150 N and 450 N while significant effect was displayed when the compression force was increased to 750 N. The trend started to change from increase to decrease when the compression was further increased to 900 N. For bending depth, increasing it from 3mm to 6mm produced obvious effect on the maximum elongation while when it was further increased, much less effect could be seen, this observation was the same as predicted by the theoretical analysis model presented in Section 4.2. A similar trend was also observed for the stroke speed. For the tensile speed, an obvious negative effect was found when it was increased from 1.6 mm/min to 3.2 mm/min. The specimen thickness also produced insignificant effect when the thickness was increased from 1.2 mm to 1.5 mm.

For material AA6082-T6, both bending depth and stroke speed had a positive effect on the maximum elongation through the whole investigated variation ranges of these two factors, while specimen thickness showed a slightly negative effect. Tensile speed firstly showed a slightly negative effect when increased from 1.6 mm/min to 2.4 mm/min, however when it was further increased to 3.2 mm/min, the effect of tensile speed became insignificant. Increasing the compression from 600 N to 900 N led to a slight reduction of the maximum elongation, while further increasing it to 1200 N, an increase of the maximum elongation was observed. A similar trend of minor drop in the maximum elongation could also be observed when increasing the compression from 150 N to 300 N for material AA5251-H22.

#### 4.4.3 Investigation into the compression and bending effect

The second stage experimental results provided evidences that the compression force and the bending depth were the most influential factors in the TCBC test for material AA5251-H22. In addition, bending effect was not only affected by the bending depth, but also by the specimen thickness. Further evaluation by the full factorial design of the experiments was conducted to investigate the effect of these two deformation modes.

#### 4.4.3.1 Compression effect

In this test, all the factors were fixed except for the compression. The specimen used had a thickness of 1.5mm, the bending depth was set to be 9mm, the stroke speed and the tensile speed were maintained as 1.5 mm/s and 2.4 mm/min respectively. A greater range of the compression force varying from 150 N to 1500 N was investigated in order to obtain a more comprehensive understanding of the effect of compression on the material formability in the TCBCB test.

The relationship between different values of the compression and the obtained maximum elongations is shown in Figure 4.10. Error bars were marked in Figure 4.10 to show the level of variance in the test results. It is obvious that maximum elongations obtained were quite stable, which proved the repeatability of the test rig.

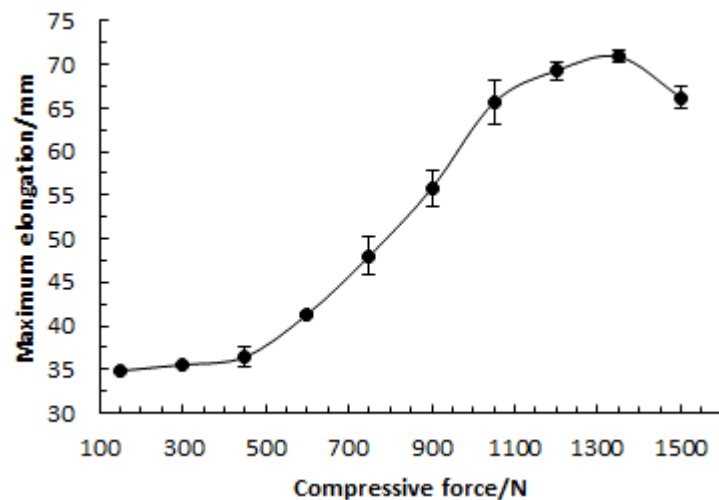


Figure 4.10 The influence of compression on the maximum elongation in TCBC

A different trend of the results from the Taguchi Design of the Experiments results can be observed, in which compression forces of less than 900 N were investigated. The compression force firstly had a positive effect on the maximum elongation before it reached 1300 N while an adverse trend occurred when the compression force was further increased to 1500 N.

An explanation to the shape of the curve can be made by comparing the fracture locations of the tested specimens. In these tests, when the compression was large enough, fracture occurred at a location where the bending and compression rollers started to switch the cyclic movement direction. When the compression was moderate, the plastic deformation in the contact zone could be shared by a large area to compensate for the tension effect. However, when the compression force was large enough, the contact area yielded easily by compression and created a weak zone over a short period of time of cyclic loading.

This observation corresponds to the finding from the theoretical analysis presented in Section 4.2 that the tensile speed has an adverse effect on the maximum elongation of the specimen. If the tensile speed is set to infinitely small, the whole TCBC process is transformed to a cyclic rolling process so that the deformation can be extremely large without the occurrence of fracture.

#### 4.4.3.2 Bending effect

Different from the compression effect, which is only determined by the magnitude of the compression force, bending effect from a static point of view can be affected by the bending roller radius, bending depth and the specimen thickness. According to Schrader and Elshennawy [237], the bending effect can be affected by the tool radius, blank thickness and bending angle in their study. In the TCBC test in this study, the diameter of the rollers is kept to be 10mm and the bending angle is determined by the bending depth. Therefore the bending effect in the TCBC test is affected by two factors, the thickness of the sheet blank and the bending depth. The larger the bending depth and the specimen thickness are, the greater the bending effect is.

Four sets of the further experiment were conducted. In the first two sets of the experiment, the compression was maintained to be 900 N and the material thickness was 1.5 mm. In the first set, the bending depth was varied at 0 mm, 3.0 mm, 6.0 mm and 9.0 mm respectively. In the second set of the tests, the thickness was varied to be 1.0 mm, 1.2 mm and 1.5 mm respectively. In the last two sets of the tests, the compression was set to be zero and bending depth was set to be 9 mm. The variation of the specimen thickness was the same as that in the first two sets of the tests. The stroke speed and the tensile speed were fixed to be 1.5 mm/s and 2.4 mm/min respectively. The relationship between the bending depth/specimen thickness and the maximum elongation of the specimen is shown in Figure 4.11 and error bars were marked. As can be seen in Figure 4.11 (a), within the investigated variation range of the bending depth, an obvious trend of enhanced maximum elongation could be observed when the bending depth was increased, with or without the compression effect. For different specimen thicknesses, a different trend was observed when tested with or without the compression effect. As shown in Figure 4.11 (b), when no compression force was applied, increasing the specimen thickness from 1.0 mm to 1.2 mm then to 1.5 mm only achieved a limited increase of the maximum elongation. While when a greater compression of 900 N was applied, the maximum elongation increased significantly first then dropped considerably.

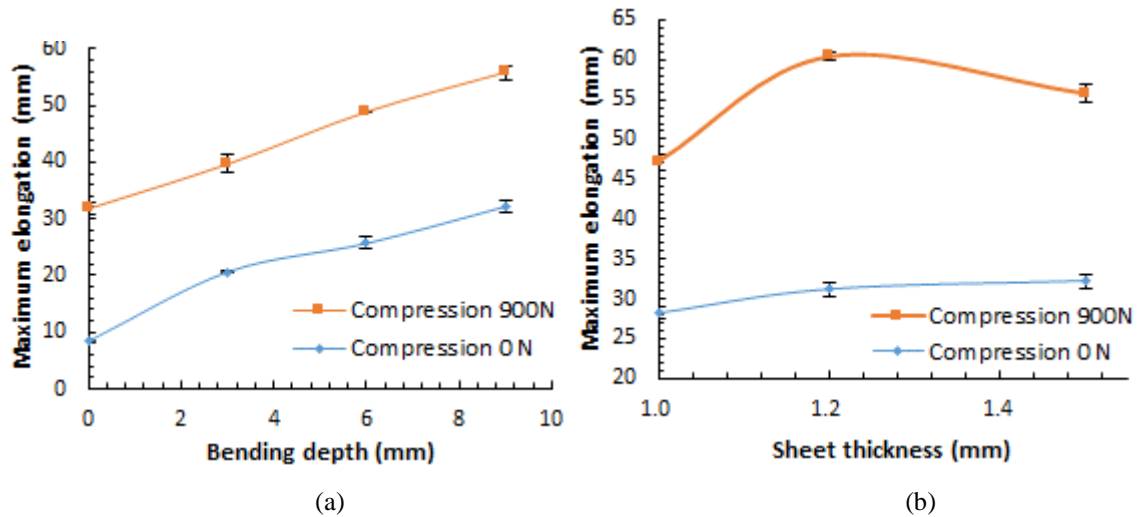


Figure 4.11 Maximum elongation under different compression forces with varying: (a) bending depth; (b) specimen thickness

#### 4.5 FE Damage Modelling of TCBC Test

Although the TCBC test has enormously simplified the analysis of the material deformation in DSIF, the developed TCBC test rig, as shown in Figure 4.2, still does not facilitate a direct observation of the deformation history of the deformed material during the test. Techniques such as the digital image correlation (DIC) could not be applied because the contact areas were covered by the moving rollers. Laser-engraved grids on the outer surface of the specimen were used by Fang et al. [60] to calibrate the strain distribution on the convex surface of the deformed area in SPIF. Combined with the thickness measurement, the strain distribution in three major directions could be obtained. However, in DSIF the abrasion from the contact between outer surface of the specimen and the additional tool will damage the grid. A direct experimental measurement of strains and stresses in the TCBC test by using laser-engraved grids is not feasible.

Finite element (FE) method has been proved to be both effective and efficient in investigating the material deformation history by obtaining process-related variables during the process. In this section, FE simulation models of the TCBC and TCB process were established with shear-modified GTN model developed in Chapter 3. Stress and strain distributions as well as the damage indicator void volume fraction during the test process were obtained and compared. Based on the results, the material deformation and fracture behaviour in the tests were evaluated.

#### 4.5.1 FE modelling of TCBC process

Considering the high non-linearity resulting from contact conditions and the large material plastic deformation, the FE modelling of the TCBC and TCB processes was performed using the Abaqus/Explicit solver. Material AA5251-H22 was used in the model.

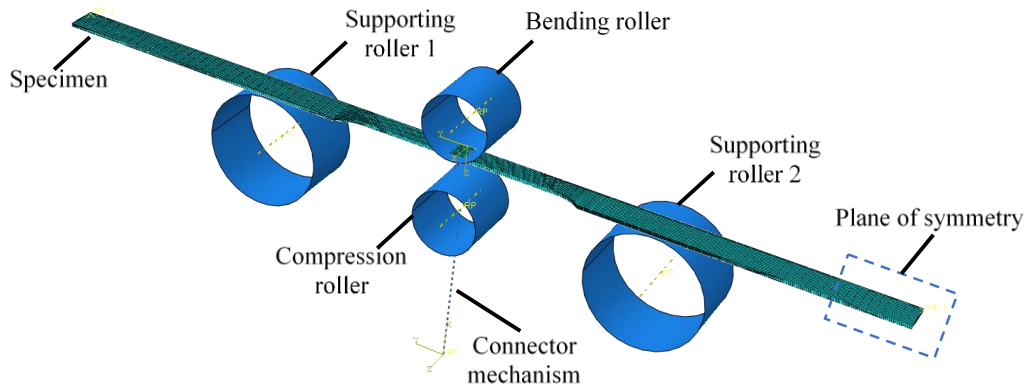


Figure 4.12 FE modelling of TCBC test

Solid element with reduced integration points C3D8R was used for specimen in the FE modelling for modelling accuracy and efficiency. According to the mesh convergence analysis results for the damage model in Section 3.2, the element size of 0.5 mm was used in the central area of the specimen while the arms were meshed to be 2 mm. Five layers of elements were used in the thickness direction in order to observe the effect of bending and compression on the deformation behaviour and to avoid hourglassing for the reduced integration element type used in this modelling. Meshing of the specimen is shown in Figure 4.12.

All rollers in the FE model of the TCBC test were defined as rigid bodies and their movements were controlled by the displacement boundary conditions. The specimen was fixed on one end while was stretched on the other end at a tensile speed of 2.4 mm/min. The bending roller and the compression roller moved together at a speed of 1.5 mm/s. The compression was applied by an axial connector mechanism supporting the compression roller with a preload of 600 N. The bending depth was defined as 9 mm. To reduce the computational time, only half of the specimen was modelled by applying the axisymmetric boundary condition, as shown in Figure 4.12. Local coordinate systems were established on every single element in order to obtain stress components in the directions normal to the element surfaces of the bent specimen after deformation. As a

comparison, another FE model of TCB test, without applying compression force, was also established in which all other parameters were kept the same.

## 4.5.2 FE modelling results

### 4.5.2.1 FE damage modelling results

The total time before the occurrence of fracture in the tested specimen in the TCB test was 623.6s. While for the TCBC test, the process time was 620.1s. As shown in Figure 4.13, since the tensile speed of the clamp was 0.04 mm/s, the total maximum elongation of the specimen in the FE modelling was 24.94 mm and 24.8 mm for TCB and TCBC test respectively. According to the experimental results, the averaged maximum elongation of the specimen in the TCB test was 28.3 mm and in the TCBC test, it was 34.1mm, using the same values of parameters adopted in the FE modelling.

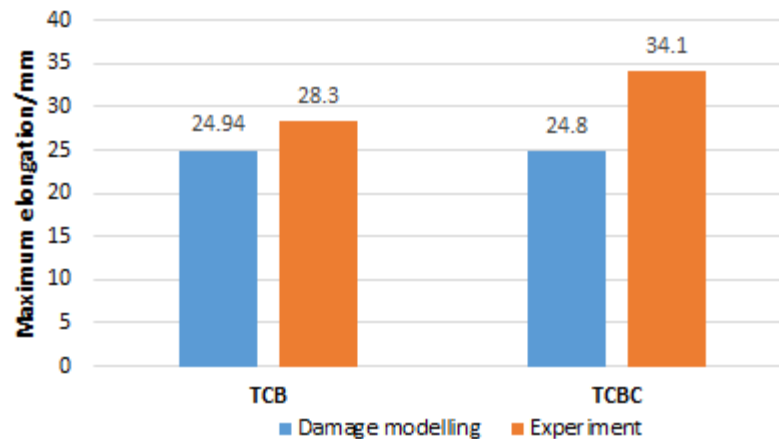


Figure 4.13 Comparison of maximum elongations of the specimens in the TCB and TCBC tests in the FE damage modelling and experiment

For TCB test, the error between the experiment and simulation was 11.87%. The difference between the simulation and the experiment was only 3.36 mm. In the tests, part of the operations were manually conducted, including the positioning and clamping of the specimen, application of the compressive force and application of bending depth. The application of the compressive force and the bending depth was controlled by adjusting the length of the springs through corresponding screws. Inaccurate positioning of the screws would lead to imprecise loadings of the springs or unbalanced position of the bending/compression roller, which ultimately resulted in error between the experiment and the FE simulation. While the error caused by the clamping of the specimen could be ignored since grooves were manufactured to increase the friction between the specimen and the clamp and keep the specimen from sliding during the test. The acceleration and deceleration of the motors could also lead to a difference between the experiment and FE

simulation. Considering all these factors in the experiment, the error was acceptable. By comparison, for TCBC test, the error was 27.27%, the prediction of the maximum specimen elongation obtained by the damage modelling was much smaller than the test result. Furthermore, the prediction made by the damage modelling for the TCBC test was even smaller than that for the TCB test, which was contrary to the experimental results. The shear-modified GTN model was proved to be not suitable to give an accurate prediction of the maximum elongation of the specimen in the TCBC test.

The force-displacement curves in the TCB and TCBC tests were extracted from the FE results. As shown in Figure 4.14, similar with the experimental test (shown in Figure 4.8), the force in both tests oscillated during the test in certain patterns due to the cyclic movement of the rollers. The application of the compression in the TCBC test resulted in lower tensile force compared with that in the TCB test. In addition, at the later stage of deformation, both curves, especially the one for the TCBC test, presented variations with irregular patterns, owing to the occurrence of element deletion during that time period.

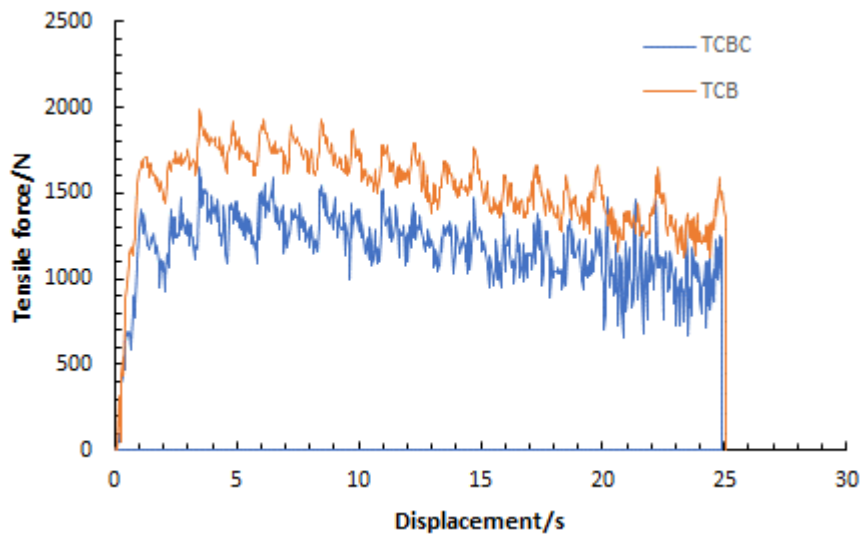


Figure 4.14 Force-displacement curves recorded from tests under different loading conditions

The distribution of the damage indicator, void volume fraction (VVF, SDV2) upon the occurrence of fracture was extracted from FE results for both TCB and TCBC tests. As shown in Figure 4.15, unlike the uniaxial tensile test, in which the largest damage concentrated at one location (see Figure 3.8), multiple potential weak zones appeared on the outer surface of the specimen for both models. Fracture of the specimen occurred a few cycles after the deletion of the first element. When the tool(s) moved away from the material, the damage in that area stopped increasing until the tool(s) moved back again.

In other words, the fracture in the tests was delayed. This phenomenon confirmed the effect of cyclic loading on the material deformation behaviour in the experiment.

The bending effect can be roughly reflected by the distribution of VVF in elements on the concave side and convex side of the specimen. Obviously, as shown in Figure 4.15, the damage on the convex side was generally higher than that on the concave side.

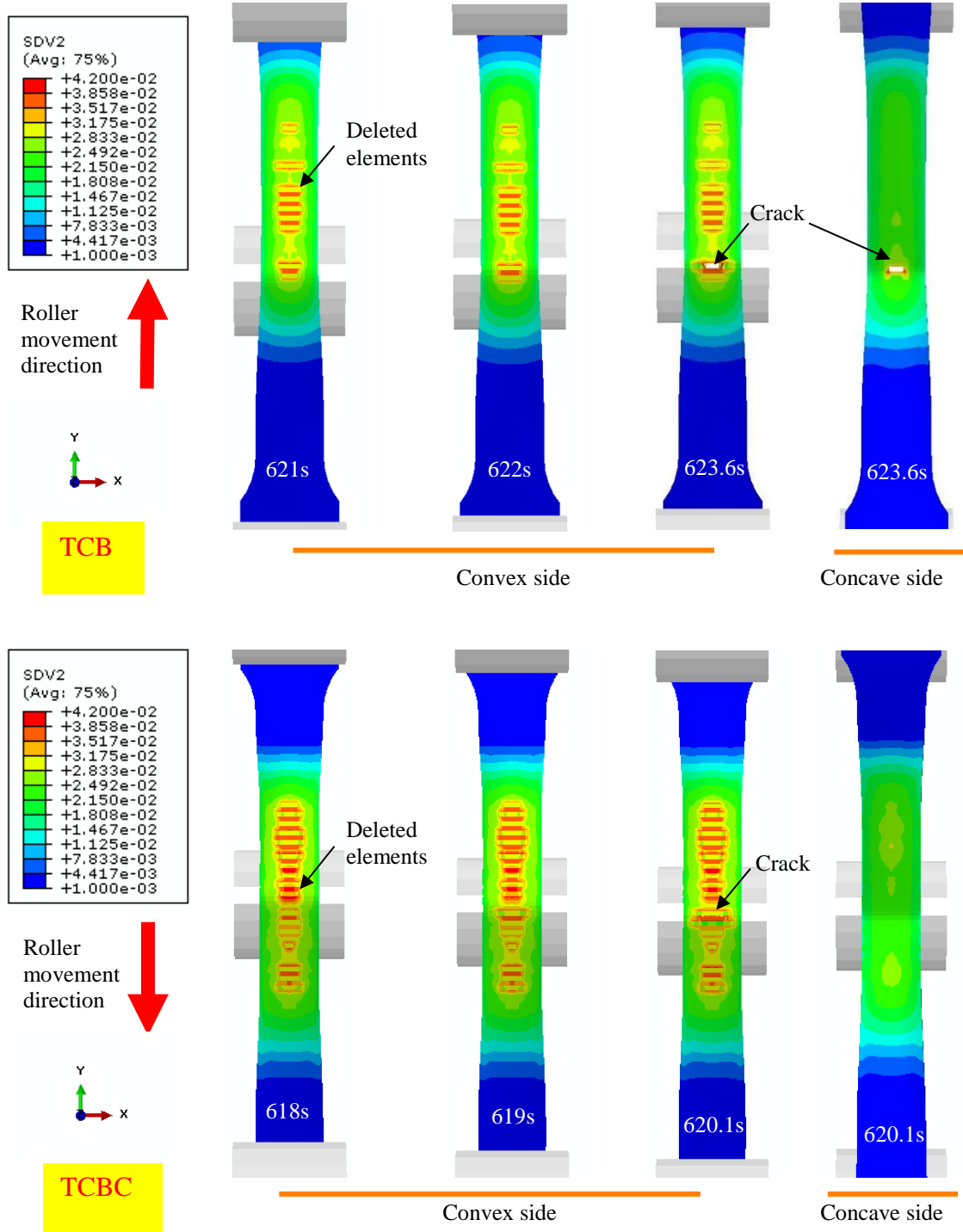


Figure 4.15 Evolution of VVF (SDV2) of elements in the thickness direction in TCB damage modelling in the last three steps upon fracture

In order to present the bending, compression and the cyclic loading effects in a clearer way, equivalent plastic strain and VVF history of three elements at the crack locations, located on the convex surface, the middle surface and the concave surface of the specimen for both the TCB and TCBC tests were extracted from the FE modelling results, as shown in Figure 4.16

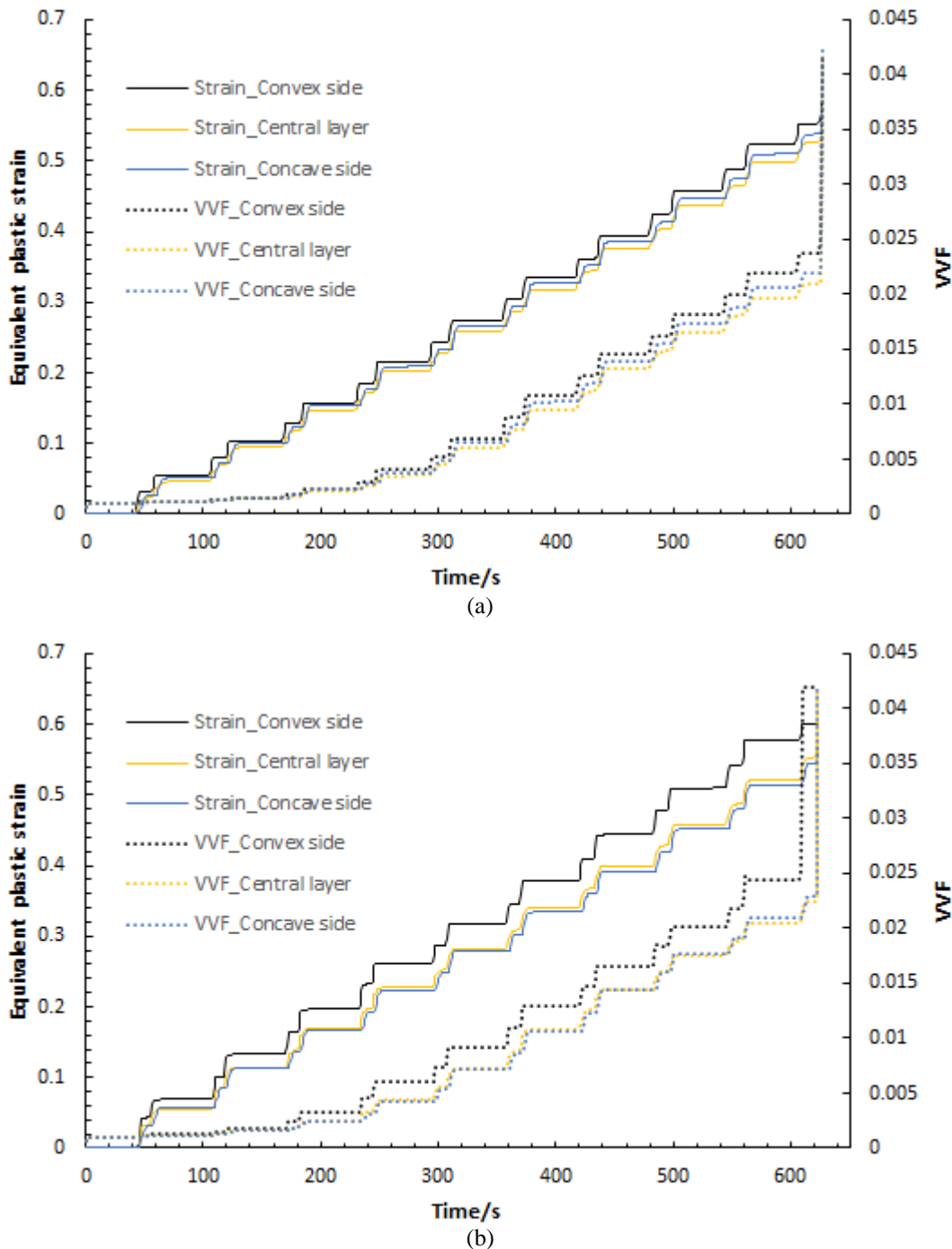


Figure 4.16 Evolution of equivalent plastic strain and VVF of three elements at the crack location along the thickness direction in damage modelling of: (a) TCB test; (b) TCBC test

. Stair-like accumulation of both the equivalent plastic strain and VVF could be observed, which suggested the existence of localized material deformation. Material plastic

deformation only occurred periodically when the bending tool was in contact with the specimen in that area. When the tool moved away from that location, the strains kept almost unchanged until the tool moved back again.

The bending effect could also be reflected by the variations of equivalent strain and VVF along the thickness direction. For both models, the equivalent strains of the elements on different surfaces were different. Generally, the elements on the convex side of the specimen underwent the highest level of deformation, while the elements on the central and concave surfaces were less deformed. Correspondingly, the VVFs of the elements on different surfaces were also different.

The introduction of compression affected the material deformation in the TCBC model. As shown in Figure 4.16, the difference between the equivalent plastic strains of the elements on the concave side and the convex side in TCBC test was much larger than that in the TCB test. In addition, in the TCB test, as shown in Figure 4.16 (a), the equivalent plastic strain of the element on the concave side was slightly higher than that on the central layer. However, on the TCBC test, as shown in Figure 4.16 (b), it was the opposite, the equivalent plastic strain of the element the central layer was slightly higher than that on the concave side. The introduction of compression intensified the material deformation on the convex side of the specimen.

#### 4.5.2.2 Comparison between TCB and TCBC tests

As presented in Section 4.5.2.1, the results obtained from the damage model using the shear-modified GTN model were not accurate, especially for the TCBC model. In order to compare the TCB test and the TCBC test, FE models of the two tests without damage model were established. The same parameters and settings were used in the FE damage modelling. Local coordinate systems were established on every single element in order to obtain stress components in the directions normal to the element surfaces after specimen deformation. For both TCBC and TCB tests, equivalent plastic strain history of three elements located on the convex surface, the middle surface and the concave surface of the specimen at the location in the thickness direction were extracted from the FE modelling results, as shown in Figure 4.17.

Similar to the results obtained from the damage modelling, stair-like evolution of the equivalent plastic strains and their inhomogeneous distribution along the thickness direction in both tests indicated obvious feature of localized deformation and bending in both tests. However, different from the pure bending effect, in which the deformation in

the central layer should be under the smallest deformation, in the TCBC and TCB tests, the elements in the convex side of the specimen showed the largest plastic deformation. The central layers had the second largest plastic strain and the concave side elements had the smallest, which indicated a superimposed tension effect in addition to the bending effect.

The introduction of the compression force improved the formability of the material. As shown in Figure 4.17, the equivalent plastic deformation of the elements in the TCBC test was obviously larger than those in the TCB test after the same period of testing time. Since the tensile speed was the same for both tests, larger plastic deformation means thinner specimen and larger deformation in the specimen longitudinal direction, as a result a smaller tensile force was needed to pull the specimen to reach the same level of plastic deformation, as recorded in the experiment shown in Figure 4.8. Since the fracture in the TCBC test was caused by tension according to the experiment, less tensile effect led to greater plastic deformation before the occurrence of fracture.

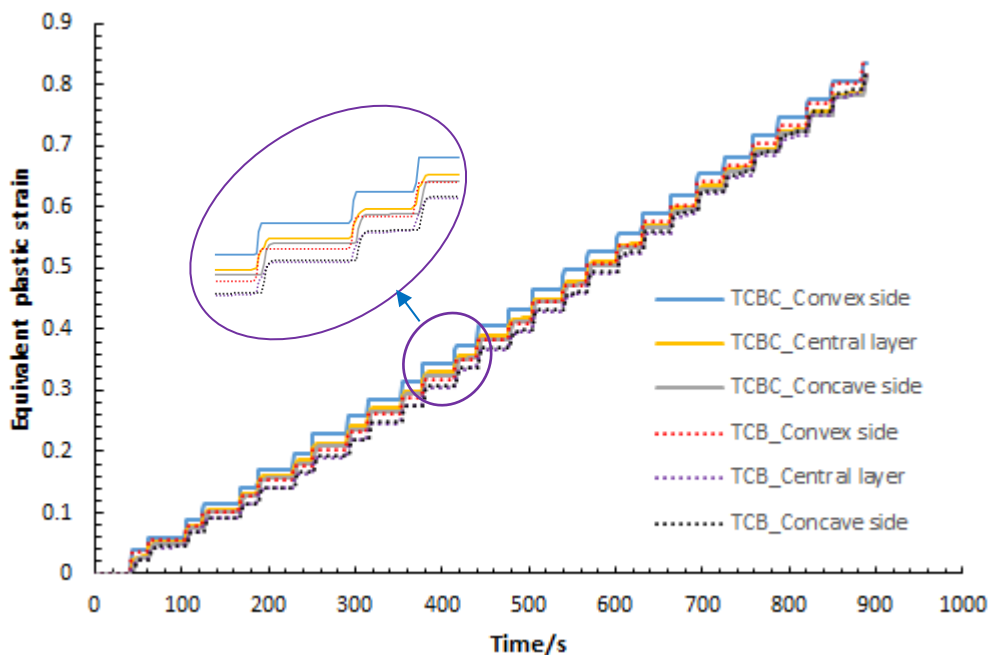


Figure 4.17 Evolution of equivalent plastic strains of elements in the thickness direction in TCBC and TCB modelling

The bending effect can also be observed when comparing the distribution of the tensile stress in the longitudinal direction across the thickness in the contact area in the local coordinates, as shown in Figure 4.18. For both tests within the contact area, the elements on the concave side were under compression in the longitudinal direction, while on the convex side, they were under tension.

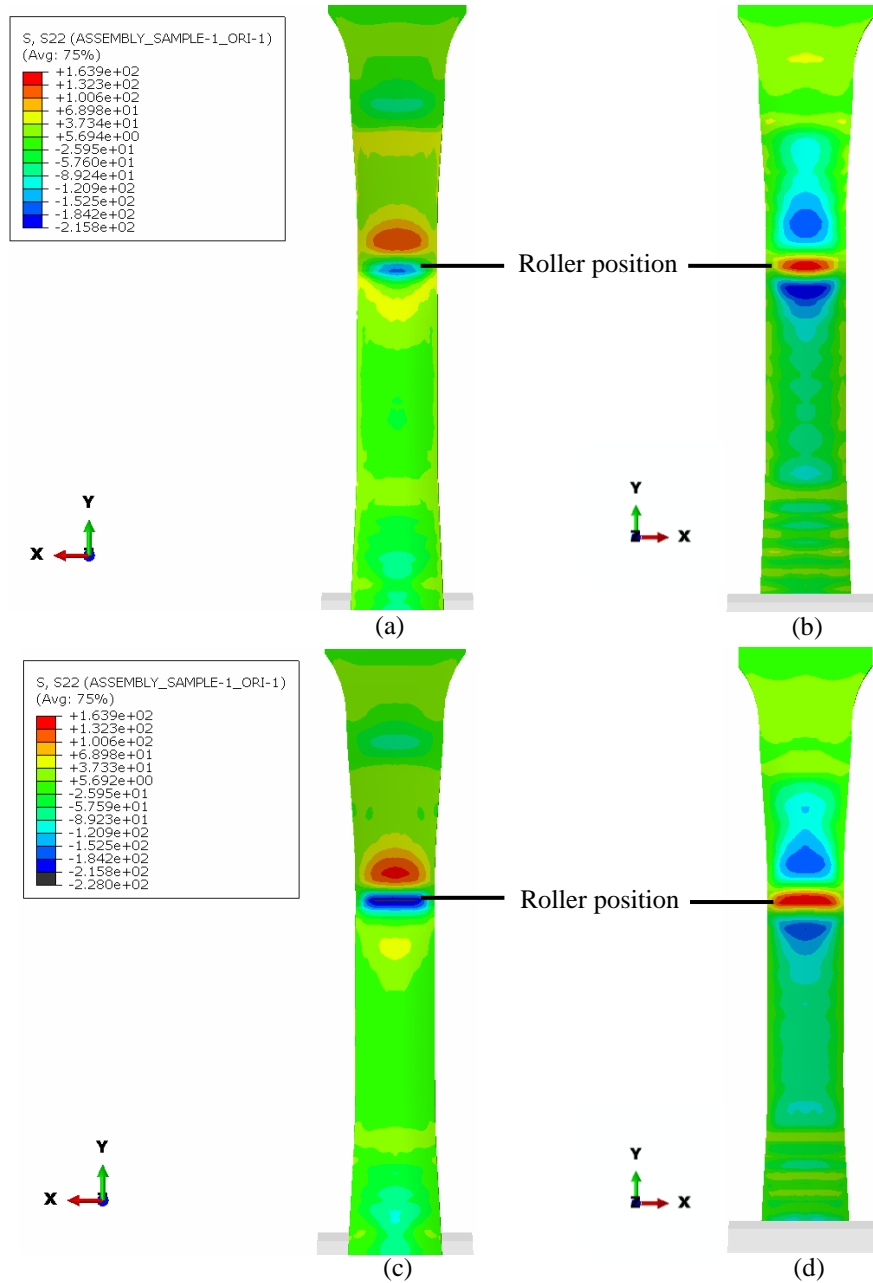


Figure 4.18 Stress distribution (MPa) in the specimens in the longitudinal direction during the uniform material deformation: (a) TCBC test concave side; (b) TCBC test convex side; (c) TCB test concave side; (d) TCB test convex side

In addition, the difference between the equivalent plastic strain of the elements on the concave side and the central layer was much larger in the TCBC test than that in the TCB test, as shown in Figure 4.17. This indicated that the bending effect in the TCB test was much more obvious thus the neutral plane of the thickness was shifting from the central layer to the concave side of the specimen surface during the thinning process of the specimen. While in the TCBC test, the introduction of the compression force led to a more homogeneous distribution of plastic deformation in the thickness direction thus less

severe bending effect, creating a less obvious gradient of plastic deformation across the thickness direction.

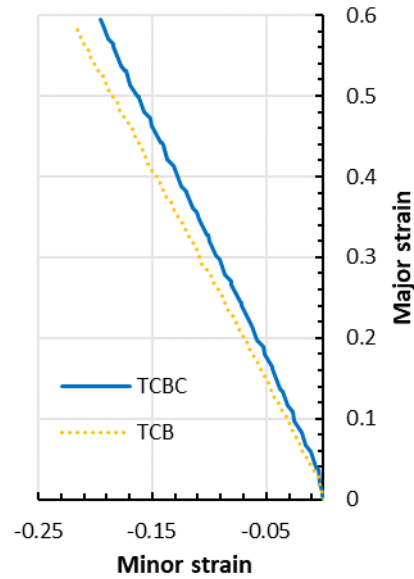


Figure 4.19 Strain paths of elements in FE modelling of TCBC and TCB tests

Strain components of the elements, which located on the outer surface in the centre of the specimen, were extracted from both FE models in the local coordinate system. It is obvious that in the TCBC test, the largest plastic deformation of the specimen occurred in the longitudinal direction. As a result, the strain component in the longitudinal direction was treated as the major strain and the strain component in the specimen width direction was treated as the minor strain, the strain paths of the elements in the TCBC and TCB tests were plotted, as shown in Figure 4.19. The non-linear strain paths reflected the effect of cyclic loading on the material deformation. For TCBC test, the introduction of the compressive force reduced the material deformation in the lateral direction while elongations of the specimens in the longitudinal direction were the same. The difference between the strain paths obtained from the DSIF and SPIF processes (as shown in Figure 3.25) was less obvious than that between the TCBC and TCB tests. The difference could be caused by two factors. Firstly, geometric constrains between the TCBC tests and the ISF processes was different. In the TCBC and TCB tests, the material was under near plane stress condition. However, in the ISF processes, the material was confirmed to be under a strain state between plane strain and equi-biaxial tension. Secondly, how the tension was applied onto the material was different. In the TCBC and TCB tests, the tension was applied by the continuous stretching force from the clamp. By comparison, in the ISF processes, the sheet blank was only clamped on the outer edges, once the tool(s) moved away from the material, the tension applied on that area would be partially released

due to the loss of constraint. As a result, the strain paths obtained from the tests were different from the ISF processes.

## 4.6 Discussion

According to the experimental results, the material formability was further enhanced in TCBC test compared with that in the TCB test and the uniaxial tensile test, especially for material AA5251-H22. The FE modelling results confirmed the strong localized material plastic deformation in the TCBC test. Compared with that in the TCB test, the material tested under the TCBC reached higher plastic deformation with less tensile deformation, which led to higher maximum elongation of the specimen in the TCBC test. The stair-like accumulation of equivalent plastic deformation and delayed crack formation were observed in the FE modelling of TCBC and TCB tests. This was also observed in the developed FE models of SPIF and DISF processes to form a hyperbolic cone. The same observation was reported by Mirnia et al. [65] in the FE simulation of SPIF process and by Smith et al. [31] in the FE simulation of SPIF and ADSIF. The localized material deformation in the TCBC test confirmed that the newly developed TCBC test could be a reasonable representation of the DSIF process.

### 4.6.1 Effect of investigated deformation modes in the TCBC test

The introduction of the compression effect produces a significant difference between the continuous bending under tension (CBT) test [48] and the TCBC test. As observed from the experimental results, the existence of compression force further improved the material formability in the TCBC test. The compression force was shown to be the most influential factor affecting the material formability in the experiment while the bending effect, which was the most influential factor in the CBT test, was comparatively weakened in the TCBC test, as also observed from the FE simulation results of the TCBC and TCB tests.

The localized material deformation is further strengthened under the TCBC condition. The tensile force needed for yielding was smaller which further delayed the fracture caused by the tension effect. As reported in Section 4.5, in the FE modelling of the TCBC test for the material AA5251-H22, the bending compressive force was set to be 600 N while the bending depth was 9 mm. According to the FE results, a distribution of the stress component at beginning of the test in the thickness direction in the specimen along the longitudinal direction is shown in Figure 4.20. Obviously, the contact between the rollers and the specimen can affect the distribution of the stress, the compression

generated from the contact can result in lower value of stress in the thickness direction. As a result, the distribution of the stress in the thickness direction can be an indicator to the contact area between the rollers and the specimen. As shown in Figure 4.20, the size of a single element in the longitudinal direction is 0.5 mm, which means that the length of the contact area in the longitudinal direction was about 1.5 mm, while the width of the specimen was 12.5 mm, which formed a contact area of 18.75 mm<sup>2</sup>.

In the TCBC test of AA5251-H22, the maximum compression force applied was 900 N, the geometric constrain between the rollers and the specimen was kept the same, assume that the contact area was similar to analytical result of 18.75 mm<sup>2</sup>, the value of the compressive stress contributed by the compressive force applied by the roller was 48 MPa, which was far smaller than the yielding stress of the material of 156 MPa. As for the material AA6082-T6, the maximum compressive force applied was 1200 N, consequently contributing a compressive stress of 64 MPa, which was smaller than its yielding stress as well.

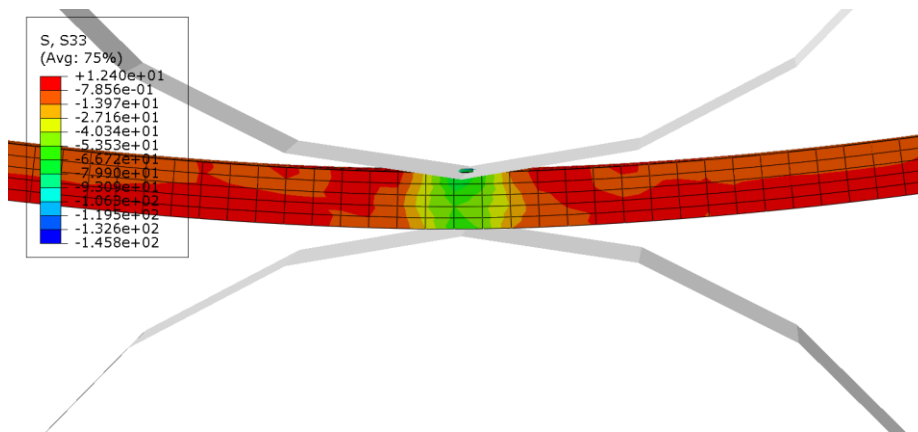


Figure 4.20 Distribution of the stress in the thickness direction in the FE result

The compressive stress resulted from the compressive force applied by the roller was not large enough to generate the plastic deformation itself in the investigated ranges of the factor. The tensile stress was essential to drive the plastic deformation in TCBC test. As a result, according the Tresca yielding law, the higher the compressive force applied, the less tensile force was needed for plastic deformation, which contributed to the deformation stability of the process, as suggested by Emmens and van den Boogaard [68]. In addition, the material in the contact area would be under lower stress triaxiality, which would slow down the accumulation of damage in the material and promote the formability [54].

However, when the compressive force was increased beyond a certain limit, the fracture of the specimen occurred earlier. A similar phenomenon was also observed by Lu et al. [30] when performing the DSIF test, in which the maximum forming angle of the conic part started to decrease when the supporting pressure of the compression tool was increased to be higher than 600MPa. In their case, the earlier fracture was attributed to surface damage by the excessive pressure from the tools. However, in the TCBC test, the rollers were free to rotate around their own axis therefore no obvious surface damage caused by the tools was observed on either side of the specimen. A possible explanation could be when the compression force was larger enough, the material in the contact zone was prone to yield even with a small tensile force applied, according to the Tresca yielding criterion. Therefore, the fracture was more susceptible to the tension effect thus leading to early fracture.

The influence of the tensile speed was also different between the CBT/TCB and the TCBC tests. In the CBT/TCB test, the existence of tension was crucial to achieve the plastic deformation. If no tension existed, the whole process was degenerated to a pure bending test, thus a formability enhancement over the conventional forming processes was not feasible. By comparison, without the tension effect, the material formability enhancement in the TCBC process could still be achieved. In addition, without tension effect, the damage evolution was suppressed due to the compression dominated plastic deformation, which further maximised the material formability. The same concept of compression dominating deformation could be reflected in the process of the accumulative-DSIF (ADSIF) [31] where the tools moved outwards and upwards from the centre of the bottom of the toolpath. In ADSIF, the compression from the supporting tool reduced the tensile force needed for the plastic deformation. Furthermore, the reciprocating movements of the tools from inside to outside resulted in a free end of the ADSIF formed part which further reduced the tensile force.

By comparing CBT test and TCBC test results, it was obvious that the existence of superimposed compression onto the material deformation not only changed the relative significance of various deformation modes on the material but also introduced the interaction effect between these deformation modes. In the CBT test [48], the stretching speed and the bending depth combined to produce the bending effect while in the TCBC test, as analysed in Section 4.2, the effect of stretching speed was significantly weakened due to the introduction of the compression effect. This showed that the effect of every single deformation mode could not be isolated in the analysis.

The selection of the variation ranges of the testing parameters to achieve the maximum material formability in the TCBC process depended on the material type. The reason was twofold. Firstly, different types of materials showed a different degree of sensitivity to the variations of the parameters tested in the experiment. In this study, material AA5251-H22 was obviously more sensitive to the parameters investigated and the variation ranges led to a significant material formability enhancement in the test. While AA6082-T6 only displayed a slight increase of the maximum elongation when the similar variation ranges of the parameters were used. Furthermore, the interaction between the process parameters made it very difficult to predict the trend of the formability enhancement when the parameters were varied; there was no general trend observed.

Based on the findings in the TCBC test, a guidance to maximize the material formability in the DSIF process could be proposed. A different level of the compression force may be required for a different material. The gradient of the toolpath in the vertical movement direction should be appropriate to avoid excessive tension effect in the meridional direction of the formed ISF part when the forming tool deforming the material, this also should be considered when determining the vertical step of the toolpath.

#### 4.6.2 Limitations of current TCBC test

##### 4.6.2.1 Limitations of the current TCBC test method

Some limitations were observed in the current investigation of the TCBC tests in this study. In the experiments conducted, the variation ranges of the factors investigated were limited due to the limited capability of the current TCBC test rig design, especially for the material AA6082-T6. A greater variation range of the factors should be investigated in the future. For example, for both types of materials, the stroke speed presented a positive effect on the material formability but the degree of the influence tended to decrease while the stroke speed was increased. A new trend of the effect of the stroke speed on the material formability may emerge when the testing range of the parameter variations could be extended.

The shearing effect along the roller movement direction resulted from the friction between the tools and the specimen was neglected in the current TCBC test due to the fact that the magnitude of rolling friction between the rollers and the specimen surfaces was much smaller than sliding friction. If the rollers could be fixed to prevent self-rotation around their own axis, the friction-related shearing effect could be more obvious, and the magnitude of the frictional effect could be evaluated by using different types of lubricants.

The magnitude of bending effect in the TCBC test could be affected by bending depth, roller radius and material thickness. In the current test, only bending depth and material thickness were varied while the bending roller radius was kept constant as 10mm. Further experiments using rollers with different radii could be conducted.

The results obtained from the Taguchi Design of the Experiments with four factors and the third stage experiments demonstrated the interactive effect between the key factors tested. However, the interactive effect of all important parameters can only be appropriately investigated by introducing the interaction factors into the design of the experiments. It cannot be analysed using the current experimental design of four factors, more factors representing interactive effects between the current four factors need to be considered in the test design and more sets of experiment can be conducted.

The FE results revealed that although the TCBC test created a localized deformation in the material, the strain paths were still different from those obtained from the ISF processes due to the difference in the loading conditions and geometrical constraints of the sheet material. To achieve a better simplified representation of the ISF processes, the geometrical constrain in the ISF processes should be taken into consideration in developing simplified testing methods in the future.

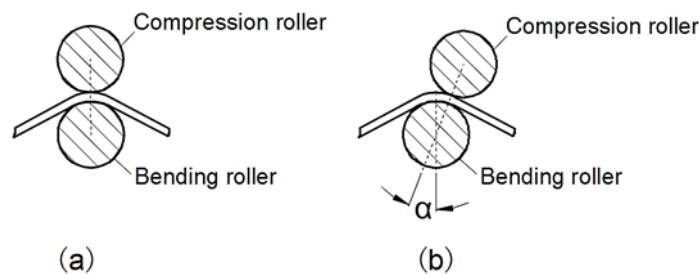


Figure 4.21 Schematic of the relative tool positions in DSIF: (a) two rollers supporting each other without shift; (b) two rollers opposing each other with a shifting angle of  $\alpha$

In DSIF process, the relative position of the two tools was reported to be an important factor affecting the material formability in DSIF since it changed the contact conditions which led to different strain and stress distributions in the specimen [30]. Using the current TCBC test rig, the compression roller was positioned to touch the centre of the bending area of the specimen, created by the bending roller, as shown in Figure 4.21 (a). If the compression roller could be shifted to be away from the centre of the bending area, as shown in Figure 4.21 (b), the relative position of the two tools in the DSIF process, could be evaluated, subsequently its influence on the formability could be investigated.

#### 4.6.2.2 Limitation of the FE damage modelling for the TCBC test

As for the FE damage modelling, the shear-modified GTN model predicted premature fracture in both TCB and TCBC tests. Moreover, it underestimated the maximum elongation in the TCBC test substantially. The results were consistent with the FE damage modelling results obtained the ISF processes. However, comparing with the ISF FE damage model predictions, the TCB prediction was much closer to the experimental result.

In the TCBC tests and the ISF processes, similar deformation modes were applied in the FE damage models. The variation of prediction accuracy may be explained by two reasons. Firstly, the GTN type models have been proved to be most effective under tension-dominated deformation processes. Their accuracy in predicting material deformation under low/negative stress triaxiality is unsatisfactory even with the shear-modified extensions [175, 238]. Due to the fact that material deformation in the TCB test was driven by the tension from the clamp, tensile effect in the TCB test was more dominant than that in the ISF processes and TCBC test, giving a higher predicting accuracy of the FE model. Secondly, as reported by Guzmán et al. [232], complicated geometrical constraints in ISF processes might be one of the reasons limiting the application of the GTN model in ISF process. Comparing with ISF, the geometric constraints in the TCB and TCBC tests were much simpler, thus giving a higher predicting accuracy of the tests. In order to make better prediction of the ISF/TCBC process, further modification to the GTN model should be made or damage models which are capable of modelling processes under a wide range of stress triaxiality should be adopted.

## 4.7 Summary

A new testing method, the tension under bending and compression (TCBC) test, is developed in this study to investigate the effect of various deformation modes on the material formability enhancement in DSIF. Based on the results obtained from the theoretical analysis, experimental testing and the FE modelling, the following conclusions can be made:

- Among the four deformation modes, the compression was the most significant factor affecting the material formability in the TCBC test for two materials tested, AA5251-H22 and AA6082-T6;

- Bending in general was beneficial to the material formability improvement in the TCBC test, however its effect can be influenced by the magnitude of compression loading applied;
- Different materials showed different sensitivity to the variation of the tested parameters when investigating the material formability enhancement, in this study, material AA5251-H22 was far more sensitive than AA6082-T6;
- Localised deformation in the contact zone was clearly evident in both the TCBC and TCB tests, which was further strengthened in the TCBC test when an appropriate range of the compression was applied, reducing the tensile force required for initiating plastic deformation thus delaying the occurrence of fracture;
- To maximize the material formability in the DSIF process, the magnitudes of the compression and the vertical increment of the tool path should be optimised when forming different materials and geometries to avoid excessive tensile force and early material fracture.
- The TCBC test method demonstrated its potential to be a simplified method in testing the material deformation and investigating the fracture mechanisms for DSIF to replace the current test method using the DSIF process itself for material formability studies.

# 5 BIAXIAL TENSION UNDER BENDING AND COMPRESSION TEST

The effect of loading path on the formability enhancement is overlooked in the TCBC test. To investigate the influence of loading path on the material formability in ISF, another testing method, namely the Biaxial Tension under Bending and Compression (BTBC) test is proposed and a test platform has been developed in Section 5.1. Design of the cruciform test specimen is presented in Section 5.2. Using the developed test platform and the designed specimen, the BTBC test on material AA5251-H22 has been performed, design of the experiment and the experimental results are reported in Section 5.3 and Section 5.4 respectively. To obtain the deformation history of the material in the test, FE modelling of the BTBC test has been conducted, as presented in Section 5.5. Based on the experiment and FE simulation, discussions are made in Section 5.6. A summary of the key conclusions obtained from current study are given in Section 5.7.

## 5.1 Concept of BTBC Test and Rig Development

The TCBC test enabled the capability of investigation on the effect of the existing loading conditions (deformation modes) on the material formability in ISF process. However, in the planer directions of the specimens in the TCBC test, the material is under geometric constrain in only one direction, the longitudinal direction of the specimen. While in SPIF, it has been proved that the material is under a strain state between plane strain and equi-

biaxial tension depending on the process parameters and geometry of the part being deformed. The loading path has been reported to have a major effect on the material formability, as reviewed in Chapter 1. The serrated strain path in ISF was reported by Centeno et al. [88] and Eyckens et al. [51], and was confirmed by the FE simulation results in this study, as reported in Chapter 3. The effect of loading path on the material formability could not be reflected in the TCBC test and the strain paths obtained from the TCB/TCBC tests were significantly different from those obtained from ISF processes.

In addition, the introduction of compression further improves material formability in DSIF. However, to which degree the material formability can be enhanced and how it differs from the prediction made by the traditional testing methods remain unexplored.

Furthermore, as concluded by Centeno et al. [88] in the Nakazima test, the bending effect itself could not explain the much delayed fracture in ISF. The cyclic loading is another factor that should also be attributed to the increased formability in ISF.

To overcome the limitations of previous tests, the biaxial tension under bending and compression (BTBC) test is proposed in this study, in which both biaxial tension, compression and cyclic loading are taken into consideration.

### 5.1.1 Concept of BTBC test

As reviewed in Chapter 2, generally biaxial loading can be applied onto the material in two ways. In the first way, specimens with dog-bone shaped geometries are used and the punch pushes the specimen to deform it. Biaxial tension can be generated due to the geometric constraints to the specimen. In the other way, a cruciform specimen is used and biaxial in-plane tension can be directly applied by pulling the arms of the specimen. Multiple loading conditions are required to be applied onto the specimen in the BTBC test and their magnitudes must be adjustable. By comparison, the second way is more straightforward and allows for the controlling of bending and relaxation of the tension in the test. As a result, in this research, the second test method was used.

A schematic of the concept of BTBC testing method is shown in Figure 5.1. In the test, the cruciform specimen is stretched on all ends in both directions. By controlling the tensile speed, the strain ratio between the two directions can be varied. The bending effect is provided by pushing the bending tool with a hemispherical head against the specimen to a certain depth. By changing the bending depth, the degree of the bending effect can be varied. On the other side of the specimen, another tool, the rear tool, is pushed against

the specimen as well to provide compression to the specimen. By controlling the supporting force from the rear tool, the compressive effect can be varied.

The cyclic loading can be realized by controlling movement of the bending tool and the tensile force. During the test process, if the loadings applied onto the specimen can be released and be applied at certain frequency, cyclic effect can be controlled. The bending tool can be lifted up from the sheet and the tensile force from the arms can be released to remove the loadings. Furthermore, the bending can be reapplied by positioning the bending tool to the original depth, tension can be resumed by simply applying the tension again.

In summary, compared with traditional biaxial tensile test, bending, compression and cyclic loading are introduced in the BTBC test. The magnitude of the bending and compression can be varied by controlling the bending depth and supporting force. As a result, the effect of the loading path on the material formability can be investigated under complex loading conditions.

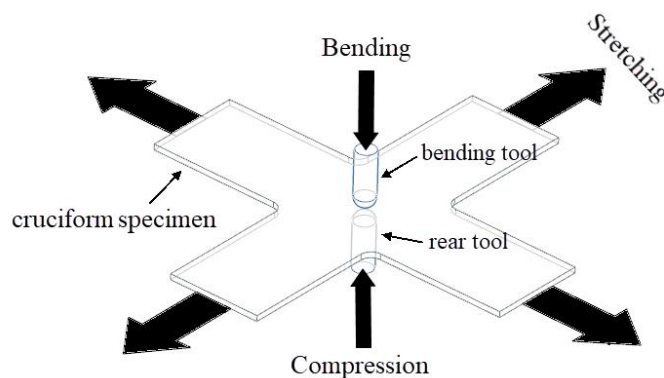
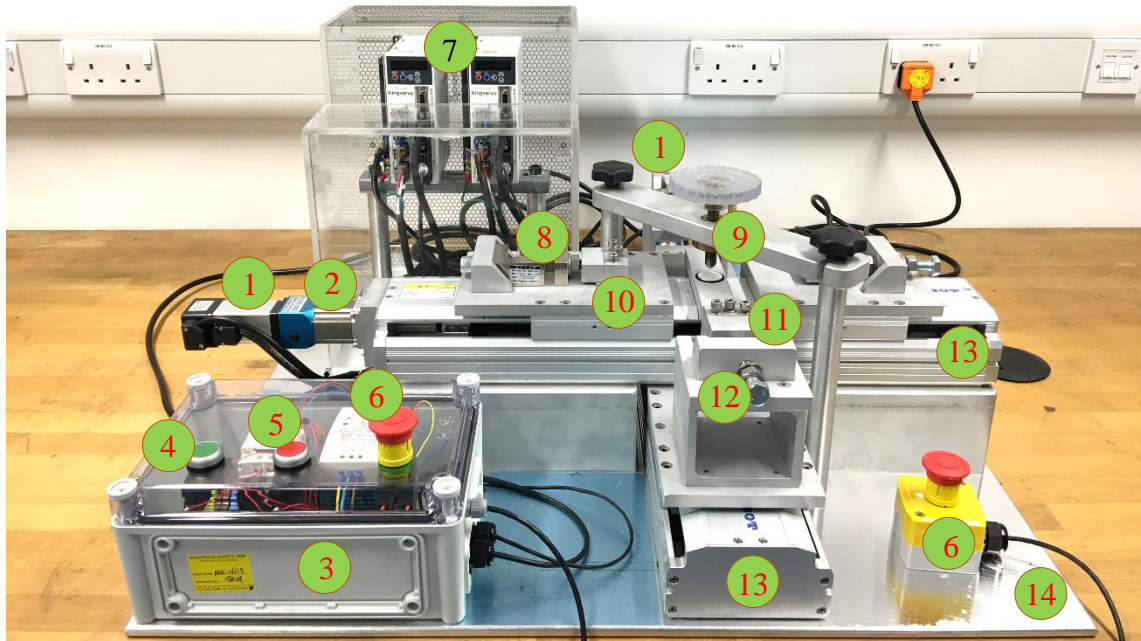


Figure 5.1 Schematic of biaxial tension under bending and compression test

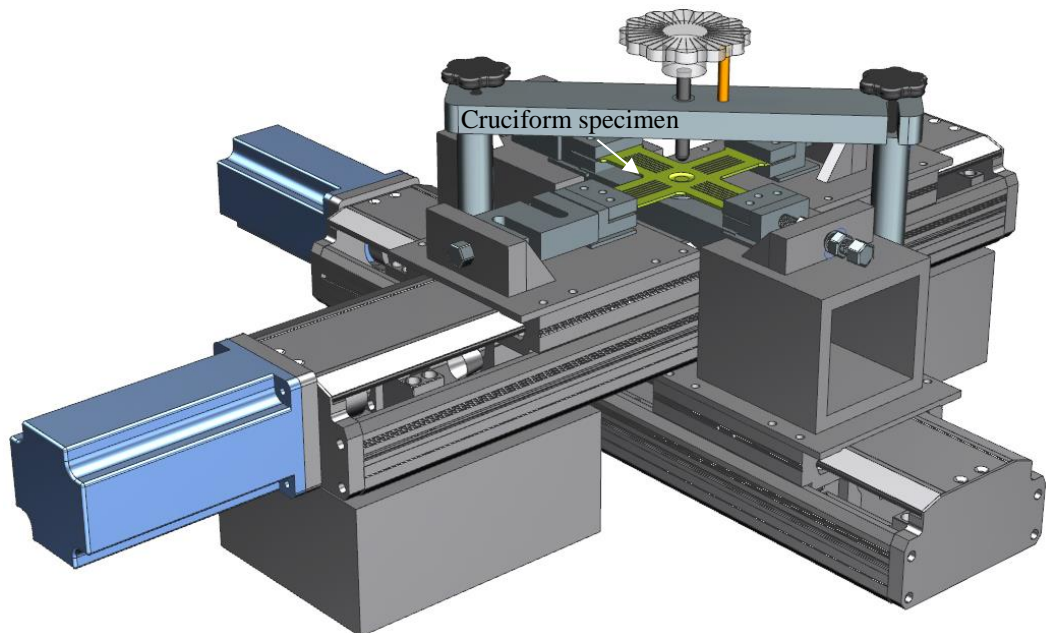
### 5.1.2 Development of BTBC test rig

Based on the proposed concept, the BTBC test rig was designed and manufactured. Similar with the TCBC test rig, the rig comprises of two main components, the mechanical part and the electrical part, as shown in Figure 5.2 (a). The mechanical part consists of structures designed to apply the loading conditions, and the CAD design of the mechanical structures is shown in Figure 5.2 (b). The electrical part is designed to control the motors. It consists of the power control box and the motor controlling system. In order to guarantee the safety in case of unexpected movement of the structure, emergency stop buttons are installed onto the rig. Both parts are fixed onto a thick aluminium plate to maintain the stability, rigidity and integrity of the structure. The whole platform is put on an experiment table to avoid oscillation during the testing process.



1. Motor; 2. Gearbox; 3. Power control box; 4. Power On button; 5. Power Off button;  
6. Emergency Stop button; 7. Motor controller; 8. Load cell; 9. Bending tool; 10. Spring;  
11. Clamp; 12. Clamp position adjustment screw set; 13. Bidirectional linear screw; 14. Base plate

(a)



(b)

Figure 5.2 Developed BTBC test platform: (a) full assembly; (b) CAD design of the mechanical structure

### 5.1.2.1 Application of biaxial tension

As reviewed in Section 2.2.2, in order to apply biaxial tension onto the cruciform specimen in the biaxial tensile test, two types of structures have been developed. The first type, the link mechanism converts the downward movement of the punch to biaxial tension in the planar directions and the strain ratio applied is fixed if the structure is not changed; while the second type directly apply tension onto the arms and the strain ratio can be varied without any change to the structure. By comparison, the later reduces errors that can be caused by the manufacturing and assembly processes of the former comparatively complex structures. In addition, it maintains high adaptability and flexibility since the structure is fixed. As a result, the second type, varied-ratio structure was used in this study.

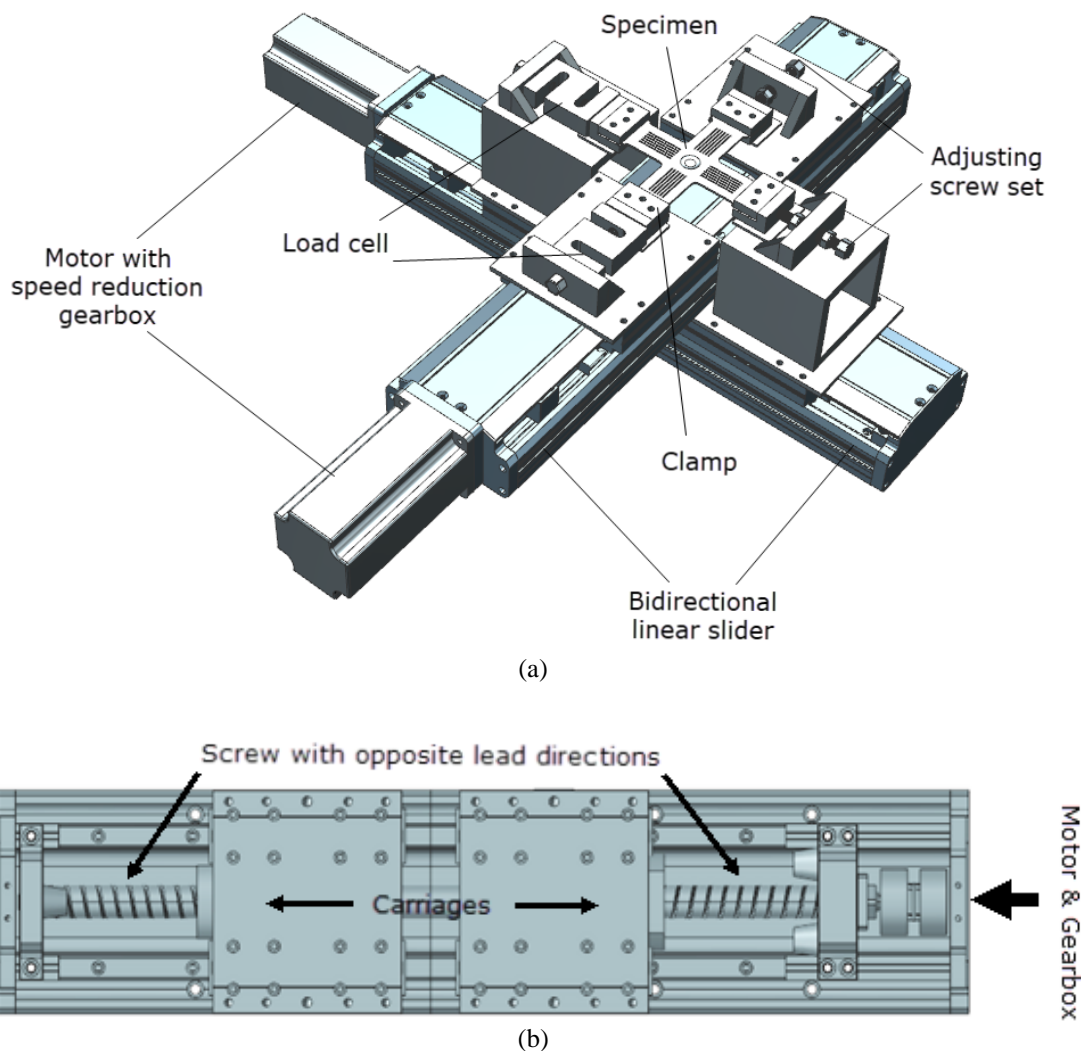


Figure 5.3 The biaxial tension loading components: (a) CAD representation of the biaxial loading components; (b) CAD drawing of the bidirectional linear screw slider;

Commonly, in the proposed second type testing platforms, including the commercial ones, tension are applied onto the four arms of the cruciform specimen by four linear motors or linear screw sliders driven by four motors, one for each arm. In order to guarantee that the centre of the cruciform specimen maintains its position through the test, the tensile speed in the opposite directions must be kept equal. To simplify the positioning requirement of the motors and the clamps and to reduce the cost, instead of using four motors/sliders, two bidirectional linear screw sliders are used, as shown in Figure 5.3 (a). The structure of the slider are shown in Figure 5.3 (b). Different from traditional screw sliders, in which the lead direction of the thread is the same along the length of the whole screw, the effective length of the linear screw in the bidirectional linear screw slider is divided into two parts, the lead direction of the threads in one part is opposite to those in the other part. The lead of the screws in the bidirectional slider is 5 mm. One carriage is fitted to each side of the linear screw. As a result, once the screw is motivated by the motor, the two carriages will move in the opposite directions simultaneously at the same speed.

As shown in Figure 5.3 (a), the two bidirectional linear screw sliders are positioned perpendicular to each other. The first slider is fixed onto the base directly while the other slider is positioned above the first one and they cross over in the middle point of the effective length of the sliders. In this way, only two motors are needed to drive the sliders, each motor is responsible for the movement in one planar direction. The compact structure of the bi-directional sliders also reduces the requirement of positioning accuracy for the motors/sliders. As for the controlling system, the synchronization of the motors in the opposite directions can also be avoided.

The sliders are driven by the servomotor HML40-01030LI, which has a rated rotational speed of 3000 rpm and a constant rated output torque 0.32 N·m. In order to obtain a lower speed range and a higher and stable output torque from the motor, a planetary gearbox DS042-L2 with speed reduction ratio of 70:1 is coupled with each motor. As a result, the rated rotational speed of the servomotor-gearbox system is reduced to 43 rpm while the output torque applied onto the slider shaft is increased to 22.4 N·m.

The rotational speed of the servomotors can be varied by using the motor controllers and the movement of both motors can be started simultaneously with the help of the power control box, thus the effect of strain ratio can be investigated. In particular, if the motor in the transverse direction stays static and the motors in the longitudinal direction runs in

a certain speed, plane strain condition can be created. If both motors run at the same speed, it corresponds to the equi-biaxial tension condition.

#### 5.1.2.2 Application of bending and compression

Bending is applied by a tool with hemispherical head. Considering the dimension of the specimen and the commonly used tool size in the ISF processes, the diameter of the bending tool is decided to be 5 mm. As shown in Figure 5.4, a supporting structure is designed to support the bending tool. In the supporting structure, the bending tool is held by the bridge, pointing to the centre of the specimen. The bridge is supported by two aluminium rods (the supporting pillars), which are fixed onto the base plate. Threads are cut onto the bending tool, by turning the bending tool clock-wisely, the tool will move downwards and it will push the centre of the specimen. The bending tool is attached to a plastic transparent wheel, on which marks are inscribed. By counting the number of marks while turning the wheel, the downward distance of the tool can be calculated, thus the bending depth can be controlled.

In order to facilitate the installing and uninstalling process of the specimen, a notch is cut on the one side of the bridge. As shown in Figure 5.4, when loading/unloading the specimen from the clamps, the bridge can rotate around the screw on the left side. As a result, the space above the specimen will be totally free, making it easier for the specimen to be installed/uninstalled from the rig.

Compression to the target area of specimen is applied by the spring positioned on the other side of the sheet, as shown in Figure 5.4. The spring is housed in the spring holder, which is fixed onto the second slider. A steel cap is placed on top of the spring so that a surface contact between the specimen and the spring can be made. In order to guarantee that the specimen is in contact with the cap when springs with different lengths are used, caps with different thicknesses are manufactured. The thickness of the steel cap adopted in the test depends on the gap between the spring and the lower surface of the specimen. When the spring is compressed due to the downward movement of the bending tool, supporting force is generated. In addition, springs with different stiffness can be used in the test, so that the magnitude of the compressive force can be controlled without changing the bending depth, making the compression effect independent of the bending effect.

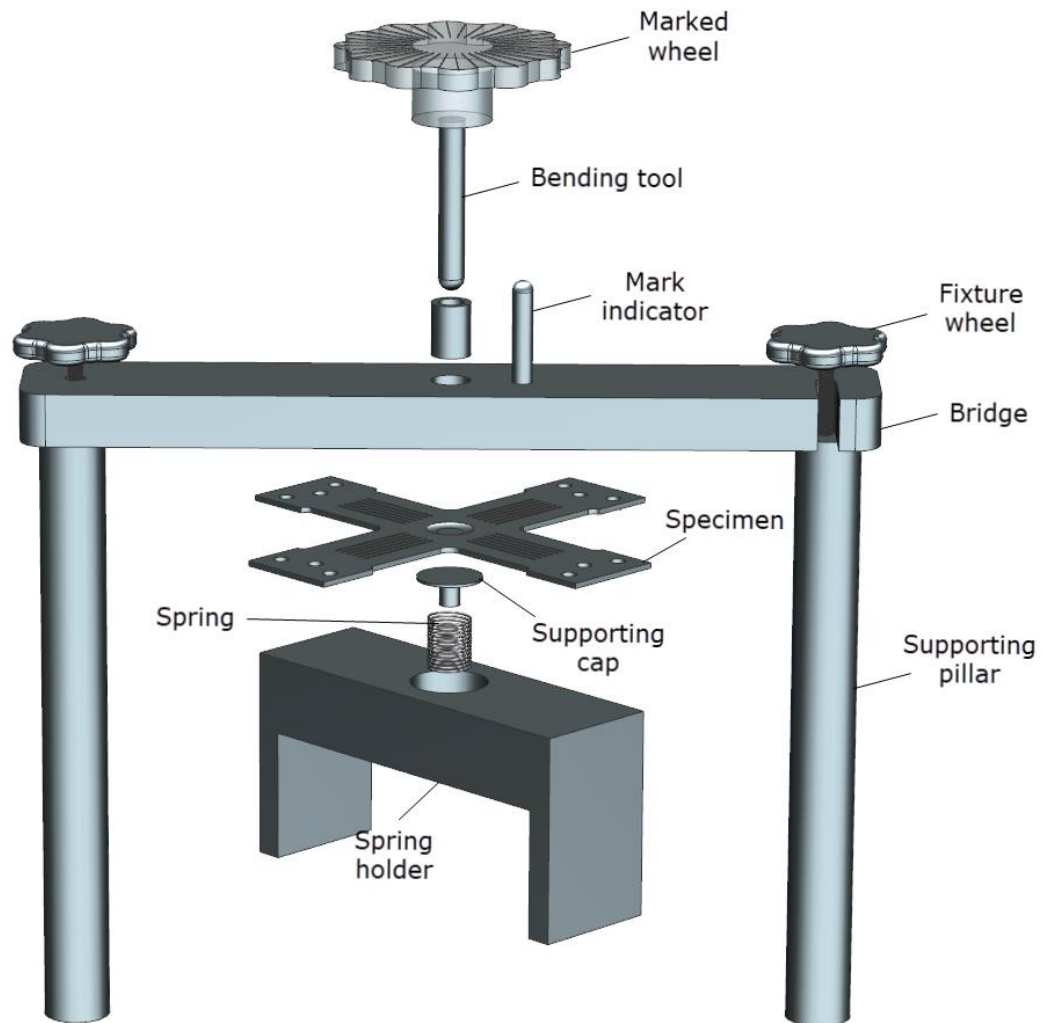


Figure 5.4 Explosive view of the bending and compression application structure in the BTBC test rig

## 5.2 Optimization of Cruciform Specimen

### 5.2.1 Design of the cruciform specimen

As reviewed in Chapter 2, the geometry of the cruciform specimen designed for biaxial tensile test should satisfy three conditions: cross shape, slots in the arms and tapered thickness in the centre of the specimen.

Based on the geometries designed in the published literature [112, 116] for the thin metal sheet and taking the dimensions of the bidirectional sliders into consideration, a prototype design of the cruciform specimen for material AA5251-H22 was proposed for the current study, as shown in Figure 5.5. Length of the specimen was 170 mm in the planar directions. The original thickness of the sheet was 2 mm and the thickness of the central area was reduced to 0.75 mm. The diameter of the central area was 10 mm, matching the dimension of the bending tool. Slots with a length of 35 mm were created in the arms,



In order to optimize the three parameters, a FE model of the equi-biaxial tensile process was established by using the Abaqus/Explicit solver. As shown in Figure 5.6, considering that the specimen was symmetric about both central planes and the loadings applied were also symmetrical, only a quarter of the specimen was used in this model in order to improve computational efficiency of the simulations. Symmetric boundary conditions were applied onto the cross-sections of the specimen. The clamping area of the arms were defined to be rigid, while the rest of the specimen was deformable. The tensile speed of the clamps was all equal to be 1mm/min. Solid element type C3D4 was used in the meshing process. Element size in the central zone and its neighboring area was set to be 0.25 mm, while in the arms and in the clamping areas, it was set to be 2 mm. Considering the results obtained in the uniaxial tensile test, the maximum achievable equivalent plastic strain for material AA5251-H22 was around 0.15 and in the biaxial test generally higher strains can be obtained, it is decided in the optimization process the simulation should be terminated when the maximum equivalent plastic strain of the elements reached 0.2.

The variations of the values of the investigated parameters were also selected based on the former geometries designed published in the literature [112, 116], as shown in Table 5.1. The arm width was first decided, then the radius of the central area, and the slot number was the last to be optimized.

Table 5.1 Ranges of the values of the parameters to be optimized for the cruciform specimen

<b>Parameters</b>	<b>Parameter Variation Range</b>
Arm width	30, 32, 34 mm
Central area radius	9, 10 mm
Slot number	3, 4, 5, 6

According to Song [112], in order to guarantee that the fracture appears right in the center of the specimen, the centre should be the thinnest. While in this research, the main purpose was to limit the maximum deformation to the central zone, not necessarily in the right centre of the specimen. In order to achieve this, in the FE simulation, the objective of the optimization was to find out the parameter values that could yield the largest deformation in the central zone, rather than in the arms or in the slots.

### 5.2.3 Optimization results

The optimization process of the arm width was first run and the strain distribution in the specimen with different arm widths was extracted when the largest equivalent plastic deformation of the element reached around 0.2. The location of the element with the largest deformation was marked out in the results. The radius of the central area was set to be 9 mm and three slots were cut in each arm.

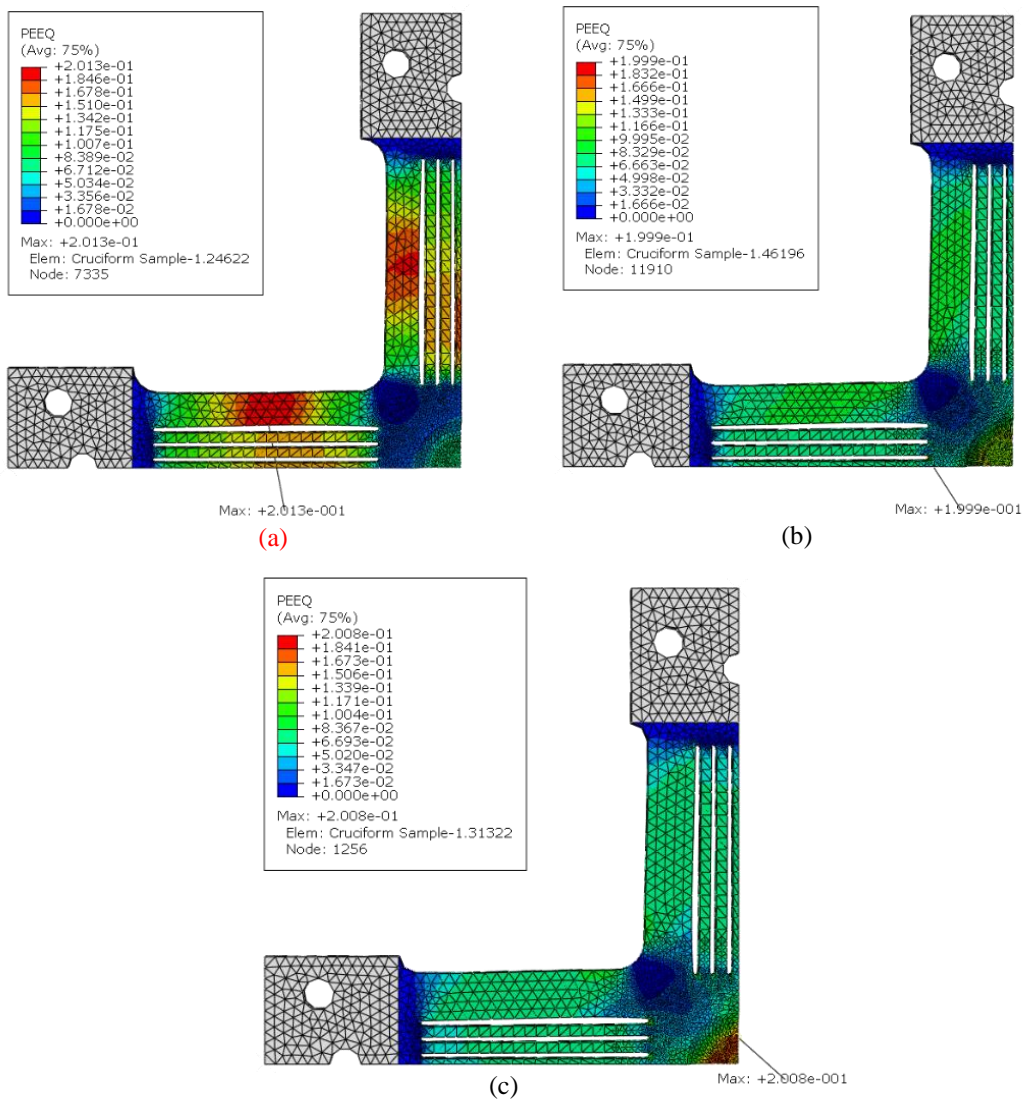


Figure 5.7 Equivalent plastic strain distribution in the specimen with different arm widths: (a) 30 mm; (b) 32mm; (c) 34mm

As shown in Figure 5.7, when the arm width was 30 mm, the largest plastic deformation appeared in the arm and an obvious of distortion was observed, which indicated the fracture would first appear in the arms. While when the arm width was 32 mm, the largest deformation appeared at the end of the slot. When it was increased to 34 mm, the largest

deformation appeared in the central area. As a result, the arm width was determined to be 34 mm.

As shown in Figure 5.7 (c), the largest material deformation appeared in the central zone for the specimen with the arm width of 34 mm. However, it was some distance away from the very centre of the specimen. In order to test whether it could be shifted to be closer to the centre, the radius of the central zone was increased from 9 mm to 10 mm. As shown in Figure 5.8 (a), instead of being in the bottom central area, the largest plastic deformation occurred in the transition area between the arm and the central area. In addition, by comparison, plastic deformation was more concentrated in the central area when the radius was 9 mm. As a result, the radius of the central area used in the specimen design stayed 9 mm.

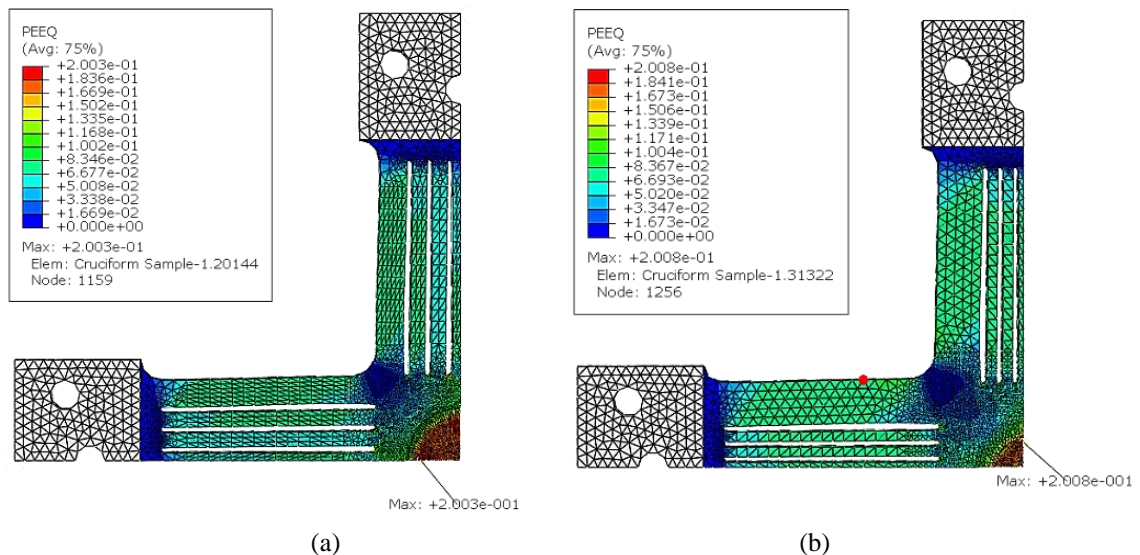


Figure 5.8 Equivalent plastic strain distribution in the specimen with different radii of the central area:

(a) 10 mm; (b) 9 mm

Considering the manufacturing cost and the fact that increasing the number of slots would weaken the strength of the arm, the deformed specimens with a slot number of 3, 4, 5 and 6 were compared. As shown in Figure 5.9, fewer slots in the arms created less damage to the arms, as shown by the less plastic deformation in the arms. The arm area in the specimen with 3 arms underwent the least degree of deformation while the one with 6 arms was deformed the highest in the arms. However, only the specimen with 6 arms produced the highest plastic deformation in the central area, while for the rest, the highest deformation all occurred at the tips of the slots. As a result, the number of slots in the arm was kept to be 6.

## Biaxial Tension under Bending and Compression Test

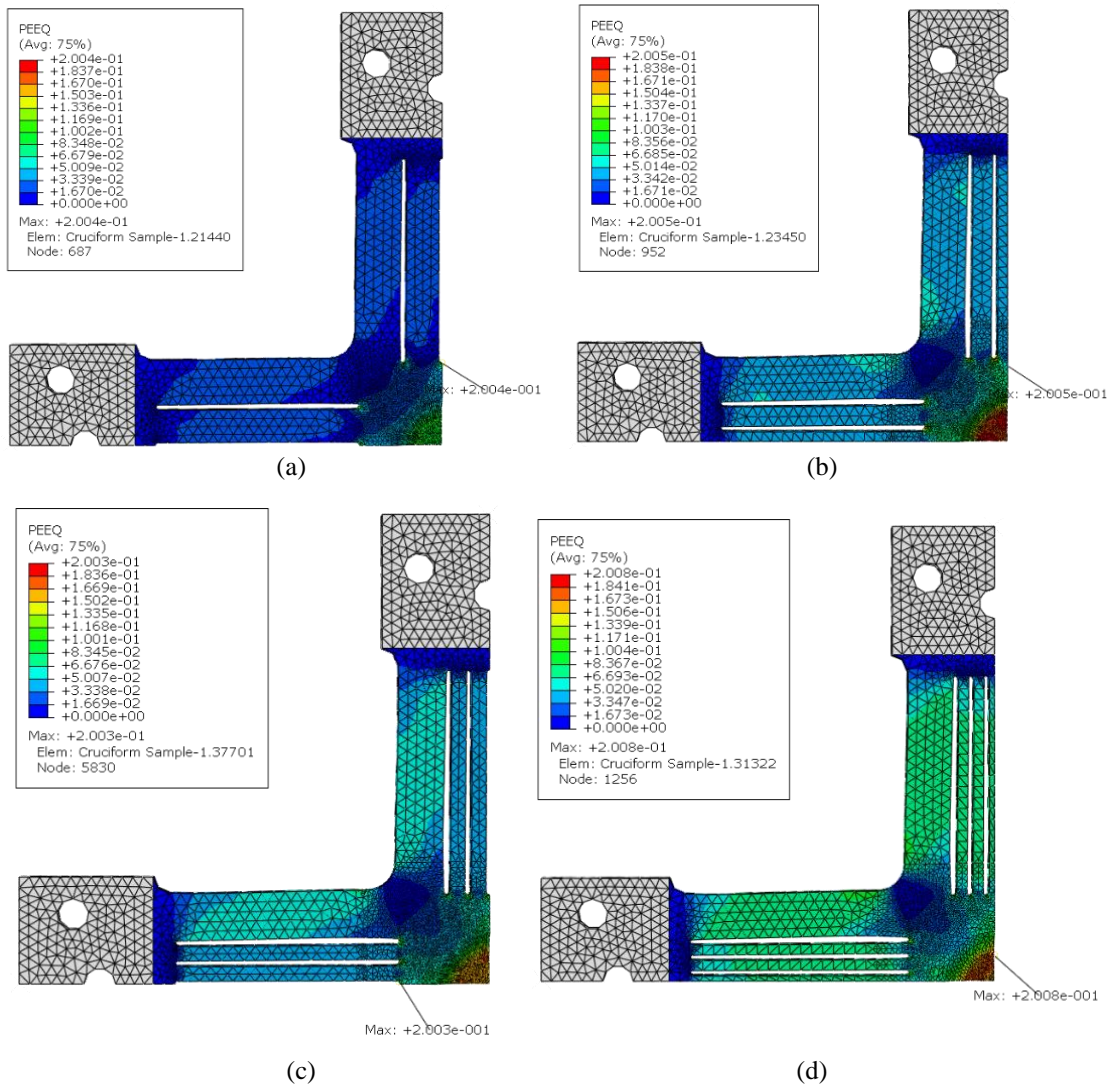


Figure 5.9 Strain distribution in the specimen with different numbers of slots in the arms: (a) 3 slots; (b) 4 slots; (c) 5 slots; (d) 6 slots

Combining all the results obtained from the FE optimization analysis, the geometry of the cruciform specimen for this study was decided and specimens were manufactured. Detailed dimensions of the optimized cruciform specimen are shown in Figure 5.10. The outer profile of the specimen was cut by electrical discharge machining (EDM). Then the holes, slots and central thickness reduction was machined by tools with different sizes. The front and back sides of the machined specimen can be seen in Figure 5.10.

The configuration of the test rig makes it difficult to measure material deformation in the target zone of the cruciform specimen with DIC devices or other method directly. In order to obtain the strain distribution on the surface of the specimen after each test, grid pattern was inscribed onto the surface of the specimen with laser, as shown in Figure 5.11. The grid consists of circles with a diameter of 1mm, and the pattern covered a central area of 10 mm × 10 mm. After deformation, the perfect circle would be distorted to be an

elliptical shape. By measuring the major and minor axes of the ellipse, and comparing those with the circle radius, the strain in each direction could be calculated.

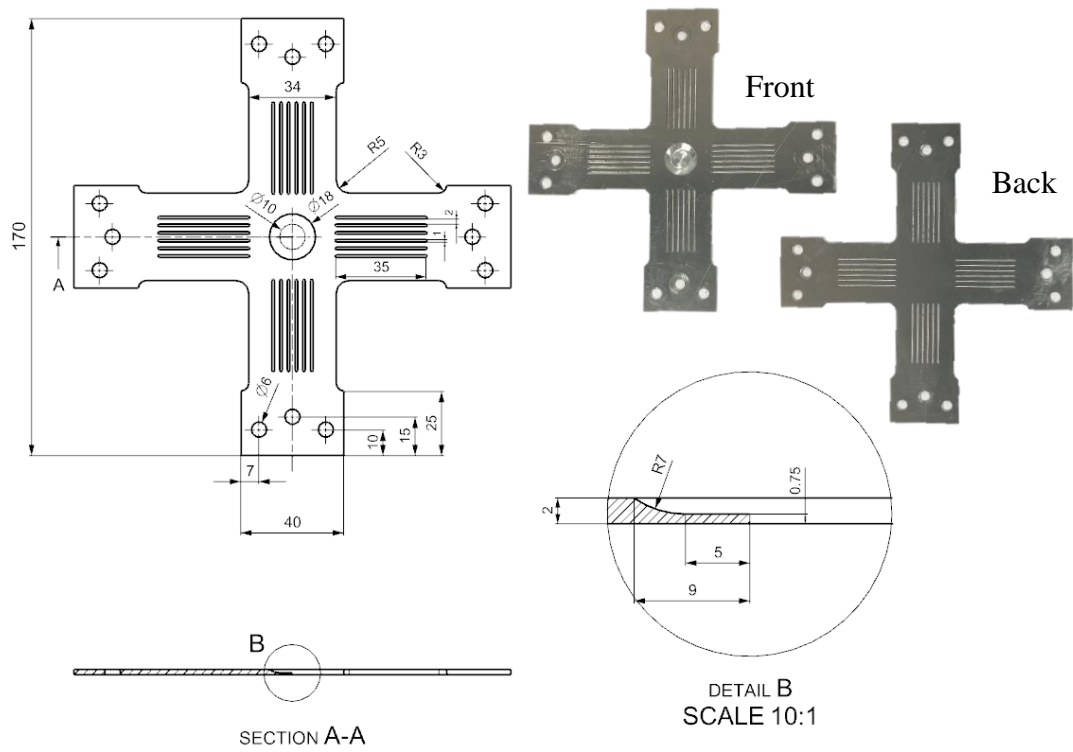


Figure 5.10 Optimized geometry of the cruciform specimen

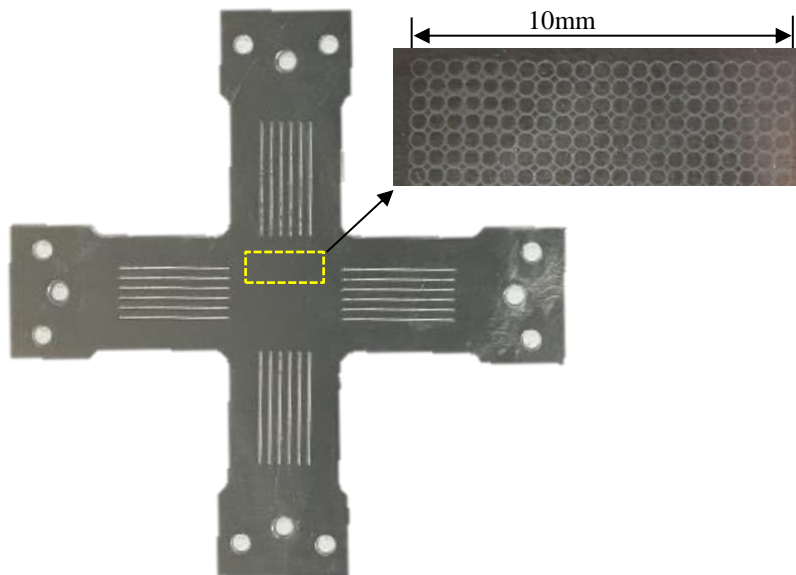


Figure 5.11 Grid inscribed onto the surface of the cruciform specimen

## 5.3 Design of the Experiment and Experimental Procedures

### 5.3.1 Design of the experiment

In order to investigate the influence of strain path on the material formability, the experiment was divided into two groups, corresponding to the two common strain conditions in ISF. As shown in Table 5.2, in the first group, the specimens were tested under plane strain condition, while in the second group, the specimens were loaded under equi-biaxial tension condition. For each group, five sets of tests were performed and in each test the specimen was under different loading condition, including: (a) pure tension; (b) bending with tension; (c) tension, bending with cyclic loading; (d) tension, bending and compression; (e) tension, bending and compression with cyclic loading. As a result, there were ten sets of experiment in total in the BTBC test. In this way, the effect of the loading conditions on the material formability under different strain paths could be investigated.

Table 5.2 Design of the experiment in the BTBC test

Test No.		Bending	Compression	Cyclic loading
1	Plane strain			
2		✓		
3		✓		✓
4		✓	✓	
5		✓	✓	✓
6	Biaxial			
7		✓		
8		✓		✓
9		✓	✓	
10		✓	✓	✓

The motor speed was set to be 35 rpm, creating a moderate tensile speed of the 2.5 mm/min by the slider, as adopted by Shao [112] in the biaxial tensile test. In the TCBC test, the bending depth of 6 mm and compressive force of 900 N produced an obvious improvement of material formability for the material AA5251-H22. Considering that in

the BTBC test, the bending tool head is hemispherical with a radius of 5 mm, the dual contact area between the tool, the supporting plate and the specimen should be a fraction of that in the TCBC test. Assuming that the radius of the contact area is 1 mm, the area of the contact zone should be about 1/6 of that in the TCBC test. As a result, in order to maintain a similar level of stress with the TCBC test, the bending depth was set to be 7 mm in the BTBC test. The stiffness of the spring used in the test was 23.4 N/mm, resulting in a supporting force of 163.8 N. The values of the process parameters are listed in Table 5.3.

Table 5.3 Values of the process parameters in the BTBC test

<b>Tested parameters</b>	<b>Parameter value</b>
Tensile speed	2.5 mm/min
Bending depth	7 mm
Compression force	163.8 N

Cyclic loading of tension, bending and compression onto the specimen was manually controlled. In the ISF test, the tool radius of 5-10 mm is commonly used while the vertical step per revolution about the central axis of the cone shape is 0.1-1 mm, which makes that the number of contact between the tool and the material is around 10 when the tool incrementally deforms the same region of the material. As a result, the unloading/loading process would be performed 10 times in each test where cyclic loading was required to be applied. The time gap between each unloading/loading process was 1/10 of the total time of the pure plane strain and pure biaxial tension tests before the fracture of the specimen. After the 10 cyclic loading, the specimen would be continuously deformed with the loadings until fracture occurred. The unloading of the bending effect was made by lifting up the bending tool until the contact between the tool and the specimen was removed. The unloading of tension was applied by reversing the motor rotation with a small angle so that the clamps were moved back and the tensile force was decreased to a minimal value.

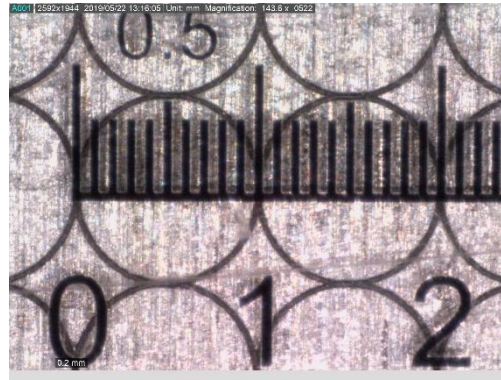


Figure 5.12 Measurement of the radii of the undeformed circles with the portable microscope

The deformation of the material can be determined by the distortion of the inscribed circles on the sheet surface in the planar directions. The radii of the circles were measured by a portable microscope, the original shape of the circles is shown in Figure 5.13. In order to obtain the maximum deformation of the material achieved before fracture, the radii of the circles close to the cracks were measured.

### 5.3.2 Experimental procedures

Before each test to commence, the spring and the steel cap were put in position if required. The specimen was placed on the clamps and secured by the bolts. In order to avoid the specimen surface damage caused by the bending tool when turning the bending tool to make it move downward, two circular covers of thin plastic were put on the centre of the specimen. The bending tool was carefully adjusted until the tip of the tool touched the top of the plastic covers. Then the specimen was bent by the bending tool to the tested bending depth specified in Table 5.3. The speed of the both motors was adjusted to the specified values and could be switched on simultaneously. When cyclic loading was required, the bending tool would be driven down and lifted up at the frequency as detailed in Section 5.3.1. The tension could also be released at the same frequency by reversing the motor until the tensile forces were reduced to minimal according to the load cell monitors. The specimen was deformed and stretched until fracture occurred. Each test was performed twice to capture enough data for analysis and to ensure the repeatability of the test.

## 5.4 Experimental Results

### 5.4.1 Plane strain condition

For the plane strain condition, fractured specimens in Tests 1-5 are shown in Figure 5.13. The relative position of the specimen in relation to the stretching direction is demonstrated

by the schematic. For the pure plane strain condition, the fracture occurred abruptly and a huge crack appeared across the central area of the specimen, as shown in Figure 5.13 (a). While with other loading conditions applied, the cracks were largely constrained to the centres of the specimens. In addition, the orientations of the cracks were all perpendicular to the stretching direction, suggesting that the tension applied contributed to the occurrence of fracture in all the tests.

The radii of the circles near the cracks were measured by using the microscope. As shown in Figure 5.14, for the measured circles, one radius was parallel to the crack, while the other radius line was perpendicular to the first one. For Tests 4 and 5, in which compression was involved, as shown in Figure 5.14 (d) and (e), the contact area between the tool and supporting plate was too small for a full deformed circle to be obtained for the measurement in that area near the crack. As a result, the distance or half distance of the crossing points between the inscribed circles was measured to determinate the strains.

The true strains in the two directions were calculated according to the measurement of the radii of the deformed circles, and they were plotted in the minor strain-major strain space in order to compare the material formability between different tests. As shown in Figure 5.15, the relative position of the calibrated area of the specimen in relation to the stretching direction is demonstrated by the schematic. Compared with the condition of pure plane strain with only tension, the other four tests all presented much higher forming limit when subjected to the more complicated loading conditions. Among these four conditions, generally, material forming limits under tension and bending condition showed the lowest forming limit (Test 2), followed by tension, bending and compression (Test 4), then tension, bending and cyclic loading (Test 3). Material showed highest formability under tension, bending, compression and cyclic loading (Test 5).

In addition, comparing Test 2 and Test 4, it was clear that material formability was slightly enhanced when compression was superimposed into tension and bending. By comparing Test 2 and Test3, Test 4 and Test 5, respectively, it was clear that the major strains in the tensile direction were increased significantly from roughly 0.15 to 0.19 and 0.16 to 0.22 respectively when cyclic loading was introduced. It indicated that the cyclic loading could improve the material forming limit considerably.

Biaxial Tension under Bending and Compression Test

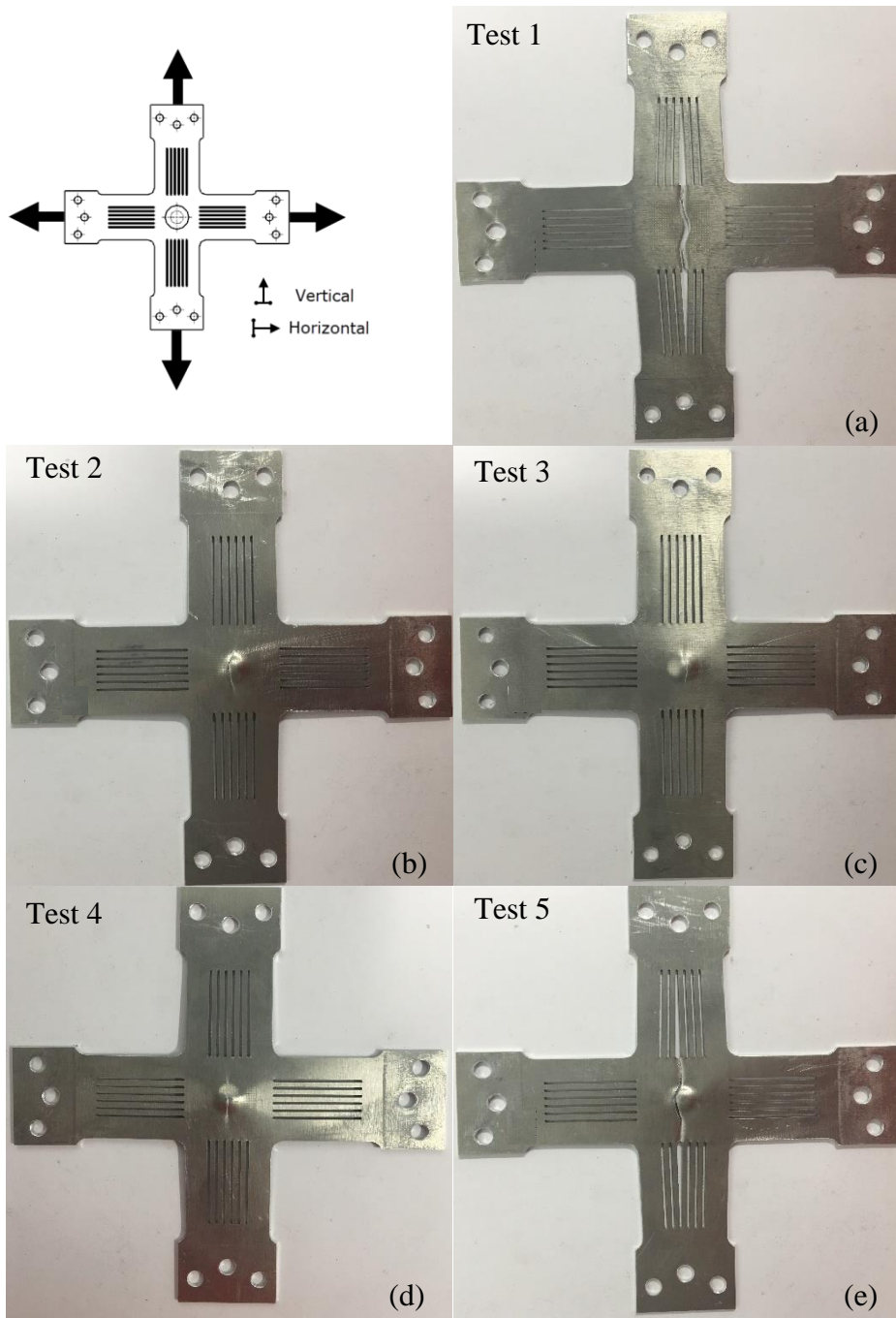


Figure 5.13 Specimens after deformation under plane strain condition: (a) pure tension; (b) tension and bending; (c) tension, bending and cyclic loading; (d) tension, bending and compression; (e) tension, bending, compression and cyclic loading

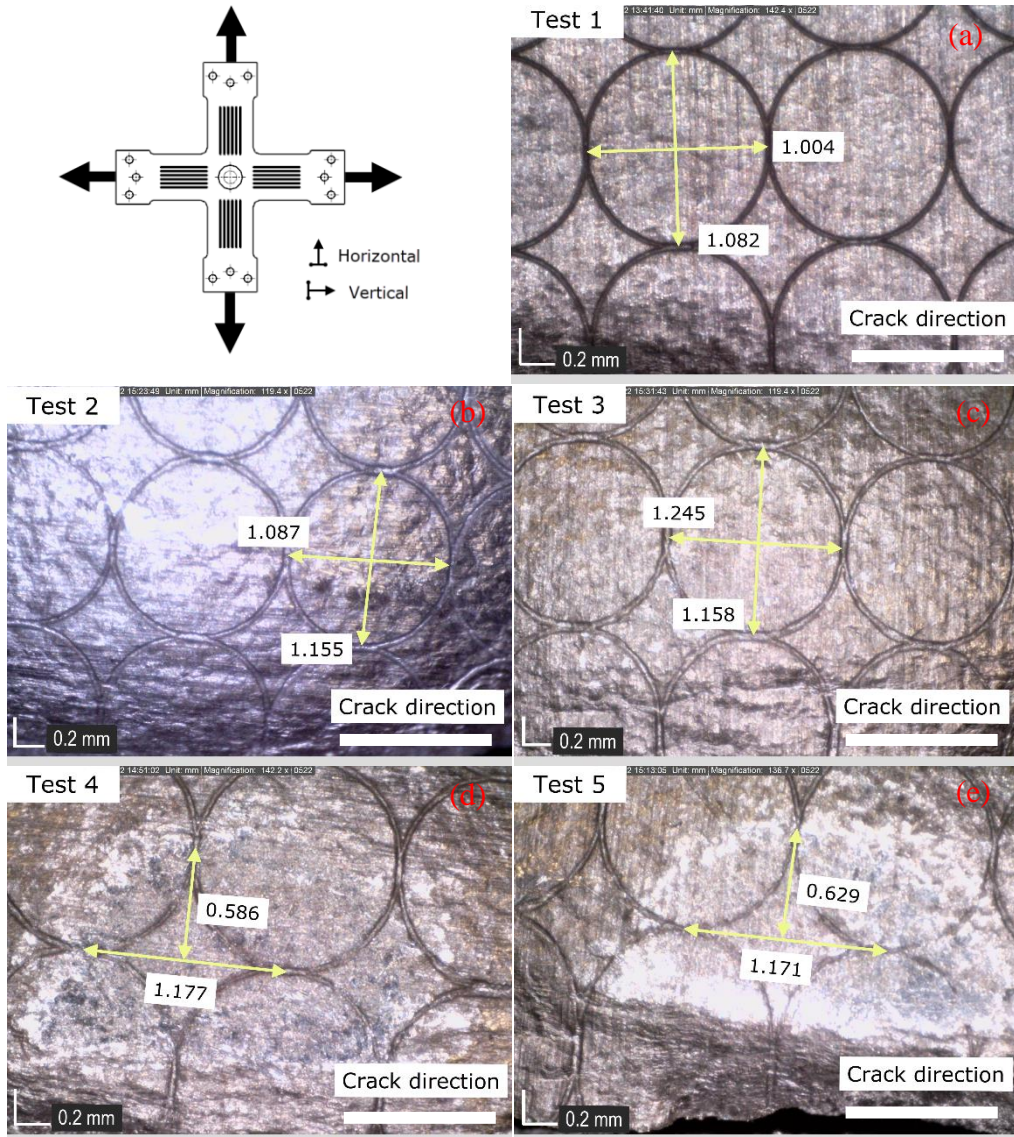


Figure 5.14 Deformed circles on the specimen surface under plane strain deformation: (a) pure tension; (b) tension and bending; (c) tension, bending and cyclic loading; (d) tension, bending and compression; (e) tension, bending, compression and cyclic loading

The loading conditions changed the plastic deformation history of the material in the tests. As can be seen in Figure 5.15, the distribution of the points in the Major strain-Minor strain space can be categorized into two types. In Test 1, the points were all close to the pure plane strain condition, while in the other four tests, the points were closer to equibiaxial tension condition. The difference was caused by the bending effect. In the tests, bending was applied by the bending tool with a hemispherical head. While bending was being applied and the arms were clamped, consequently the geometrical constraints led to biaxial deformation in the central area. However, when comparing Test 2 and Test 3, it is clear that the strain increment only happened in the major strain direction (the tensile

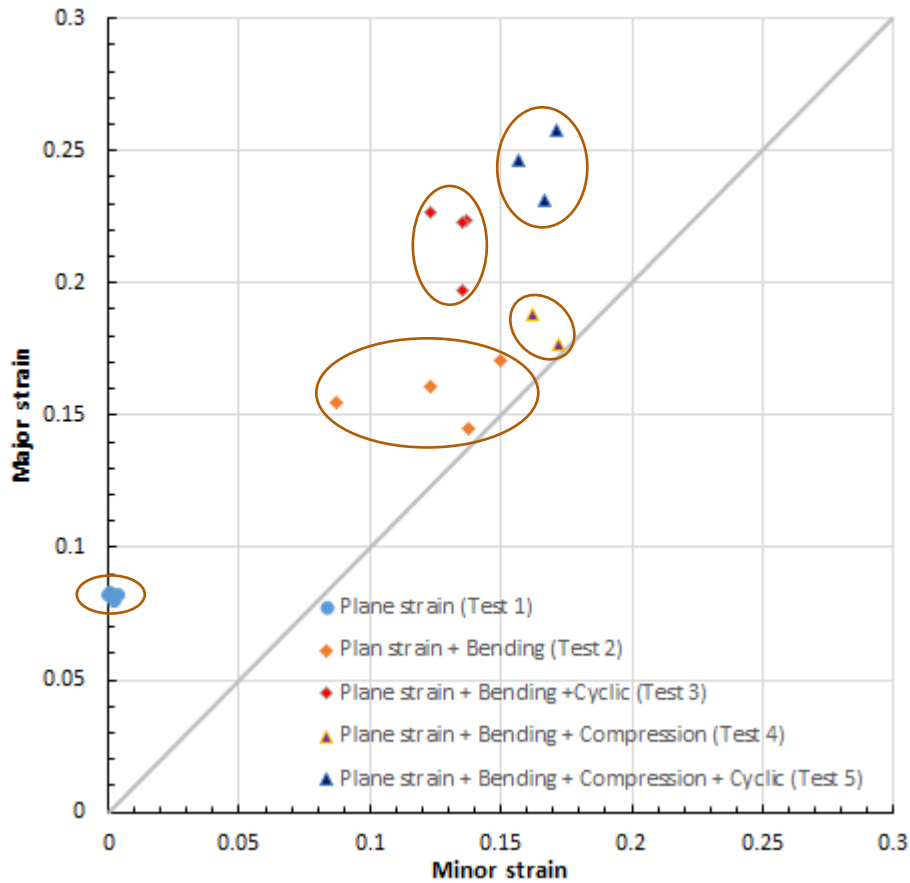


Figure 5.15 Formability improvement under BTBC loading conditions and plane strain condition

direction). The same trend can also be observed for the Test 4 and 5, suggesting the formability improvement in the tests under plane strain condition.

### 5.4.2 Equi-biaxial tension condition

The fractured specimens in Tests 6-10 are shown in Figure 5.16. The relative position of the specimen in relation to the stretching directions is demonstrated by the schematic. Similar to the Tests 1-5, the crack in the specimen under pure equi-biaxial tensile test also appeared across the central area, while in the other specimens, the cracks were more confined to the contact area between the tool and the specimen, especially in Tests 9 and 10. The two radii of the circles near the cracks, the distance or half distance of the crossing points between the inscribed circles were measured for the calculation of the strains, as shown in Figure 5.17. The cracks were also all perpendicular to the horizontal stretching direction, similar with that in the specimens under plane strain condition.

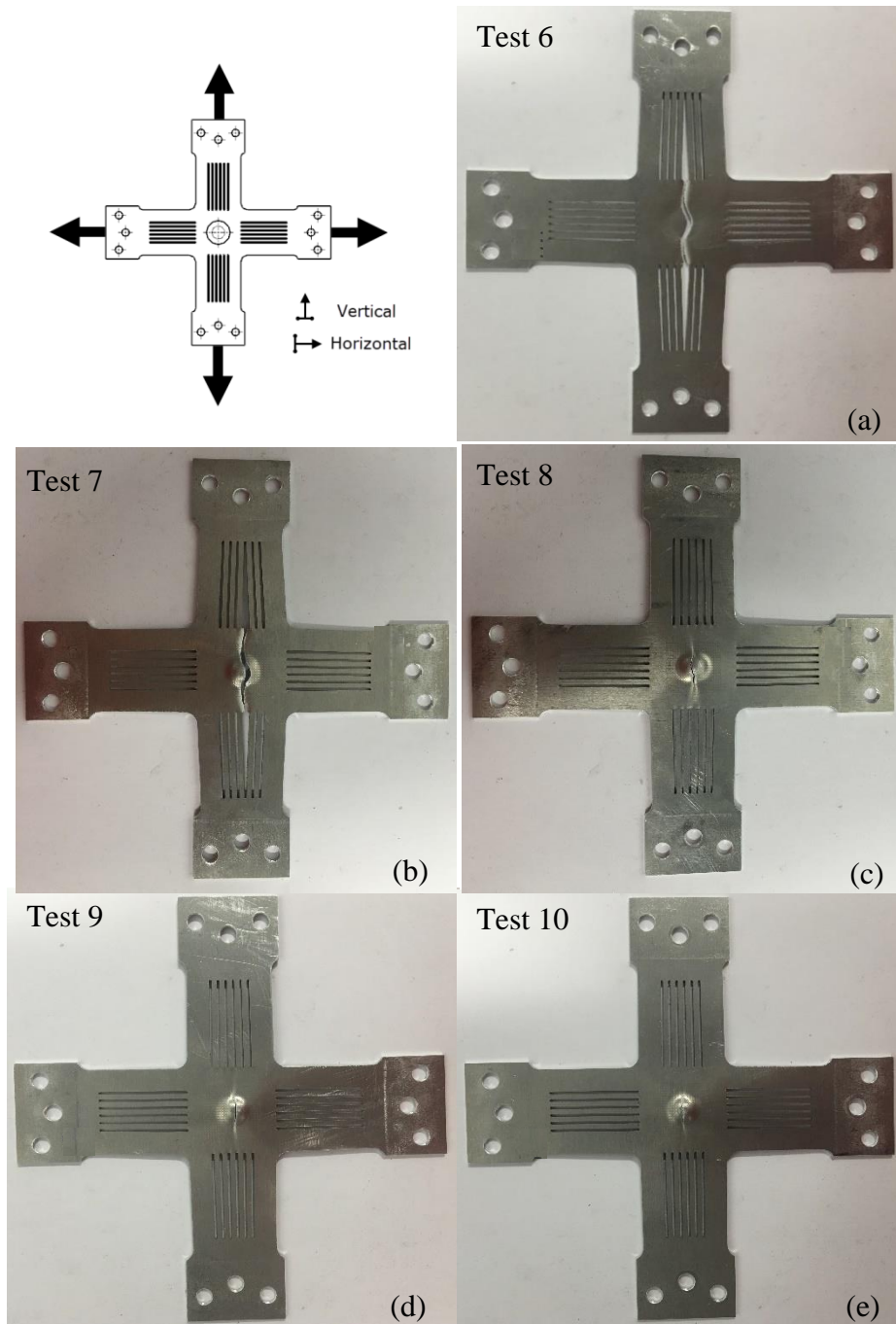


Figure 5.16 Specimens after deformation under equi-biaxial tension condition: (a) pure tension; (b) tension and bending; (c) tension, bending and cyclic loading; (d) tension, bending and compression; (e) tension, bending, compression and cyclic loading

## Biaxial Tension under Bending and Compression Test

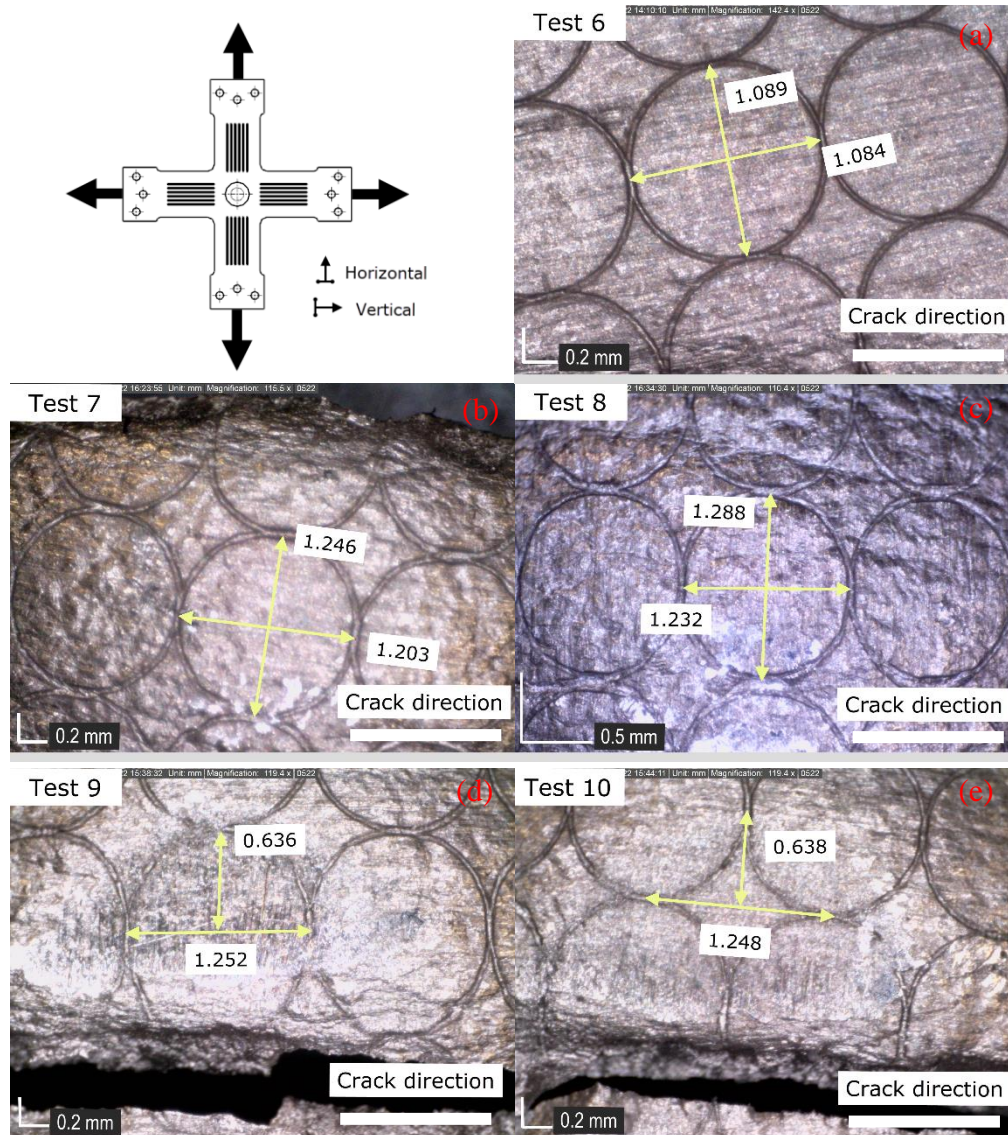


Figure 5.17 Deformed circles on the specimen surface in BTBC test under equi-biaxial tension condition: (a) pure tension; (b) tension and bending; (c) tension, bending and cyclic loading; (d) tension, bending and compression; (e) tension, bending, compression and cyclic loading

Based on the measurement, the true strains near the cracks were obtained, as plotted in Figure 5.18. The relative position of the calibrated area of the specimen in relation to the stretching direction is demonstrated by the schematic. Obviously, the formability of the material was increased when subjected to the complicated loading conditions. Moreover, when cyclic loading was applied to the tension and bending condition, the material formability was clearly increased, by comparing Tests 7 and 8. However, when cyclic loading was performed with tension, bending and compression, no clear formability enhancement can be observed, as shown in Tests 9 and 10. In addition, although introducing compression into bending and tension improved the material formability, as shown in Test 7 and Test 9, material deformation in Test 8 remained close to that in Test

9 and 10 as well, no clear boundary could be observed between these points shown in Figure 5.18.

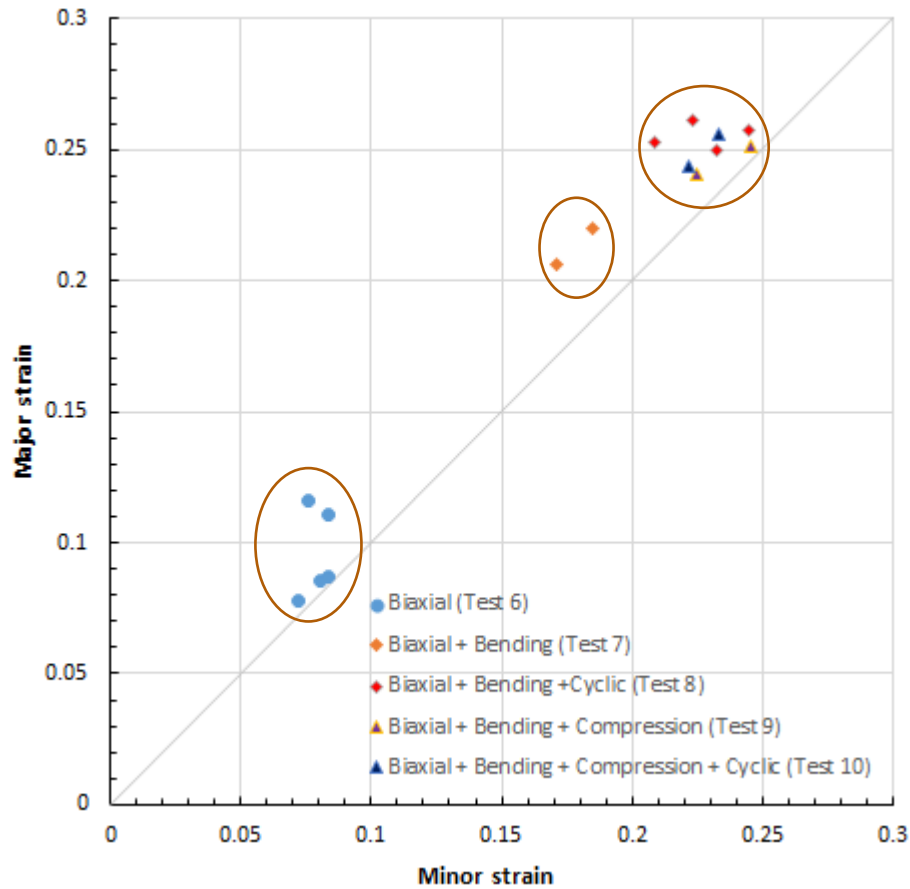


Figure 5.18 Formability improvement under BTBC loading conditions and equi-biaxial condition

Theoretically, under equi-biaxial tensile loading condition, the major strain and minor components in the central area of the specimen should be equal, especially for Test 7 to Test 10, in which the material deformation was more confined to the central area as confirmed in Figure 5.16. However, as shown in Figure 5.18, the strain components obtained from the tests were away from the grey equi-biaxial line, the difference between the major strain and the minor strain could be as large as 0.05, which was about 20% of the strain components. The difference between the material deformations in the planar direction could also be reflected by the direction of the cracks in the specimens. As shown in Figure 5.16, under equi-biaxial loading condition, the cracks were all perpendicular to the horizontal stretching direction, suggesting that the deformation in the horizontal direction was greater than that in the vertical direction.

The deviation of the strain states from the equi-biaxial tensile condition was caused by the mechanical structure of the developed rig. As shown in Figure 5.3, the tension in the two directions was applied to the specimen by the movement of the carriages in the

sliders. For the sliders, in order to move smoothly, the motors will not only overcome the tensile force ( $F_1, F_2$ ) respectively, but also the extra load ( $M_1, M_2$ ) onto the shaft from the moment. A schematic illustration of the loading on to the sliders is shown in Figure 5.19. Under equi-biaxial tensile condition, assuming that plastic anisotropy is ignored, the force required for the plastic deformation in the two transverse directions should be equal, that is  $F_1 = F_2$ . However, in order to apply biaxial tension on the same surface, slider 1 was positioned above slider 2, as a result, in the vertical direction, the distance between the clamps and the carriage surface in slider 1 ( $h_1$ ) is much larger than that in slider 2 ( $h_2$ ), leading to a higher moment for the carriages to overcome with in one direction than the other,  $M_1 > M_2$ . Higher moment will create higher pressure onto the slider shaft, and the difference between the loads in the two directions resulted in the mismatch of the movement of the two motors and ultimately the deviation of the strain states from the ideal equi-biaxial tensile state. As a comparison, in the commercial biaxial tensile testing platform developed by Roell/Zwick [122], the four motors are positioned on the same surface, consequently the loads the motors to be overcome in different directions are equal and a better synchronization of the motors can be achieved.

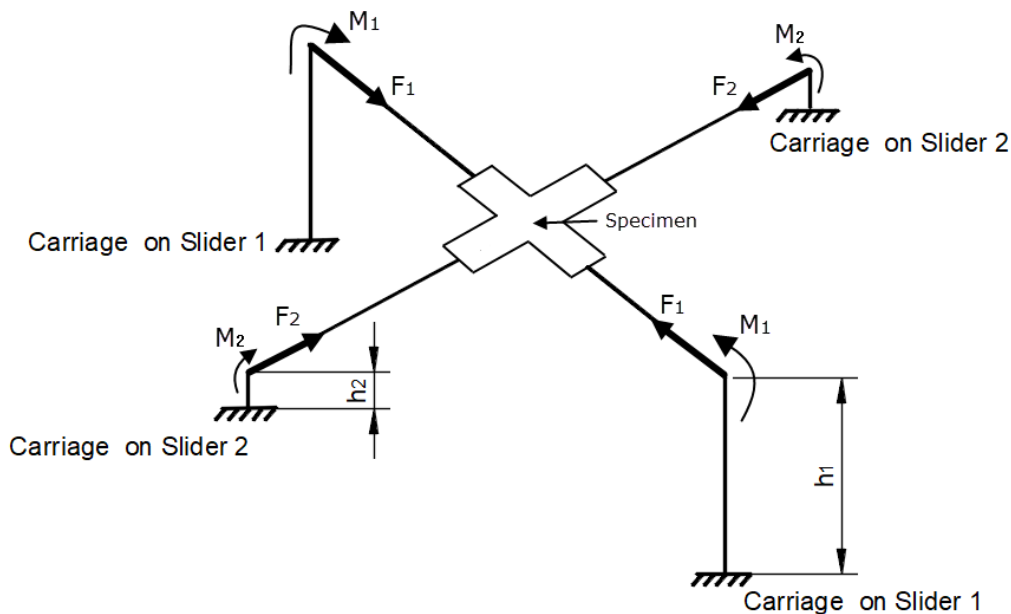


Figure 5.19 Schematic of the loading on to the sliders during the test

## 5.5 FE Modelling of BTBC Test

Similar to that in the TCBC test, the target area of the specimen was covered by the test rig in the BTBC test. To reveal the mechanism behind the material deformation in the BTBC test, FE modelling of the tests was performed.

### 5.5.1 FE model development

Considering the high non-linearity resulted from contact conditions and the large plastic material deformation, the FE modelling of the BTBC process was performed using the Abaqus/Explicit solver. Material AA5251-H22 was used in the model. As shown in Figure 5.20, same with the FE model for cruciform specimen optimization process, only a quarter of the specimen was modelled in order to save the computational time. The mesh of the specimen was also kept the same, as well as the element type.

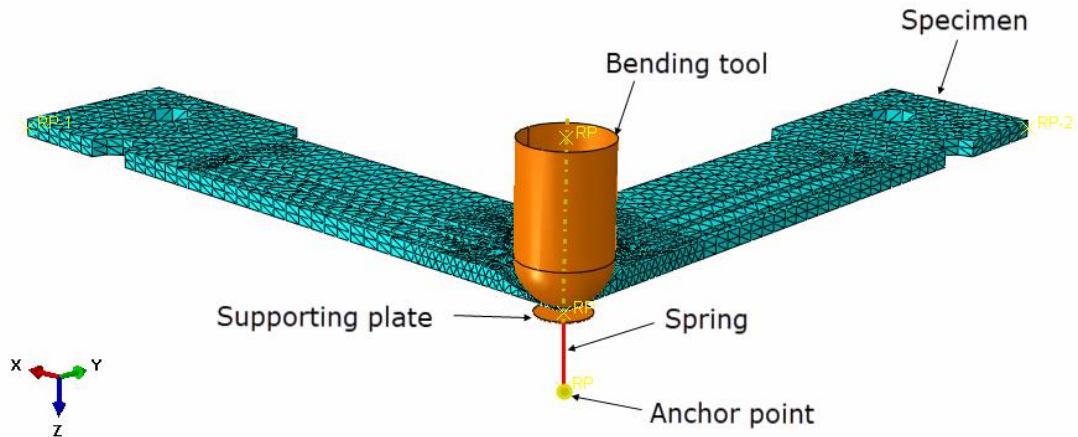


Figure 5.20 FE modelling of BTBC test

Bending was applied by the bending tool. As shown in Figure 5.20, a bending tool was positioned against the specimen, pointing to the centre of the specimen. In order to provide compression to the specimen, on the other side of the specimen, a plate was pressed closed to the surface, the plate was supported by a spring. The spring was supported by an anchor point, which was fixed. The stiffness of the spring was same to the one used in the tests, which was 23.4 N/mm. For the tests without compression effect, the supporting plate was excluded from the analysis. Friction was ignored in the FE model. The parameters in the FE models were kept consistent with those used in the experiment.

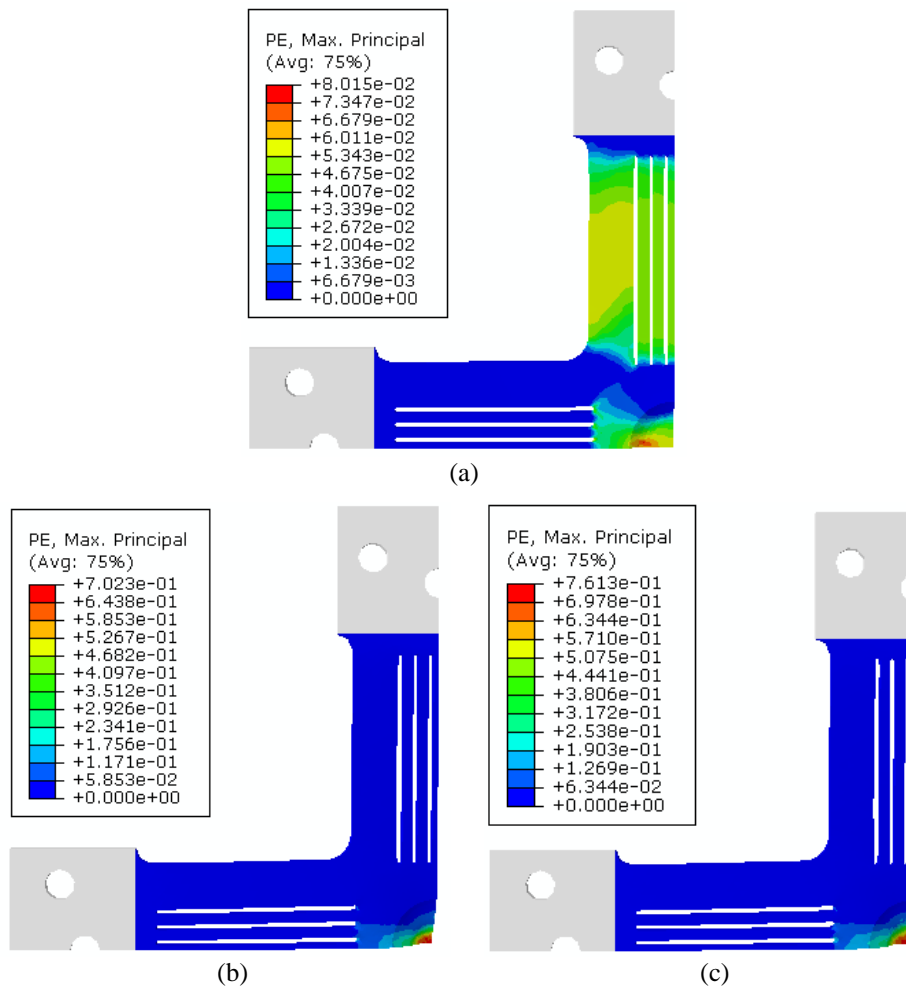
The bending tool and the supporting plate were defined as rigid bodies and their movements were controlled by the displacement boundary conditions. Two sets of FE models were developed, one for plane strain condition and another for equi-biaxial tension condition, corresponding to the experimental design. For the plane strain condition, one arm was fixed at the clamping area while the other arm followed the movement defined by the boundary condition. For the equi-biaxial tension condition, the two arms moved synchronically.

### 5.5.2 FE modelling results

#### 5.5.2.1 Distribution of material deformation in the specimens

According to the orientations of the cracks in the experimental tests, the maximum principal strain was chosen as the indicator of material deformation in the FE models. In the experiment, fracture of the specimen happened when the major strain was around 0.08 under plane strain condition. As a result, the distribution of the maximum principal strain in the specimen at the time when the maximum principal strain in the FE model of Test 1 reached 0.08 was extracted from the FE simulation results, as shown in Figure 5.21.

As shown in Figure 5.21 (a), under pure plane strain condition, the maximum principal strain peaked near the boundary of the central area, while when additional loading conditions were applied, the highest value of the maximum principal strain all shifted to the very centre of the specimen, which matched the shapes of the cracks observed in the experiment.



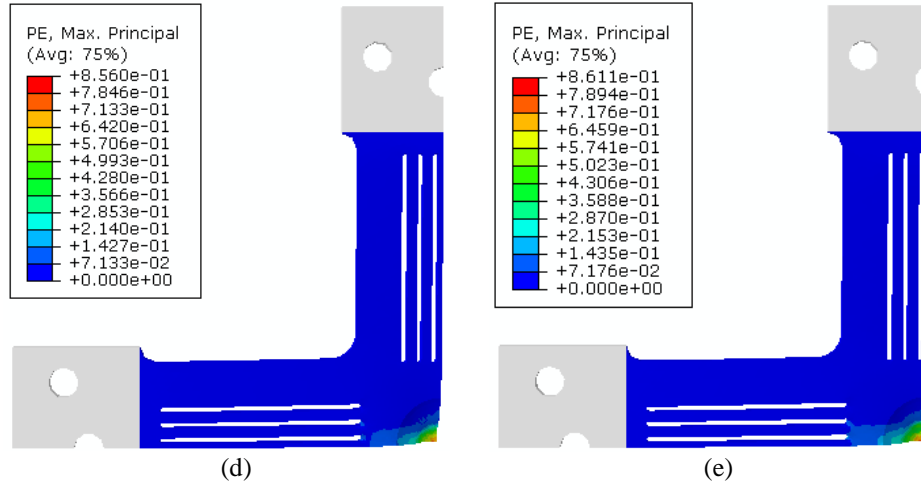
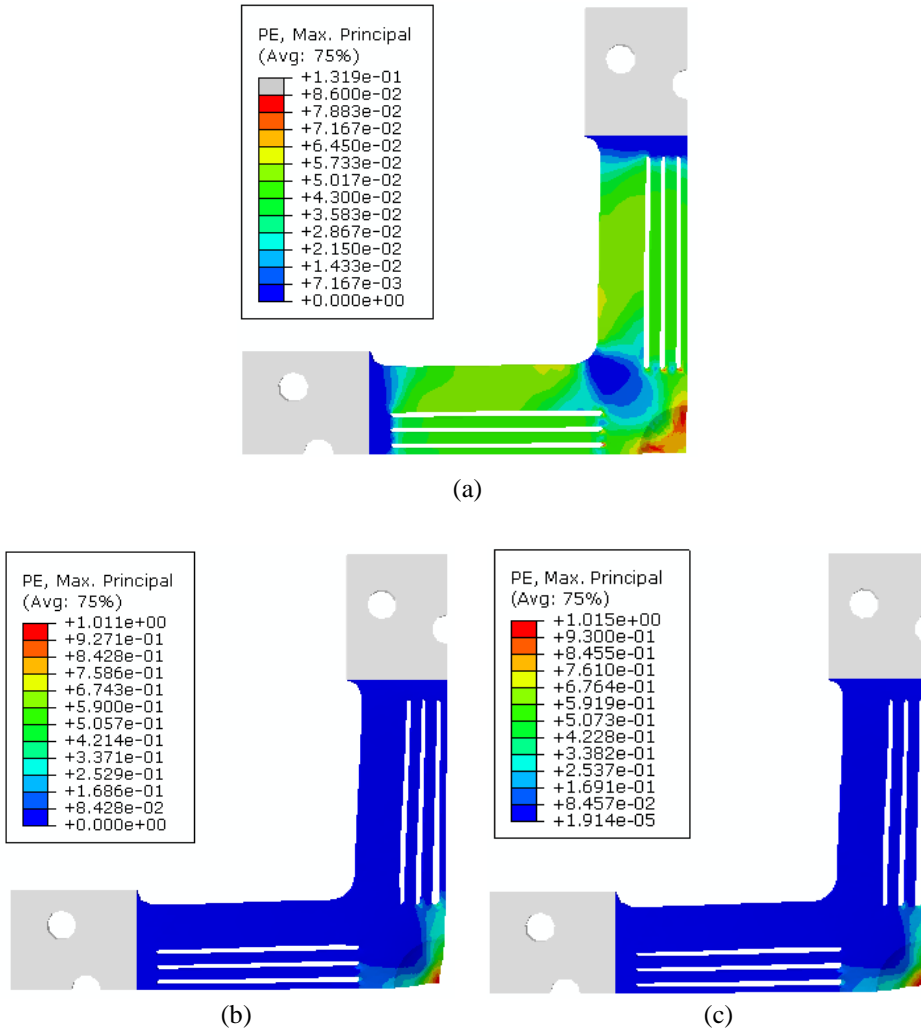


Figure 5.21 Distribution of maximum principal strain in the specimen under plane strain condition: (a) pure tension; (b) tension and bending; (c) tension, bending and cyclic loading; (d) tension, bending and compression; (e) tension, bending, compression and cyclic loading



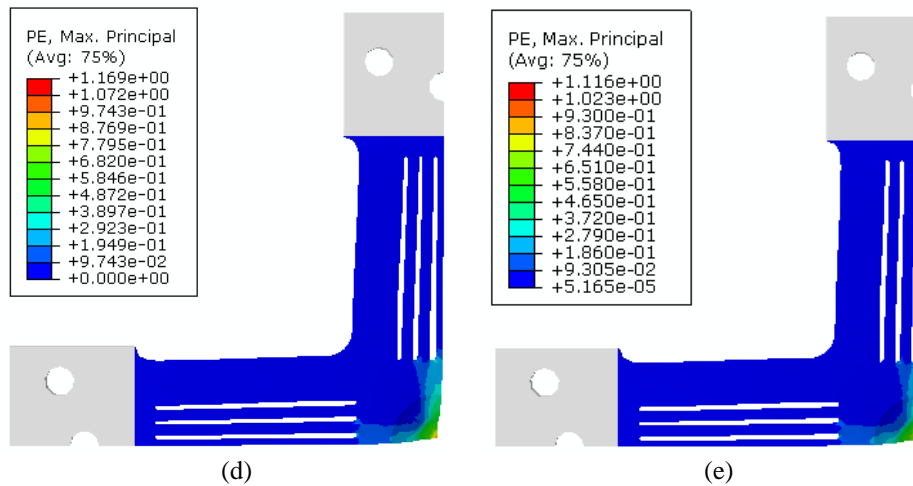


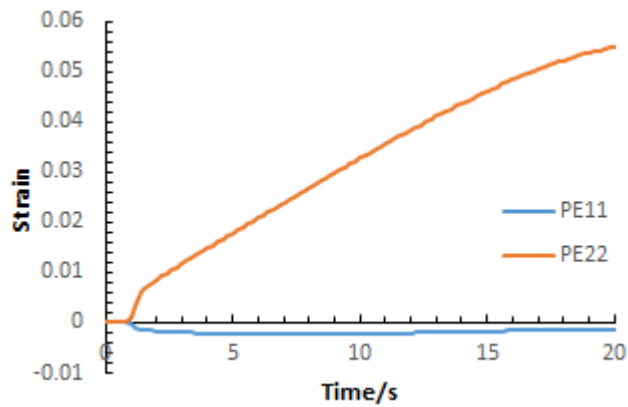
Figure 5.22 Distribution of maximum principal strain in the specimen under equi-biaxial tension condition: (a) pure tension; (b) tension and bending; (c) tension, bending and cyclic loading; (d) tension, bending and compression; (e) tension, bending, compression and cyclic loading

The introduction of bending and compression contributed to the localized material deformation. By comparing Figure 5.21 (b) and (c) with (d) and (e), it can be found that the distribution of the maximum principal strain was more homogeneous in the central areas in (b) and (c) than that in (d) and (e), indicating that the introduction of compression further strengthened localized material deformation. Similar contribution of the bending and compression effects to the localized deformation under equi-biaxial tension condition can also be observed from Figure 5.22. In Figure 5.22 (b) and (c), the area showing the highest level of maximum principal strain (red colour) was still quite obvious. By comparison, in Figure 5.22 (d) and (e), the maximum principal strain was constrained to the very centre of the specimen.

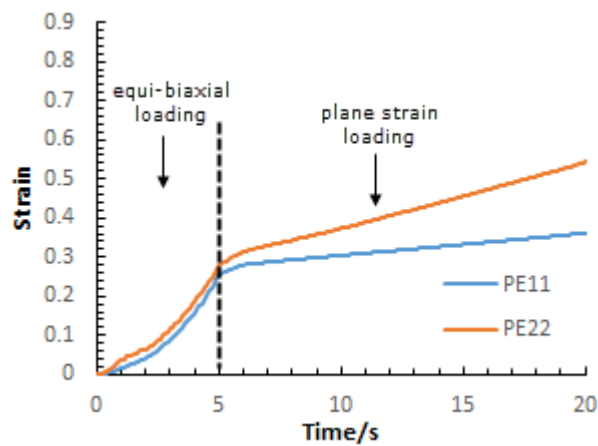
### 5.5.2.2 Material deformation under plane strain tensile loading

According to the experiment, for the equi-biaxial tensile conditions, the strain components in the central region of the specimens obtained in the BTBC test were close to be ideally equi-biaxial, as shown in Figure 5.18, which proved the application of the equi-biaxial tensile loading in the test was successful. However, as a comparison, for plane strain conditions, the obtained strain components shift away from the ideal plane strain condition, which is the y axis, except for the pure plane strain loading, as shown Figure 5.15. The deviation of the obtained strain modes from the ideal conditions resulted from the application of bending by the hemispherical tool. Equi-biaxial loading was applied to the central area of the specimen when the tool pushed the specimen to the designed depth. The equi-biaxial tensile condition might be strengthened when cyclic loading condition was applied in the test since multiple bending loadings existed in these

tests. How material was deformed by the application of plane strain loading condition to the central region of the specimen was not clear in the test. As a result, the evolution history of the plastic strain components in the two movement loading conditions was extracted from the FE modelling results, as shown in Figure 5.23. Under pure plane strain loading condition, as shown in Figure 5.23 (a), it is obvious that plastic strain in direction 1 is much higher than that in direction 2 and it is plane strain condition. When bending was first applied, in direction 1, the strain component increased from 0.26 to 0.36, while in the other direction, the strain component increased from 0.28 to 0.54, as shown in Figure 5.23 (b). When cyclic loading of bending was applied, the strain component increased from 0.26 to 0.30 in one direction and from 0.28 to 0.37, as shown in Figure 5.23 (c). A similar trend was also observed for the more complicated loading conditions with compression, as shown in Figure 5.23 (d) and (e).

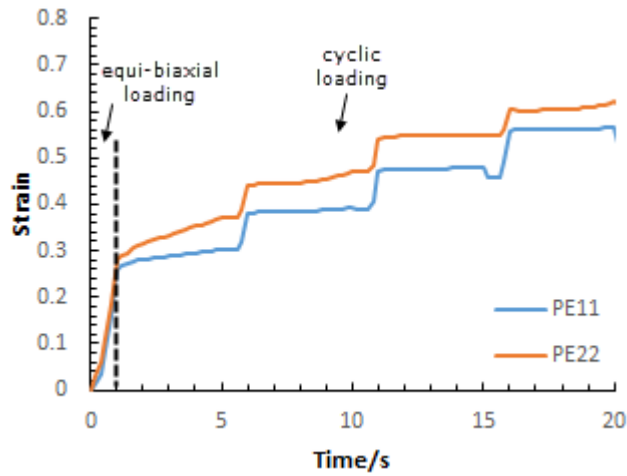


(a)

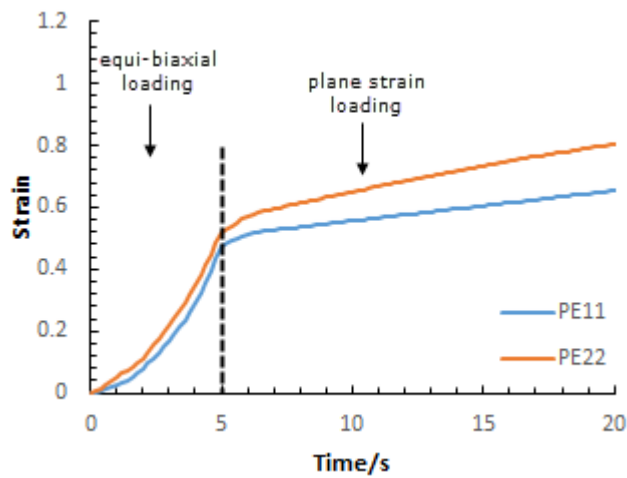


(b)

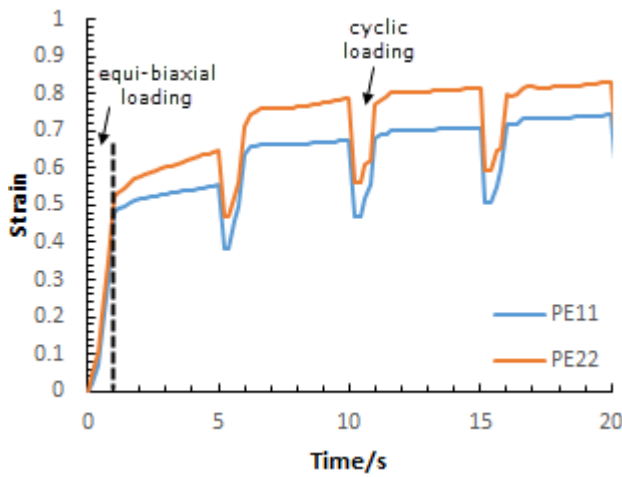
## Biaxial Tension under Bending and Compression Test



(c)



(d)



(e)

Figure 5.23 History of strain components of the element 51712 in the central region in the BTBC tests under different loading conditions: (a) pure plane strain; (b) plane strain and bending; (c) plane strain, bending and cyclic loading; (d) plane strain, bending and compression; (e) plane strain, bending, compression and cyclic loading

In general, under complicated loading conditions, the existence of bending tool changed the transmission of loading from the arms to the central area of the specimens. The ideal

plane strain condition was not perfectly maintained in the central region of the specimens. However, the difference between the strain components was still obvious even under complicated loading conditions, the material deformation in the direction in which the tensile loading was applied was much larger than that in the direction in which the arms were fixed.

#### 5.5.2.3 Effect of individual loading conditions

In order to investigate the effect of bending, compression and cyclic loading on the material deformation behaviour in the BTBC tests, the equivalent plastic strain history of three elements at the centre of the specimen along the thickness direction was also extracted from the FE simulation results of Test 3 and 5, in which cyclic loading was applied. The locations of the elements are shown in Figure 5.24. Only plane strain condition was analysed due to its obvious formability improvement under different loading conditions in the experimental tests.

As shown in Figure 5.24, it is obvious that the curves obtained from Test 5 were much higher than those obtained from Test 3, which meant higher degree of deformation at the centre of the specimen in Test 5. Different from the TCBC test, in which the rollers kept moving, creating contact areas prone to be plastically deformed between the rollers and the specimen, in the BTBC test, the area which was most significantly deformed in the specimen was almost the same. The introduction of compression in Test 5 led to a greater localized material deformation, confining the plastic deformation to the very centre of the specimen, the result was also consistent with the findings obtained from Figure 5.21.

Bending effect can be reflected by the different degrees of plastic deformation in the three elements along the thickness direction in the both tests. In Test 3, element 3 on the outer side of the specimen underwent the highest degree of deformation, element 2 on the central layer came second while element 1 on the inner side was the least deformed. By comparison, in Test 5, element 3 still was the most significantly deformed along the history; however, element 1 was the second and element 2 on the central layer was the last. The introduction of compression in Test 5 changed the distribution of deformation in the thickness direction. A possible explanation could be that the supporting force from the supporting plate strengthened the contact effect between the bending tool and the specimen, lowering the yielding stress thus leading to higher plastic deformation.

A clear pattern of loading cycles can be obtained from the stair-like evolution of the equivalent plastic strain. As shown in Figure 5.24, in both tests, material deformation

occurred when the bending or tension was applied. However, the deformation increase caused by the step of stretch-bending from the bending tool was higher than that caused by the step of tension in both tests, especially in Test 5. More specifically, judging from the duration of time, the increase was more obvious when the bending tool pushed the specimen to the designed depth at each cycle after relaxation of bending and stretching effect. While there was still increase from the application of subsequent biaxial tension, it was not as obvious as the former loading condition.

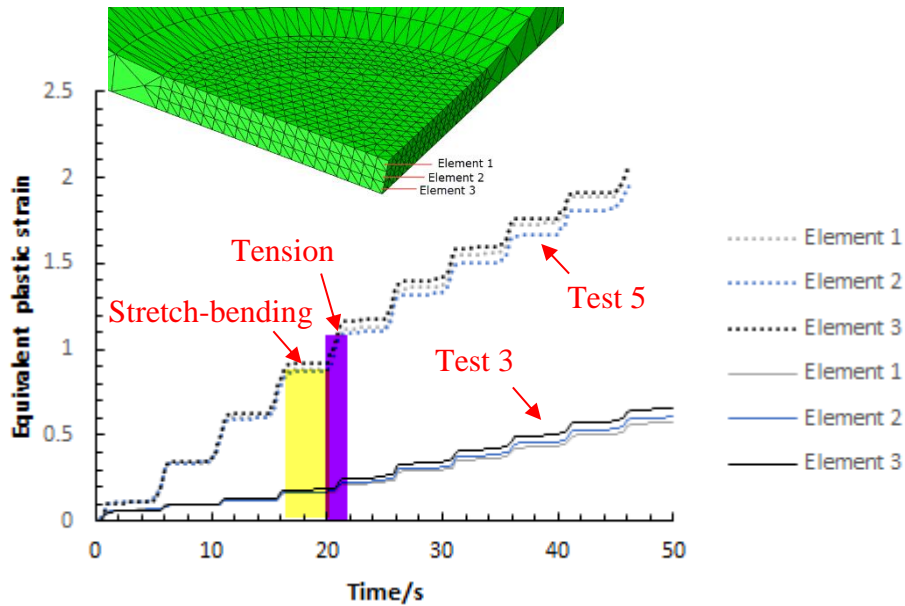


Figure 5.24 Strain evolution history of the elements in the centre under plane strain condition

Checking the FE models for Test 3, it was found that obvious springback occurred each time when bending and tension were relaxed, making the bending tool to deform the specimen before the application of biaxial tension, as shown in Figure 5.25. For Test 5, in which extra compression was applied, the bottom surface of the specimen was supported by the spring mechanism. Lifting the bending tool away from the specimen would not only trigger the springback of the specimen but also release the constraint on the spring, making the spring push the specimen. As a result, the difference between the specimen profiles before and after lifting the tool was higher than that in Test 3. Consequently, the equivalent plastic strain increment caused by the downward movement of the bending tool was more obvious in Test 5 than that in Test 3, as shown in Figure 5.24.

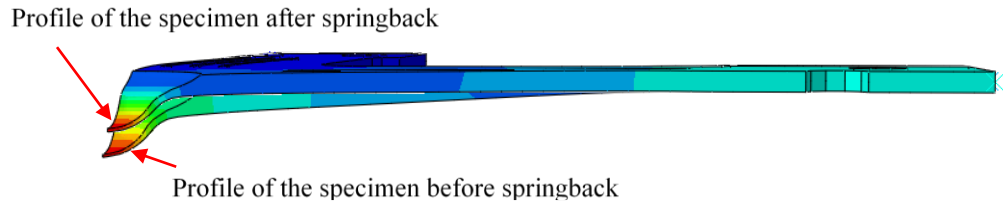


Figure 5.25 Springback detected in the FE model for Test 3

## 5.6 Discussion

### 5.6.1 The effect of BTBC loading conditions on material formability

Bending, compression and cyclic loading were successfully applied in the designed BTBC rig. Plane strain and equi-biaxial loadings onto the specimen were effective, as reflected by the trend of formability improvement in Figure 5.15 and Figure 5.18. The introduction of the bending, compression and cyclic loading onto biaxial tension contributed to the deformation localization and improved material formability of material AA5251-H22 in the BTBC test, under both plane strain condition and equi-biaxial tension condition. The finding was consistent with the research on the ISF process and that from the TCBC test. While the capability of allowing the change of the loading path makes the BTBC test a supplementary tool to the TCBC test for a more comprehensive understanding of the ISF processes.

Furthermore, as predicted by Centeno et al. [88] in the Nakazima test, the formability improvement in ISF could not be solely explained by bending under tension. From this perspective, based on the configuration of the tests, the BTBC test can be treated as a complimentary test to the Nakazima test. The introduction of compression and cyclic loading effect both further improved material formability in the BTBC test, as confirmed by the experimental tests and FE simulations.

Albeit the fact that similar loading conditions were applied in the BTBC test and the TCBC test, the difference of geometric constrains and loading patterns between the BTBC test and TCBC test led to different material deformation behaviours. In the TCBC test, the tension was constantly applied by the moving clamp from one end and it was pointed out in Chapter 4 that tension was a determinant part creating plastic deformation. As a result, the tension was never relaxed during the test and consequently no springback existed. While in the BTBC test, the deliberate relaxation of the applied loading conditions led to obvious springback, which intensified material deformation when reapplying the loading conditions, especially bending. As mentioned in the Chapter 1,

springback is an important feature in ISF, affecting geometric accuracy of the parts manufactured. According to the BTBC test, strong springback may also lead to higher plastic deformation caused by tension in the meridional direction in ISF process, which is resulted from the downward movement of the forming tool. Tension will lead to thickness reduction of the sheet. As a result, the sheet metal is weakened and its possibility of reaching higher plastic deformation is compromised.

The tested material presented different deformation behaviours under different loading paths. Under plane strain condition, it was clear that the application of bending improved material formability, which was further improved by the superimposition of compression. Moreover, when cyclic loading of the bending, compression and tension was applied, material formability could be further enhanced. The strains in the Major strain-Minor strain space were clearly separated.

By comparison, under the equi-biaxial tension condition, it was evident that bending helped improve material formability, which was further strengthened by cyclic loading or compression. However, introducing cyclic loading into bending and compression did not necessarily improved the material formability further. This phenomenon may be explained by the fact that compared with plane strain loading, under equi-biaxial loading, the material at the centre of the specimen was under larger degree of deformation after same time of deformation, as shown in Figure 5.21 and Figure 5.22. As a result, the sheet thickness was thinner under equi-biaxial condition, making it susceptible to the loading and more prone to fracture when the deformation was large enough. It may also be caused by the loading strategy adopted in the tests. In the tests with cyclic loading, instead of constantly applying the loading-unloading cycles until fractured happened, only ten cycles were applied. In biaxial loading condition, the application of compression or cyclic loading alone might have already contributed significantly to the localized deformation in the specimen, creating a similar degree of plastic deformation in the central area after certain cycles. Using different loading strategy may lead to a different result.

### 5.6.2 Limitations of current test

The limitations of the current test comes from two aspects, including the design of the test rig and the experimental test itself. The test rig has proved its capability to perform the BTBC test, providing different loading paths, bending depths and compressive forces. However, the application of bending and cyclic loading was totally manual, which inevitably would introduce errors into the test results. More effort should be devoted to

the improvement on the automation of cyclic loading in the rig. For example, another motor-powered loading system can be integrated with the bending tool so that the cyclic movement of the tool can be more precisely controlled.

The effect of the deformation modes themselves, including bending, compression and cyclic loading have not been investigated in the current test, considering that it had been successfully analysed in the TCBC test. However, it could be still beneficial to the understanding of material deformation behaviour under different loading conditions with variations of the magnitude of the deformation modes.

Furthermore, the application of bending with a bending tool introduced equi-biaxial loading into the test, which broke the consistency of the loading condition and might have an impact on the material deformation behaviour. More research on the influence of loading path on the material deformation behaviour should be devoted to clarifying the possible impact of the non-consistent loading path. Alternatively, modification to the test should be made to exclude the equi-biaxial loading from the plane strain condition.

## 5.7 Summary

Another new testing method, the biaxial tension under bending and compression (BTBC) test, is developed in this study to investigate the effect of loading path on the material formability enhancement under various deformation modes presented in ISF processes. Based on the results obtained from experimental testing and the FE modelling, the following conclusions can be made:

- Material formability can be improved under a combined deformation modes of biaxial tension, bending, compression and cyclic loading;
- The trend of formability improvement is different under different loading paths, it is more clear under plane strain condition than under equi-biaxial condition;
- The BTBC test could be used as a simplified representation of the material deformation in the DSIF process.

# 6 CONCLUSION AND PERSPECTIVES FOR FUTURE WORK

In this chapter, a conclusion of current research including a summary and contribution to the knowledge will be firstly presented in Section 6.1. Further work to tackle the limitations of the current research are outlined in Section 6.2.

## 6.1 Conclusion

In the field of metal forming, material deformation behaviour and formability in the forming processes are generally investigated by the material testing methods, for example uniaxial tensile test and shear test. Material testing methods provide a standard for the comparison of the material deformation behaviour as well as a simplified perspective to understand material deformation behaviour in the more complicated metal forming process. However, in ISF process, materials present distinct deformation behaviour from the conventional sheet metal forming processes, which cannot be directly explained by the current existing material testing methods. While at the same time, the complexity of the ISF processes makes the current investigation into the loading conditions (deformation modes) in ISF simply descriptive and empirical, how these loading conditions affects the deformation behaviour in ISF independently and interactively have not been clearly investigated in the published literature.

The TCBC test and the BTBC test provide another solution to understand a complicated sheet metal forming process. Fundamentally, material deformation in a sheet metal forming process is driven by the three factors, material properties, loading conditions and loading path.

According to the published research and experimental test and FE simulations of ISF process in this research, it has been confirmed that material deformation in ISF was related to material types and the effect of tension, bending, shearing and cyclic effects existed in ISF process. The delayed fracture in ISF process was also observed in ISF by FE damage modelling of ISF process using the shear-modified GTN model. In the TCBC test, the combination of these loading conditions was applied onto the material in a simplified manner. The individual and combined effects of the loading conditions were successfully analysed by experimental tests and FE simulations. The unique characteristics of localized plastic deformation and enhanced material formability in ISF were also observed in the TCBC test. The effect of the material types on the material formability in ISF was also tested by using different types of materials in the TCBC test. The TCBC test was proved to be capable to represent material deformation in ISF.

Plane strain condition and equi-biaxial stretching condition are the two most common strain conditions observed in ISF process. However, in the TCBC test, the strain path effect was not considered. In the BTBC test, the material deformation behaviour under different combinations of the loading conditions and different loading paths was examined. It opened up a way to understanding the formability enhancement in SPIF and DSIF when manufacturing different geometries. The combination of the TCBC tests and the BTBC test provides an alternative to understand the complicated ISF process in a more fundamental and simplified way.

### 6.1.1 Summary

This Ph.D. research is focused on the mechanism of material formability enhancement and fracture behaviour in the ISF process. In order to reveal the deformation behaviour of material AA5251-H22 and AA6082-T6, experimental test of SPIF process with the materials were conducted. To reveal material deformation characteristics during the forming process, FE damage modelling of both SPIF and DSIF processes with the shear-modified GTN model was performed. According to the experimental and FE simulation results, it can be concluded that:

- Localized material deformation is the main deformation characteristic in ISF, including SPIF and DSIF, material deformation only occurs when the forming tool(s) moves close or is in contact with the material;
- Tensile, bending, shearing and cyclic effects all exist in SPIF, while in DSIF, in addition to these effects, compressive effect is also influential to the material deformation behaviour;
- The shear-modified GTN model is not suitable for modelling the ISF process of material AA5251-H22 due to the drawbacks of the model itself and the complex deformation modes and loading conditions in ISF, its applicability in ISF process may depend on the material properties.

Since material formability can be influenced by both the loading conditions and the loading path, considering the complicated geometrical constraints and loading history, simplified testing methods, including the Tension under Cyclic Bending and Compression (TCBC) test and the Biaxial Tension under Bending and Compression (BTBC) test were proposed in this research. Based on the concepts, corresponding test platforms were designed and manufactured. Using the developed test platforms, material tests were carried out based on the design of the experiment respectively. FE simulations of the test processes were carried out to explain the deformation behaviour in the experiment. The influence of deformation modes (loading conditions) on the material formability was investigated in the TCBC test, based on the results from all the experiment and FE simulations, conclusions can be made as follows:

- The investigated deformation modes contribute to the localized material deformation in TCBC test, making it to be a suitable simplified investigating method for the complicated ISF process;
- Different materials present different degree of material formability enhancement in TCBC, material AA5251-H22 is more sensitive to the loading conditions than AA6082-T6;
- The compression force is the most significant factor affecting the material formability in TCBC test for both AA5251-H22 and AA6082-T6;
- The shear-modified GTN model is effective in predicting the deformation in tension-dominated TCBC test while it introduces considerable inaccuracy

when stress triaxiality is relatively low, which is the case in the DSIF process and the BTBC test.

Investigating the influence of loading path on the material formability under complex loading conditions, the BTBC test is complementary to the TCBC test since the loading path is ignored in the TCBC test. According to the experimental and FE simulation results, following conclusions can be made:

- The investigated deformation modes contribute to the formability enhancement in BTBC test under both plane strain condition and equi-biaxial tension condition;
- Loading path has a deciding effect on the material formability, under plane strain condition, the material formability can be clearly improved step by step if bending, compression and cyclic loading is superimposed to tension in different tests. However, under equi-biaxial tension condition, material formability would not show clear improvement when additional deformation modes were applied.

### 6.1.2 Contribution to the Knowledge

Based on the factors affecting material formability, including material mechanical properties, loading conditions and loading paths, this Ph.D. project proposed simplified testing methods to investigate formability and fracture behaviour in the ISF process. The contribution of this research to the knowledge lies in:

- Identifying the key deformation modes in ISF with FE damage model and evaluated the applicability of the shear-modified GTN model in the deformation processes with complex loading conditions;
- Proposing two simplified material testing methods to investigate the effect of key factors, including material mechanical properties, loading conditions and loading paths on the material deformation behaviour and fracture behaviour in ISF;
- Developing two material testing platforms to conduct the tests, by analysing the test results, the influence of the investigated factors on material deformation behaviour was examined, based on which guidance for the ISF process was proposed.

## 6.2 Perspectives for Future Work

In the current research, the shear-modified GTN damage model has been proved not suitable for predicting fracture for the test material AA5251-H22 in the ISF process, however it identifies the progressive damage accumulation during the process, unveiling some of the deformation behaviours in ISF process. The damage modelling of ISF process is still a promising method in investigating material deformation in ISF process. The limited applicability of GTN-related damage models in ISF may result from the limitations of the damage models in modelling materials with different mechanical properties or micro-structures, or different and complicated loading conditions, as discussed in Chapter 3. Two possible solutions can be made to improve the current research. First of all, the influence of the material types on the applicability of GTN-related damage model in ISF modelling should be examined, more materials should be tested if possible. In addition, if a more suitable damage model could be found in the currently existing damage models or could be developed to model ISF process, a better presentation of the ISF material damage development can be made.

A better description of the material deformation behaviour, for example Bauschinger effect and the material anisotropy will contribute to a more accurate prediction in the sheet metal forming process. By comparing force predictions made by FE simulation using isotropic and kinematic hardening models in SPIF, Flores et al. [239] reported that an accurate simulation of material in SPIF required a mix-hardening model. While in the BTBC test, material anisotropy can be more obvious. Introducing material anisotropy in to the FE modelling of BTBC test will improve the accuracy of the results.

The developed test rigs in the current research have been proved to be capable to perform the tests, however they have a few limitations. To achieve an in-depth understanding of the ISF process, adjustment to the test rigs can be made. For the TCBC test rig, shearing effect is currently ignored, as well as the relative position between the bending tool and the compression tool. How to bring shearing deformation mode into the specimen and making it adjustable are useful. In addition, the tools' sizes are fixed so that the bending effect is partially investigated. The test rig can be more versatile, more features can be added into the test rig so that more variations of the process parameters can be tested, creating a more comprehensive investigation of ISF.

For the BTBC rig, the cyclic loading can only be manually applied, which can be both time consuming and is dependent on the operator, an improvement to the automation of the test rig can increase the test efficiency and accuracy of the test.

# 7 REFERENCES

- [1] *DIN 8582 Manufacturing processes forming - Classification, subdivision, terms and definitions*. 2003, Deutscher Normenausschuß: Beuth Verlag, Berlin.
- [2] Altan, T., B. Lilly, and Y. Yen, *Manufacturing of dies and molds*. CIRP Annals-Manufacturing Technology, 2001. **50**(2): p. 404-422.
- [3] Walczyk, D.F. and D.E. Hardt, *Design and analysis of reconfigurable discrete dies for sheet metal forming*. Journal of Manufacturing Systems, 1998. **17**(6): p. 436-454.
- [4] Haas, E., R.C. Schwarz, and J.M. Papazian, *Design and test of a reconfigurable forming die*. Journal of Manufacturing processes, 2002. **4**(1): p. 77-85.
- [5] Yang, S., et al., *Influences of process and material parameters on quality of small-sized thin sheet-metal parts drawn with multipoint tooling*. Procedia Manufacturing, 2018. **15**: p. 992-999.
- [6] Hussain, G. and L. Gao, *A novel method to test the thinning limits of sheet metals in negative incremental forming*. International Journal of Machine Tools and Manufacture, 2007. **47**(3): p. 419-435.
- [7] Skjødt, M., M.H. Hancock, and N. Bay. *Creating helical tool paths for single point incremental forming*. in *Key Engineering Materials*. 2007. Trans Tech Publ.
- [8] Malhotra, R., N. Reddy, and J. Cao, *Automatic 3D spiral toolpath generation for single point incremental forming*. Journal of manufacturing science and engineering, 2010. **132**(6): p. 061003.
- [9] Lu, B., et al., *Feature-based tool path generation approach for incremental sheet forming process*. Journal of Materials Processing Technology, 2013. **213**(7): p. 1221-1233.
- [10] Emmens, W., A. Boogaard, and D. Weijde, *The FLC, enhanced formability, and incremental sheet forming*. 2009.
- [11] Amino, M., et al. *Current status of "Dieless" Amino's incremental forming*. in *11th International Conference on Technology of Plasticity, ICTP 2014*. 2014. Nagoya, Japan: Procedia Engineering.

- [12] Jeswiet, J., et al., *Asymmetric single point incremental forming of sheet metal*. CIRP Annals-Manufacturing Technology, 2005. **54**(2): p. 88-114.
- [13] Lu, B., et al., *Titanium based cranial reconstruction using incremental sheet forming*. International Journal of Material Forming, 2014: p. 1-10.
- [14] Edward, L., *Apparatus and process for incremental dieless forming*. 1967, Google Patents.
- [15] Emmens, W., G. Sebastiani, and A.H. van den Boogaard, *The technology of incremental sheet forming—a brief review of the history*. Journal of Materials Processing Technology, 2010. **210**(8): p. 981-997.
- [16] Li, Y., et al., *A review on the recent development of incremental sheet-forming process*. The International Journal of Advanced Manufacturing Technology, 2017: p. 1-24.
- [17] Behera, A.K., et al., *Single point incremental forming: An assessment of the progress and technology trends from 2005 to 2015*. Journal of Manufacturing Processes, 2017. **27**: p. 37-62.
- [18] Li, J., J. Shen, and B. Wang, *A multipass incremental sheet forming strategy of a car taillight bracket*. The International Journal of Advanced Manufacturing Technology, 2013. **69**(9-12): p. 2229-2236.
- [19] Zhang, H., et al., *Thickness control in a new flexible hybrid incremental sheet forming process*. Proceedings of the Institution of Mechanical Engineers, Part B: Journal of Engineering Manufacture, 2017. **231**(5): p. 779-791.
- [20] Ambrogio, G., et al., *Application of Incremental Forming process for high customised medical product manufacturing*. Journal of Materials Processing Technology, 2005. **162**: p. 156-162.
- [21] Allwood, J.M., D. Braun, and O. Music, *The effect of partially cut-out blanks on geometric accuracy in incremental sheet forming*. Journal of Materials Processing Technology, 2010. **210**(11): p. 1501-1510.
- [22] Ambrogio, G., et al., *Influence of some relevant process parameters on the dimensional accuracy in incremental forming: a numerical and experimental investigation*. Journal of Materials Processing Technology, 2004. **153**: p. 501-507.
- [23] Bambach, M., B.T. Araghi, and G. Hirt, *Strategies to improve the geometric accuracy in asymmetric single point incremental forming*. Production Engineering, 2009. **3**(2): p. 145-156.
- [24] Micari, F., G. Ambrogio, and L. Filice, *Shape and dimensional accuracy in single point incremental forming: state of the art and future trends*. Journal of Materials Processing Technology, 2007. **191**(1): p. 390-395.
- [25] Wagoner, R.H., H. Lim, and M.-G. Lee, *Advanced issues in springback*. International Journal of Plasticity, 2013. **45**: p. 3-20.
- [26] Silva, M. and P. Martins, *Two-point incremental forming with partial die: theory and experimentation*. Journal of materials engineering and performance, 2013. **22**(4): p. 1018-1027.
- [27] Tanaka, S., et al. *Residual stress in sheet metal parts made by incremental forming process*. in *Proceedings of the 9th International Conference on Numerical Methods in Industrial Forming Processes*. 2007. AIP Publishing.

- [28] Wang, Y., et al. *Experimental study on a new method of double side incremental forming*. in *Proceedings of the 2008 International Manufacturing Science and Engineering Conference, MSEC*. 2008.
- [29] Malhotra, R., et al., *Improvement of geometric accuracy in incremental forming by using a squeezing toolpath strategy with two forming tools*. *Journal of manufacturing science and engineering*, 2011. **133**(6): p. 061019.
- [30] Lu, B., et al., *Investigation of material deformation mechanism in double side incremental sheet forming*. *International Journal of Machine Tools and Manufacture*, 2015. **93**: p. 37-48.
- [31] Smith, J., et al., *Deformation mechanics in single-point and accumulative double-sided incremental forming*. *The International Journal of Advanced Manufacturing Technology*, 2013. **69**(5-8): p. 1185-1201.
- [32] Reddy, N.V. and R. Lingam. *Double Sided Incremental Forming: Capabilities and Challenges*. in *Journal of Physics: Conference Series*. 2018. IOP Publishing.
- [33] Malhotra, R., et al., *Accumulative-DSIF strategy for enhancing process capabilities in incremental forming*. *CIRP Annals-Manufacturing Technology*, 2012. **61**(1): p. 251-254.
- [34] Banabic, D., et al., *Advances in anisotropy and formability*. 2010. **3**(3): p. 165-189.
- [35] Embury, J. and J. Duncan, *Formability maps*. *Annual Review of Materials Science*, 1981. **11**(1): p. 505-521.
- [36] Emmens, W.C., *Formability: A review of parameters and processes that control, limit or enhance the formability of sheet metal*. 2011: Springer Science & Business Media.
- [37] Filice, L., L. Fratini, and F. Micari, *Analysis of material formability in incremental forming*. *CIRP annals-Manufacturing technology*, 2002. **51**(1): p. 199-202.
- [38] Kim, T. and D.-Y. Yang, *Improvement of formability for the incremental sheet metal forming process*. *International Journal of Mechanical Sciences*, 2000. **42**(7): p. 1271-1286.
- [39] Fratini, L., et al., *Influence of mechanical properties of the sheet material on formability in single point incremental forming*. *CIRP Annals-Manufacturing Technology*, 2004. **53**(1): p. 207-210.
- [40] Shim, M.-S. and J.-J. Park, *The formability of aluminum sheet in incremental forming*. *Journal of Materials Processing Technology*, 2001. **113**(1): p. 654-658.
- [41] Dieter, G.E. and D.J. Bacon, *Mechanical metallurgy*. Vol. 3. 1986: McGraw-hill New York.
- [42] Shakeri, M., A. Sadough, and B. Dariani, *Effect of pre-straining and grain size on the limit strains in sheet metal forming*. *Proceedings of the Institution of Mechanical Engineers, Part B: Journal of Engineering Manufacture*, 2000. **214**(9): p. 821-827.
- [43] Tajally, M. and E. Emadoddin, *Mechanical and anisotropic behaviors of 7075 aluminum alloy sheets*. *Materials and Design*, 2011. **32**(3): p. 1594-1599.

- [44] Marciniak, Z. and K. Kuczyński, *Limit strains in the processes of stretch-forming sheet metal*. International journal of mechanical sciences, 1967. **9**(9): p. 609IN1613-612IN2620.
- [45] Eyckens, P., A. Van Bael, and P. Van Houtte, *Marciniak–Kuczynski type modelling of the effect of through-thickness shear on the forming limits of sheet metal*. International Journal of Plasticity, 2009. **25**(12): p. 2249-2268.
- [46] Allwood, J.M. and D.R. Shouler, *Generalised forming limit diagrams showing increased forming limits with non-planar stress states*. International Journal of Plasticity, 2009. **25**(7): p. 1207-1230.
- [47] Obermeyer, E.J. and S.A. Majlessi, *A review of recent advances in the application of blank-holder force towards improving the forming limits of sheet metal parts*. Journal of Materials Processing Technology, 1998. **75**(1-3): p. 222-234.
- [48] Emmens, W. and A. Van den Boogaard, *Incremental forming by continuous bending under tension—an experimental investigation*. Journal of Materials Processing Technology, 2009. **209**(14): p. 5456-5463.
- [49] Yoshida, K., T. Kuwabara, and M. Kuroda, *Path-dependence of the forming limit stresses in a sheet metal*. International Journal of Plasticity, 2007. **23**(3): p. 361-384.
- [50] Milligan, R., W. Koo, and T. Davidson, *The Bauschinger effect in a high-strength steel*. Journal of Basic Engineering, 1966. **88**(2): p. 480-488.
- [51] Eyckens, P., et al. *Forming limit predictions for the serrated strain paths in single point incremental sheet forming*. in *AIP Conference Proceedings*. 2007. AIP.
- [52] Ha, J., M.-G. Lee, and F. Barlat, *Strain hardening response and modeling of EDDQ and DP780 steel sheet under non-linear strain path*. Mechanics of Materials, 2013. **64**: p. 11-26.
- [53] Gatea, S., H. Ou, and G. McCartney, *Review on the influence of process parameters in incremental sheet forming*. The International Journal of Advanced Manufacturing Technology, 2016. **87**(1-4): p. 479-499.
- [54] Martins, P., et al., *Theory of single point incremental forming*. CIRP Annals-Manufacturing Technology, 2008. **57**(1): p. 247-252.
- [55] Jackson, K. and J. Allwood, *The mechanics of incremental sheet forming*. Journal of materials processing technology, 2009. **209**(3): p. 1158-1174.
- [56] Kobayashi, S., I. Hall, and E. Thomsen, *A theory of shear spinning of cones*. Journal of Engineering for Industry, 1961. **83**(4): p. 485-494.
- [57] Lu, B., et al., *Mechanism investigation of friction-related effects in single point incremental forming using a developed oblique roller-ball tool*. International Journal of Machine Tools and Manufacture, 2014. **85**: p. 14-29.
- [58] Kalpakcioglu, S., *On the mechanics of shear spinning*. Journal of Engineering for Industry, 1961. **83**(2): p. 125-130.
- [59] Allwood, J., D. Shouler, and A.E. Tekkaya. *The increased forming limits of incremental sheet forming processes*. in *Key Engineering Materials*. 2007. Trans Tech Publ.

- [60] Fang, Y., et al., *Analytical and experimental investigations on deformation mechanism and fracture behavior in single point incremental forming*. Journal of Materials Processing Technology, 2014. **214**(8): p. 1503-1515.
- [61] Li, Y., et al., *Deformation mechanics and efficient force prediction in single point incremental forming*. Journal of Materials Processing Technology, 2015. **221**: p. 100-111.
- [62] Maqbool, F. and M. Bambach, *Dominant deformation mechanisms in single point incremental forming (SPIF) and their effect on geometrical accuracy*. International Journal of Mechanical Sciences, 2018. **136**: p. 279-292.
- [63] Xue, L., *Damage accumulation and fracture initiation in uncracked ductile solids subject to triaxial loading*. International journal of solids & structures, 2007. **44**(16): p. 5163-5181.
- [64] Malhotra, R., et al., *Mechanics of fracture in single point incremental forming*. Journal of Materials Processing Technology, 2012. **212**(7): p. 1573-1590.
- [65] Mirnia, M.J. and M. Shamsari, *Numerical prediction of failure in single point incremental forming using a phenomenological ductile fracture criterion*. Journal of Materials Processing Technology, 2017. **244**: p. 17-43.
- [66] Wu, S., N. Song, and F.A. Pires. *A Comparative Study of Failure with Incremental Forming*. in *Journal of Physics: Conference Series*. 2016. IOP Publishing.
- [67] Gatea, S., et al., *Modelling of ductile fracture in single point incremental forming using a modified GTN model*. Engineering Fracture Mechanics, 2017. **186**: p. 59-79.
- [68] Emmens, W. and A. Van den Boogaard, *An overview of stabilizing deformation mechanisms in incremental sheet forming*. Journal of Materials Processing Technology, 2009. **209**(8): p. 3688-3695.
- [69] Eyckens, P., et al., *Strain evolution in the single point incremental forming process: digital image correlation measurement and finite element prediction*. International journal of material forming, 2011. **4**(1): p. 55-71.
- [70] Demeri, M.Y., *The stretch-bend forming of sheet metal*. Journal of Applied Metalworking, 1981. **2**(1): p. 3-10.
- [71] El-Domiaty, A., M. Shabara, and M.J.T.I.J.o.A.M.T. Al-Ansary, *Determination of stretch-bendability of sheet metals*. 1996. **12**(3): p. 207-220.
- [72] Taraldsen, A., *Stabilized tensile testing (ie without local necking)*. Materialprüfung, 1964. **6**(6): p. 189-228.
- [73] Rosochowski, A. and L. Olejnik, *Damage evolution in mild steel*. J International journal of mechanical sciences, 1988. **30**(1): p. 51-60.
- [74] Benedyk, J., N. Parikh, and D. Stawarz, *A method for increasing elongation values for ferrous and nonferrous sheet metals (Ferrous and nonferrous sheet metals neck formation prevention for increasing elongation in tensile tests, using continuous plastic bending method)*. Journal of Materials, 1971. **6**: p. 16-29.
- [75] Silva, M., et al., *Revisiting single-point incremental forming and formability/failure diagrams by means of finite elements and experimentation*. The Journal of Strain Analysis for Engineering Design, 2009. **44**(4): p. 221-234.

- [76] Hussain, G., et al., *The effect of variation in the curvature of part on the formability in incremental forming: An experimental investigation*. International Journal of Machine Tools and Manufacture, 2007. **47**(14): p. 2177-2181.
- [77] Silva, M., et al., *Single-point incremental forming and formability—failure diagrams*. The journal of strain analysis for engineering design, 2008. **43**(1): p. 15-35.
- [78] Anderson, T.L., *Fracture mechanics: fundamentals and applications*. 2017: CRC press.
- [79] Hussain, G., L. Gao, and Z. Zhang, *Formability evaluation of a pure titanium sheet in the cold incremental forming process*. The International Journal of Advanced Manufacturing Technology, 2008. **37**(9): p. 920-926.
- [80] Isik, K., et al., *Formability limits by fracture in sheet metal forming*. Journal of Materials Processing Technology, 2014. **214**(8): p. 1557-1565.
- [81] Suresh, K. and S.P. Regalla, *Analysis of formability in single point incremental forming using finite element simulations*. Procedia Materials Science, 2014. **6**: p. 430-435.
- [82] Ai, S., et al., *Evaluation of deformation stability and fracture mechanism in incremental sheet forming*. International Journal of Mechanical Sciences, 2017. **124**: p. 174-184.
- [83] El-Sebaie, M. and P. Mellor, *Plastic instability conditions in the deep-drawing of a circular blank of sheet metal*. International Journal of Mechanical Sciences, 1972. **14**(9): p. 535-540.
- [84] Silva, M.B., et al., *Failure mechanisms in single-point incremental forming of metals*. The International Journal of Advanced Manufacturing Technology, 2011. **56**(9-12): p. 893-903.
- [85] Madeira, T., et al., *Failure in single point incremental forming*. The International Journal of Advanced Manufacturing Technology, 2015. **80**(9-12): p. 1471-1479.
- [86] Bambach, M., M. Todorova, and G. Hirt. *Experimental and numerical analysis of forming limits in CNC incremental sheet forming*. in *Key Engineering Materials*. 2007. Trans Tech Publ.
- [87] Emmens, W. and A.H. van den Boogaard, *Contact effects in bending affecting stress and formability*. International journal of material forming, 2010. **3**(1): p. 1159-1162.
- [88] Centeno, G., et al., *Critical analysis of necking and fracture limit strains and forming forces in single-point incremental forming*. Materials & Design, 2014. **63**: p. 20-29.
- [89] Morales, D., et al., *Bending effect in the failure of stretch-bend metal sheets*. International Journal of Material Forming, 2009. **2**: p. 813-816.
- [90] Stoughton, T.B. and J.W. Yoon, *A new approach for failure criterion for sheet metals*. International Journal of Plasticity, 2011. **27**(3): p. 440-459.
- [91] Seong, D., et al., *Suppression of necking in incremental sheet forming*. International Journal of Solids and Structures, 2014. **51**(15): p. 2840-2849.

- [92] Smith, L., et al., *Influence of transverse normal stress on sheet metal formability*. International Journal of Plasticity, 2003. **19**(10): p. 1567-1583.
- [93] Meier, H., C. Magnus, and V. Smukala, *Impact of superimposed pressure on dieless incremental sheet metal forming with two moving tools*. CIRP Annals-Manufacturing Technology, 2011. **60**(1): p. 327-330.
- [94] Valoppi, B., et al., *On the Fracture Characterization in Double-Sided Incremental Forming of Ti6Al4V Sheets at Elevated Temperatures*. Procedia Manufacturing, 2017. **10**: p. 407-416.
- [95] *ASTM E8/E8M-13 Standard test methods for tension testing of metallic materials*. 2013, ASTM International: West Conshohocken, PA.
- [96] *Abaqus User's Manual, Version 6.14-1*. Providence, RI: Dassault Systems Simulia Corp.
- [97] Yoon, J.Y., *Evaluation of Formability and Determination of Flow Stress Curve of Sheet Materials with Dome Test*. 2012, The Ohio State University.
- [98] Tucker, G., *Texture and earing in deep drawing of aluminium*. Acta Metallurgica, 1961. **9**(4): p. 275-286.
- [99] *ISO 16808 Metallic materials—sheet and strip—determination of biaxial stress-strain curve by means of bulge test with optical measuring systems*. 2013, ISO.
- [100] LĂZĂRESCU, L., et al., *Characterization of plastic behaviour of sheet metals by hydraulic bulge test*. 2012. **22**: p. s275-s279.
- [101] Groseclose, A., et al., *Determination of biaxial flow stress using frictionless dome test*. Procedia Engineering, 2014. **81**: p. 1079-1083.
- [102] Bruschi, S., et al., *Testing and modelling of material behaviour and formability in sheet metal forming*. CIRP Annals-Manufacturing Technology, 2014. **63**(2): p. 727-749.
- [103] *ISO 12004-1:2008 Metallic materials -- Sheet and strip -- Determination of forming-limit curves -- Part 1: Measurement and application of forming-limit diagrams in the press shop*. 2013, ISO.
- [104] Kikuma, T. and K. Nakazima. *Effects of deforming conditions and mechanical properties on the stretch-forming limits of steel sheets*. in *PROC INTERNAT CONF SCI TECHNOL IRON STEEL, TOKYO, 1971,--II--*, 827-831. 1971.
- [105] *ISO 16842 Metallic materials-Sheet and strip-Biaxial tensile testing method using a cruciform test piece*. 2014, ISO.
- [106] *Standard Test Methods for Tension Testing of Metallic Materials*. 2016, ASTM International.
- [107] Kuwabara, T., S. Ikeda, and K. Kuroda, *Measurement and analysis of differential work hardening in cold-rolled steel sheet under biaxial tension*. Journal of Materials Processing Technology, 1998. **s 80–81**(98): p. 517-523.
- [108] Hanabusa, Y., H. Takizawa, and T.J.J.o.M.P.T. Kuwabara, *Numerical verification of a biaxial tensile test method using a cruciform specimen*. 2013. **213**(6): p. 961-970.
- [109] Kelly, D., *Problems in creep testing under biaxial stress systems*. The Journal of Strain Analysis for Engineering Design, 1976. **11**(1): p. 1-6.

- [110] Hannon, A. and P. Tiernan, *A review of planar biaxial tensile test systems for sheet metal*. Journal of materials processing technology, 2008. **198**(1): p. 1-13.
- [111] Yu, Y., et al., *Design of a cruciform biaxial tensile specimen for limit strain analysis by FEM*. Journal of materials processing technology, 2002. **123**(1): p. 67-70.
- [112] Song, X., *Identification of forming limits of sheet metals with an in-plane biaxial tensile test*. 2018, INSA de Rennes.
- [113] Zidane, I., et al. *Optimization of biaxial tensile specimen shape from numerical investigations*. in *Numisheet 2008*. 2008.
- [114] Demmerle, S. and J.P. Boehler, *Optimal design of biaxial tensile cruciform specimens*. Journal of the Mechanics & Physics of Solids, 1993. **41**(1): p. 143-181.
- [115] Green, D., et al., *Experimental investigation of the biaxial behaviour of an aluminum sheet*. International Journal of Plasticity, 2004. **20**(8): p. 1677-1706.
- [116] Shao, Z., et al., *Development of a new biaxial testing system for generating forming limit diagrams for sheet metals under hot stamping conditions*. Experimental Mechanics, 2016. **56**(9): p. 1489-1500.
- [117] Ferron, G. and A. Makinde, *Design and development of a biaxial strength testing device*. Journal of Testing and Evaluation, 1988. **16**(3): p. 253-256.
- [118] Barroso, A., et al. *Biaxial testing of composites in uniaxial machines: manufacturing of a device, analysis of the specimen geometry and preliminary experimental results*. in *ECCM15-European conference on composite materials, Venice (Italy)*. 2012.
- [119] Merklein, M. and M. Biasutti, *Development of a biaxial tensile machine for characterization of sheet metals*. Journal of Materials Processing Technology, 2013. **213**(6): p. 939-946.
- [120] Wu, X.-D., M. Wan, and X.-B. Zhou, *Biaxial tensile testing of cruciform specimen under complex loading*. Journal of materials processing technology, 2005. **168**(1): p. 181-183.
- [121] Makinde, A., L. Thibodeau, and K. Neale, *Development of an apparatus for biaxial testing using cruciform specimens*. Experimental mechanics, 1992. **32**(2): p. 138-144.
- [122] Zwick/Roell. *Biaxial testing machine*. 2017; Available from: <https://www.zwick.com/biaxial-testing-machines/cruciform-testing-machine>.
- [123] Yin, Q., et al., *An experimental and numerical investigation of different shear test configurations for sheet metal characterization*. International Journal of Solids and Structures, 2014. **51**(5): p. 1066-1074.
- [124] Kim, J.H., et al., *The shear fracture of dual-phase steel*. International Journal of Plasticity, 2011. **27**(10): p. 1658-1676.
- [125] Miyauchi, K. *Stress--Strain Relationship in Simple Shear of In-Plane Deformation for Various Steel Sheets*. in *Efficiency in Sheet Metal Forming, IDDRG 13 th Biennial Congress*. 1984.
- [126] *ASTM B831-14 Standard Test Method for Shear Testing of Thin Aluminum Alloy Products*. 2014, ASTM International: West Conshohocken, PA.

- [127] Brosius, A., et al., *A new shear test for sheet metal characterization*. steel research international, 2011. **82**(4): p. 323-328.
- [128] Yoshida, F., T. Uemori, and K. Fujiwara, *Elastic–plastic behavior of steel sheets under in-plane cyclic tension–compression at large strain*. International Journal of Plasticity, 2002. **18**(5-6): p. 633-659.
- [129] Cláudio, R., L. Reis, and M. Freitas, *Biaxial high-cycle fatigue life assessment of ductile aluminium cruciform specimens*. Theoretical Applied Fracture Mechanics, 2014. **73**: p. 82-90.
- [130] Bauschinger, J., *On the change of position of the elastic limit of iron and steel under cyclic variations of stress*. Mitt. Mech.-Tech. Lab., Munich, 1886. **13**(1).
- [131] Stephens, R.I., et al., *Metal fatigue in engineering*. 2000: John Wiley & Sons.
- [132] *ASTM E606/E606M-12 Standard Test Method for Strain-Controlled Fatigue Testing*. 2012, ASTM International: West Conshohocken, PA.
- [133] Wilson, I. and D. White, *Cruciform specimens for biaxial fatigue tests: An investigation using finite-element analysis and photoelastic-coating techniques*. Journal of Strain Analysis, 1971. **6**(1): p. 27-37.
- [134] Hill, R., *The mathematical theory of plasticity*. Vol. 11. 1998: Oxford university press.
- [135] Swift, H.W., *Plastic instability under plane stress*. Journal of the Mechanics and Physics of Solids, 1952. **1**(1): p. 1-18.
- [136] Arrieux, R., *Determination and use of the forming limit stress diagrams in sheet metal forming*. Journal of Materials Processing Technology, 1995. **53**(1-2): p. 47-56.
- [137] Atkins, A., *Fracture mechanics and metal forming: damage mechanics and the local approach of yesterday and today*. Fracture Research in Retrospect, Balkema, Rotterdam, 1997: p. 327-350.
- [138] Chaboche, J., *Phenomenological aspects of continuum damage mechanics*, in *Theoretical and Applied Mechanics*. 1989, Elsevier. p. 41-56.
- [139] Keeler, S.P. and W.A. Backofen, *Plastic instability and fracture in sheets stretched over rigid punches*. Asm Trans Q, 1963. **56**(1): p. 25-48.
- [140] Goodwin, G.M., *Application of strain analysis to sheet metal forming problems in the press shop*. SAE Transactions, 1968: p. 380-387.
- [141] Emmens, W., D. van der Weijde, and A. van den Boogaard. *The FLC, enhanced formability, and incremental sheet forming*. in *Proceedings of the International Deep Drawing Research Group IDDRG 2009 International Conference*. 2009.
- [142] Kleemola, H. and M. Pelkkikangas, *Effect of predeformation and strain path on the forming limits of steel, copper and brass*. J Sheet Met Ind, 1977. **64**(6): p. 591-592.
- [143] Stoughton, T.B., *A general forming limit criterion for sheet metal forming*. International Journal of Mechanical Sciences, 2000. **42**(1): p. 1-27.
- [144] Stoughton, T.B. and J.W. Yoon, *Path independent forming limits in strain and stress spaces*. International Journal of Solids Structures, 2012. **49**(25): p. 3616-3625.

- [145] Haque, M.Z. and J.W. Yoon, *Stress based prediction of formability and failure in incremental sheet forming*. International journal of material forming, 2016. **9**(3): p. 413-421.
- [146] Muscat-Fenech, C., S. Arndt, and A. Atkins. *The determination of fracture forming limit diagrams from fracture toughness*. in *4th International Sheet Metal Conference, University of Twente, The Netherlands*. 1996.
- [147] Kachanov, L.M., *Rupture time under creep conditions*. International journal of fracture, 1999. **97**(1-4): p. 11-18.
- [148] Rabotnov, Y.N., *Creep problems in structural members*. 1969.
- [149] Chaboche, J.-L., *Continuum damage mechanics: Part I—General concepts*. Journal of applied mechanics, 1988. **55**(1): p. 59-64.
- [150] Jonas, J. and B. Baudelet, *Effect of crack and cavity generation on tensile stability*. Acta Metallurgica, 1977. **25**(1): p. 43-50.
- [151] Quoc, T.B., et al., *Cumulative fatigue damage under stress-controlled conditions*. Journal of Basic Engineering, 1971. **93**(4): p. 691-698.
- [152] Lemaitre, J., *A continuous damage mechanics model for ductile fracture*. Journal of engineering materials and technology, 1985. **107**(1): p. 83-89.
- [153] Lee, S.W. and F. Pourboghrat, *Finite element simulation of the punchless piercing process with Lemaitre damage model*. International journal of mechanical sciences, 2005. **47**(11): p. 1756-1768.
- [154] Hambli, R., *Comparison between Lemaitre and Gurson damage models in crack growth simulation during blanking process*. International Journal of Mechanical Sciences, 2001. **43**(12): p. 2769-2790.
- [155] Bariani, P., S. Bruschi, and A. Ghiotti, *Advances in predicting damage evolution and fracture occurrence in metal forming operations*. Journal of Manufacturing Processes, 2012. **14**(4): p. 495-500.
- [156] Garrison Jr, W. and N. Moody, *Ductile fracture*. Journal of Physics Chemistry of Solids, 1987. **48**(11): p. 1035-1074.
- [157] McClintock, F.A., *Plasticity aspects of fracture*, in *Engineering Fundamentals and Environmental Effects*. 1971, Elsevier. p. 47-225.
- [158] McClintock, F.A., *A criterion for ductile fracture by the growth of holes*. Journal of applied mechanics, 1968. **35**(2): p. 363-371.
- [159] Rice, J.R. and D.M. Tracey, *On the ductile enlargement of voids in triaxial stress fields\**. Journal of the Mechanics and Physics of Solids, 1969. **17**(3): p. 201-217.
- [160] Gurson, A.L., *Continuum theory of ductile rupture by void nucleation and growth: Part I—Yield criteria and flow rules for porous ductile media*. Journal of engineering materials and technology, 1977. **99**(1): p. 2-15.
- [161] Tvergaard, V. and A. Needleman, *Analysis of the cup-cone fracture in a round tensile bar*. Acta metallurgica, 1984. **32**(1): p. 157-169.
- [162] Tvergaard, V., *Shear deformation of voids with contact modelled by internal pressure*. International Journal of Mechanical Sciences, 2008. **50**(10-11): p. 1459-1465.

- [163] Xue, L., *Constitutive modeling of void shearing effect in ductile fracture of porous materials*. Engineering Fracture Mechanics, 2008. **75**(11): p. 3343-3366.
- [164] Nahshon, K. and J. Hutchinson, *Modification of the Gurson model for shear failure*. European Journal of Mechanics-A/Solids, 2008. **27**(1): p. 1-17.
- [165] Nielsen, K.L. and V. Tvergaard, *Effect of a shear modified Gurson model on damage development in a FSW tensile specimen*. International Journal of Solids and Structures, 2009. **46**(3-4): p. 587-601.
- [166] Tvergaard, V., K.L. Nielsen, and P.o. Solids, *Relations between a micro-mechanical model and a damage model for ductile failure in shear*. Journal of the Mechanics, 2010. **58**(9): p. 1243-1252.
- [167] Brocks, W., et al., *Application of the Gurson model to ductile tearing resistance, in Constraint Effects in Fracture Theory and Applications: Second Volume*. 1995, ASTM International.
- [168] Kami, A., et al., *Application of a GTN damage model to predict the fracture of metallic sheets subjected to deep-drawing*. Proceedings of the Romanian Academy, Series A, 2014. **15**: p. 300-309.
- [169] Ying, L., et al., *On the numerical implementation of a shear modified GTN damage model and its application to small punch test*. International Journal of Material Forming, 2017: p. 1-13.
- [170] Oyane, M., et al., *Criteria for ductile fracture and their applications*. Journal of Mechanical Working Technology, 1980. **4**(1): p. 65-81.
- [171] Cockcroft, M. and D. Latham, *Ductility and the workability of metals*. J Inst Metals, 1968. **96**(1): p. 33-39.
- [172] Johnson, G.R. and W.H. Cook, *Fracture characteristics of three metals subjected to various strains, strain rates, temperatures and pressures*. Engineering fracture mechanics, 1985. **21**(1): p. 31-48.
- [173] Wierzbicki, T., et al., *Calibration and evaluation of seven fracture models*. International Journal of Mechanical Sciences, 2005. **47**(4-5): p. 719-743.
- [174] Bai, Y. and T. Wierzbicki, *A new model of metal plasticity and fracture with pressure and Lode dependence*. International journal of plasticity, 2008. **24**(6): p. 1071-1096.
- [175] Malcher, L., F.A. Pires, and J.C. De Sá, *An assessment of isotropic constitutive models for ductile fracture under high and low stress triaxiality*. International Journal of Plasticity, 2012. **30**: p. 81-115.
- [176] Brüning, M., S. Gerke, and V. Hagenbrock, *Micro-mechanical studies on the effect of the stress triaxiality and the Lode parameter on ductile damage*. International Journal of Plasticity, 2013. **50**: p. 49-65.
- [177] Lou, Y., J.W. Yoon, and H. Huh, *Modeling of shear ductile fracture considering a changeable cut-off value for stress triaxiality*. International Journal of plasticity, 2014. **54**: p. 56-80.
- [178] Kumar, A., et al. *Failure prediction in incremental sheet forming based on Lemaitre damage model*. in *Journal of Physics: Conference Series*. 2018. IOP Publishing.

- [179] Wang, C., et al., *FEM Investigation of Ductile Fracture Prediction in Two-Point Incremental Sheet Metal Forming process*. Procedia engineering, 2017. **207**: p. 836-841.
- [180] Ilyas, M., G. Hussain, and C. Espinosa, *Failure and strain gradient analyses in incremental forming using GTN model*. International Journal of Lightweight Materials Manufacture, 2018.
- [181] Gatea, S., H. Ou, and G. McCartney. *Numerical simulation and experimental investigation of ductile fracture in SPIF using modified GTN model*. in *MATEC Web of conferences*. 2015. EDP Sciences.
- [182] Smith, J., et al. *Application of a shear-modified GTN model to incremental sheet forming*. in *AIP Conference Proceedings*. 2013. AIP.
- [183] Li, J., et al., *Numerical simulation of incremental sheet forming based on GTN damage model*. The International Journal of Advanced Manufacturing Technology, 2015. **81**(9-12): p. 2053-2065.
- [184] Chu, C. and A. Needleman, *Void nucleation effects in biaxially stretched sheets*. Journal of engineering materials and technology, 1980. **102**(3): p. 249-256.
- [185] Tvergaard, V., *Influence of voids on shear band instabilities under plane strain conditions*. International Journal of fracture, 1981. **17**(4): p. 389-407.
- [186] Tvergaard, V., *On localization in ductile materials containing spherical voids*. International Journal of fracture, 1982. **18**(4): p. 237-252.
- [187] Tvergaard, V., *Behaviour of voids in a shear field*. International Journal of Fracture, 2009. **158**(1): p. 41-49.
- [188] Reis, F., et al., *A comparison of shear mechanisms for the prediction of ductile failure under low stress triaxiality*. International Journal of Structural Integrity, 2010. **1**(4): p. 314-331.
- [189] Simo, J.C. and T.J. Hughes, *Computational inelasticity*. Vol. 7. 2006: Springer Science & Business Media.
- [190] Aravas, N., *On the numerical integration of a class of pressure-dependent plasticity models*. International Journal for numerical methods in engineering, 1987. **24**(7): p. 1395-1416.
- [191] Interational, A., *ASTM B831-14, Standard Test Method for Shear Testing of Thin Aluminum Alloy Products*. 2018.
- [192] Cao, T.-S., et al., *Characterization of ductile damage for a high carbon steel using 3D X-ray micro-tomography and mechanical tests—Application to the identification of a shear modified GTN model*. Computational Materials Science, 2014. **84**: p. 175-187.
- [193] Kami, A., et al., *Numerical determination of the forming limit curves of anisotropic sheet metals using GTN damage model*. Journal of Materials Processing Technology, 2015. **216**: p. 472-483.
- [194] Wang, X., et al., *Evaluating the applicability of GTN damage model in forward tube spinning of aluminum alloy*. Metals, 2016. **6**(6): p. 136.
- [195] Steglich, D., T. Siegmund, and W. Brocks, *Micromechanical modeling of damage due to particle cracking in reinforced metals*. Computational Materials Science, 1999. **16**(1-4): p. 404-413.

- [196] Guiglionda, G. and W. Poole, *The role of damage on the deformation and fracture of Al-Si eutectic alloys*. Materials Science and Engineering: A, 2002. **336**(1-2): p. 159-169.
- [197] Zhang, Z., C. Thaulow, and J. Ødegård, *A complete Gurson model approach for ductile fracture*. Engineering Fracture Mechanics, 2000. **67**(2): p. 155-168.
- [198] Chhibber, R., et al., *Estimation of Gurson material parameters in bimetallic weldments for the nuclear reactor heat transport piping system*. Proceedings of the Institution of Mechanical Engineers, Part C: Journal of Mechanical Engineering Science, 2008. **222**(12): p. 2331-2349.
- [199] Bhattacharya, A., et al., *Testing and modelling of material behaviour and formability in sheet metal forming*. Journal of Manufacturing Science & Engineering, 2016. **133**(6): p. 621-627.
- [200] Xu, D., et al., *Mechanism investigation for the influence of tool rotation and laser surface texturing (LST) on formability in single point incremental forming*. International Journal of Machine Tools and Manufacture, 2013. **73**: p. 37-46.
- [201] Ludwik, P., *Über den Einfluß der Deformationsgeschwindigkeit bei bleibenden Deformationen mit besonderer Berücksichtigung der Nachwirkungserscheinungen*. Physikalische Zeitschrift, 1909. **10**(12): p. 411-417.
- [202] Voce, E., *A practical strain hardening function*. Metallurgia, 1955. **51**: p. 219-226.
- [203] Min, H., L. Fuguo, and W. Zhigang, *Forming limit stress diagram prediction of aluminum alloy 5052 based on GTN model parameters determined by in situ tensile test*. Chinese Journal of Aeronautics, 2011. **24**(3): p. 378-386.
- [204] Brunet, M., S. Mguil, and F. Morestin, *Analytical and experimental studies of necking in sheet metal forming processes*. Journal of Materials Processing Technology, 1998. **80**: p. 40-46.
- [205] CHEN, Z.-y. and X.-h. DONG, *DUCTILE DAMAGE ANALYSIS FOR FRACTURE IN SHEET METAL FORMING BASED ON GTN MESOSCOPIC DAMAGE MODEL [J]*. Engineering Mechanics, 2009. **7**: p. 041.
- [206] Liu, J., W. Liu, and W. Xue, *Forming limit diagram prediction of AA5052/polyethylene/AA5052 sandwich sheets*. Materials & Design, 2013. **46**: p. 112-120.
- [207] Amaral, R., et al. *Evaluation of ductile failure models in Sheet Metal Forming*. in *MATEC Web of Conferences*. 2016. EDP Sciences.
- [208] Teng, B., W. Wang, and Y. Xu, *Ductile fracture prediction in aluminium alloy 5A06 sheet forming based on GTN damage model*. Engineering Fracture Mechanics, 2017. **186**: p. 242-254.
- [209] Feng, F., et al., *Application of a GTN damage model predicting the fracture of 5052-O aluminum alloy high-speed electromagnetic impaction*. Metals, 2018. **8**(10): p. 761.
- [210] Abbasi, M., et al., *Application of the GTN model to predict the forming limit diagram of IF-Steel*. Journal of Mechanical science and Technology, 2012. **26**(2): p. 345-352.

- [211] Minitab Inc, U., *MINITAB release 17: statistical software for windows*. 2014, Minitab Inc, USA.
- [212] Croarkin, C., P. Tobias, and C. Zey, *Engineering statistics handbook*. 2002: NIST iTL.
- [213] Chipperfield, A. and P. Fleming, *The MATLAB genetic algorithm toolbox*. 1995.
- [214] Liu, Y., S. Murakami, and Y. Kanagawa, *Mesh-dependence and stress singularity in finite element analysis of creep crack growth by continuum damage mechanics approach*. European journal of mechanics. A. Solids, 1994. **13**(3): p. 395-418.
- [215] Gen, M. and R. Cheng, *Genetic algorithms and engineering optimization*. Vol. 7. 2000: John Wiley & Sons.
- [216] Kang, J., et al., *Constitutive behavior of AA5754 sheet materials at large strains*. Journal of engineering materials and technology, 2008. **130**(3): p. 031004.
- [217] Gao, F., L. Gui, and Z. Fan, *Experimental and numerical analysis of an in-plane shear specimen designed for ductile fracture studies*. Experimental mechanics, 2011. **51**(6): p. 891-901.
- [218] Sun, Q., et al., *Analysis of edge crack behavior of steel sheet in multi-pass cold rolling based on a shear modified GTN damage model*. Theoretical and Applied Fracture Mechanics, 2015. **80**: p. 259-266.
- [219] Mobasher, B., *Textile fiber composites: Testing and mechanical behavior*, in *Textile Fibre Composites in Civil Engineering*. 2016, Elsevier. p. 101-150.
- [220] Nguyen, D., et al., *Finite element method study of incremental sheet forming for complex shape and its improvement*. Proceedings of the Institution of Mechanical Engineers, Part B: Journal of Engineering Manufacture, 2010. **224**(6): p. 913-924.
- [221] Benedetti, M., et al., *Single-point incremental forming of sheet metals: Experimental study and numerical simulation*. Proceedings of the Institution of Mechanical Engineers, Part B: Journal of Engineering Manufacture, 2017. **231**(2): p. 301-312.
- [222] Durante, M., et al., *The influence of tool rotation on an incremental forming process*. Journal of Materials Processing Technology, 2009. **209**(9): p. 4621-4626.
- [223] Essa, K., *Finite element prediction of deformation mechanics in incremental forming processes*. 2011, University of Birmingham.
- [224] Henrard, C., et al., *Forming forces in single point incremental forming: prediction by finite element simulations, validation and sensitivity*. Computational mechanics, 2011. **47**(5): p. 573-590.
- [225] Esmaeilpour, R., et al., *Comparison of 3D yield functions for finite element simulation of single point incremental forming (SPIF) of aluminum 7075*. International Journal of Mechanical Sciences, 2017. **133**: p. 544-554.
- [226] Nath, M., et al. *Comparison of Texture and Surface Finish Evolution During Single Point Incremental Forming and Formability Testing of AA 7075*. in *TMS Annual Meeting & Exhibition*. 2018. Springer.

- [227] Ducobu, F., E. Rivière-Lorphèvre, and E. Filippi, *On the introduction of adaptive mass scaling in a finite element model of Ti6Al4V orthogonal cutting*. Simulation Modelling Practice Theory, 2015. **53**: p. 1-14.
- [228] Wang, L. and H. Long, *Investigation of material deformation in multi-pass conventional metal spinning*. Materials & Design, 2011. **32**(5): p. 2891-2899.
- [229] Skjødt, M., et al., *Multi stage strategies for single point incremental forming of a cup*. International Journal of Material Forming, 2008. **1**(1): p. 1199-1202.
- [230] Kim, Y. and J. Park, *Effect of process parameters on formability in incremental forming of sheet metal*. Journal of materials processing technology, 2002. **130**: p. 42-46.
- [231] Silva, M., et al., *Revisiting the fundamentals of single point incremental forming by means of membrane analysis*. International Journal of Machine Tools and Manufacture, 2008. **48**(1): p. 73-83.
- [232] Guzmán, C.F., et al., *Damage prediction in single point incremental forming using an extended Gurson model*. International Journal of Solids and Structures, 2017.
- [233] Guzmán, C.F., *Experimental and numerical characterization of damage and application to incremental forming*. 2016, PhD thesis University of Liège <http://hdl.handle.net/2268/192884>.
- [234] Moser, N., et al. *An investigation into the mechanics of double-sided incremental forming using finite element methods*. in *AIP Conference Proceedings*. 2016. AIP Publishing.
- [235] Fu, Z., et al., *Tool path correction algorithm for single-point incremental forming of sheet metal*. The International Journal of Advanced Manufacturing Technology, 2013. **64**(9-12): p. 1239-1248.
- [236] Ai, S., B. Lu, and H. Long, *An analytical study of new material test method for tension under bending and compression in double side incremental forming*. Procedia Engineering, 2017. **207**: p. 1982-1987.
- [237] Schrader, G.F. and A.K. Elshennawy, *Manufacturing processes and materials*. 2000: Society of Manufacturing Engineers.
- [238] Jiang, W., Y. Li, and J. Su, *Modified GTN model for a broad range of stress states and application to ductile fracture*. European Journal of Mechanics-A/Solids, 2016. **57**: p. 132-148.
- [239] Flores, P., et al., *Model identification and FE simulations: effect of different yield loci and hardening laws in sheet forming*. International journal of plasticity, 2007. **23**(3): p. 420-449.

# 8 APPENDICES

APPENDIX 1 SUBROUTINE FOR SHEAR-MODIFIED GTN MODEL.....206

## APPENDIX 1 SUBROUTINE FOR SHEAR-MODIFIED GTN MODEL

```

subroutine vumat (
C-----
C Definition of the variables
C-----
C Read only variables -
C Variables passed in for information, cannot be redefined
1 nblock, ndir, nshr, nstatev, nfieldv, nprops, lanneal,
2 stepTime, totalTime, dt, cmname, coordMp, charLength,
3 props, density, strainInc, relSpinInc,
4 tempOld, stretchOld, defgradOld, fieldOld,
3 stressOld, stateOld, enerInternOld, enerInelasOld,
6 tempNew, stretchNew, defgradNew, fieldNew,
C Write only variables -
C Variables to be defined
5 stressNew, stateNew, enerInternNew, enerInelasNew )
C
include 'vaba_param.inc'
C
dimension props(nprops), density(nblock),
1 coordMp(nblock,*),
2 charLength(*), strainInc(nblock,ndir+nshr),
3 relSpinInc(*), tempOld(*),
4 stretchOld(*), defgradOld(*),
5 fieldOld(*), stressOld(nblock,ndir+nshr),

```

6 stateOld(nblock,nstatev), enerInternOld(nblock),  
 7 enerInelasOld(nblock), tempNew(\*),  
 8 stretchNew(\*), defgradNew(\*), fieldNew(\*),  
 9 stressNew(nblock,ndir+nshr), stateNew(nblock,nstatev),  
 10 enerInternNew(nblock), enerInelasNew(nblock)

C

dimension sig(ndir+nshr), dy(ndir+nshr), ss(ndir+nshr),  
 11 st(ndir+nshr), Prin\_Stress(3), Prin\_Strain(3)  
 dimension xnorm(nblock, ndir+nshr), xstress(ndir+nshr),  
 12 xstressNew(ndir+nshr), princStress(3), princStressNew(3),  
 13 sPrime(3)

C-----

C Definition of constants

C-----

parameter (zero=0., one=1., two=2., three=3., six=6.,nine=9.,  
 14 half=0.5, threeHalves=1.5, third=one/three, twoThirds=two/three,  
 15 newton=50, toler=1.0d-6, toler2 = 1.0d-10,  
 16 pi=3.14159265358979323846)

C-----

C For plane strain, axisymmetric, and 3D cases using  
 C the GTN\_SHEAR damage model with von Mises equivalent  
 C stress and piecewise-linear isotropic hardening.

C-----

C

C-----

C User- input material mechanical properties  
 C props(1) Young's modulus

## Appendices

- C props(2) Poisson's ratio
- C props(3-5) the constants in the GTN model q1-q3
- C props(6-9) vvf related parameters in GTN model
- C xmu -- G shear modulus
- C alamda -- lame constant
- C xkv -- bulk modulus

C-----

e = props(1)

xnu = props(2)

q1 = props(3)

q2 = props(4)

q3 = props(5)

C

f0 = props(6)

fn = props(7)

fc=props(8)

ff=props(9)

C

en = props(10)

sn = props(11)

C

skw = props(12)

C

nflag\_Tension = props(13)

C

fu=one/q1

nvalue = nprops / 2 - 10

C

$$\text{twomu} = e / (\text{one} + x_{\text{nu}})$$

$$x_{\text{mu}} = \text{half} * \text{twomu}$$

$$\text{threemu} = \text{threeHalves} * \text{twomu}$$

$$\text{sixmu} = \text{three} * \text{twomu}$$

$$\text{alamda} = x_{\text{nu}} * \text{twomu} / (\text{one} - \text{two} * x_{\text{nu}})$$

$$x_{\text{kv}} = \text{twomu} * (\text{one} + x_{\text{nu}}) / (\text{three} * (\text{one} - \text{two} * x_{\text{nu}}))$$

C

C-----

C Elasticity part, beginning of the deformation, before yielding happens,

C follow Hooke's Law

C-----

```
if ( stepTime .eq. zero ) then
```

```
  do i = 1, nblock
```

```
    trace = strainInc(i,1) + strainInc(i,2) + strainInc(i,3)
```

```
    stressNew(i,1) = stressOld(i,1) + twomu * strainInc(i,1) +
```

```
    █                                alamda * trace
```

```
    stressNew(i,2) = stressOld(i,2) + twomu * strainInc(i,2) +
```

```
    █                                alamda * trace
```

```
    stressNew(i,3) = stressOld(i,3) + twomu * strainInc(i,3) +
```

```
    █                                alamda * trace
```

```
    stressNew(i,4) = stressOld(i,4) + twomu * strainInc(i,4)
```

C

```
if ( nshr .gt. 1 ) then
```

```
  stressNew(i,5) = stressOld(i,5) + twomu * strainInc(i,5)
```

```
  stressNew(i,6) = stressOld(i,6) + twomu * strainInc(i,6)
```

```
end if
```

end do

else

C-----

C In this part, trial stress/back stress based on Hook's Law will be

C calculated first to check if yielding condition has been met

C eqplasOld -- equivalent plastic strain STATE(\*,1)

C fOld -- void volume fraction STATE(\*,2)

C Element deletion flag-- STATE(\*,3)

C YieldOld/YieldNew---equivalent microscopic stress STATE(\*,4)

C fmod -- standarized vvf

C-----

do i = 1, nblock

nflag = 0

C

C Calculate stress and strain based on ealstic hypothesis

C

trace = strainInc(i,1) + strainInc(i,2) + strainInc(i,3)

stressNew(i,1) = stressOld(i,1)+ twomu \* strainInc(i,1) +

■ alamda \* trace

stressNew(i,2) = stressOld(i,2)+ twomu \* strainInc(i,2) +

■ alamda \* trace

stressNew(i,3) = stressOld(i,3)+ twomu \* strainInc(i,3) +

■ alamda \* trace

stressNew(i,4)=stressOld(i,4) + twomu \* strainInc(i,4)

C

if ( nshr .gt. 1 ) then

stressNew(i,5)=stressOld(i,5) + twomu \* strainInc(i,5)

```
stressNew(i,6)=stressOld(i,6) + twomu * strainInc(i,6)
```

```
end if
```

```
C
```

```
do k1=1, ndir+nshr
```

```
sig(k1) = stressNew(i, k1)
```

```
end do
```

```
C
```

```
C Mean stress calculation
```

```
smean = third * (sig(1) + sig(2) + sig(3))
```

```
C
```

```
C von Mises stress calculation
```

```
smises = (sig(1) - sig(2)) ** 2 + (sig(2) - sig(3)) ** 2 +
```

```
■ (sig(3) - sig(1)) ** 2
```

```
do k1 = ndir + 1, ndir + nshr
```

```
smises = smises + six * sig(k1) ** 2
```

```
end do
```

```
smises = sqrt(smises / two)
```

```
C
```

```
C Stress triaxiality calculation
```

```
tri = smean / smises
```

```
C
```

```
C Calculate shear related parameters
```

```
call vsprinc( 1, sig, Prin_Stress, ndir, nshr )
```

```
C
```

```
do k2 = 1, 3
```

```
sPrime(k2)=Prin_Stress(k2) - smean
```

```
end do
```

C

```
sj = sPrime(1) * sPrime(2) * sPrime(3)
w = 1.0 - (( 27.0 * sj ) / ( 2.0 * smises ** 3)) ** 2
```

C

```
eqplas0 = stateOld(i,1)
eqplas = eqplas0
```

C

```
syield0 = stateOld(i,7)
if ( syield0 .lt. 0.1 )    syield0 = props(21)
syield = syield0
```

C

C Equivalent strain

```
equi_strain = (strainInc(i,1)) ** 2 + (strainInc(i,2)) ** 2
+ (strainInc(i,3)) ** 2
do k1 = ndir + 1 , ndir + nshr
    equi_strain = equi_strain + two * (strainInc(i,k1)) ** 2
end do
equi_strain = sqrt( two / three * equi_strain )
```

C

C Equivalent strain rate

```
rate = (strainInc(i,1) / dt) ** 2 + (strainInc(i,2) / dt)** 2 +
+ (strainInc(i,3) / dt) ** 2
do k1 = ndir + 1 , ndir + nshr
    rate = rate + two * (strainInc(i,k1) / dt) ** 2
end do
rate = sqrt( two / three * rate )
```

C

C The vvf

```

fi = stateOld(i,2)

if (fi .lt. f0)  fi = f0

freal = fi

if (freal .lt. fc) then

    xkf=one

else

    xkf= (fu-fc)/(ff-fc)

end if

f=fc+xkf*(freal-fc)

```

C

C GTN yield function

```

gtnp1 = ( smises / syield ) ** 2

gtnp2 = two * f * q1 * cosh( three / two * q2 * smean / syield )

gtnp3 = one + q3 * ( f ** 2 )

fai = gtnp1 + gtnp2 - gtnp3

```

C

C Plastic modification

```

if( fai .ge. toler ) then

    nflag = 1

```

C

C Initialization of the variables in the iteration

```

dp = zero

dq = zero

deqps = zero

```

C Nucleation closure if stress triaxiality is negative

```

if (tri .ge. toler) then

```

```
A0 = fn / sqrt( two * pi ) / sn * exp(zero -
```

```
█ ( ( eqplas0 - en ) / sn ) ** 2 / two )
```

```
else
```

```
    A0 = zero
```

```
end if
```

```
C
```

```
    A = A0
```

```
C
```

```
    p = -smean
```

```
    q = smises
```

```
    fgr = zero
```

```
    fnu = zero
```

```
C-----
```

```
C Newton-Raphson Iteration
```

```
C-----
```

```
    do kewton = 1 , newton
```

```
C
```

```
    call vuhard(syield1, hard, eqplas, nvalue, props(21))
```

```
C
```

```
    xgp=-three*q1*q2*f/syield1*sinh(-threeHalfs*q2*p/syield1)
```

```
    xgq=two*q/(syield1**2)
```

```
    f1=-(dq*xgp + dp*xgq)
```

```
    f2=-((q/syield)**2+two*q1*f*
```

```
█ cosh(-threeHalfs*q2*p/syield)-(1.d0+q3*f**2))
```

```
C
```

```
    if( abs(f1) .ge. toler .OR. abs(f2) .ge. toler ) then
```

```
C
```

C Calculate deep and deeq

C Partial derivatives of the variables

C

$$xhH1=(p*dp-q*dq)/((1.d0-freal)*(syield1**2))*hard$$

$$xhH2=(-p*dp+q*dq)/((1.d0-freal)**2*syield1)$$

$$xh2H1=A*xhH1+A*((en-eqplas)/(sn**2))*deqps$$

$$xh2H2=-dp+A*xhH2$$

$$xhp=-dp/((1.d0-freal)*syield1)$$

$$xh2p=A*xhp$$

$$xhq=dq/((1.d0-freal)*syield1)$$

$$xh2q=A*xhq$$

$$xhdp=-(p+xkv*dp)/((1.d0-freal)*syield1)$$

$$xh2dp=(1.d0-freal)+A*xhdp$$

$$xhdq=q/((1.d0-freal)*syield1)$$

$$xh2dq=A*xhdq$$

C

$$c11=(1.d0-xh2H2)/((1.d0-xhH1)*(1.d0-xh2H2)-xhH2*xh2H1)$$

$$c12=xhH2/(-xhH2*xh2H1+(1.d0-xhH1)*(1.d0-xh2H2))$$

$$c21=xh2H1/((1.d0-xhH1)*(1.d0-xh2H2)-xhH2*xh2H1)$$

$$c22=(1.d0-xhH1)/(-xhH2*xh2H1+(1.d0-xhH1)*(1.d0-xh2H2))$$

C

$$xH1dp=c11*(xhdp+xkv*xhp)+c12*(xh2dp+xkv*xh2p)$$

$$xHH2dp=c21*(xhdp+xkv*xhp)+c22*(xh2dp+xkv*xh2p)$$

$$xH1dq=c11*(xhdq-threemu*xhq)+c12*(xh2dq-threemu*xh2q)$$

$$xHH2dq=c21*(xhdq-threemu*xhq)+c22*(xh2dq-threemu*xh2q)$$

C

$$xgp=-three*q1*q2*f/syield1*sinh(-threeHalfs*q2*p/syield1)$$

$$xgq=two*q/(syield1**2)$$

$$xgp2=nine*q1*q2*q2*f*cosh(-threeHalfs*q2*p/syield1)$$

$$*/(two*syield1**2)$$

$$xgq2=two/(syield1**2)$$

$$xgpq=zero$$

C

$$xgH1=(-two*(q**2)/(syield1**3)+three*q1*q2*p*f/(syield1**2)$$

$$*sinh(-threeHalfs*q2*p/syield1))*hard$$

$$xgH2=two*q1*xkf*cosh(-threeHalfs*q2*p/syield1)-two*q3$$

$$*xkf*f$$

$$xgpH1=hard*three*q1*q2*f/(syield1**2)*$$

$$(sinh(-threeHalfs*q2*p/syield1)$$

$$+(-threeHalfs*q2*p/syield1)$$

$$*cosh(-threeHalfs*q2*p/syield1))$$

$$xgpH2=-three*q1*q2/syield1*xkf*sinh(-threeHalfs*q2*p/syield1)$$

$$xgqH1=-four*q/(syield1**3)*hard$$

$$xgqH2=zero$$

C Solve ddp ddq

$$xf1dp=xgq + dp*xgqH1 *xH1dp+dq*(xgp2*xkv+xgpH1 *xH1dp+xgpH2*xHH2dp)$$

$$xf1dq=xgp + dp*(xgq2*(-threemu)+xgqH1 *xH1dq)$$

$$+ dq*(xgpH1 *xH1dq+xgpH2*xHH2dq)$$

$$xf2dp= xgp*xkv + xgH1 *xH1dp + xgH2*xHH2dp$$

$$xf2dq= xgp*(-threemu) + xgH1 *xH1dq + xgH2*xHH2dq$$

$$b1= -(dq*xgp + dp*xgq)$$

$$b2=-((q/syield1)**2+two*q1*f*$$

$$cosh(-threeHalfs*q2*p/syield1)-(one+q3*f**2))$$

C-----

$$ddq=(b1*xf2dp-b2*xf1dp)/(xf1dq*xf2dp-xf2dq*xf1dp)$$

$$ddp=(b1*xf2dq-b2*xf1dq)/(xf1dp*xf2dq-xf1dq*xf2dp)$$

C

$$dp = dp + ddp$$

$$dq = dq + ddq$$

C

$$p = -smean + xkv * dp$$

$$q = smises - threemu * dq$$

$$deqps = (-p * dp + q * dq) / ((one - freal) * syield1)$$

C

C Void evolution

$$fgr = (one - freal) * dp$$

$$fnu = A * deqps$$

C

C Update stress components

do k1 = 1 , ndir

$$ss(k1) = -p + (sig(k1) - smean) / smises * q$$

end do

do k1 = ndir + 1 , ndir + nshr

$$ss(k1) = sig(k1) / smises * q$$

end do

C

C fshear update

call vsprinc( 1, ss, Prin\_Stress, ndir, nshr )

$$sj = (Prin\_Stress(1) + p) * (Prin\_Stress(2) + p) *$$

$$\blacksquare (Prin\_Stress(3) + p)$$

$$w = 1.0 - ((27.0 * sj) / (2.0 * q ** 3)) ** 2$$

```
fshear = skw * freal * w * dq
```

C

```
df= fgr + fnu + nflag_Tension * fshear
```

```
freal = fi + df
```

```
if (freal .lt. fc) then
```

```
    xkf=one
```

```
else
```

```
    xkf=(fu-fc)/(ff-fc)
```

```
end if
```

```
f=fc+xkf*(freal-fc)
```

C

```
eqplas = eqplas0 + deqps
```

C

```
if ((-p) .ge. toler) then
```

```
    A1 = fn / sqrt( two * pi ) / sn * exp(zero -
```

```
    ( ( eqplas - en ) / sn ) ** 2 / two )
```

```
else
```

```
    A1 = zero
```

```
end if
```

C

```
A=A1
```

C

```
call vuhard(syield, hard1, eqplas, nvalue, props(21))
```

C

C Check convergence

```
else
```

```
exit
```

end if

ncount=ncount+1

end do

C Update state variables

stateNew(i,1) = eqplas

stateNew(i,2) = freal

C

stateNew(i,3) = stateOld(i,3) + fgr

stateNew(i,4) = stateOld(i,4) + fnu

stateNew(i,5) = stateOld(i,5) + fshear

C

C the value of 1 means the points are active, 0 means deletion

if (stateNew(i,2) .le. ff) then

stateNew(i,6)= one

else

stateNew(i,6)= zero

end if

C

stateNew(i,7)= syield1

C Update plastic strain

do k1 = 1, ndir

dy(k1) = dp / three +

■ three / two \* dq / smises \* (sig(k1) - smean)

end do

do k1 = ndir + 1, ndir + nshr

dy(k1) = three / two \* dq / smises \* sig(k1)

end do

```
do k1 = 10 , 10 + ndir + nshr - 1
    stateNew(i,k1) = stateOld(i,k1) + dy(k1-9)
end do
```

C

C Get principle strain

```
do k1 = 10 , 10 + ndir + nshr - 1
    st(k1-9) = stateNew(i,k1)
end do

call vsprinc( 1 , st , Prin_Strain, ndir, nshr )

do k1 = 1 , 2
    if ( Prin_Strain(k1) .lt. Prin_Strain(k1+1) ) then
        temp = Prin_Strain(k1)
        Prin_Strain(k1) = Prin_Strain(k1+1)
        Prin_Strain(k1+1) = temp
    end if
end do

if ( Prin_Strain(1) .lt. Prin_Strain(2) ) then
    temp = Prin_Strain(1)
    Prin_Strain(1) = Prin_Strain(2)
    Prin_Strain(2) = temp
end if
```

C

C Update stress

```
do k1 = 1 , ndir
    stressNew(i,k1) = -p + ( sig(k1) - smean ) / smises * q
end do

do k1 = ndir + 1 , ndir + nshr
```

```
stressNew(i,k1) = sig(k1) / smises * q
```

```
end do
```

C

C Stress triaxiality

C

```
stateNew(i,18) = -p / q
```

```
stateNew(i,19) = ( stressNew(i,1) + stressNew(i,2) +
```

```
stressNew(i,3) ) / three / q
```

C

```
stateNew(i,20) = stateOld(i,20) + skw * freal * w * sd / q
```

```
stateNew(i,24) = dt
```

```
stateNew(i,25) = equi_strain
```

```
stateNew(i,26) = kewton
```

```
stateNew(i,27) = deqps
```

```
stateNew(i,28) = dp
```

```
stateNew(i,29) = dq
```

```
stateNew(i,30) = nflag
```

C

C Update the specific internal energy

```
stressPower = one / two * (
```

```
stressOld(i,1) + stressNew(i,1) ) * strainInc(i,1)
```

```
+ ( stressOld(i,2) + stressNew(i,2) ) * strainInc(i,2)
```

```
+ ( stressOld(i,3) + stressNew(i,3) ) * strainInc(i,3) )
```

```
do k1 = ndir + 1 , ndir + nshr
```

```
stressPower = stressPower + two * ( stressOld(i,k1) +
```

```
stressNew(i,k1) ) * strainInc(i,k1)
```

```
end do
```

C

```
enerInternNew(i) = enerInternOld(i) + stressPower / density(i)
```

C

C Update the dissipated inelastic specific energy -

```
plasticWorkInc = one / two * (
    * ( stressOld(i,1) + stressNew(i,1) ) * dy(1)
    * + ( stressOld(i,2) + stressNew(i,2) ) * dy(2)
    * + ( stressOld(i,3) + stressNew(i,3) ) * dy(3) )
do k1 = ndir + 1 , ndir+nshr
    plasticWorkInc = plasticWorkInc +
    * two * ( stressOld(i,k1) + stressNew(i,k1) ) * dy(k1)
end do
enerInelasNew(i) = enerInelasOld(i)
    * + plasticWorkInc / density(i)
```

C-----

C Purely Elastic

C-----

```
else
stateNew(i,1) = stateOld(i,1)
stateNew(i,2) = fi
stateNew(i,3) = stateOld(i,3)
stateNew(i,4) = stateOld(i,4)
stateNew(i,5) = stateOld(i,5)
```

C

```
if (stateNew(i,2) .le. ff) then
    stateNew(i,6) = one
else
```

```
stateNew(i,6)= zero
```

```
end if
```

C

```
stateNew(i,7) = syield0
```

```
stateNew(i,8) = w
```

```
do k1 = 10 , 10 + ndir + nshr - 1
```

```
stateNew(i,k1) = stateOld(i,k1)
```

```
end do
```

```
stateNew(i,16) = stateOld(i,16)
```

C

C Update the specific internal energy

```
stressPower = one / two * (
```

```
█ ( stressOld(i,1) + stressNew(i,1) ) * strainInc(i,1)
```

```
█ + ( stressOld(i,2) + stressNew(i,2) ) * strainInc(i,2)
```

```
█ + ( stressOld(i,3) + stressNew(i,3) ) * strainInc(i,3) )
```

```
do k1 = ndir + 1 , ndir + nshr
```

```
stressPower = stressPower + two * ( stressOld(i,k1) +
```

```
█ stressNew(i,k1) ) * strainInc(i,k1)
```

```
end do
```

C

```
enerInternNew(i) = enerInternOld(i)
```

```
█ + stressPower / density(i)
```

C

C Update the dissipated inelastic specific energy -

```
enerInelasNew(i) = enerInelasOld(i)
```

```
end if
```

```
end do
```

C

end if

C

return

end

C

C-----

C Material hardening subroutine vuhard, stepwise

C-----

subroutine vuhard (syield, hard, eqplas, nvalue, table)

include 'vaba\_param.inc'

C

dimension table(2\*nvalue)

C

parameter(zero=0.)

C

C Set yield stress to last value of table, hardening to zero

C

syield=table(nvalue)

hard=zero

C

C If more than one entry, search table

C

if(nvalue.gt.1) then

do k1=1, nvalue-1

eqpl1=table(nvalue+k1+1)

if(eqplas.lt.eqpl1) then

```
eqpl0=table(nvalue+k1)
```

```
C
```

```
C Yield stress and hardening
```

```
C
```

```
deqpl=eqpl1-eqpl0
```

```
syiel0=table(k1)
```

```
syiel1=table(k1+1)
```

```
dsyiel=syiel1-syiel0
```

```
hard=dsyiel/deqpl
```

```
syield=syiel0+(eqpl1-eqpl0)*hard
```

```
C
```

```
exit
```

```
end if
```

```
end do
```

```
end if
```

```
C
```

```
return
```

```
end
```